UNIVERSITY OF SOUTHAMPTON

FACULTY OF ENGINEERING AND PHYSICAL SCIENCES

ENGINEERING SCIENCES

Complexity of flow motion

by

Marjola Thanaj

Thesis for the degree of Doctor of Philosophy

March 2020

UNIVERSITY OF SOUTHAMPTON

ABSTRACT

FACULTY OF ENGINEERING AND PHYSICAL SCIENCES

Biomedical Engineering

Thesis for the degree of Doctor of Philosophy

Complexity of flow motion

by Marjola Thanaj

The analysis of complex physiologic time series has been the focus of considerable attention since simple mathematical models cannot be found to describe them. Signals derived from skin microvascular networks using Laser Doppler flowmetry (LDF) have been broadly investigated using both linear and nonlinear dynamical methods providing significant information about the microvascular function. This study aims to explore complexity methods that can quantify the changes in the complex flow motion characteristics from the human microcirculation in a range of pathophysiological states.

Time and frequency domain analysis were used to define the signal values from the microvascular perfusion and their power contribution using the spectral analysis to quantify the different properties modulating the network perfusion. Nonlinear complexity methods were used to quantify the signal regularity by evaluating the presence of repeated patterns providing complexity variants at single and across multiple spatial and temporal scales. Further, a new approach, attractor reconstruction analysis, was used providing quantitative measures of the microvascular system in phase space and a visual representation in the shape and variability of the signal producing a two-dimensional attractor with features like density and symmetry.

The skin blood flux (BF) and tissue oxygenation (OXY) signals obtained from a combined Laser Doppler flowmetry (LDF) and white light spectroscopy (WLS) device were investigated using time domain, frequency domain and the nonlinear methods in the skin of a healthy cohort during increased local warming. This study revealed multiple oscillatory components with a remarkable increase in the cardiac activity during thermally induced vasodilation. There was also shown a significant attenuation in the complexity across multiple scales and a significant drop in the attractor density measures during increased local warming.

Subsequently, both linear and nonlinear methods were used to investigate the LDF signals obtained from groups of individuals at an increased cardiovascular disease (CVD) risk, categorised

with presence or absence of type 2 diabetes and use of calcium channel blocker (CB) medication. The results showed an increase on the high frequency cardiac activity with CB treatment. There was a significant decrease in the complexity of the blood flux signals as the CVD risk increases across multiple time scales. Also, there is a decline with progression of CVD risk in the measures derived from attractor reconstruction analysis. The highest separability between these groups was achieved using the attractor and complexity measures combined.

In conclusion, time and frequency domain analysis alone were insufficient to estimate the complex dynamics of the microvascular network during the application of a standard stressor. Nonlinear analysis provides a better characterisation of the flexibility of the system in a range of pathophysiological conditions. Together these mathematical approaches were able to quantify different microvascular functional states. With machine learning techniques this should allow the classification of the tissue perfusion features providing a use for clinical assessment.

Table of Contents

List of Tables

List of Tables

List of Figures

List of Figures

List of Figures

DECLARATION OF AUTHORSHIP

I, Marjola Thanaj declare that this thesis and the work presented in it are my own and has been generated by me as the result of my own original research.

Complexity of flow motion

I confirm that:

1. This work was done wholly or mainly while in candidature for a research degree at this University;
2. Where any part of this thesis has previously been submitted for a degree or any other qualification at this University or any other institution, this has been clearly stated;
3. Where I have consulted the published work of others, this is always clearly attributed;
4. Where I have quoted from the work of others, the source is always given. With the exception of such quotations, this thesis is entirely my own work;
5. I have acknowledged all main sources of help;
6. Where the thesis is based on work done by myself jointly with others, I have made clear exactly what was done by others and what I have contributed myself;
7. [Delete as appropriate] None of this work has been published before submission [or] Parts of this work have been published as: [please list references below]:

Signed: .....

Date: .....

Acknowledgements

Throughout my PhD and the writing of this thesis I have received a great deal of support and assistance. These three years have been an incredible journey and learning experience, gaining excellent technical and team working skills and meeting great people along the way. First, I would like to thank my supervisors, Dr. Andrew Chipperfield and Prof. Geraldine Clough, whose mentoring and expertise was invaluable in the formulating of the research topic and methodology in particular. Your expertise, assistance, guidance and encouragement have been very generous and helpful in continually improving the quality of the research.

I would like to thank the UK Engineering and Physical Sciences Research Council for funding my research. I would also like to acknowledge Katarzyna Z. Kuliga and Eleonora Scorletti for recruiting the study participants.

Thank you to my family in Greece for their moral support and to my beloved brother in the U.S for always supporting and encouraging me throughout my PhD. In addition, I would like to thank my colleagues and office mates, Kam, Mim, Josh, He, Mostafa and all my friends here in Southampton for making me stay enjoyable. Thank you for all great moments we spent together.

Thanaj Marjola

Southampton, UK

March 2020

Definitions and Abbreviations

ApEn	Approximate Entropy
AU	Arbitrary Unit
AVA shunts	Arterio-Venous Anastomosis shunts
BZ	Biological Zero
BF	Blood Flux
CB	Calcium channel Blocker
CD	Correlation Dimension
CVD	Cardiovascular Disease
deoxyHb	Deoxygenated Haemoglobin
DM0	Absence of type 2 diabetes mellitus
DM1	Presence of type 2 diabetes mellitus
ETC	Effort To Compress complexity
FFT	Fast Fourier Transform
FT	Fourier Transform
IQR	Interquartile Range
LDF	Laser Doppler Flowmetry
LL	Lowlanders
LLE	Largest Lyapunov Exponent
LOO	Leave-One-Out Cross-Validation Discriminant Analysis
LZC	Lempel and Ziv Complexity
METC	Multiscale Effort To Compress complexity
MSE	Multiscale Entropy
MLZC	Multiscale Lempel and Ziv Complexity

NAFLD	Non-Alcoholic Fatty Liver Disease
NASH	Non-Alcoholic SteatoHepatitis
NSRPS	Non-Sequential Recursive Pair Substitution
oxyHb	Oxygenated Haemoglobin
OXY	Tissue Oxygenation
PU	Laser Doppler Perfusion Unit
PORH	Post-Occlusive Reactive Hyperaemia
PSD	Power Spectral Density
SampEn	Sample Entropy
SD	Standard Deviation
SO_2	Oxygen Saturation (%)
SPAR	Symmetric Projection Attractor Reconstruction
SVM	Support Vector Machine
T2DM	Type 2 Diabetes Mellitus
totalHb	Total haemoglobin
WT	Wavelet Transform
WLS	White Light Spectroscopy

Chapter 1: Introduction

In recent years, the occurrence of cardiovascular diseases (CVD) has increased dramatically [1]. Chronic diseases related to CVD, such as diabetes and obesity, are the leading causes of death worldwide. According to Diabetes UK, 2.9 million people are diagnosed with diabetes in the United Kingdom and it is estimated that by 2035 this number will rise up to 6.25 million people increasing the cost of CVD to the National Health Service (NHS) budget by a further 40% from current spending levels [1-3]. Changes in the circulatory system arising from these diseases are very significant factors in morbidity and mortality. This research will investigate novel approaches to assessing the microcirculation with the ultimate aim of improving diagnoses and therapeutic interventions. Non-invasive medical devices are very useful nowadays for monitoring of the blood flux and have an important impact on pathophysiological assessment and they help to enhance diagnosis made by professionals. Earlier detection of vascular dysfunction and its degradation is a potentially valuable tool for improving interventions in healthcare and evaluating new therapies.

Signal processing methods have improved the utility of biomedical engineering applications and they can provide useful information for diagnosis. Biosignal analysis have proven very useful for identifying characteristics of the blood flux and provide information about health or disease. For that reason the investigation of the complex dynamics in blood flux signals as a metric of (micro)vascular function is a promising technique as there is evidence that it can detect changes in the small vessels before they present in the larger ones [4].

This chapter provides an overview of biomedical signals obtained from such non-invasive devices used to conduct this research and the main physiological factors that influence the microvascular blood flow. The main objectives of the research are identified and an overview of the structure of this thesis is presented. Finally, a list of publication derived from the work of this thesis is given.

1.1 Overview

In general, biomedical signals are those which arise in living organisms that can be continually measured and monitored. Common and well-known examples include those that measure electrical activity, such as Electroencephalogram (EEG), electrocardiogram (ECG) [5, 6] and electromyogram (EMG) [7], all of which are established in clinical usage. Biomedical signal processing refers to a range of techniques encompassing the fundamental theory, applications, algorithms and implementations of techniques that transform a raw biosignal from an abstract

measurement to a meaningful interpretation. This includes spectral analysis to determine the power-frequency composition of a biosignal, data mining for statistical analysis of relationships between large numbers of variables and system identification to model the processes underlying the observed signal(s).

Signals from the human skin microvascular system have been widely investigated in healthy groups using various perturbation methods [8, 9], as well as in different pathological conditions such as diabetes, obesity, hypertension, insulin resistance, hypoxia and non-alcoholic fatty liver disease [10-13]. An early detection of the abnormal changes may help to avoid serious microvascular complications by quantifying these changes in the human skin microcirculation at an early stage of the disease in order to define the best treatment and thus improve the health outcomes. However, the microvascular function can be implicated in a wide variety of factors. Skin microvascular perfusion contribute to impairment in elderly subjects when exposed to thermal provocation [14, 15]. Microcirculation has been also influenced by myriad of other factors including gender [16], body site [17], skin pigmentation [18], smoking [19], vasoactive medication [20], and even sedentary life style [21]. Therefore, several sources of variability should be considered when assessing skin microcirculation.

Non-invasive methods have been used to investigate the microvascular function. Over the last few decades [22], a non-invasive technique widely used in basic and clinical research, is Laser Doppler Flowmetry (LDF). The LDF technique is non-invasive and allows continuous recording of the blood flux. LDF measures the perfusion in the skin referring to the blood flow in the microcirculation which consists of the capillaries, small arteries, small veins and shunting vessels [23]. One of the larger benefits of this technique is that it can be used to investigate changes of blood flux in response to a given stimuli with a minimal impact on microcirculation. Studies conducted on the tissue based on the visible light spectrum have been used developing non-invasive assessment of tissue oxygenation both at macrovascular and microvascular level. White light spectroscopy (WLS), is another non-invasive technique based on the visible light suitable for the investigation of the human tissue oxygenation [24]. Recently, the combined LDF and WLS techniques allow for coetaneous investigation of blood flux (BF) and oxygenation parameters (OXY).

However, these methods lack repeatability and precision, due to the heterogeneous anatomy of the skin, making the measurements on the same site at different occasions almost impossible. Moreover, LDF measure of blood flow is not expressed as absolute unit, i.e. ml s^{-1} $(100\ g)^{-1}$ [25], but in arbitrary units, known as perfusion units (PU) and WLS measures the tissue oxygenation in arbitrary units (AU). Also, both LDF and WLS are very sensitive to movement of the measurement probe and optical fibre. Much previous use of both LDF and WLS techniques has been to explore

microvascular control mechanisms within the skin through computer processing of the blood flux and oxygenation signals. The time and frequency domain analysis and the contribution of spectral properties in the frequency domain are the most used techniques with which signals derived from the microvascular perfusion have been analysed (see, for example, [26-28]). However, further methodologies ought to be explored for investigating changes in vascular function. Recent research [4], had shown that the measure of the information, or randomness, of the blood flow can indicate a vascular dysfunction that trace the inception and the progression of diseases related to CVD such as diabetes. Therefore, it is important to study these analysis methods in various groups of people with such diseases.

1.2 Aims and Objectives of the Research

The broad aim of this research is to investigate properties of blood flux and oxygenation signals obtained from human volunteers. Initially, this work focused on analysing data, acquired from previous studies, of blood flux and oxygenation measured by a combined LDF-WLS device for healthy volunteers during skin perturbation, in order to explore the frequency components of these signals using Fast Fourier (FFT) and Wavelet Transformation. Several nonlinear complexity methods that have been used widely to quantify the complexity of a time series and are well suited to the analysis of one-dimensional biomedical signals such as sample entropy (SampEn), Lempel and Ziv complexity (LZC) and effort to compress complexity (ETC) are then considered. Although, since biological systems operate across multiple spatial and temporal scales, multiscale analysis is applied to these complexity measures to better quantify the information expressed by the microvascular dynamics over multiple time scales. Moreover, the Symmetric Projection Attractor Reconstruction (SPAR) analysis is used providing quantitative measures of the microvascular system in phase space and a visual representation in the shape and variability of the signal producing a two-dimensional with features like density and symmetry.

These techniques are shown to be a useful tool for analysing signals from complex networks, like blood flux and tissue oxygenation signals in the microvasculature. It has been suggested that the loss of complexity in a physiological time series is indicative of disease [29]. In this research, the complexity of human microvascular perfusion, in various pathophysiological conditions, is examined in more detail.

The primary aim of this research is therefore to explore nonlinear analysis methods for the investigation of the complex dynamics of the microvascular perfusion, as an indicative measure of system's adaptability and potentially disease state. In the first instance, using skin blood flux and oxygenation from data from healthy volunteers in two haemodynamic steady states, at 33℃ and

during local warming to 43°C to generate local thermal heating (LTH), the properties of these signals and the complexity measures can be evaluated. This can then be extended to pathological states and a further study of the blood flow signals from a group with non-alcoholic fatty liver disease (NAFLD) is used to determine if these metrics can be employed to help discriminate between groups at an increased cardiovascular disease risk (CVD). The objectives of the study can thus be described as follows:

- To explore the frequency components of signals using FFT-based and/or WT-based analysis to understand the properties of the processes underlying them.
- To perform nonlinear complexity analysis of the signals to identify suitable parameters of these algorithms, their applicability and limitations and better understand how the information content in them changes in response to external stimuli.
- To develop multiscale methods for the analysis of these signals and establish properties of these approaches, e.g. time constant dependencies, and benchmark metrics for comparison with studies in pathophysiological states.
- To apply a new approach for the attractor reconstruction analysis and provide a quantitative characterisation of the microvascular system in phase space and a visual representation in the shape and variability of the signal producing a two-dimensional attractor.

1.3 Applicability of the Research

This study aims to explore complexity methods that can quantify the changes in the complex flow motion characteristics from the human microcirculation in a range of pathophysiological states. This research may be of great help in determination of vascular dysfunction by quantifying the degree of adaptability in microvascular networks through the changes in the information content of the blood flux signals during perturbation and to investigate the differences of the information content of the microvascular dysfunction under a pathophysiological state. The time series analysis can be used to inform how a loss of system flexibility may prevent microvascular systems from adapting to an imposed stressor and to explore the behavior of microvascular system in different pathophysiological conditions.

1.4 Thesis Structure

Chapter 2 introduces the biomedical signals and provides an overview of the signal processing techniques. Then, the physiology of skin and evaluates the current literature in the field of microcirculatory blood flow, is described. The relevant and necessary mathematical approaches to quantify the microvascular dynamics using both linear and nonlinear analysis, are described.

Chapter 3 employs time and frequency domain analysis to assess and characterize the changes in skin blood flux and oxygenation signals from fifteen healthy volunteers. Chapter 4 develops the use of nonlinear analysis at a single and in multiple time scales in healthy volunteers during skin local heating to examine different haemodynamic states. Chapter 5 presents results from the multi-study analysis using both linear and nonlinear analysis, to assess the variability of the LDF signals from subgroups at an increased cardiovascular disease risk (CVD) categorised with presence or absence of type 2 diabetes and use of calcium channel blocker medication. Chapter 6 present the results from the application of a new approach for attractor reconstruction analysis to better evaluate the changes of the microvascular network under a dynamic change in the skin microcirculation. Finally, Chapter 7 concludes this work and provides future directions.

1.5 Contributions

The multidisciplinary nature of this thesis, combining the elements of engineering techniques with clinical approaches enable the following main contributions to the body of knowledge:

- Establishing the applicability of LZC, SampEn, ETC complexity and multiscale analysis of the simultaneously recorded healthy human skin blood flux and oxygenated haemoglobin signals during skin local heating. These methods showed a substantial decrease during vasodilated perfusion state due to increased local heating and were able to identify different microvascular states.
- Investigation of skin blood flux variability from individuals at increased CVD risk using time, frequency and complexity analysis. The multiscale complexity analysis reported a significant attenuation in the network's flexibility and adaptability with increasing CVD risk. Complexity-based and particularly, multiscale-based analysis showed good discrimination capabilities.
- Applying the efficacy of the attractor reconstruction approach as a potential method of identifying changes in the microvascular function from the human microcirculation in a range of pathophysiological states. The measures derived from attractor reconstruction combined with the nonlinear indexes, were able to identify the changes of the features in shape and variability of the blood flow signals under different conditions.

1.6 List of Publications and Presentations

Journal papers:

Complexity of Flow Motion

- M. Thanaj, A. J. Chipperfield, and G. F. Clough, "Analysis of microvascular blood flow and oxygenation: Discrimination between two haemodynamic steady states using nonlinear measures and multiscale analysis," *Comput. Biol. Med.,* vol. 102, pp. 157-167, 2018.
- A. J. Chipperfield, M. Thanaj, E. Scorletti, C. D. Byrne, and G. F. Clough, "Multi-domain analysis of microvascular flow motion dynamics in NAFLD," *Microcirculation,* vol. 0, no. 0, p. e12538, 2019.
- D. Carey, M. Thanaj, T. Davies, E. Gilbert-Kawai, M. Kay, D. Z. H. Levett, M. G. Mythen, D. S. Martin, M. P. Grocott, A. J. Chipperfield, and G. F. Clough, "Enhanced flow-motion complexity of skin microvascular perfusion in Sherpas and lowlanders during ascent to high altitude," *Scientific Reports,* vol. 9, no. 1, p. 14391, 2019.
- A.J. Chipperfield, M. Thanaj, G.F. Clough, Multiscale, multidomain analysis of microvascular flow dynamics, *Experimental Physiology*, 2019; 1 - 7.

Book Chapters

- M. Thanaj, A. J. Chipperfield, and G. F. Clough, "Complexity-based analysis of microvascular blood flow in human skin," *Understanding Complex Systems, Biological Oscillators at Systems Levels,* (Submitted for publication), Springer book series, 2020

Conference papers:

- M. Thanaj, A. J. Chipperfield, and G. F. Clough, "Multiscale Analysis of Microvascular Blood Flow and Oxygenation," Singapore, 2019: Springer Singapore, pp. 195-200.
- M. Thanaj, A. J. Chipperfield, and G. F. Clough, "Attractor Reconstruction Analysis for Blood Flow Signals," Conference: 41st International Engineering in Medicine and Biology Conference (EMBC 2019).

Oral Presentations:

- Multiscale complexity of microvascular blood flow and oxygenation. Postgraduate Conference of Engineering Sciences 2018, University of Southampton.
- Multiscale analysis of microvascular blood flow and oxygenation. World Congress of Medical Physics and Biomedical Engineering 2018, Prague, Czech Republic.
- Attractor Reconstruction Analysis for Blood Flow Signals. 41st International Engineering in Medicine and Biology Conference (EMBC 2019), Berlin, Germany.

Chapter 2: Background and Literature Review

In this chapter, the research background material and literature review are presented. The chapter starts with a brief introduction to the biomedical signal, different types of biosignals and an overview of signal processing techniques. Then, a brief description of the anatomy and physiology of the skin circulatory system and a review of the primary technique used to assess microcirculation, are then presented. After that, a technical background on the methods for analysis of blood flow and oxygenation signals including time and frequency domain together with a technique to quantify the complexity of these signals are discussed.

2.1 Biomedical Signals

2.1.1 Biomedical Signal Measurement Systems

Biomedical signals are variations in space and/or time that carry information about biological events such as heartbeat or the contraction of a muscle. Common examples include those that measure electrical activity such as Electroencephalogram (EEG), electrocardiogram (ECG) [5, 6] and electromyogram (EMG) [7], thermal activity such as measurement of temperature and mechanical activity such as muscle movement and blood pressure [30], all of which contain useful information about a biological event and are well established in clinical use.

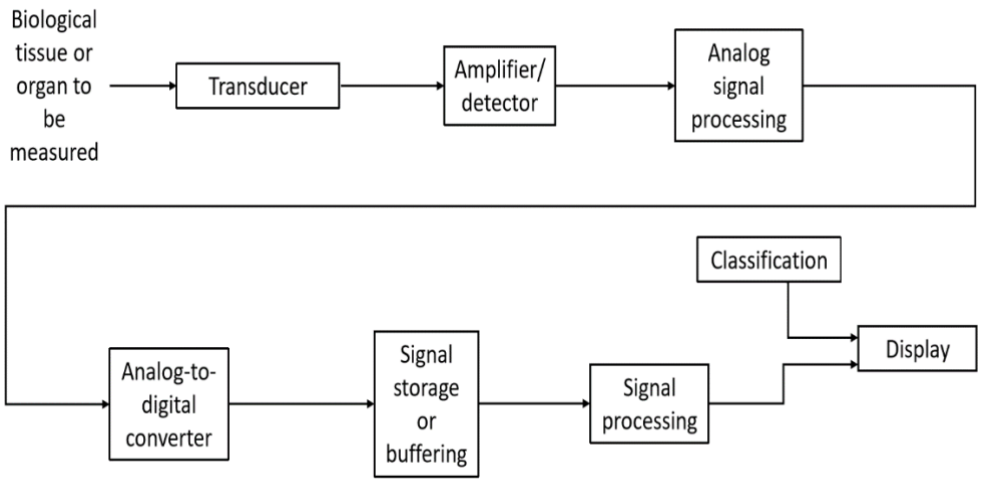

Figure 2.1 Block diagram of a typical biomedical measurement system.

The acquisition of biomedical signals can be achieved in various ways. A typical measurement system of biosignals as shown in Figure 2.1, contain detectors and transducer to convert the biological into an electric signal usually detected from electrodes or probes placed on the site of

observation. A data acquisition device, often including an amplifier, and analog signal processing is required, for the amplification and for the lowpass or bandpass filtering of the signals. The analog signal will then be converted to digital through an analog to digital converter (ADC) and then the signal is stored in a signal storage format followed by further digital signal processing such as averaging, spectral and wavelet analysis [31, 32]. In some diagnostic applications, more sophisticated techniques are applied such as classification algorithms to define the classes of a tissue in disease state [31]. The output of this system is then displayed from the display layout such as a monitor.

2.1.2 Biomedical Signal Processing

Biomedical signal processing refers to a range of techniques encompassing the fundamental theory, applications, algorithms and implementations of techniques that transform a raw biosignal from an abstract measurement to a meaningful interpretation. Biosignals, as all digital signals, are categorised into linear and nonlinear signals and each of these categories are further classified into stationary, in which statistical properties of the signal such as mean, standard deviation (SD), variance etc. remain constant over time, and non-stationary, in which the signals have varying mean over time [31, 33]. It is therefore, necessary to fully understand the nature of the biosignals before applying any linear and nonlinear signal processing techniques.

2.1.2.1 Linear Signal Analysis

The most straightforward measures that can provide some fundamental information of the signals are the mean, root mean-squared value (RMS) and variance however, these basic measures do not always tell us much about the information carried in the signals [31]. Several time domain techniques such as correlation-based analysis have been applied to calculate the similarity between time series, most frequently used for determining the time delay for which the signal remains correlated with itself [34] and convolution to quantify the output of a linear time series in response to any input, more commonly used in digital filtering [35]. However, many biological signals exhibit more useful information for diagnosis when examined in the frequency domain.

Spectral analysis has been used to determine the power-frequency composition of a biosignal providing a useful representation of the overall signal spectrum. Frequency domain analysis such as fast Fourier transform (FFT) based on the power spectrum analysis, describes how the power of the time series varies with frequency [5] and Wavelet transform (WT) is a time-localized and frequency domain analysis developed to obtain both the time and frequency properties of a signal [36].

Signals from the human cardiovascular system have been widely assessed using the frequency domain analysis [37-42]. An illustrative example reproduced from Bračič, et al. [42], of a respiratory, ECG, heart rate variability (HRV), blood pressure and blood flow signal and their frequencies in time-averaged wavelet transform recorded from a healthy human subject, is shown in Figure 2.2. Note that all signals were detrended, by forcing their mean to zero and filtered using moving average with a 160 second window and apart from ECG signals, were resampled at 10Hz. It can be seen that even though there are few differences in the frequencies between these cardiovascular signals, several dominant frequency peaks appear at the same frequency range as indicated in dashed lines. As explained in [42], this shows that the WT measurement on the cardiovascular signals can detect the regulatory mechanisms reflected from the cardiovascular system at the site of observation, making the frequency domain analysis an important technique for identifying the oscillatory dynamics of the cardiovascular system. Further on in this thesis, frequency domain analysis methods will be demonstrated, in order to explore the frequency components of signals derived from the microvascular perfusion.

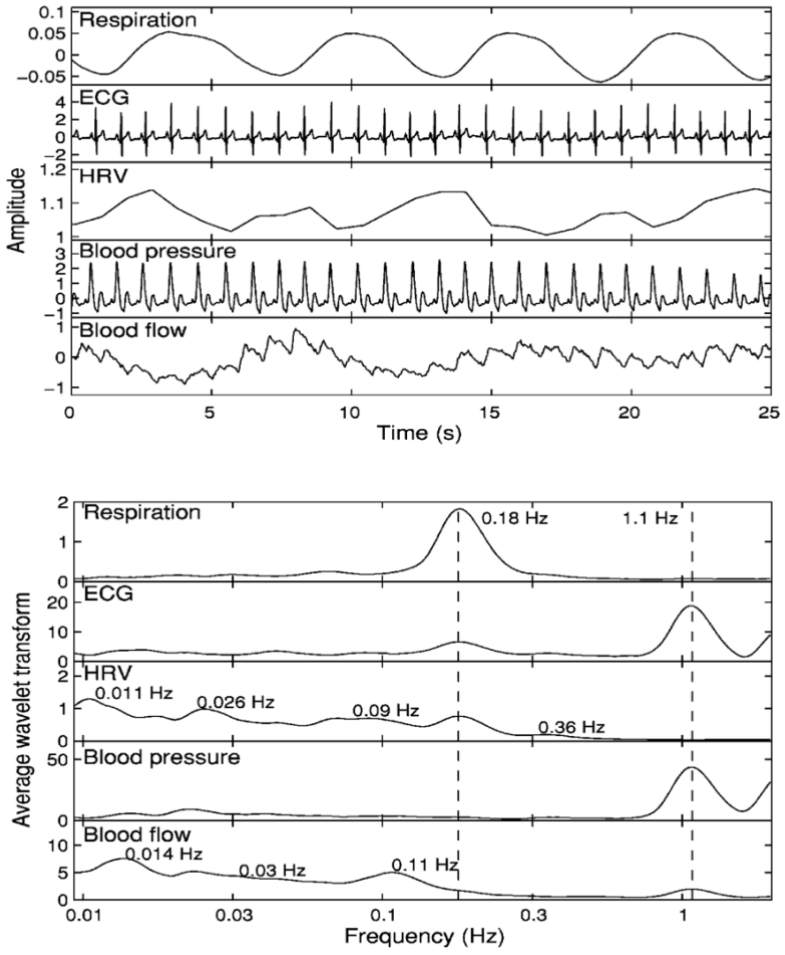

Figure 2.2 Example of respiratory, ECG, HRV, blood pressure and blood flow signals and their WT analysis. Figure reproduced from [42], with kind permission from the authors.

2.1.2.2 Nonlinear Signal Analysis

So far, linear analysis methods such as spectral analysis, have been broadly applied for the analysis of biomedical signals however, many biosignals contain complex nonlinear dynamics that cannot be explained through linear signal processing. A nonlinear system is defined when the systems output is not proportional to the systems input. The signals from a nonlinear system contain irregularities that appear more complex than the signals from linear systems. These signals contain complex information that make signal processing challenging and require new techniques [31]. The information theory also known as entropy describe the measurement of the information that is gained or lost in the signal, otherwise it is a measurement of disorder in the signal. The measurement of signal information was first introduced by Shannon [43], who estimated the information content of stochastic irregular data. Since then, several nonlinear complexity measures have been applied to quantify nonlinear complex physiological signals [4, 40, 44-46]. Further on in this thesis, nonlinear analysis methods will be demonstrated, to quantify the complex dynamics of signals derived from the microvascular perfusion and explain why treatment of such signals with linear methods alone are insufficient.

In the following sections of this chapter, an overview of the skin physiology as well as the techniques to assess the cutaneous perfusion will be first introduced. Then, the tools to quantify both the linear and nonlinear dynamics of these signals will be thoroughly described.

2.2 Physiology of Skin Microcirculation

2.2.1 Human Circulatory System

The human circulatory system has two main functions: one is the rapid transport of oxygen, blood and nutrients to the tissues and organs and the other is to regulate blood pressure generated from the heartbeat [47, 48]. Figure 2.3 shows a simple diagram of the human circulation. The blood is ejected from left ventricle and flows through the aorta and then to smaller arteries, arterioles and the capillary network where the major regulation of tissue perfusion occurs (Figure 2.4). The blood returns to the heart through a convergent system of veins and finally fills the right ventricle and atrium from where it will be transported to the pulmonary system and oxygenated. After oxygenated blood enters again the left atrium and completes a full body circulation.

A sufficient diffusion of oxygen to tissue is a vitally important transport mechanism inside the cells and between the cells and the blood flow. The diffusional transport rate is similarly important to deliver nutrients inside the cells but the time t that it takes to move all the substances in a direction over a distance x increases with the square distance, as shown by Einstein:

$$t \propto x^2 \tag{2.1}$$

Therefore, as described by Levick [47], diffusional transport is slower over large distances than shorter ones. The diffusion of oxygen across blood membrane inside the lungs is referred to as the cardiovascular system and its purpose is to carry oxygen from the lungs to every cell of the body to satisfy the metabolic need of the tissue. The delivery of oxygen and nutrients to the cells is called the microcirculation and refers to the circulation of the blood in the smallest blood vessels including the arterioles (mean diameter: 30 µm), capillaries (3 - 7 µm) and venules (30 - 35 µm) [49]. A typical capillary network is shown in Figure 2.4.

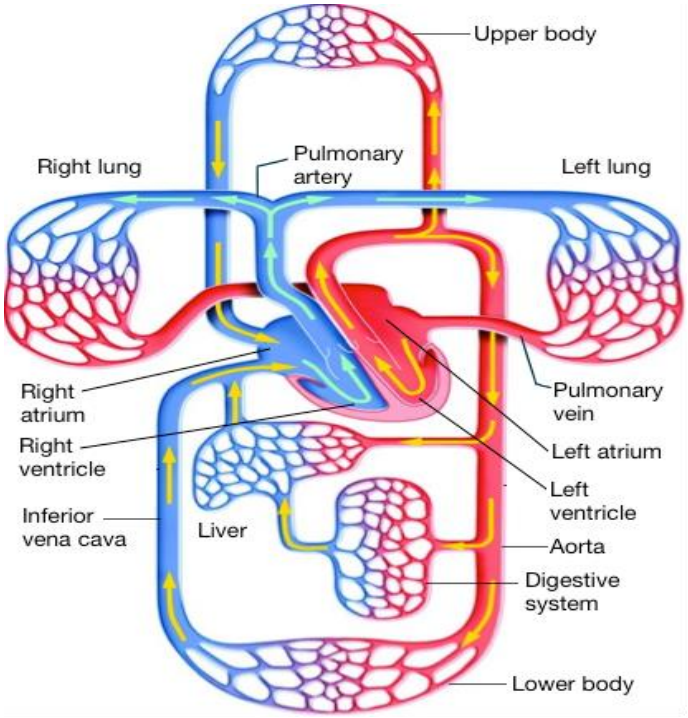

Figure 2.3 The human circulatory system. Reproduced from clinicaverde.com.

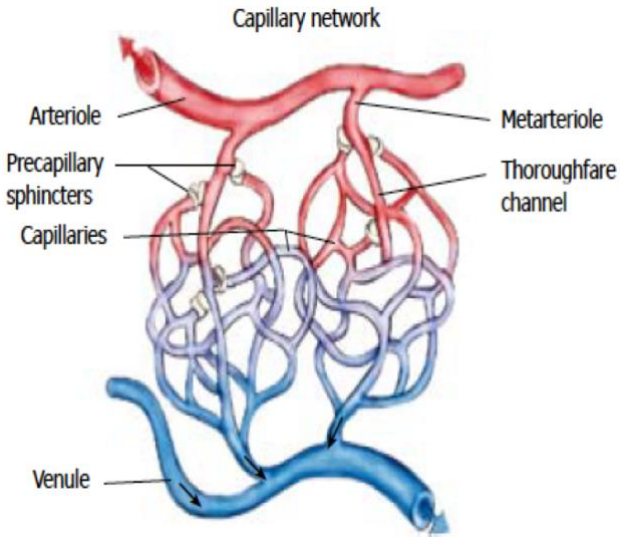

Figure 2.4 The capillary network. Reproduced from [50] (Open access journal).

A fundamental function to understand the microcirculation is by controlling the peripheral vascular resistance and the blood pressure. According to Darcy's law, resistance is the pressure drop per unit flow through a vessel or a group of vessels. The biggest pressure drop occurs through the smallest arteries and arterioles. These arteries and arterioles are called resistance vessels. When resistance vessels are dominant to the resistance flow, they turn local perfusion up or down according to the local demand [47]. Thus, when the resistance decreases, the local blood flow increases and the resistance vessels dilate. This is referred to as vasodilation while the opposite effect is called vasoconstriction and occurs when the local resistance rises and the local blood flow reduces.

2.2.2 Cutaneous Microcirculation

The human skin is the largest organ in the body and it accounts for about 30% of total body weight [51]. It distinguishes, separates, and protects the organism from its surroundings. Skin plays an important immunity role in protecting the body against pathogens, because it interfaces with the environment. The skin is composed of three layers: the epidermis, dermis and hypodermis [52, 53], as illustrated in Figure 2.5.

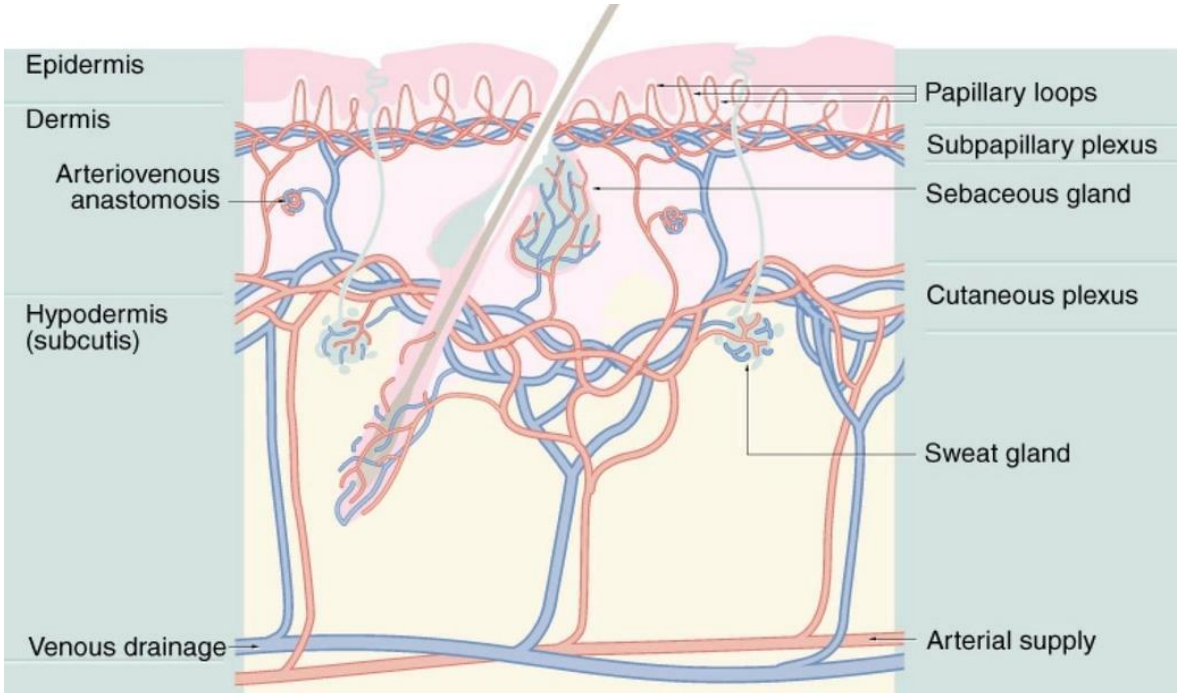

Figure 2.5 Representation of the human skin anatomy. Reproduced from [54] with kind permission from Kuliga.

The epidermis is the outer skin layer. It forms a waterproof barrier to the outer world that keeps out water, sunlight, heat and cold. It consists of four or five layers depending on the region of the skin. The epidermal cells are formed at the basal cell layer. The cells which make up the epidermis

move up the layer changing their shape as they die due to the isolation from the blood. When these cells die, they form a layer mostly containing keratin, which is responsible for keeping water in the body and keeping out pathogens and other chemicals that may cause infection to the skin. The dermis is located beneath the epidermis and is composed of epithelial tissue, containing collagen and elastic fibres that protects the body from stress and strain. It consists of blood vessels that provide the tissue with nutrients and waste removal from its own cells. The hypodermis lies underneath the dermis and is the deepest skin layer. It is not a part of the skin and its purpose is to attach the skin to bone and muscle and supply it with blood vessels and nerves. The hypodermis contains connective tissue, adipose tissue and elastin that participate in the thermal isolation of the body.

Human skin microcirculation is heavily influenced by the ambient temperature. Skin is the main thermoregulatory organ of the body and it uses variation of microvascular perfusion to regulate the heat loss. When the temperature of the skin is high due to a physiological perturbation, such as local skin warming, the arterioles, venules and veins begin to dilate and this is called thermal vasodilation. If the local environment is warm, the blood vessels dilate and the volume of oxygenated blood flow increases in order to dispel the excess of the heat [55]. Conversely, local cooling of the skin causes vasoconstriction to reduce heat loss.

There are other regulatory mechanisms that contribute to the total blood flow motion. The blood perfusion exhibits periodic physiological oscillations that have been shown to reflect the influence of heartbeat, which is the highest frequency oscillation observed in flow motion. Then, the next highest frequency is the respiratory activity. The frequency below respiration is thought to represent the regulation of blood pressure, where the smooth muscle cells respond to the changes in vascular pressure in the vessel's walls and is known as myogenic activity. Two additional components that occur in lower frequencies are the neurogenic activity and metabolic activity.

The microvascular system is a complex dynamical system and skin regulation is therefore a complex process [36, 56]. The endothelial function has been closely linked with microvascular mechanisms. The endothelium plays an important role in controlling the blood flow. The endothelial function is defined as the ability of the endothelial cells to deliver factors that regulate the behavior of the vessels and cause vasodilation [55, 57, 58]. Impaired endothelial function is related to diseases such as coronary heart disease and peripheral artery disease and therefore the assessment of the endothelial function may help to detect functional changes related to the progression of these diseases.

Skin microcirculation is an accessible site for non-invasive assessments. Skin microcirculation measurements may provide information about the condition in deeper tissues and can be

representative for the microvascular function of muscles, kidney and tissues with a difficult accessibility [57]. Therefore, the microcirculation of the skin can be considered as a source of information about microvascular function and can be useful to understand dysfunction resulting from disease.

The dysfunctions in the microcirculation are associated with diseases such as peripheral vascular disease, coronary disease and diabetes, which are a major factor for cardiovascular disease (CVD). Another, relevant to the CVD is the non-alcoholic fatty liver disease and is defined by a clustering of pathologies that are related to the CVD risk and diabetes. The patterns of the skin blood flow signals, and the complex components, from people with macrovascular disease are thought to be an important factor in the investigation of the mechanisms that contribute to the microvascular dysfunction and may help distinguish various diseases.

2.3 Assessment of the Microcirculation

There are several assessment methods to study microvascular function. The microcirculatory blood flow can be investigated both invasively and non-invasively. The most relevant to this research are the non-invasive techniques. Some of the most current techniques for measuring the blood flow with the working principles as well as the advantages and disadvantages, are briefly described as:

Volume Displacement Plethysmography. This technique measures the changes in the volume of blood flow by a strain gauge set around the limb. Changes in the volume can be studied by observing the waveform as these changes occur and are representative for the arterial blood flow, and the pulsatility of that flow increases with perfusion. However, this method is lacking in terms of accuracy [59].

Vital Capilaroscopy. This method assesses the morphology of the capillary and is mostly used on the nail folds to measure the diameter, density or loop size with the use of the microscope. This technique provides a good resolution and a direct in vivo observation of the capillaries [60]. However, it does not give quantitative measurement and cannot be used to assess the overall skin microcirculation.

Orthogonal Polarisation Spectral (OPS) Imaging. This device allows the visualization of the blood vessels by illuminating the tissue with green polarized light absorbed by haemoglobin. This method measures the vascular density, the diameter and the blood flow and displays images of capillaries and venules. It is a useful tool for in vivo visualisation and for quantifying the movement of red blood cells (RBCs) and observing at individual vessels by image analysis software [61].

However, the resolution of the images may be low due to movement artefacts and imaging processing can be time consuming.

White Light Spectroscopy (WLS) assesses, non-invasively, the oxygenation of tissue and the concentration of the RBC. This method uses the white light in the visible to near-infrared band and fluctuations in the reflected near-infrared light are caused by the moving RBCs. This technique is widely used and can provide additional information about the different types and features of oscillation in the dynamics of the blood flow in the same tissue volume [62]. In this work, this technique will also be employed using a combined probe with laser Doppler Flowmetry.

Laser Doppler Flowmetry (LDF) is a non-invasive technique that enables a sensitive and continuous assessment of blood flow. This method is based on the Doppler shift of the emitted laser light travelling through the tissue and reflected from the moving RBCs. The main disadvantage of this method is that it is very sensitive to movement that induces artifacts to the recording signal.

Each method presented provides a different approach for measuring the blood flow in the microcirculation. Laser Doppler Flowmetry has become a gold standard for the continuous and non-invasive measurement of blood perfusion without causing any harm or injury on the physiological state of the tissue. This technique is accurate when quantifying changes in perfusion in the skin and is assessed in skin circulation to monitor the blood flow in various pathophysiological conditions [63]. White light spectroscopy has been applied to study the changes of the oxygen content in the microcirculation and is most suitable for non-invasive, continuous measurement of the tissue oxygenation. These two methods are described in more detail in the next sections.

2.3.1 Laser Doppler Flowmetry

2.3.1.1 Theory of LDF

The Laser Doppler Flowmetry technique is based on the Doppler effect use for monitoring the skin microcirculation blood flow. The principle of Doppler effect, as shown in Figure 2.6, refers to a slight frequency shift that arises in light, guided by optical fibres, which is scattered by moving red blood cells (MRBCs) and then detected and received by photodetectors [23, 64].

Figure 2.7 provides the overview of the theory behind the LDF technique. When a laser beam illuminates in the surface of the tissue, incident photons interact with the tissue and scatter by MRBCs. The direction of the scattered light particles is dependent on the movement of the RBCs that they interact with. The laser light, which is scattered in the tissue under observation, has different frequencies, so the distance from every source in each point of the detector varies spatially. Some of the scattered photons also interact with the MRBCs that move with different

velocities and directions. This distribution of the velocities and directions of the moving RBCs within arterioles, capillaries and venules generates a photocurrent whose spectrum includes a Doppler shift – the frequency change of the light when reflected by MRBCs. The shifted light causes fluctuations in the detected signal, which can therefore be analyzed by plotting the power spectrum $P(\omega)$ of the fluctuations present [23, 65, 66].

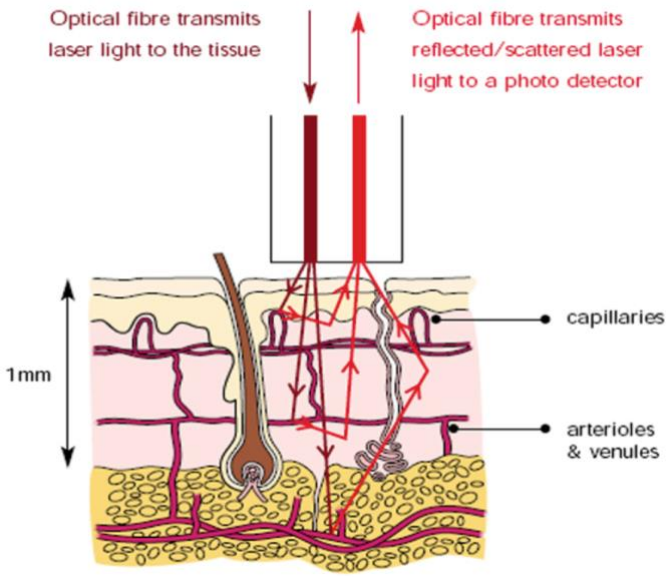

Figure 2.6 The principles of LDF. Reproduced with kind permission from Moor Instruments Ltd.

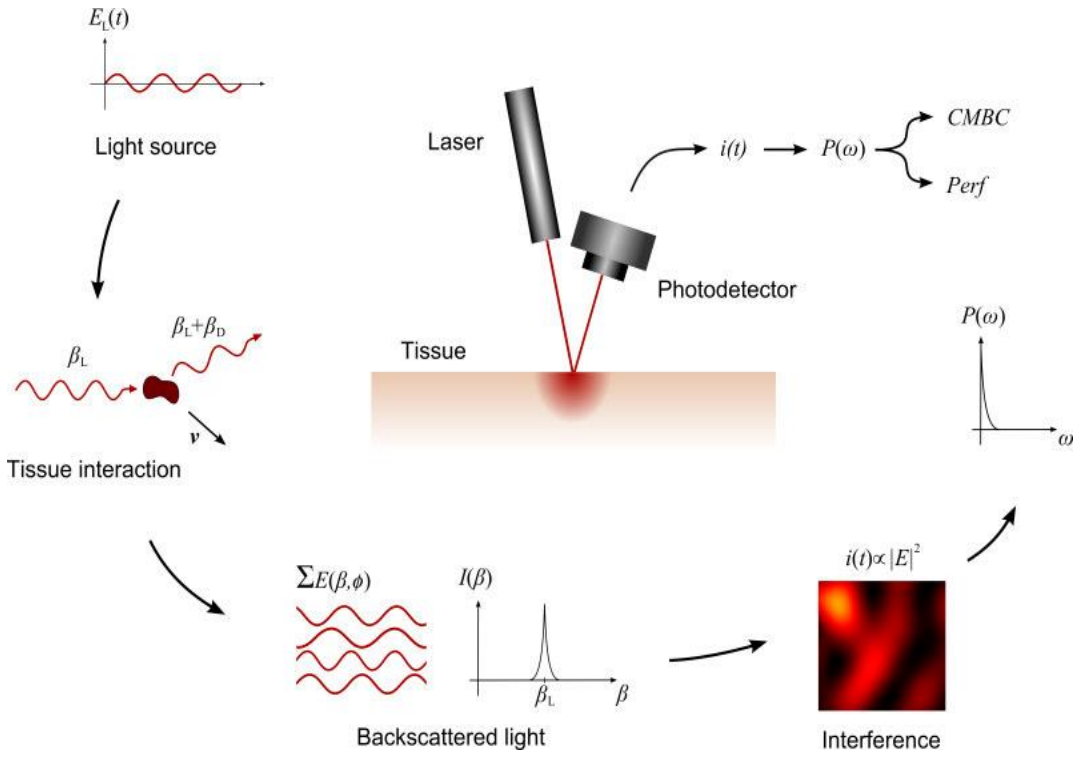

Figure 2.7 A summary of the theory behind Laser Doppler Flowmetry. Reproduced from Fredriksson, et al. [65] with kind permission from the authors.

By further derivations of the power spectral density, it can be shown that the concentration of moving red blood cells ($CMBC$), often referred to as blood volume and the tissue perfusion ($Perf$) can be estimated from the to the integral of the frequency-weighted Doppler power spectrum. Thus,

$$CMBC \propto \int P(\omega) \tag{2.2}$$

$$Perf \propto \int \omega \cdot P(\omega) \tag{2.3}$$

Consequently, $CMBC$ and $Perf$ estimates, in equations 2.2 and 2.3, are dependent on the power spectral density $P(\omega)$) and therefore the photocurrent, which is related to the number of MRBCs in the volume that are scattered. As shown in Figure 2.8, the power in the fingertip is comprised in higher frequencies than the power on the forearm skin. This may denote higher speed of the MRBCs and/or multiple scattering of the MRBCs [23].

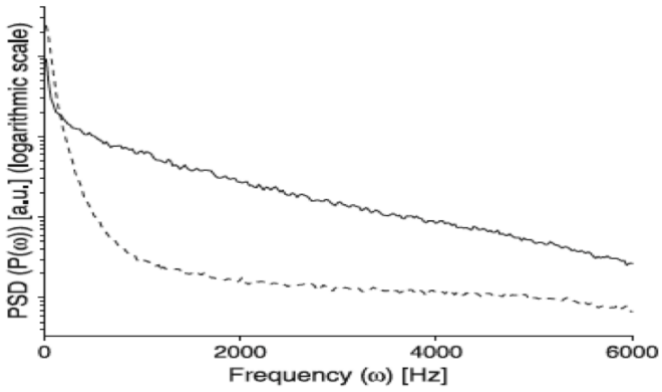

Figure 2.8 Power spectral density versus frequency measured on the forearm (dashed line and fingertip (solid line). Reproduced from [23], Copyright (2020) with permission from Springer Nature.

2.3.1.2 Measurements

Figure 2.9 VMS-LDF device, Moor Instruments Ltd. Reproduced with kind permission from Moor Instruments Ltd

A typical LDF device for measuring the skin blood flux is shown in the Figure 2.9, manufactured by Moor Instruments Ltd, UK. The optical system of the device has a power diode of 785 nm laser wavelength, 20mW high power, wide separation of 4mm and a 785 nm laser wavelength, 1mW low power probe, standard separation of 0.5mm. Recent studies [68], have shown that the rate of the photons detected from the standard probe are significantly higher than the ones detected from the wide probes, and therefore a wide separation probe may be used to detect vessels in deeper tissues. The 1mW laser has a penetration depth of 1mm and the 20mW laser reaches depths around 3mm.

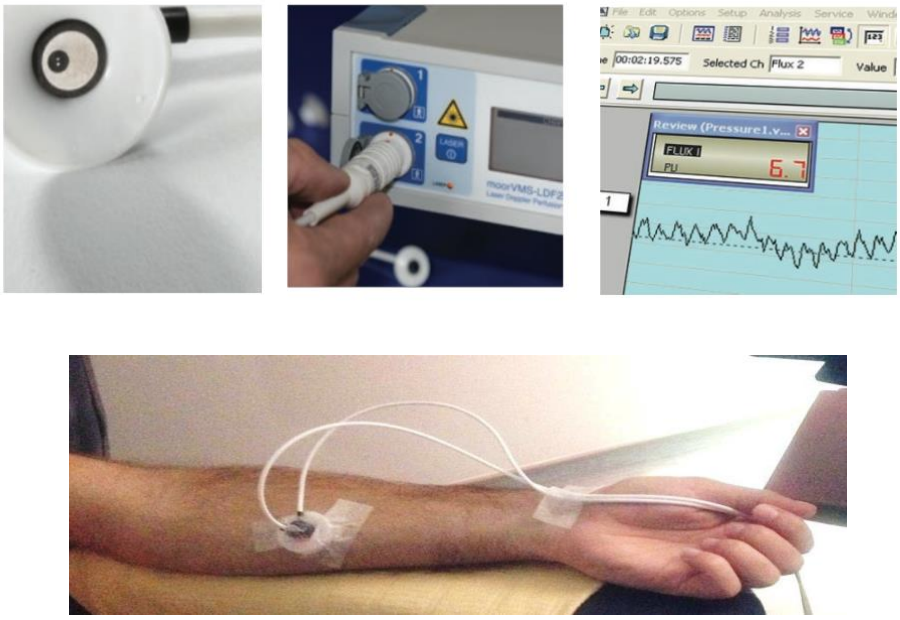

Figure 2.10 LDF-WLS probe and the implementation for the measurement of skin blood flux on the forearm. Reproduced with kind permission from Moor Instruments Ltd (upper figures) Kuliga [54] (lower figure).

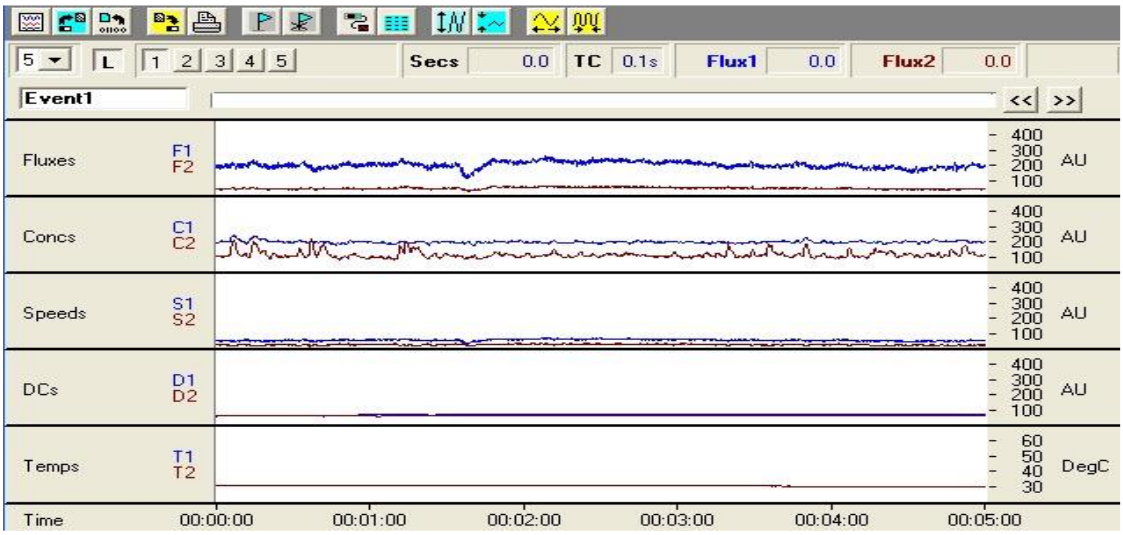

Figure 2.11 LDF Software showing the recording of the signal. Reproduced with kind permission from Moor Instruments Ltd.

Figure 2.10 shows the measurement of LDF skin blood flux of a volunteer being tested, where the combined LDF and WLS probe were placed in the forearm. The LDF signals can be displayed from the software of the device. Figure 2.9 illustrates a typical blood signal of the measurements of flux, concentration of the red blood cell, speed and temperature. The flux measured by the high power probe (wide separation) is denoted as F1 and the flux measured by low power probe (standard separation) is F2. The concentration of red blood cell and speed are also measured, giving an indication about the concentration and speed of moving red blood cells in the tissue sample volume. Temperature monitoring is essential to capture variation of the skin temperature during assessment. In later sections, these signals will be analysed using Matlab (R2019a, Mathworks, UK) as this gives us greater control over the time-series analysis than the software provided by the manufacturer.

2.3.1.3 Technical Limitations of LDF

A number of technical issues arise from LDF measurement which are briefly described below.

Arbitrary Units: One of the inherent limitations of the currently available LDF device is that they cannot express the blood flow in absolute flow units, like the urinary flow rate in ml/min. This is because of the variation of the structure in the capillaries and the small blood vessels. For that reason, arbitrary or perfusion units (AU or PU) are used as physical quantitative units.

Movement Artefacts: The LDF measurements can be very sensitive to either tissue motions, movements between the tissue and the probe tip that cause movement artefacts to the signal. Many technological improvements have been established to overcome this limitation by choosing fibres with smaller diameters to reduce the measuring volume sensitivity to the movement artefacts, however it still remains a real challenge for professionals [66].

Biological Zero: It has also been found that there is a flux signal during arterial occlusion measurements which is present even when there is no flow, so the perfusion signal will not be zero even if there is no perfusion in the tissue. This signal is called biological zero (BZ) and is likely to be generated from Brownian motion of RBCs. Many researchers suggest the movement decomposition of the moving blood cell's speed in the vessel [69], although, it has also been suggested that this subtraction is not a very valuable analytical method for solving the biological zero problem.

Reproducibility of the Measurements: Repeated measurements on the same site of the skin don't result in the same perfusion values. Results obtained by recording at a single site using the LDF probe may not be representative for the entire tissue. However, Kuliga [54] in a recent study, showed that by marking the measurement sites and performing repeated measurements the

following day by placing the probe on the same site increases the correlation coefficient of the signals.

2.3.2 White Light Spectroscopy

The theoretical framework, the hardware and the measurements of the WLS device are briefly described in this section.

2.3.2.1 Theory of WLS

The main chromophore concentrations in the human skin are haemoglobin (oxygenated and deoxygenated) and the melanin. Haemoglobin (Hb) is the main protein of red blood cells, it binds and releases oxygen molecules, forming oxygenated and deoxygenated haemoglobin, and transports them around the body. Haemoglobin is stronger in visible wavelength range and the absorption spectrum depends on the oxygen content bound to it.

Melanin is a natural pigment found in the epidermis absorbs, that protects the skin from UV damage. It has been reported that melanin shows a higher attenuation in lower wavelength of the spectra within the visible and infrared light, than the oxygenated haemoglobin and deoxygenated haemoglobin [24, 70]. The large absorption of melanin in the spectrum is one of the factors that might affect the performance and need to be considered before starting the recordings [24].

The WLS device is used to measure the oxygen content in the tissue and can vary a lot with the attenuation of the spectrum wavelength. The algorithm of the WLS device is based on the modified Beer-Lambert Law which describes the optical interaction between photons and the tissue chromophores [24].

$$A(\lambda) = \varepsilon(\lambda) \times c \times l(\lambda, c) + G(\lambda) \tag{2.4}$$

where A is the attenuation, λ is the wavelength of the light, ε is the molar extinction coefficient of the chromophores, c is the molar concentration of the chromophores, l is the mean path length and G is the scattering loss. Attenuation A is defined as:

$$A(\lambda) = \log_{10}\left(\frac{I_o(\lambda)}{I(\lambda)}\right) \tag{2.5}$$

where I is the reflected light and I_o is the incident light.

2.3.2.2 Hardware

A spectrometer for detecting the reflectance light was used with wavelength range 350-800nm [24]. The light is guided inside the device by two fibres, one for transmitting and the other for

delivering. These two fibres are connected to external fibres and probes on the front panel of the device. An optical block is designed with constitutional lens and low-pass filter in order to improve light coupling efficiency and to remove possible interference from the high wavelength spectrum of the light to a laser Doppler detector in a modular system. A common combined LDF-WLS device with the combined probe is shown in Figure 2.12.

Figure 2.12 The combined blood flux and tissue oxygen monitor. Reproduced with kind permission from Moor Instruments Ltd.

2.3.2.3 Measurements

The white light emitted from the WLS device, penetrates the skin and is absorbed differently for the oxygenated and deoxygenated haemoglobin within the moving RBCs. The oxygenated haemoglobin produces a double-peak spectrum, whereas deoxygenated haemoglobin oxyHb generates a single-peak spectrum.

The resulted spectrum is analyzed to computes the percentage of the oxygen delivered in the RBCs. This percentage is the oxygen saturation (SO_2) and is indirectly measured in arbitrary units (AU) and expressed as:

$$SO_2 = \frac{oxyHb}{oxyHb + deoxyHb} \tag{2.6}$$

where $oxyHb$ is the oxygeanated haemoglobin with oxygen and $deoxyHb$ is the deoxygenated haemoglobin that does not carry oxygen. The SO_2 parameter is commonly used to refer the tissue oxygenation. However, because of the fact that the SO_2 only measures the ratio if the oxygenated haemoglobin relative to the total haemoglobin ($totalHb = oxyHb + deoxyHb$) in the blood, it is important to measure the oxyHb and deoxyHb additionally.

Figure 2.13 shows the measurement of the blood flux and the oxygenation signals from the skin of a healthy volunteer during rest. The WLS method combined with the LDF technique provide the measurements of the skin blood flux and tissue oxygenation simultaneously and are useful for the study of the characteristics of these measurements [24]. The combined method will be briefly discussed in chapter 3.

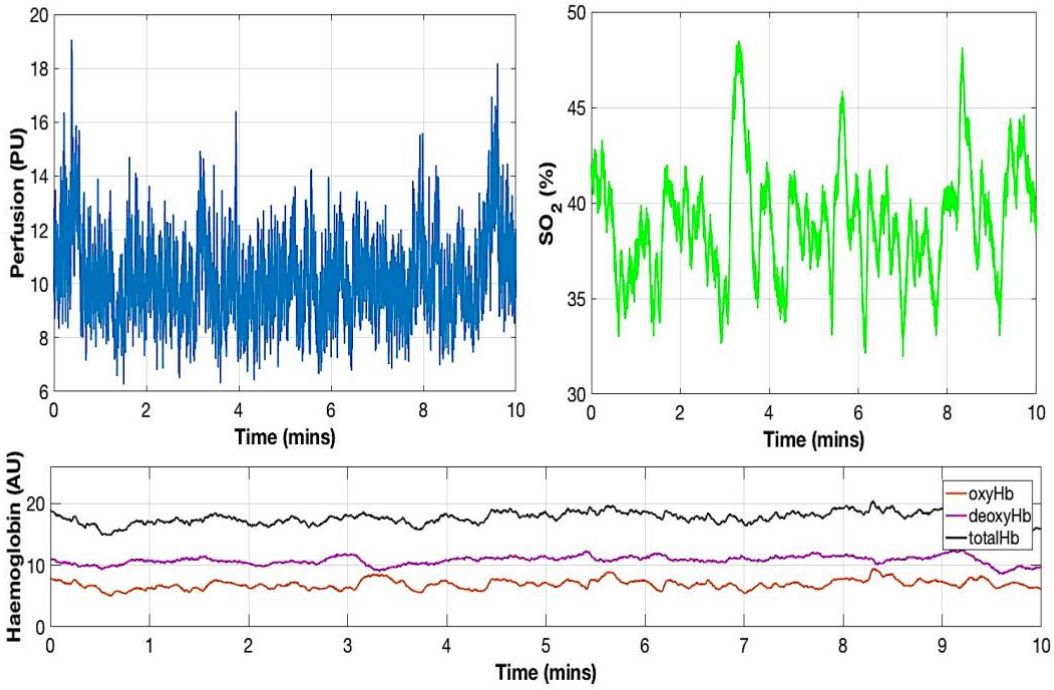

Figure 2.13 Resting skin blood flux (top right plot), oxygen saturation (SO_2) (top left plot), and haemoglobin concentration (bottom plots).

2.4 Spectral and Wavelet Analysis Methods

The LDF and WLS techniques have been mostly used to monitor the blood flux and oxygenation signals from the skin. Signal processing techniques, performed on these signals, aim to extract considerable information for the physiology and pathology of skin microcirculation. The analysis of the signal may contain various signal processing techniques such as transformation into the frequency domain and the analysis of time and frequency contents of the signal. All the above methods could provide significant insights from different aspects.

2.4.1 Fast Fourier Transform and Power Spectral Density

2.4.1.1 Fourier Transform

The Fourier Transform (FT) is the transformation of the time series into the frequency domain. Fourier analysis is the decomposition of the signal into a set of complex sinusoidal functions. These functions include frequencies that are mathematically related to the original signal [28, 71]. The Fourier transform of a signal $x(t)$ is defined as:

$$F[x(t)] = \int_{-\infty}^{\infty} x(t) \cdot e^{-j\omega t} dt \tag{2.7}$$

which uses Euler's complex exponential formula $e^{-j\omega} = \cos\omega + j\sin\omega$, where $\omega = 2\pi f = 2\pi / T$ is the frequency that refers to the periodic function with frequencies that are multiples of the frequency (f) which is inversly proportional to the period (T) of the original signal $x(t)$. When the signal is non-periodic, the period reaches the infinite boundary and hence the frequency will become very low. This continuous function in frequency domain is referred to as the Discrete Fourier Transform (DFT). The mathematical algorithm that computes the DFT is the Fast Fourier Transform (FFT). FFT manages to decrease the number of the calculations for computing DFT. DFT achieves the fastest calculations when the number of the signal samples is a power of two.

2.4.1.2 Power Spectral Density

The Power Spectral Density (PSD) describes the contribution to the power in the frequency components across a spectrum. The PSD is referred to as the spectral power distribution that would be found per time unit, considering that the total power of the signal for the whole time is infinite. The power spectrum as describe by Semmlow [26], is calculated as the square magnitude of the FT of the signal over frequency f (Equation 2.10):

$$P_{xx}(f) = |X(f)|^2 \tag{2.8}$$

One method to estimate the spectral density of a signal is by using the periodogram. This method is a measure of the PSD and can be defined as the average of the direct FFT signal [72].

To estimate the power of the signal at different frequencies the most commonly used method is Welch's method. Welch's method is an enhancement on the common periodogram estimating method and this can be defined in two different ways, one is by averaging the periodogram with segments and the other is by averaging the periodogram with overlapping segments [26, 72]. Welch's method further described in chapter 3 where the spectral content of LDF signals are considered.

2.4.2 Wavelet Transform

A transform is a reassigning of the signal that gives other information than the original signal. The FFT provides the frequency information that gives insight about the original signal. However, this transform does not provide time localisation of the frequency characteristics of the signal, but only estimates the power for a given frequency of a signal. The wavelet transform (WT) is an alternative method that divides the signal in time sections and describes the variation of the signal over time by analysing the frequency content of each section simultaneously [26, 27].

Wavelet analysis reflects the effects of the variation in the signal by dividing the signal into segments of scale. The more time segments the signal is divided into, the lower the frequency resolution, and therefore the information for low frequencies is lost and higher frequencies are better analysed. The Wavelet Transform $W(a,b)$ of a signal $x(t)$ can be expressed mathematically as:

$$W(a,b) = \int_{-\infty}^{\infty} x(t) \cdot |a|^{-1/2} \cdot \Psi * \left(\frac{t-b}{a}\right) dt \tag{2.9}$$

where b is the translation of the signal $x(t)$, a is the scaling factor of the wavelet function Ψ. If a is greater than 1, then the wavelet function is stretched along time and if it is less than 1 then is compressed. The symbol * denotes the complex conjuction of the mother function. There are a number of mother function available including Meyer, Haar, Mexican Hat and others, but Morlet wavelet has been the most commonly used in BF and OXY signal processing. Morlet wavelet, employed as the mother function here, uses a Gaussian function modulated by a sine wave and permits extraction of rapid phase differences at each position in time and frequency and therefore improves detection and localization in both time and frequency [73, 74]. Morlet wavelet is mathematically described as:

$$\Psi(t) = \frac{1}{\sqrt[4]{\pi}} \cdot \left(e^{-i\omega_0 t} - e^{-\frac{\omega_0^2}{2}}\right) \cdot e^{-\frac{\omega_0^2}{2}} \tag{2.10}$$

where ω_0 is the main frequency which is responsible for the localization of time and frequency. A great value of ω_0 will give a better frequency localization. In Figure 2.14 are shown the real parts of the Morlet wavelet for $\omega_0 = 2\pi$ and for $\omega_0 = \pi$.

The main difference between WT and FFT is the exponential function $e^{-i\omega t}$ from Equation 2.8 which is replaced by a family of wavelets Equation 2.10. Hence, both FFT and WT provide useful information of the frequency properties of a signal however, they are computed using different mathematical algorithms and therefore their measures cannot be directly compared.

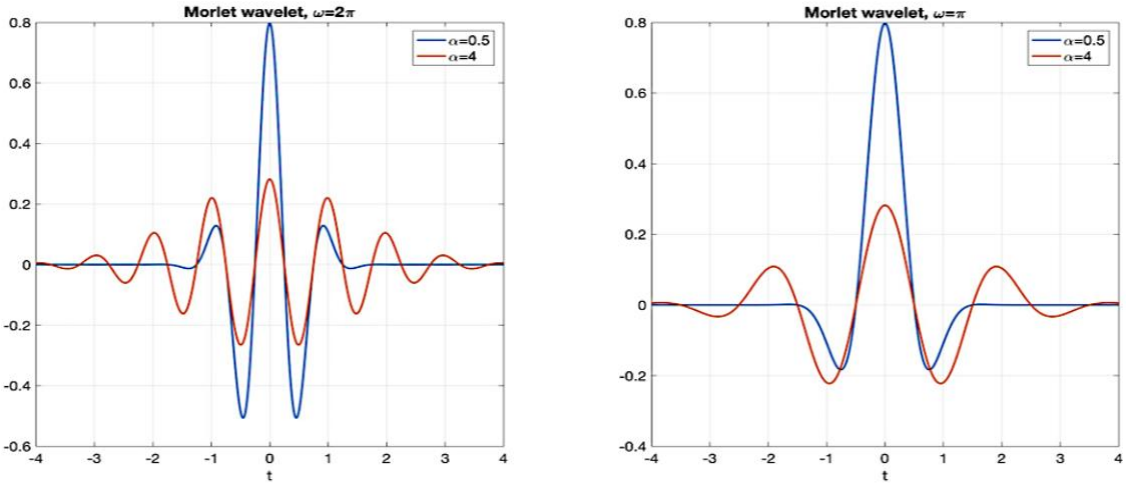

Figure 2.14 The real parts of the Morlet wavelet for ω=2π and for ω=π, for scaling factor α=0.5 (blue line) and α=4 (red line).

2.5 Nonlinear Analysis of Time Series

The existence of random, non-linear dynamics within the biomedical signal, such as LDF signals, illustrates a high complexity of the signal. Several nonlinear measures have been used widely to quantify the regularity and the randomness, respectively, of physiological signals and are well suited for the analysis of short length signals [4, 75, 76]. Approximate entropy (ApEn) [77] and Sample entropy (SampEn) [78], were used as fundamental methods to provide an important insight of the characteristics of nonlinear signals. The nonlinear methods employed here are estimated as described in the following sections:

2.5.1 Entropy-Based Analysis: Approximate Entropy

The study of the quantification of the signal by its information content was first proposed by Shannon [43], who developed a mathematical algorithm that determine the entropy of the system. Although, Shannon's entropy is a standard measure of entropy and does not consider the nonlinear dynamics of the system [31]. The most commonly used entropy algorithm, which is based on the dimension algorithm and the Sinai-Kolmogorov entropy (KSE) [79], using a correlation integral to calculate entropy, is the correlation dimension developed by Grassberger and Procaccia [80].

Similar to KSE and correlation dimension, approximate entropy (ApEn) introduced by Pincus [77], provides an applicable finite sequence formulation that discriminates the data sets by a measure of randomness, from totally regular to completely random [77, 81]. ApEn assigns non-negative patterns in time series, with larger values of ApEn corresponding to more irregularity and smaller values corresponding to more regularity in the data.

To measure ApEn, two input parameters, m, a positive integer that denotes the length of the compared runs and r, a positive real number that denotes the tolerance window, must be defined. ApEn measures the logarithmic likelihood that runs of patterns that are close (within r) for m contiguous observations remain close (within the same tolerance window r) on subsequent incremental comparisons. Given a time series of N data $x(n) = x(1), x(2), \dots, x(N)$, the ApEn can be computed as follows [81]:

- Form $N - m + 1$ vectors $X(1) \dots X(N - m + 1)$ defined by: $X(i) = [x(i), x(i + 1), \dots, x(i + m - 1)]$, $i = 1 \dots N - m + 1$.
- Define the distance between $X(i)$ and $X(j)$ as:

$$d[X(i), X(j)] = \max_{k=1,2,\dots,m} |x(i + k - 1) - x(j + k - 1)| \quad (2.11)$$

- Denote $N^m(i) =$ number of $X(j)$ $(j = 1 \dots N - m + 1)$ such that $d[X(i), X(j)] \leq r$ and define for each $i, 1 \leq i \leq N - m + 1$,

$$C_i^m(r) = N^m(i)/N - m + 1 \; . \quad (2.12)$$

The $C_i^m(r)$ measures, within the tolerance r the regularity of the frequency of the patterns similar to a given pattern of window length m.

- Next, define:

$$\Phi^m(r) = (N - m + 1)^{-1} \sum_{i=1}^{N-m+1} \ln C_i^m(r) \quad (2.13)$$

- By increasing the run length find $C_i^{m+1}(r)$ and $\Phi^{m+1}(r)$.
- From a given N data points, define $ApEn$ by:

$$ApEn(m, r, N) = \Phi^m(r) - \Phi^{m+1}(r) \quad (2.14)$$

As suggested by Pincus [81], the parameters values to calculate $ApEn$ are $m = 1$ and $r = 0.15$ time the standard deviation (SD) of the original time series. These input parameters produce good statistical reproducibility in $ApEn$ for time series of lengths $N \geq 60$ as considered in [77].

Example: For a time series $X = [4\ 3\ 4\ 3\ 4\ 3\ 2\ 3\ 4\ 2\ 3\ 4\ 2]$, $r = 0.15 * SD(X) = 0.1201, m = 2$ and $N = 13$

- For $m = 1$, $ApEn$ will be calculated by parsing the sequence
  $X = [$ (4) [3] (4) [3] (4) [3] ◇2 [3] (4) ◇2 [3] (4) ◇2$]$
  and based on equation (2.12), the counter matrix C_i^m will count, within the tolerance r, the number of the elements with the same value of the time series X divided to $N - m + 1$, so in X there are 5 candidates with the value "4", 5 candidates with the value "3" and 3 candidates with the value "2" (Figure 2.15).

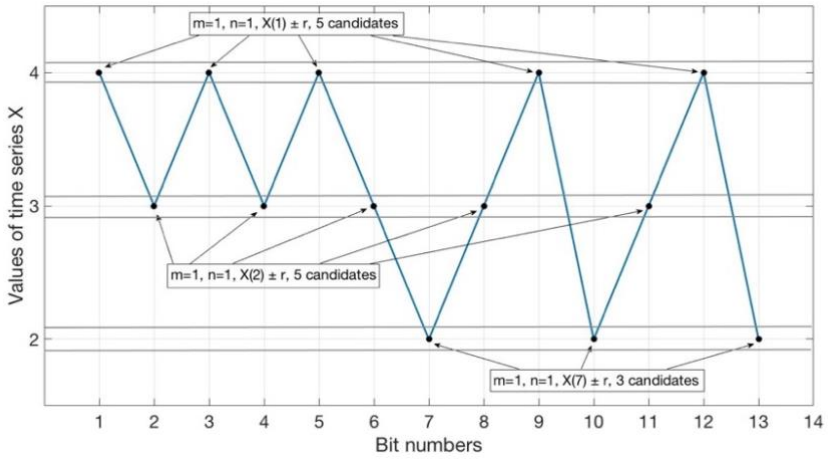

Figure 2.15 Plots of the matching for $\Phi^m(r)$, where $m = 1, n = 1$ so $X(1)$ will be the template one-sample window of comparison and $r = 0.1201$. The algorithm counts as a match the candidates that are between the range $X(1) - r < X(n) < X(1) + r$. So, for $X(1) \pm r$, there are 5 candidates matching the value in the range between the solid lines. For $X(2) \pm r$, there are 5 candidates matching and for $X(7) \pm r$, there are 3 candidates matching.

So C_i^m will be:

$$C = [\frac{5}{13-1+1}\ \frac{5}{13-1+1}\ \frac{5}{13-1+1}\ \frac{5}{13-1+1}\ \frac{5}{13-1+1}\ \frac{5}{13-1+1}\ \frac{3}{13-1+1}\ \frac{5}{13-1+1}\ \frac{5}{13-1+1}\ \frac{3}{13-1+1}\ \frac{5}{13-1+1}\ \frac{5}{13-1+1}\ \frac{3}{13-1+1}]$$

then from the equation (2.13), the correlation Φ^m will be the summary of the natural logarithm of the counter matrix C_i^mdevided to $N - m + 1$. So, $\Phi^m = -1.0524$.

- By increasing the run length find C_i^{m+1}, now the run length is $m + 1 = 2$, so in the time series X there are 3 sub-sequences with the values $[4\ 3]$, 4 sub-sequences with the values $[3\ 4]$, 1 sub-sequences with the values $[3\ 2]$, 2 sub-sequences with the values $[2\ 3]$ and 2 sub-sequences with the values $[4\ 2]$. So, from the equation (2.12), C_i^{m+1} will be:

$$C = [\frac{3}{13-2+1}\ \frac{4}{13-2+1}\ \frac{3}{13-2+1}\ \frac{4}{13-2+1}\ \frac{3}{13-2+1}\ \frac{1}{13-2+1}\ \frac{2}{13-2+1}\ \frac{4}{13-2+1}\ \frac{2}{13-2+1}\ \frac{2}{13-2+1}\ \frac{4}{13-2+1}\ \frac{2}{13-2+1}]$$

and from the equation (2.13), the correlation Φ^{m+1} will be the summary of the natural logarithm of the counter matrix C_i^{m+1}devided to $N - (m + 1) + 1$. So, $\Phi^{m+1} = -1.4435$.

- Thus, from the equation (2.14),

$$ApEn(m, r, N) = \Phi^m(r) - \Phi^{m+1}(r) = -1.0524 - (-1.4435) = 0.3911$$

As mentioned, the choice of the parameters and the length of the sequence play an important role for computing $ApEn$. Small values of r obtain less probability estimation, whereas with larger values there is a loss in the detailed information of the system. Additionally, $ApEn$ increases proportionally to the increase of the length N of the time series and therefore, the length of the data that would produce a good statistical validity of $ApEn$, need to be carefully selected [77, 82].

2.5.2 Entropy-Based Analysis: Sample Entropy

Sample Entropy (SampEn) is described as a refinement of ApEn, introduced by Pincus [77]. ApEn has proved to be a sufficient measure of the regularity for many signals, however, it is a biased measurement towards regularity and it is dependent on the length of the signal. To overcome these issues with ApEn, SampEn was developed by Richman and Moorman [78]. SampEn provides an applicable finite sequence formulation that discriminates the data sets by a measure of randomness, from totally regular to completely random. SampEn assigns non-negative patterns in time series, with larger values of entropy corresponding to more irregularity and smaller values corresponding to more regularity in the data. The regularity of the signal can be measured with the SampEn, by defining how often a short time series is repeated.

In order to measure SampEn of a time series, three parameters are defined, m, a positive integer that denotes the length of the compared runs, r, a positive real number that denotes the tolerance window and τ, the time delay. SampEn measures the logarithmic likelihood that runs of samples that are close for m continuous observations that remain close (within the same tolerance window r) on subsequent incremental comparisons. Given a time series of N data $x(n) = x(1), x(2), \dots, x(N)$, the SampEn can be computed as follows [31, 78]:

- Form $N - m + 1$ vectors $X(1) \dots X(N - m * \tau)$ defined by:

$$X(i) = [x(i), x(i+1), \dots, x(i + m * \tau)],\ i = 1 \dots N - m * \tau. \tag{2.15}$$

- Define the distance between $X(i)$ and $X(j)$ as:

$$d[X(i), X(j)] = \max_{k=1,2,\dots,m} |x(i + (k-1) * \tau) - x(j + (k-1) * \tau)| \tag{2.16}$$

- Denote $N^m(i) =$ number of $X(j)$ $(j = 1 \dots N - m * \tau)$ such that $d[X(i), X(j)] \leq r$ and defined for each $i, 1 \leq i \leq N - m * \tau$,

$$C_i^m(r) = N^m(i)/(N - m * \tau) \tag{2.17}$$

- Next, define:

$$\Phi^m(r, N, \tau) = (N - m * \tau)^{-1} \sum_{i=1}^{N-m*\tau} C_i^m(r) \tag{2.18}$$

- By increasing the run length, $C_i^{m+1}(r)$ and $\Phi^{m+1}(r, N, \tau)$ are counted. So, from a given N data points, $SampEn$ will be:

$$SampEn(m, r, N, \tau) = -\ln \frac{\Phi^m(r,N,\tau)}{\Phi^{m+1}(r,N,\tau)} \tag{2.19}$$

As suggested in the literature [7, 31, 46, 78, 81], the parameter values to calculate SampEn can be chosen as $\mathrm{m} = 2$ and $r = 0.15 \times$ SD of the time series. These parameters produce good statistical reproducibility in SampEn for time series of lengths $N \geq 60$ [81, 83].

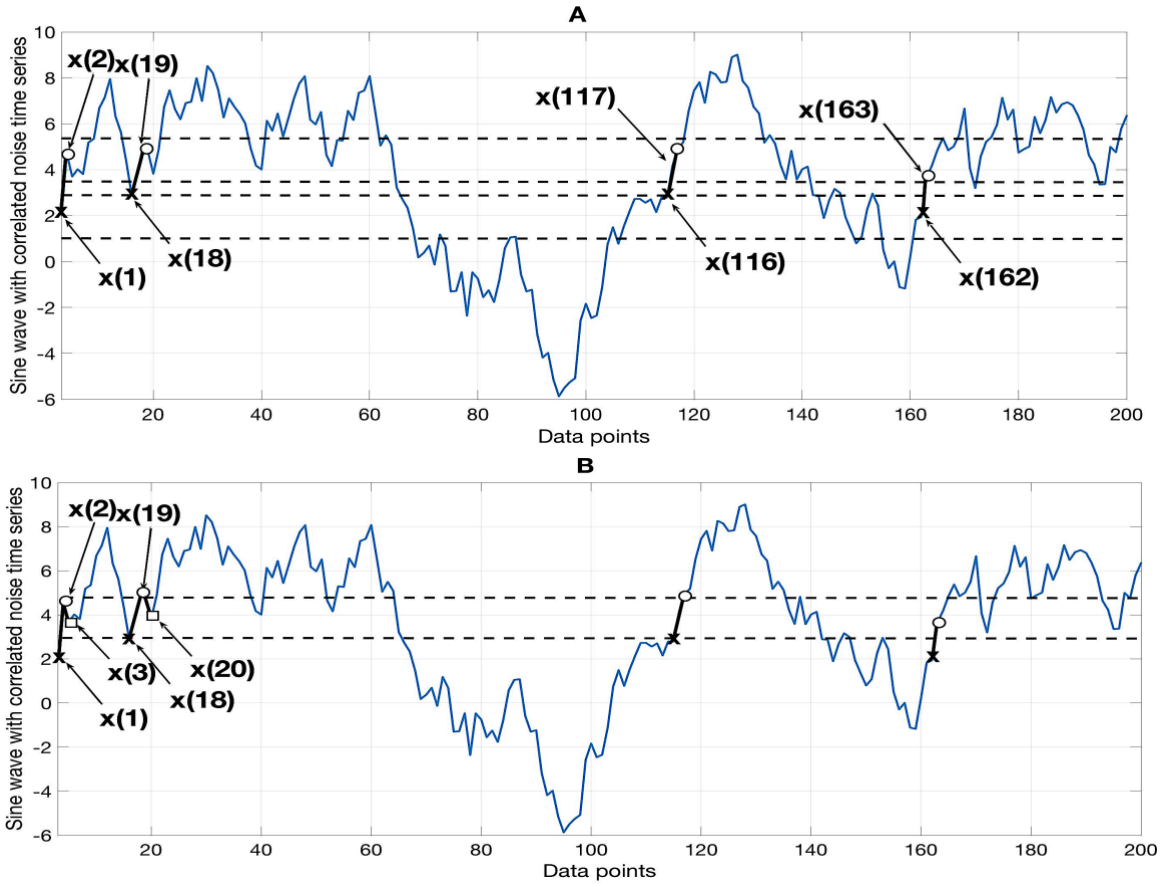

Figure 2.16 A simulated sine wave correlated with noise time series $x(1), \ldots, x(N)$, is shown to illustrate the procedure for calculating sample entropy (SampEn) for the case $m = 2$ and $r = 0.15 \times$ SD of the time series. Dashed horizontal lines around $x(1)$ and $x(2)$ at plot A, represent $x(1) \pm r, x(2) \pm 2$, respectively. Dashed horizontal lines around $x(3)$ at plot B, represent $x(3) \pm r$. The symbol "x" is used to represent the data points that match the data point $x(1)$. Similarly, the symbols "o" and "□" are used to represent the data points that match the data point $x(2)$ and $x(3)$, respectively. Consider the two-component x - o template sequence $[x(1), x(2)]$ and the three-component x - o - □ template sequence $[x(1), x(2), x(3)]$. For the segment shown, there are three x - o sequences, $[x(18), x(19)]$, $[x(116), x(117)]$ and $[x(162), x(163)]$ that match the template sequence $[x(1), x(2)]$, but only one x - o - □ sequence $[x(18), x(19), x(20)]$ that matches the template sequence $[[x(1), x(2), x(3)]$.

Figure 2.16 illustrates how SampEn values of a time series $x(1), \ldots, x(N)$ are calculated for run length $m = 2$ and tolerance window $r = 0.15 \times$ SD of the time series. As shown the numbers of sequences matching the two-component template sequences, $[x(1),\ x(2)]$, are three and the number of sequences matching the three-component template sequence, $[x(1), x(2), x(3)]$, is one. These calculations are repeated for the next two-component and three-component template sequence, which are $[x(2),\ x(3)]$, and $[x(2), x(3), x(4)]$, respectively. The number of sequences that match each of the two and three-component template sequences are again summed and added to the previous values. This procedure is then repeated for all other possible template sequences, $[x(3), \ldots ,\ x(N-2), x(N-1), x(N)]$, to determine the ratio between the total number of two-component template matches and the total number of three-component template matches. SampEn is the natural logarithm of this ratio and reflects the probability that sequences that match each other for the first two data points will also match for the next point.

2.6 Nonlinear Analysis of Binary Sequences

Nonlinear methods, based on ideas from information theory, have been used to quantify the regularity and randomness of short lengths of physiological signals and have demonstrated the potential for diagnostic capability [75]. Many researchers have applied a variety of techniques to capture the complex dynamics derived from physiological signals, such as approximate entropy [84], fractal measures [29], multifractality and wavelet analysis [85]. However, most of these algorithms require a minimum amount of stationary data to provide meaningful results. From a physiological perspective, the longer the dataset the higher the risk of having non-stationarities in the signal. Also, datasets with longer measurements may not be always be feasible or available in clinical research.

Recently, Nagaraj and Balasubramanian [86] describe three methods of quantifying complexity in terms of being better in dealing with short sequences and effective in characterizing biomedical signals. The most widely used measures in LDF signal analysis are sample entropy (SampEn) [78], Lempel and Ziv complexity (LZC) [87] and effort to compress (ETC) [88]. These nonlinear methods are based on the information content of a finite time series to calculate the randomness of its binary representation [89].

From previous studies [90, 91], it was reported that the binary conversion is sufficient to estimate the complexity in biomedical signals. Therefore, before calculating the complexity, the signal has to be first converted into a sequence of zeros and ones. Here, binary sample entropy, Lempel and Ziv Complexity, and effort-to-compress complexity are introduced as a complexity method. These methods have been used across a wide variety of biomedical applications, to

estimate and quantify symbolic sequences converted from a time series to determine the information present in a signal or a sequence.

However, conventional entropy and complexity methods have the drawback that they can only study the behaviour at one scale. To overcome this disadvantage, Costa, et al. [46] introduced an improved multiscale entropy algorithm to estimate the entropy over multiple scales. For this reason, multiscale algorithm will be described to understand the effect of scale on these nonlinear metrics. The nonlinear methods employed here are estimated as described in the following sections:

2.6.1 Binary Conversion

Many researches [4, 91, 92], convert the time series into 0-1 sequence by comparing each value with a threshold, which is usually set as the mean or the median value of the sequence, and replacing the value with zero if it is lower than the threshold and one if it is higher. In this work a different approach is considered. As suggested by Yang, et al. [93] and Ferrario, et al. [94], a straightforward way to maintain the important dynamics originated from a given signal is by using the increase and decrease encoding method, which will be referred here as delta encoding.

Let $X = x_1\ x_2 \cdots x_i$ denote a time series with an i length. The results of the encoding are compared with the previous element. If the value of the current element in the time series is increased compared to the previous value the corresponding element of the encoding sequence is set as 1. Otherwise, if it is decreased, then the value in the encoded sequence is denoted as 0. Thus, the time series is transformed into 0-1 sequence $S = s_1\ s_2 \cdots s_n$ with S_n expressed as:

$$S_n = \begin{cases} 0, & if\ x_n \leq x_{n-1}, \\ 1, & if\ x_n > x_{n-1}. \end{cases} \tag{2.20}$$

Now the binary sequence will have a length n, where $2 \leq n \leq i$, which is different from the length i in time series, referred as n-bit. Each n-bit correspond to a "word" of the binary sequence S and [90, 91] every n-bit represents the dynamics of the time series X. Figure 2.17 shows an example of the transform of a time series $X = [4\ 3\ 4\ 3\ 4\ 3\ 2\ 3\ 4\ 2\ 3\ 4\ 2]$ into 12-bit binary sequence using the delta encoding. So, the binary sequence will be $S = [0\ 1\ 0\ 1\ 0\ 0\ 1\ 1\ 0\ 1\ 1\ 0]$.

Additionally, Figure 2.18a illustrates a representation of a 10 sec epoch, from a blood flux signal, and the transformation into a binary sequence of zeros and ones, using median encoding (Figure 2.18b) and the delta encoding (Figure 2.18c). As shown, median encoding was shown to preserve fewer characteristics when compared to delta encoding and thus, delta approach will be used for the encoding of the blood flow signal in this thesis.

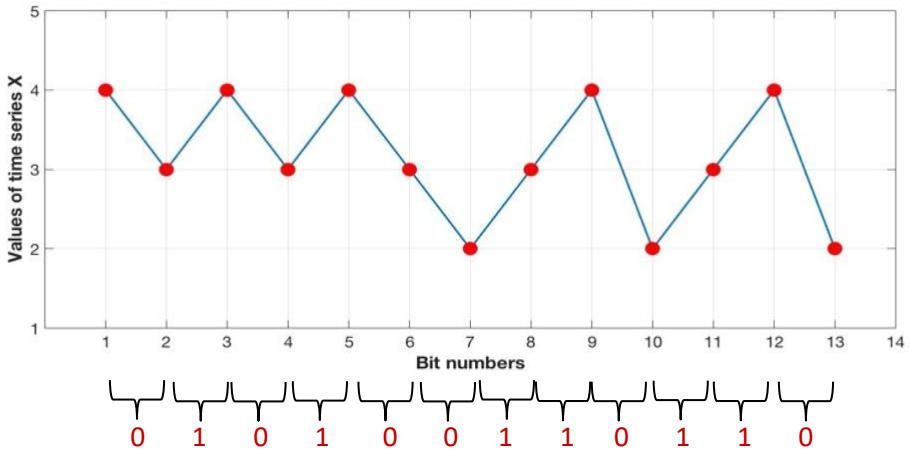

Figure 2.17 An illustration showing the transform of a time series into a 12-bit binary sequence of zeros and ones, using delta encoding.

In this example, the blood flow epoch was pre-processed with low pass filter to allow only the frequency range of the microvascular oscillation. This pre-processing will reduce any bias from noise that may affect the transformation of meaningful data points of the time series into a binary sequence.

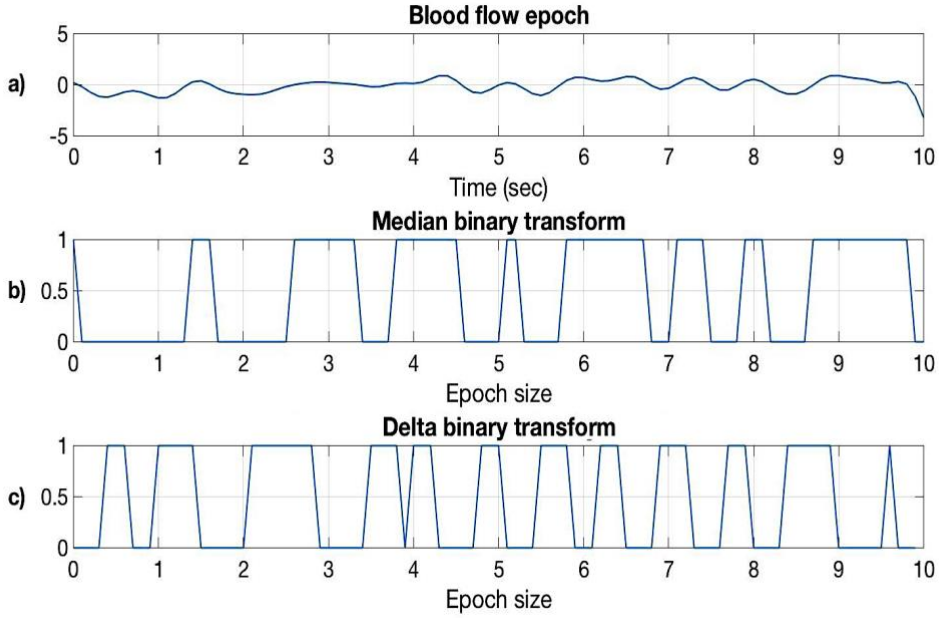

Figure 2.18 An example showing the transformation of (a) a 10 sec epoch of an LDF signal into a binary sequence of zeros and ones, (b) using median encoding (dotted line) and (c) delta encoding (solid line).

2.6.2 Binary Sample Entropy

In this study the time series will need to be first converted into a finite symbolic sequence. A sufficient conversion of the signal is the two-state sequence, a binary sequence of zeros and ones [4, 5, 90, 91, 95, 96]. Then, similar to the sample entropy of the time series, the two parameters m and r, are defined. Now, given a binary sequence of N data $s(n) = s(1), s(2), \dots, s(N)$, the binary SampEn according to Richman and Moorman [78], for the time series analysis and Skoric, et al. [97], for the analysis of the binary sequence, the sequence is computed to estimate the binary sample entropy. However, the SampEn sequence is binary and thus is limited diversity. For that reason, the number of elements of set of different k-bits vectors, is equal to 2^k and the binary SampEn is calculated as follows:

- To each of the binary sequence elements $S(i) = [s(i), s(i + 1 * \tau), \dots, s(i + m * \tau]$, $i = 1 \dots N - m * \tau$, a decimal counterpart c can be evaluated as:
$$c = \sum_{k=0}^{m-1} s_{i+k*\tau} * 2^k \quad (2.21)$$
- Define the distance between $S(i)$ and $S(j)$ as:
$$d[S(i), S(j)] = \max_{k=0,1,\dots,m-1} \left| s(i + k * \tau) * 2^k - s(j + k * \tau) * 2^k \right| \quad (2.22)$$
- Denote $N^m(l) =$ number of $S(j)$ $(j = 1 \dots N - m * \tau$ within r of $S(i)$ $(i = 1 \dots N - m * \tau)$, such that $d[S(i), S(j)] \leq r$ and defined for each $i, 0 \leq i \leq N - m * \tau$,
$$C_i^m(r) = N^m(i)/(N - m * \tau) \quad (2.23)$$
- Next, define:
$$\Phi^m(r, N, \tau) = (N - m * \tau)^{-1} \sum_{i=1}^{N-m*\tau} C_i^m(\mathrm{r}) \quad (2.24)$$
- By increasing the run length, $C_l^{m+1}(r)$ and $\Phi^{m+1}(r, N, \tau)$ are counted. So, from a given N data points, $SampEn$ will be:
$$SampEn(m, r, N, \tau) = -\ln \frac{\Phi^m(r,N,\tau)}{\Phi^{m+1}(r,N,\tau)} \quad (2.25)$$

Sample entropy requires the parameters m, r, and τ in order to provide meaningful results in the estimation of the entropy. The choice of these parameters varies for binary sequences. According to the literature [77, 78, 97], the parameters for the binary sample entropy estimation to effectively discriminate two data would be better set as $m \geq 2$, $r = 0$ or 1 and $\tau \geq 1$. The m parameter can be estimated using the false nearest neighbours method [33], however, often in the experimental data occur problems, such as drifts, so visual inspection can be also used to estimate the most suitable m as well as r parameters for analysis. The time delay τ can be obtained using either the autocorrelation function or the mutual information analysis when the correlation or mutual information between the two instances i and $i + \tau$ reaches its first relative minimum [33, 98, 99]. The parameters used in this study that produce satisfactory results after a visual inspection

of SampEn for binary sequences of both short and large lengths, were set as $m = 2, r = 0$ and $\tau = 1$. An interpretive example of the LDF signal for the choice of the parameters of the binary SampEn is shown in the supplementary figures A.1 and A.2 in Appendix A.

2.6.3 Lempel and Ziv Complexity

The idea of quantifying the randomness of a finite time series, was first introduced by Kolmogorov [100], proposing that large sequences can be restored by short computations as a measure of the complexity of that sequence. Following along the same lines, Lempel and Ziv [87], developed a complexity algorithm with the purpose to quantify and compress large data.

To measure the LZC, the signal must be first transformed into a binary sequence. Then, the sequence is parsed from left to right and the complexity increases by one unit when a new sub-sequence of continuous symbols is encountered. The LZC algorithm can be described as follows:

- Let $S = [s_1\ s_2 \cdots s_n]$ be a string that denotes a binary sequence with a finite length n that starts at the i position and finishes at the j position. So, when $i \leq j$ then $S(i,j) = \{s_1\ s_{i+1} \cdots s_j\}$
- and when $i > j$ then $S(i,j) = \{\}$, a sequence with zero length is set.
- A notation $v(S)$ is introduced which denotes the vocabulary of the sequence S and corresponds to the set of "words" that can be reconstructed from S. For example, if $S = 010$, the vocabulary $v(S)$ wil represent all the possible "words" that can be generated from the sequence, thus $v(S) = \{0,1,01,10,010\}$.The vocabulary $v(S)$ is then compared with every bit i of the binary sequence $S(i,j)$ which is up to $j-1$, so $i = 1,2,3 \ldots n, j > i$.
- Let Q denote the prefix of S that asks to the algorithm if this term is included in the substring of S, so Q can be obtained by copying the "words" of S. Then, set π as the procedure to delete the last "word" of the sequence S, so Q is a subsequence of the vocabulary $v(SQ\pi)$. A sequence S is called *reproducible,* if the incoming bit is present in $v(SQ\pi)$ and *producible* if is not present and therefore a dot · is placed after the sub-sequence to indicate the end of a new component.
- To reconstruct the sequence S, it is essential to have a production process called production history of S, $H(S) = S(1,h_1)\ S(h_1+1,h_2) \ldots S(h_{m-1}+1,h_m)$, where m are the "words" of the history and for $i = 1,2 \ldots m$, $H_i(S) = S(h_{i-1}+1,h_i)$, where h_i are the components of the history $H(S)$. The production history can be computed in two ways [87], depending on the production process of the sequence S, as follows:

- A production history is called "exhaustive" when all the components of $S(h_{i-1}+1, h_i)$ can be produced but not reproduced by the $S(1, h_{i-1})$. If each component in the history is exhaustive, with a possible exception of the last one, then the history is called exhaustive. Hence, the exhaustive production history will be denoted as $H(S)$.

  Example: For a sequence $S = 010100110110$, the sequence $H(S)$ which is the original sequence separated into components with dots by parsing of S, will be computed as follows:

  - The first digit "0" is unknown and hence has to be produced resulting into a component with a dot, so, $H(S) = 0 \cdot$.
  - For the second digit "1", is also unknown so, $S = 0$, $Q = 1$ so $SQ = 01$ and $SQ\pi = 1$, $Q \in v(SQ\pi)$, therefore production is adequate resulting in $H(S) = 0 \cdot 1 \cdot$.
  - For the third digit "0", $S = 01$, $Q = 0$ so $SQ = 010$ and $SQ\pi = 01$, $Q \in v(SQ\pi)$, therefore reproduction is adequate resulting in no change of $H(S)$ so, $H(S) = 0 \cdot 1 \cdot 0$.
  - For the fourth digit "1", $S = 01$, $Q = 01$ so $SQ = 0101$ and $SQ\pi = 010$, $Q \in v(SQ\pi)$, therefore reproduction is adequate resulting in no change so, $H(S) = 0 \cdot 1 \cdot 01$.
  - For the fifth digit "0", $S = 01$, $Q = 010$ so $SQ = 01010$ and $SQ\pi = 0101$, $Q \in v(SQ\pi)$, therefore reproduction is adequate resulting in $H(S) = 0 \cdot 1 \cdot 010$.
  - For the sixth digit "0", $S = 01$, $Q = 0100$ so $SQ = 010100$ and $SQ\pi = 01010$, $Q \in v(SQ\pi)$, therefore production is adequate resulting in $H(S) = 0 \cdot 1 \cdot 0100 \cdot$.

    ⋮
  - For the last digit "0", $S = 01010011$, $Q = 0110$ so $SQ = 010100110110$ and $SQ\pi = 01010011011$, $Q \in v(SQ\pi)$, therefore production is adequate resulting into another component with a dot, so,

    $$\boldsymbol{H(S) = 0 \cdot 1 \cdot 0100 \cdot 11 \cdot 0110 \cdot}$$

  Thus, the numbers of the components of the history $H(S)$ are equal to the length of the history, so in this example are 5.

- In order to define the complexity $c(S)$ of a sequence S, let denote $c_H(S)$ the least number of the components generated form the history $H(S)$ so,

$$c(S) = min\{c_H(S)\} \tag{2.26}$$

In this example, the number of the components of the "exhaustive" history $H(S)$ are 5 and therefore, the complexity $c(S)$ is **5**.

- With regard to Lempel and Ziv [87], the vocabulary of a sequence S is a set of "words". The "words" that are not contained in the vocabulary are called "eigenwords" and the number of the "eigenwords" is equal to the "eigenvalue" of the sequence S. The "eigenvalue" is an integer value and can be denoted as $k(S)$. Assuming that m is the largest integer of the sequence S, so that $S(m, n)$, where n is the length of the sequence, does not belong to the vocabulary of S, in that case the "eigenvalue" $k(S) = m$. Else if $S(m, n)$ belongs to the vocabulary of the sequence then the "eigenvalue" $k(S) = m - 1$. Thus, the "eigenvalue" profile of the sequence $S = 010100110110$, is now $k(S) = 122225577788$.
- From the theory, a production history, $H_i(S) = S(h_{i-1} + 1, h_i)$, is called "primitive" when h_i is the least integer such that the "eigenvalue" $k\big(S(1, h_i)\big) > S(1, h_{i-1})$. If each component in the history is primitive, with a possible exception of the last one, then the history is called primitive.
  The process for computing the "primitive" history $H(S)$ of a sequence S is easier when first computing the "eigenvalue" $k(S)$. So, for the sequence of Example I, $S = 010100110110$ the history and knowing that $k(S) = 122225577788$, the "primitive" history is:

$$\boldsymbol{H(S) = 0 \cdot 1 \cdot 0100 \cdot 11 \cdot 011 \cdot 0 \cdot.}$$

  Thus, the numbers of the components of the history $H(S)$, based on equation (2.26), are equal to the length of the history, so for the "primitive" history the complexity $c(S)$ is **6**.

Therefore, the "eigenvalue" is indicative for both production histories. As referred by Limniotis, et al. [101], the dots of the "eigenvalue" history define the dots of the "exhaustive" history and as shown, the changes of the "eigenvalue" determine the dots of the "primitive" history, with an exception of the first one. Figure A.3 in Appendix A, illustrates the flow diagram of the algorithm to calculate the complexity for a given sequence.

It is obvious that the complexity depends on the production process of the original sequence. Thus, it is significant the choice of the type of the history that could be used for estimating the complexity. According to Lempel and Ziv [87], the "primitive" type is a "clarification" of the

"exhaustive" type and is described as a different way rather than (or in addition to) the "exhaustive" type, for evaluating the complexity of a binary sequence S. It is also suggested that the "exhaustive" type is a traditional estimate of the complexity of a binary sequence S since the components of the sequence are not reproduced. In Hu, et al. [96], both complexity types were described, but the primitive type was used for convenient analysis as it is computationally easier to calculate. Other studies [101], suggest that exhaustive type is a sufficient type for calculating the LZC. In this work, the exhaustive type of complexity is employed, however both types will be demonstrated and described to justify this choice.

Many studies [91, 96, 102], describe that in order to obtain a complexity, which is independent of the length of the sequence, n, then the complexity $c(S)$ ought to be normalized. With regard to Lempel and Ziv [87], for every sequence S with a length n, the number of the components of the production process of the sequence, $c(S)$, will be: $c(S) < \frac{n}{(1-\varepsilon_n)\cdot log_a(n)}$, where a is the base of the logarithm and ε_n is a small quantity that tends to be equal to zero when the length n of the sequence is large. So, for a binary sequence with $\mathrm{a} = 2$, the normalized complexity $C(S)$ will now be:

$$C(S) = \frac{c(S)}{\frac{n}{log_2(n)}}. \tag{2.27}$$

Thus, it is justified that a large length n represents more complexity. An example of an un-normalized LZC plot and a normalized one, is illustrated in Figure 2.19. In this thesis, the normalized version of the LZC is used for convenience as it is independent of the length of the sequence and is suitable for comparing sequences with different lengths.

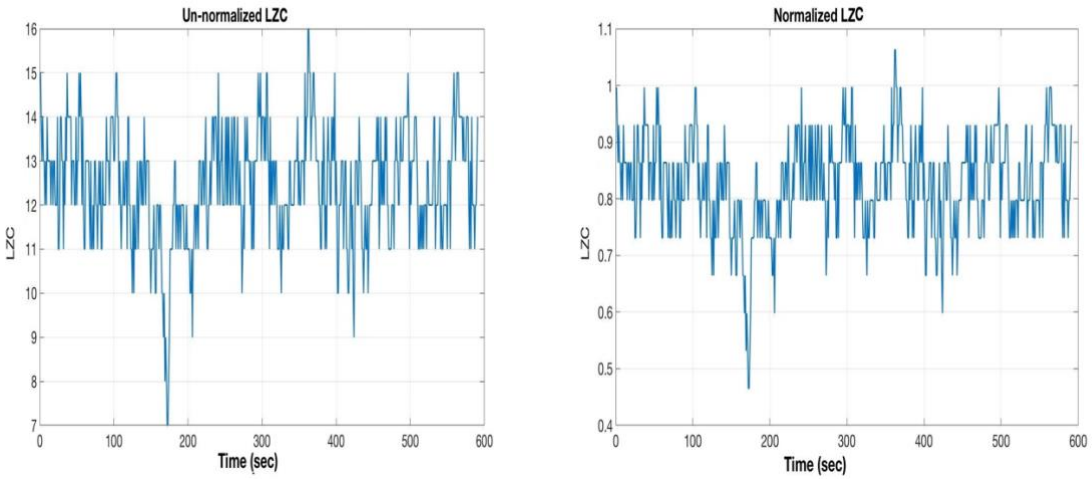

Figure 2.19 Illustration of un-normalized LZC graph (left plot) and normalized LZC graph (right plot) from the LDF signal of a healthy volunteer.

An interpretive example of the calculation of LZC for a sine wave and a sine wave with correlated noise is shown in Figure 2.20. First both sine wave signal and the same sine wave correlated with a random signal were transformed into a binary sequence and then LZC was evaluated. The parameters of the LZC were set as “exhaustive” and normalized complexity. As expected, the sine wave has lower complexity than the noisy sine wave and that is because the sine wave is a regular and periodic signal with consistent amplitude and contains very low complexity. Whereas, the noisy sine signal is no longer regular or periodic and is difficult to predict its behaviour, so the signal becomes more random with higher complexity.

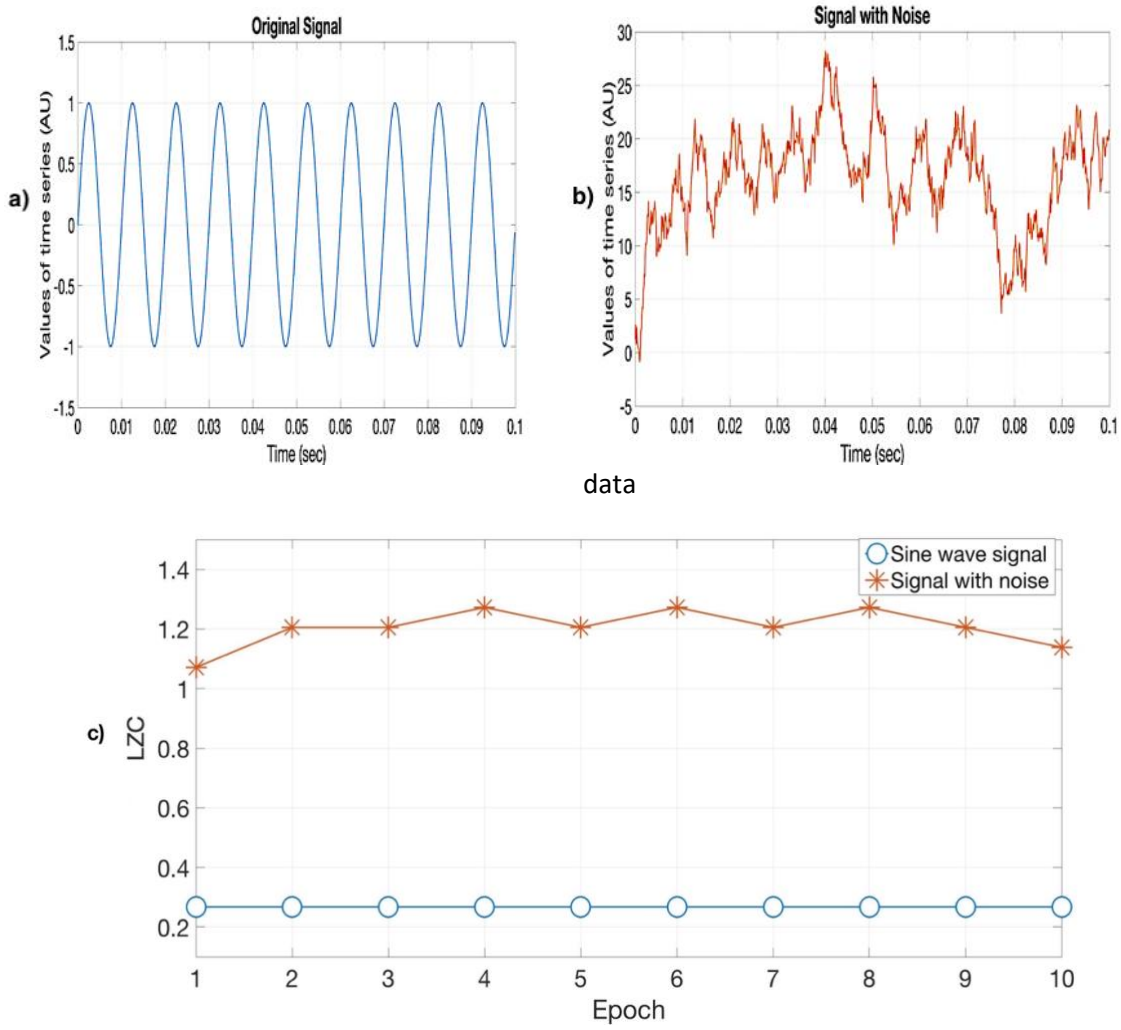

Figure 2.20 a) A 100 Hz sine wave signal, b) The same sine wave with correlated noise, c) LZC for both signals. In order to estimate the randomness by using the LZC method a sine signal was generated ($f = 100\ Hz, f_s = 10\ kHz$) and noise by generating a random signal added (using the Matlab function “cumsum” of a random signal).

2.6.4 Effort to Compress Complexity

A similar complexity method based on the lossless compression algorithm known as Non-sequential Recursive Pair Substitution (NSRPS) [103] is the Effort to compress (ETC) complexity, proposed by Nagaraj, et al. [88]. Similar to the LZC measure, the given sequence has to be first converted to a symbolic sequence. So, let a binary sequence $S = \{010100110110\}$, the algorithm can be described as follows:

- Define the pair of symbols with the maximum occurrence and replace all its non-overlapping occurrences with a new symbol, at each iteration. This procedure is repeated and is dependent on NSRPS which estimates the entropy for each operation that the algorithm obtains, providing a new sequence $S_{new_N}, N = 1 \ldots$ number of iterations, until it reaches a constant sequence.
- Now, the input sequence S is first converted into $S_{new_1} = \{22021210\}$ considering that the pair "01" has maximum occurrences compared to pairs "00", "10" and "11".
- In the next iteration, S_{new_1} is converted into $S_{new_2} = \{220330\}$ considering that the pair "21" has maximum occurrences.
- The algorithm continues in this way until there is no pair left to replace and the converted sequence becomes a constant sequence.

In this example, the algorithm converts the given sequence S as: $S = \{010100110110\} \rightarrow S_{new_1} = \{22021210\} \rightarrow S_{new_2} = \{220330\} \rightarrow S_{new_3} = \{40330\} \rightarrow S_{new_4} = \{5330\} \rightarrow S_{new_5} = \{630\} \rightarrow S_{new_6} = \{70\} \rightarrow S_{new_7} = \{8\}$.

So, according to Nagaraj, et al. [88], the ETC complexity measure is defined as:

$$N \rightarrow Number\ of\ iterations\ of\ NSPRS\ algorithm\ for\ entropy \rightarrow zero$$

More specifically, N is the number of iterations, of NSPRS algorithm, required for the given sequence to be transformed to a constant sequence with zero entropy. In this example, N is 7 and the normalized measure is computed as: $\frac{N}{L-1}, 0 \leq N-1 \leq 1$, with L=length of the sequence. In this work, the normalized measure was used.

In order to examine the implementation of the nonlinear methods through various signal lengths, first the SampEn, LZC and ETC complexity were applied in a random (generated from Matlab using the function “randn”) signal with different length (Figure 2.19). For short signals, both LZC and ETC give results that are not meaningful for the estimation of complexity, while in SampEn the values for lengths below 128 are not determined. Only values for length higher than 500 samples provide reasonable estimate of the complexity of the signal.

As shown from Figure 2.21 there is no particular reason for choosing one of the nonlinear methods for analysis over the others as both entropy and complexity becomes consistent when the signal has more than 1000 samples. However, this need to be tested in complex physiological signals in order to estimate the performance of these measures in various lengths. From this test, useful information on the decision of the minimum length of the signal used for a sufficient nonlinear analysis was obtained.

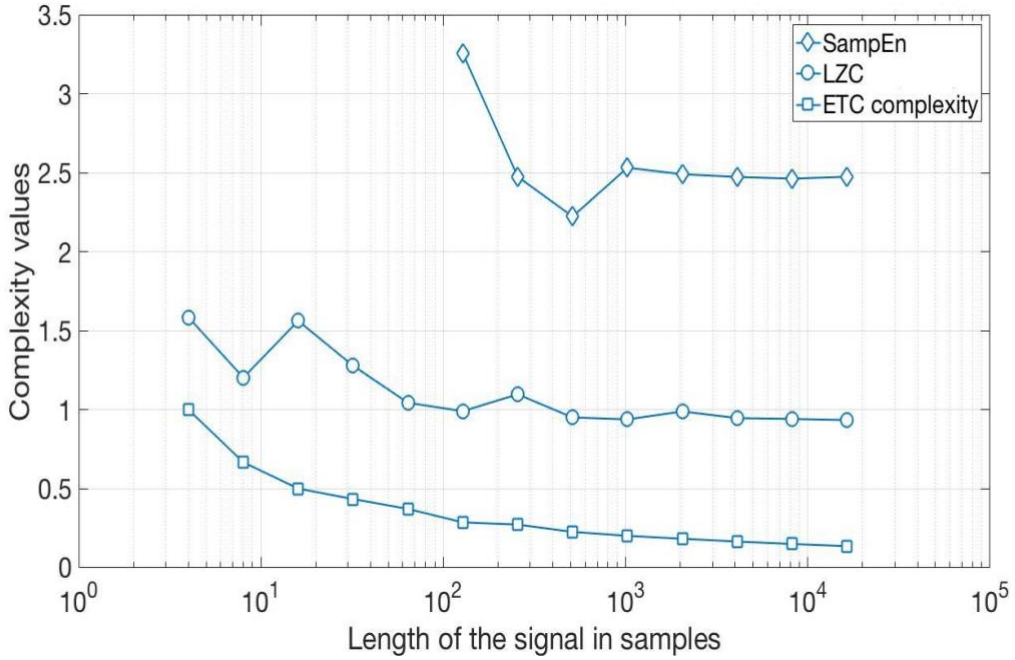

Figure 2.21 Effect of the length of a random signal on SampEn (diamond markers), LZC (circle markers) and ETC complexity (square markers). SampEn provides a meaningful estimation of the entropy for a signals > 128 samples. LZC and ETC complexity do not give any reasonable values of complexity for signals < 500 samples.

2.7 Multiscale Analysis

Entropy and complexity methods are used to analyse signals on a single scale, however, when applying these methods in physiological complex systems it is important to take into account the multiple time scales of the underlying processes modulating the signal. To examine if a signal is consistent across multiple spatial and temporal scales and does not change with different sampling frequencies, it is a necessity to measure the entropy and the complexity of the time series in multiple time scales. Here, three methods for scaling a physiological time series will be described.

1. Costa, et al. [46], proposed the Multiscale Entropy (MSE) technique for analysing biological signals using the coarse-graining method that resamples the original signal by reducing the scale of the time series and then determining the sample entropy for each scale step. Thus,

coarse graining is a method, which alters the sampling frequency of the signal by a scale factor, τ, which defines the number of the sampling levels. So, for a time series $\{x_1, \dots, x_N\}$, the coarse-grained time series, y^τ, will be:

$$y_i^\tau = \frac{1}{\tau}\sum_{i=(i-1)\tau+1}^{i\tau} x_j \,, 1 \le i \le N/\tau \,. \tag{2.28}$$

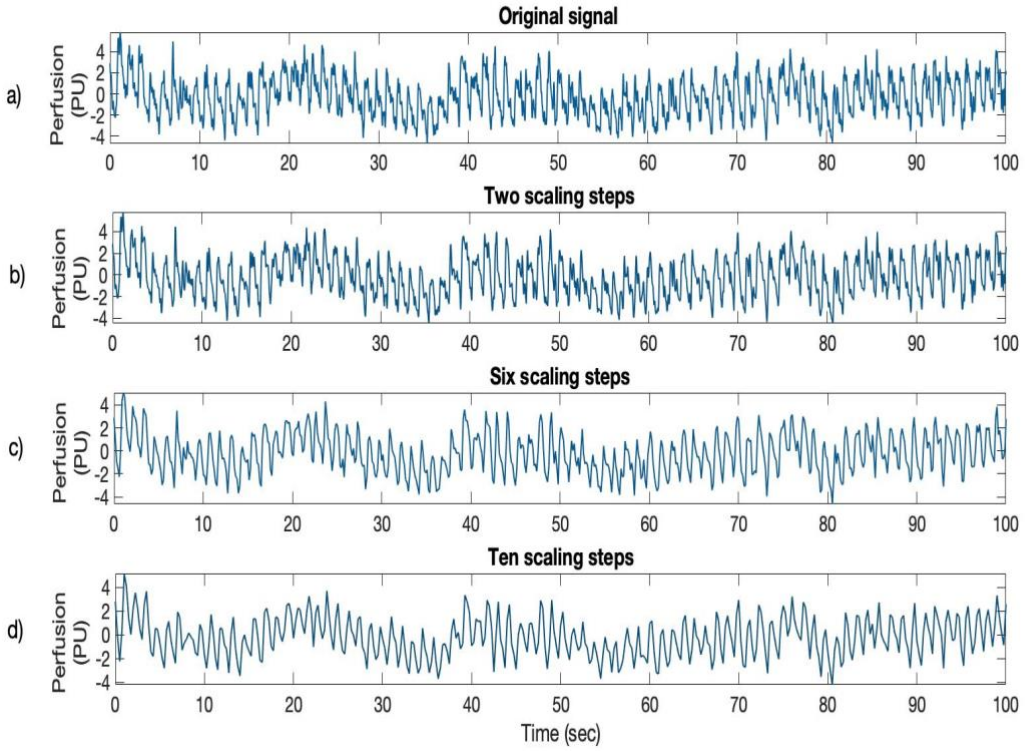

Figure 2.22 A skin BF signal coarse-grained at multiple scale lengths. a) The original signal. b) The signal scaled down by two times. c) The signal scaled down six times. d) the signal scaled down to ten times.

More specifically, this method decreases the scale of the signal by grouping the data points into a non-overlapping segment of length τ and then the average is calculated for each segment. For a scale factor one, the time series y^1 is the original signal. So, the length of each time series $\{y^\tau\}$ is the equal to the length of the original signal divided by the scale factor, τ. A straightforward way to illustrate the coarse-graining procedure is shown in Figure 2.22, using a skin BF signal coarse-grained at multiple scale lengths. Figure 2.23 also provides a more detailed description by showing the average of the data points from an illustrative part of the sine wave correlated with noise signal. The features of the signal have been expanded in many scales, although the information of the signal has remained.

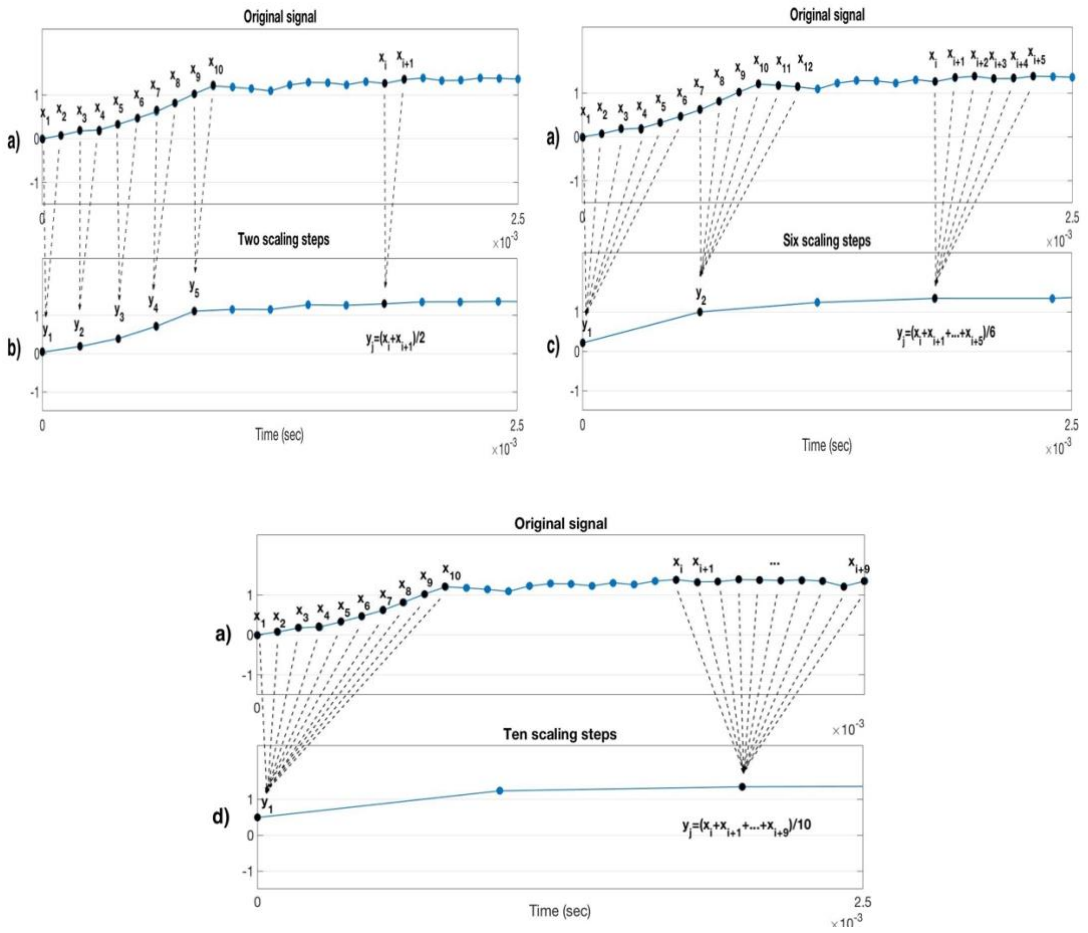

Figure 2.23 Schematic illustration of the coarse-graining method showing the averaging of the data point from a part of a sine wave with correlated white Gaussian noise. a) The original signal. b) The signal scaled down by two times. c) The signal scaled down six times. d) The signal scales down to ten times.

2. The multiscale entropy that Costa, et al. [46] introduced, reduces the time scale of the signal using a simple average which is a weak low-pass filter and does not take into account that physiological time series contain information in high frequencies which means that this method may cause distortion of the signal. To avoid this drawback, Semmlow and Griffel [31] reported an alternative method for coarse graining the signal by using a low-pass Butterworth filter instead of the average of the data points. So, the algorithm of this procedure starts by defining the cut-off frequency of the low-pass Butterworth filter which is $1/(1+\tau)$, where τ is the scale factor and then the low-pass Butterworth filter is applied. In this way the filter takes as an input the ratio of the cut-off frequency by the half of the sampling frequency. Then the filtered signal is downsampled by discarding the frequencies by $1+\tau$ and therefore reducing the number of the data points of the signal by $1+\tau$.

3. The coarse-graining method that Semmlow and Griffel [31] introduced can also be computed using the Matlab function “resample”, which applies and antialiasing finite impulse response (FIR) low pass filter to the time series and compensates for the delay introduced by the filter. So, for a time series x, the signal will be resampled as: $y^{\tau} = x\ (1{:}\ \tau{:}\ end)$, where τ is the scale factor, and the low pass filter is applied for each coarse-grained time series.

In this work, the approach proposed by Costa, et al. [46] was considered, as pre-processing techniques (see chapter 3) are applied to the signals before applying the multiscale analysis and therefore, further attenuation to the signal will be redundant.

2.8 Summary

In this chapter, a review of the background literature has been presented. Different types of biomedical signals and an overview of signal processing techniques were first introduced. In physiology, a brief description of the human circulation, especially skin microcirculation, was reviewed, highlighting the cardiovascular diseases. The assessment methods for measuring the microcirculation, where also described, with an emphasis in the LDF and WLS techniques. These measurements from the human skin are specified to provide an overview of both LDF and WLS equipment. In this thesis, signal processing techniques to analyse the characteristics of blood flux and oxygenation signals in frequency domain will be presented. Also, the use of nonlinear complexity-based and multiscale-based methods to estimate and quantify symbolic sequences converted from the time series of blood flux and oxygenation, will be considered and these techniques have also been introduced. In the following chapters, they will be applied to LDF and oxygenated haemoglobin signals.

Chapter 3: Time-Frequency Domain Analysis

In this chapter the research methodology is described and an overview of the inclusion criteria for the selection of the volunteers given. A description of the methodology of the signal analysis in time and frequency domain is provided.

3.1 Research Methodology

The data in this chapter were obtained from a group of 15 healthy young male volunteers, whose age was 29.2 ± 8.1 (mean ± SD), and were obtained from a previous study [54]. The main aim was to investigate the blood flux (BF) and oxygenation (OXY) signals in time and frequency domain using a combined laser Doppler flowmetry and white light spectroscopy method to provide a benchmark for later work.

3.1.1 Ethics Approval

The ethical aspects of the study were approved by the Research Ethics Committee of University of Southampton and Southampton General Hospital (REC Number: SOMSEC091.10; RHMMED0992). The study was performed according to the principles outlined in the Declaration of Helsinki.

3.1.2 Study Protocol and Subject Recruitment

The study was an open study of healthy individuals. All participants were asked to refrain from caffeine including drinks for at least two hours before the measurement and to avoid exercise on the day of the measurements. All studies were obtained in a temperature controlled quiet room at 23.0-23.5℃ and all volunteers were acclimatized for at least 20 minutes before the measurements were taken.

All participants were asked to stay still and avoid talking during the measurements in order to avoid movement artefacts in the signals recorded. The signals were recorded using the combined Doppler flowmetry (LD) and white light reflectance probe (Moor CP7-1000 blunt needle probe, Moor Instruments Ltd, Axminster, UK) with an LD fibre separation of 0.5 mm and SO2 separation of 1 mm, using a single point 785 nm, 1 mW low power red laser light source (moorVMS-LDF2, Moor Instruments Ltd, UK) and a 400-700 nm, <6 mW white light source (moorVMS-OXY, Moor Instruments Ltd, UK), for measuring both the blood flux and the oxygenated blood perfusion, at a sampling rate of 40 Hz.

Each volunteer was sitting comfortably with the arm at heart level and the probes were attached to the forearm for the recording of the signals. A local physiological perturbation of blood flow was performed in this study. The participants had one or more perturbations performed including post-occlusive reactive hyperaemia (PORH) initiated by a pressure cuff around the forearm, inspiratory breath holds and local skin warming by placing the probe on the surface of the skin and raising the skin temperature to 33℃ and during local thermal hyperaemia (LTH) at 43℃. Also, measurements were taken at the foot of every volunteer at ambient temperature with no further heating applied. The skin temperature was controlled using a Moor VHP1 skin heating block with moorVMS-HEAT skin heater to warm the skin between 20-45℃. Skin temperature was measured by a miniaturised negative temperature coefficient thermistor built into the heating block controlling skin warming with a precision of ±0.1℃ and resolution of 0.1℃. The heating block and probe were placed on the ventral surface of the non-dominant forearm using a double-sided sticky O-ring, approximately 10 cm from the wrist and avoiding visible veins.

The measurement protocol for the local warming consisted of a period of 20 minutes resting skin temperature then the local skin temperature was raised to 33℃ and after a period of 20 minutes the skin temperature was raised to 43℃ and retained at this temperature for 25 minutes. In the work considered here, only the latter LTH stimulus is considered.

The main exclusion criteria to satisfy the study were the following:

- Participant does not have a history of Cardiovascular Disease
- Participant is not a smoker
- Participant does not have diabetes
- Participant is not in an on-going pregnancy
- Participant does not take any medication that can affect the blood flow

All volunteers were asked to read carefully and sign an informed consent form for participating in this study.

3.2 Data Analysis

The BF and OXY recordings were obtained before and in two haemodynamic steady states at 33℃ and at 43℃. Figure 3.1 illustrates the BF, OXY and the temperature outputs of the combined LDF/OXY probe recorded and the selection of the 10 minutes segments at 33℃ and at 43℃. These segments were selected so as to minimise any transitional effects arising during warming and to be free of movement artefacts. Data were exported to Matlab (R2016b, Mathworks, UK) for pre-processing and analysis. The parameters obtained were BF in perfusion units (PU), oxygenated haemoglobin (oxyHb), deoxygenated haemoglobin (deoxyHb), total haemoglobin (totalHb = oxyHb

+ deoxyHb) in arbitrary units (AU) and tissue oxygen saturation (SO_2). SO_2 (%) is derived from the relationship SO_2 = (oxyHb/totalHb) * 100% [104].

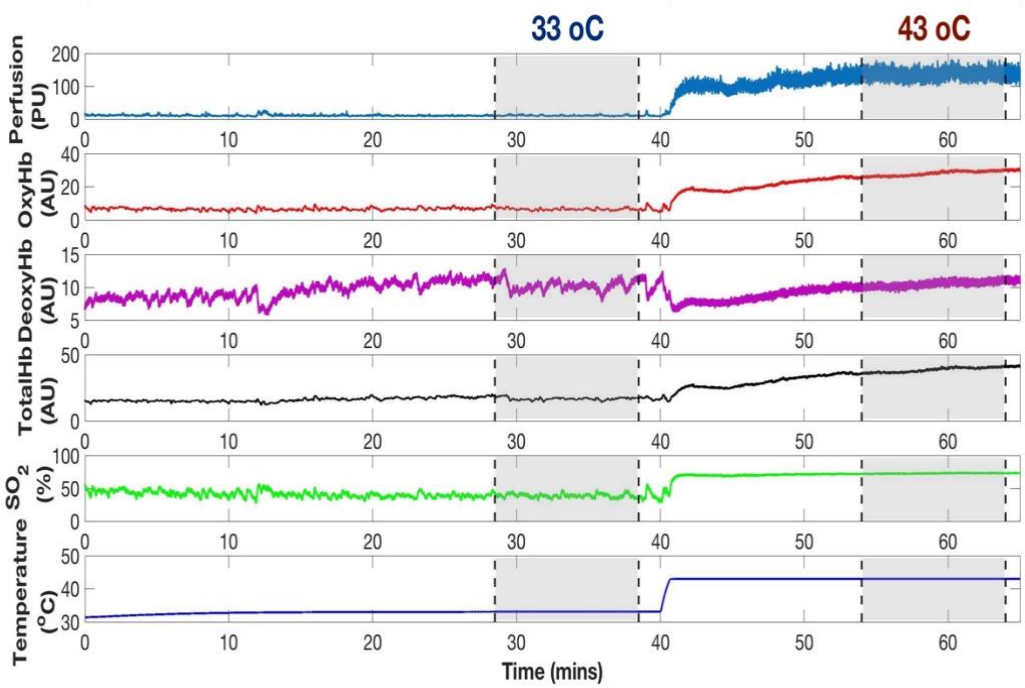

Figure 3.1 Selection of the 10 minutes segments (dashed lines) for the data analysis at 33℃ and 43℃. The signal and temperature plots were obtained from one individual (h0_02).

Here, oxyHb output was elected as the prime OXY signal for the complexity analysis as suggested by previous studies [40]. The truncated data could then be analysed and calculations made for power spectral density and wavelet analysis to better understand the behaviour of the microvascular blood flow and oxygenation using the spectral and the time-localized and frequency domain analysis. The time domain characteristics of the BF and OXY signals as well as the statistical differences between the haemodynamic steady states are summarised in [54].

3.2.1 Pre-processing

Before estimating the power spectral density, it is necessary to perform some pre-processing of the raw data. To reduce any bias from measurement noise or frequency content outside from the range of interest, the segments were filtered using a low pass finite impulse response (FIR) filter with 2Hz cut-off frequency, to attenuate high frequencies beyond the known range of microvascular oscillation and allow the frequencies of interest with a range from 0.0095 to 1.6Hz, to pass [36, 39]. FIR filter was chosen for designing and implementation convenience as well as for producing inherently stable oscillatory outputs. The data were then detrended by removing the mean and reducing overall variation and a stationarity test was performed on the processed data

to examine whether the data have a consistent variance over time. This pre-processing ensures that the analysis of the signals is not biased by noise or components outside the range of interest.

3.2.2 Power Spectral Density

The power spectrum was obtained via Fourier transformation as it gives greater flexibility in setting parameters, such as window function and overlap, such that the spectrum is reflective of the content of interest. The most common method for calculating PSD is the Welch's method, which performs an FFT on each segment and computes the squared magnitude (power spectra). In this study the Hanning window function was used, with a 200 second length and 50% overlap between windows. The 200 seconds window length is adequate because the lowest frequency of interest is 0.0095Hz, which is equal to 105 seconds thus it contains 1.9 cycles. This is sufficient to describe the frequency content of the signal at the lowest frequency of interest. The 600 seconds recording covers at least five cycles, in total, of the lowest frequency and is adequate to describe the frequency content of the physiological signals [26].

The power spectral density was estimated within the range from 0.0095 to 1.6 Hz in which the periodic activities that regulate the blood flow occur. These periodic activities have been studied by many research groups [36, 105-107] and comprise the low frequency (LF) oscillations: endothelial activity (0.0095-0.02 Hz), neurogenic activity (0.02-0.06 Hz), oscillations arising from local vasomotor myogenic activity (0.06-0.15 Hz) and the high frequency (HF) bands: respiratory activity (0.15-0.4 Hz) and oscillatory haemodynamic effects of the heart beat (0.4-1.6 Hz). Here, the PSD is evaluated for each volunteer in two haemodynamic steady states at 33°C and 43°C, respectively.

3.2.3 Time-localised Frequency Domain Analysis

The Wavelet transform can be employed to obtain a time-localised frequency domain analysis to examine how the signal content changes over time. Morlet wavelet has been used as a mother function as it has been adopted in previous studies from other researchers [36, 74, 108-110]. Based on equation (2.12) of chapter 2, Matlab function "cwt" was used to undertake the wavelet analysis with the Morlet wavelet defined as:

$$\Psi(t) = \frac{1}{\sqrt{\pi \cdot f_b}} \cdot e^{i2\pi f_c t} \cdot e^{-t^2/f_b} \tag{3.1}$$

where, f_b is the bandwidth and f_c is the centre frequency. f_c was set at 1.5 because, as described by Goupillaud, et al. [111], when a constant known as σ, which is proportional to f_c from the equation $\sigma = 2\pi f_c$, is small then some terms in the Morlet wavelet can be simplified. The

parameter f_b was set 2 because it has been shown to be an appropriate choice by other researchers [36, 39, 112].

3.2.4 Statistical analysis

Statistical analysis was performed in IBM SPSS statistics 22 (IBM United Kingdom) and Microsoft Excel 2010 (Microsoft Corporation, US). Data were tested for normal distribution using the D'Agostino & Pearson omnibus normality test [113]. Data are presented as either mean ± standard mean error (SEM) for normally distributed data or median with interquartile range (IQR) for non-normally distributed data. Normally distributed data were compared using a Student t-test and non-normally distributed data using a Mann-Whitney U-test. In all cases a value of $p < 0.05$ was taken to indicate statistical significance.

3.3 Results

3.3.1 Results of the Power Spectral Density

Figure 3.2 shows the mean of the total PSD of both BF and oxyHb signals of all healthy volunteers at 33℃ and 43℃. It is noticeable that for BF signals the mean power spectrum increases with local warming. As shown in Table 3.1, in which at 33℃ the mean value and the standard error of the mean (SEM) are 4.47 ± 1.19 and at 43℃ is 263.27 ± 43.14 for the BF signals although, no change was found for absolute total power between 33℃ and 43℃ for the oxyHb signals. In Table 3.2 the values of the power spectral density for each frequency band in terms of the mean ± SEM for comparing the power spectrum between 33 ℃ and 43 ℃ for both BF and oxyHb signals, are presented. The PSD is significantly higher at 43℃ for all the frequency bands in BF signals (p< 0.05). For oxyHb signals the absolute PSD showed significantly lower values at 43 ℃ only in the LF neurogenic band, however, at the HF bands the PSD at 43℃ increases having a significant difference between the two haemodynamic steady states (p<0.05), with a remarkable increase in the cardiac band during LTH for both signals.

Table 3.1 Total absolute PSD at 33℃ and at 43℃ respectively and the p-value for comparing the PSD of BF and oxyHb signals at 33℃ and at 43℃, for n=15 volunteers. Data are presented as mean ± SEM.

PSD	**33**℃	**43**℃	**p-value**
BF signals	4.47 ± 1.19	263.27 ± 43.14	<0.05
oxyHb signals	0.36 ± 0.06	0.39 ± 0.10	0.713

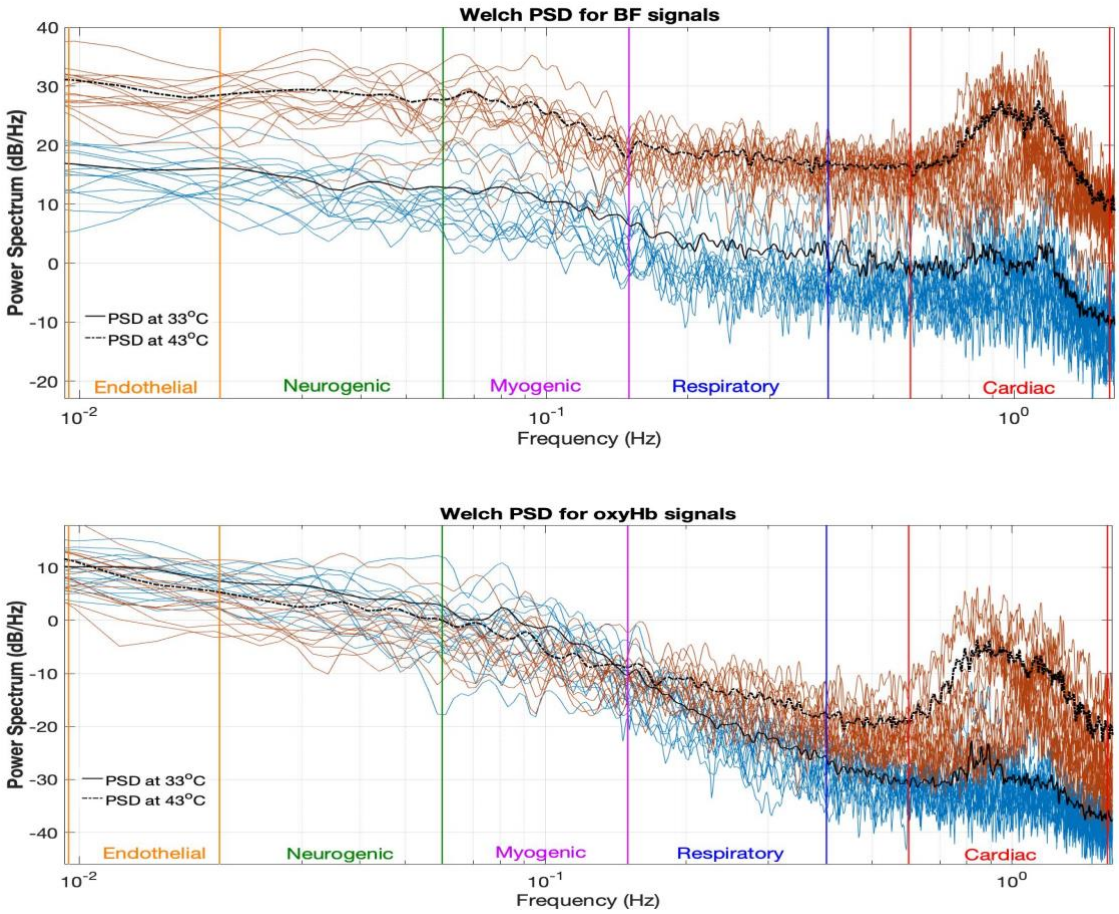

Figure 3.2 The mean PSD of the blood flux signals (top plots) and oxygenated haemoglobin (bottom plots) from all 15 healthy volunteers for all frequency bands at 33℃ (solid line) and 43℃ (dotted line). Individual spectra are shown as blue plots and red plots for all 15 volunteers at 33℃ and 43℃, respectively. PSD is plotted in a log axis as $10 \cdot \log_{10} \mathrm{PSD}$ over frequency.

Table 3.2 Absolute PSD for both BF and oxyHb signals at 33℃ and at 43℃ respectively for each frequency band, for n=15 volunteers. Data are presented as mean ± SEM.

	BF signals		**OxyHb signals**	
	33℃	**43**℃	**33**℃	**43**℃
Endothelial	0.74 ± 0.17	16.11 ± 3.41*	0.14 ± 0.03	0.14 ± 0.05
Neurogenic	1.06 ± 0.27	31.33 ± 6.82*	0.15 ± 0.03	0.08 ± 0.03*
Myogenic	1.11 ± 0.35	33.35 ± 7.94*	0.07 ± 0.02	0.04 ± 0.01
Respiratory	0.53 ± 0.22	16.60 ± 2.07*	$4.5 \cdot 10^{-3} \pm 0.9 \cdot 10^{-3}$	$1.2 \cdot 10^{-2} \pm 2.5 \cdot 10^{-3}$*
Cardiac	1.03 ± 0.28	165.88 ± 28.27*	$1.2 \cdot 10^{-3} \pm 0.3 \cdot 10^{-3}$	0.11 ± 0.03*

*Significant difference from 33℃, $p < 0.05$.

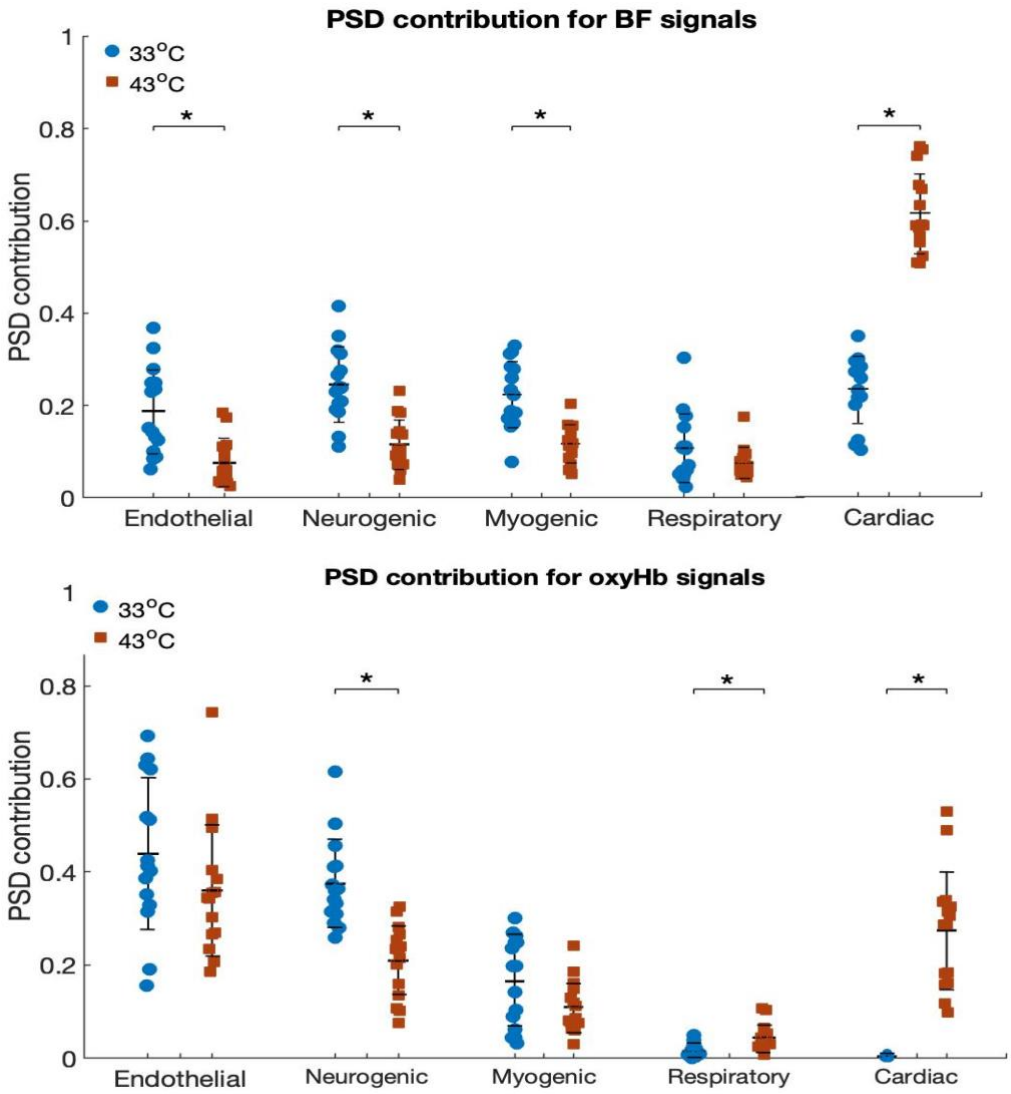

Figure 3.3 PSD contributions of the blood flux signals (left plots) and oxygenated haemoglobin (right plots) across five frequency bands recorded at the skin forearm from all 15 healthy volunteers at 33℃ in blue and 43℃ in red. Data are presented as median and IQR, $^{*}p < 0.05$.

The normalized PSD contribution calculating relative to total spectral power (0 – 1), between 33℃ and 43℃ for both BF and oxyHb signals group is shown in Figure 3.3 and Table 3.3. There was shown a significant decline in the relative LF endothelial, neurogenic and myogenic bands during LTH for the BF signals. However, during thermally induced vasodilation at 43℃, the HF activity of the heart beat showed a substantial increase, from 0.23 ± 0.02 at 33℃ to 0.62 ± 0.02 at 43℃ (mean ± SEM, $p<0.05$). Similarly, the PSD contribution of the HF respiratory and cardiac bands, increased substantially during LTH for the oxyHb signals. The LF neurogenic band showed a significant decrease at 43℃ ($p < 0.05$), although no other significant change was found in the LF bands between the two haemodynamic steady states for the oxyHb signals.

Table 3.3 Normalised PSD contribution for both BF and oxyHb signals at 33℃ and at 43℃ respectively across five frequency bands, for n=15 volunteers. Data are presented as mean ± SEM.

	BF signals		**OxyHb signals**	
	33℃	**43**℃	**33**℃	**43**℃
Endothelial	0.19 ± 0.02	0.08 ± 0.01*	0.44 ± 0.04	0.36 ± 0.04
Neurogenic	0.25 ± 0.02	0.12 ± 0.01*	0.38 ± 0.02	0.21 ± 0.02*
Myogenic	0.22 ± 0.02	0.12 ± 0.01*	0.17 ± 0.02	0.11 ± 0.01
Respiratory	0.11 ± 0.02	0.08 ± 0.01	$1.6 \cdot 10^{-2} \pm 3.5 \cdot 10^{-3}$	$4.5 \cdot 10^{-2} \pm 7.3 \cdot 10^{-3}$*
Cardiac	0.23 ± 0.02	0.62 ± 0.02*	$4.2 \cdot 10^{-3} \pm 0.7 \cdot 10^{-3}$	0.27 ± 0.03*

*Significant difference from 33℃, $p < 0.05$.

3.3.2 Results of the Wavelet Transform

The plots in Figure 3.4 show the wavelet transform and the averaged scalograms of the blood flux signal at 33℃ and 43℃ from a representative healthy volunteer (h0_02). The frequency range considered is the same as that in the PSD of section 3.2.1. The variation of average wavelet transforms against time shows the variation of the frequency components over time but is not directly comparable with the PSD. For this reason, the average of the Wavelet Transform over time can be plotted as the average scalogram as illustrated at the lower plots of Figure 3.4. Note that in the figures the values of the absolute wavelet transform are significantly higher during heating to 43℃. The short-time FFT can be used to produce a similar PSD over time to the absolute WT but would be unreliable at low frequency here due to the low number of cycles in the endothelial band.

In Figure 3.5 the WT is illustrated and the average scalogram of oxygenated haemoglobin signals between the two haemodynamic states. Similar to PSD values for oxyHb signals absolute wavelet transform indexes of the endothelial, neurogenic and myogenic band, are greater at 33℃. Although, at the following bands the absolute WT during LTH shows a remarkable increase particularly in the cardiac activity.

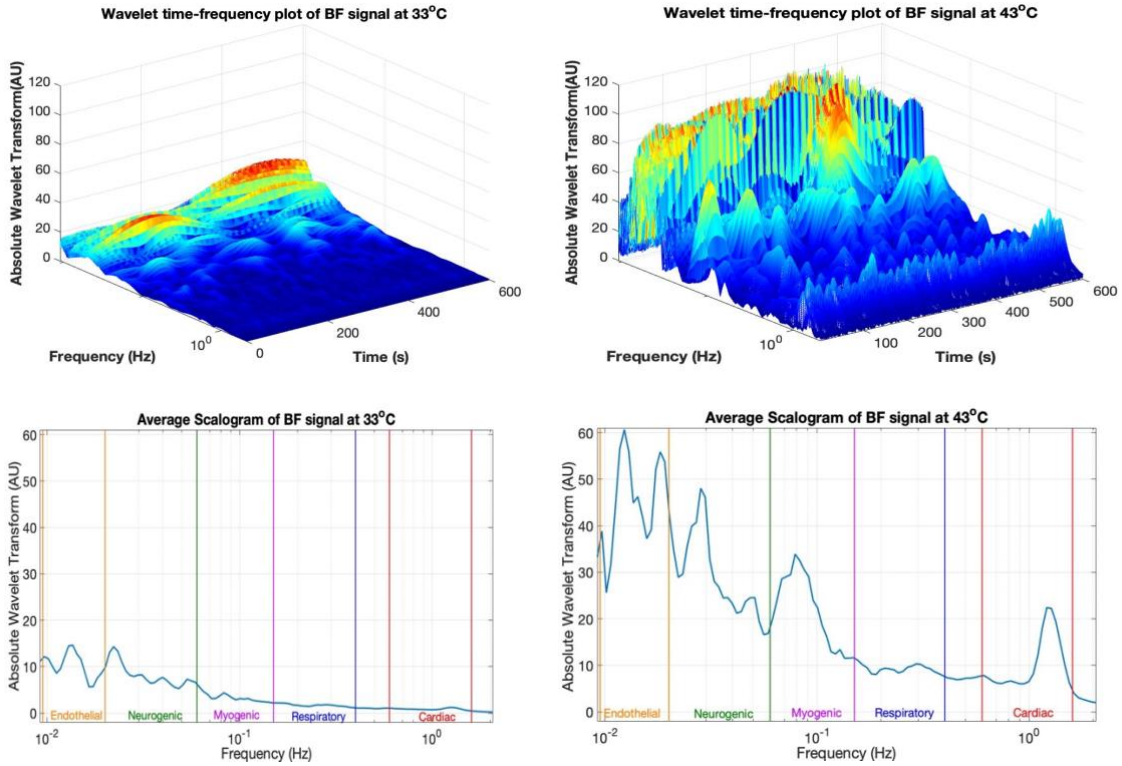

Figure 3.4 Difference of the periodic oscillation of blood BF using Wavelet Transform, obtained from one healthy individual at 33 ℃ and 43 ℃ (top plots) and the averaged scalograms showing the difference of the periodic oscillation of blood flux signals at 33℃ and 43℃ (bottom plots).

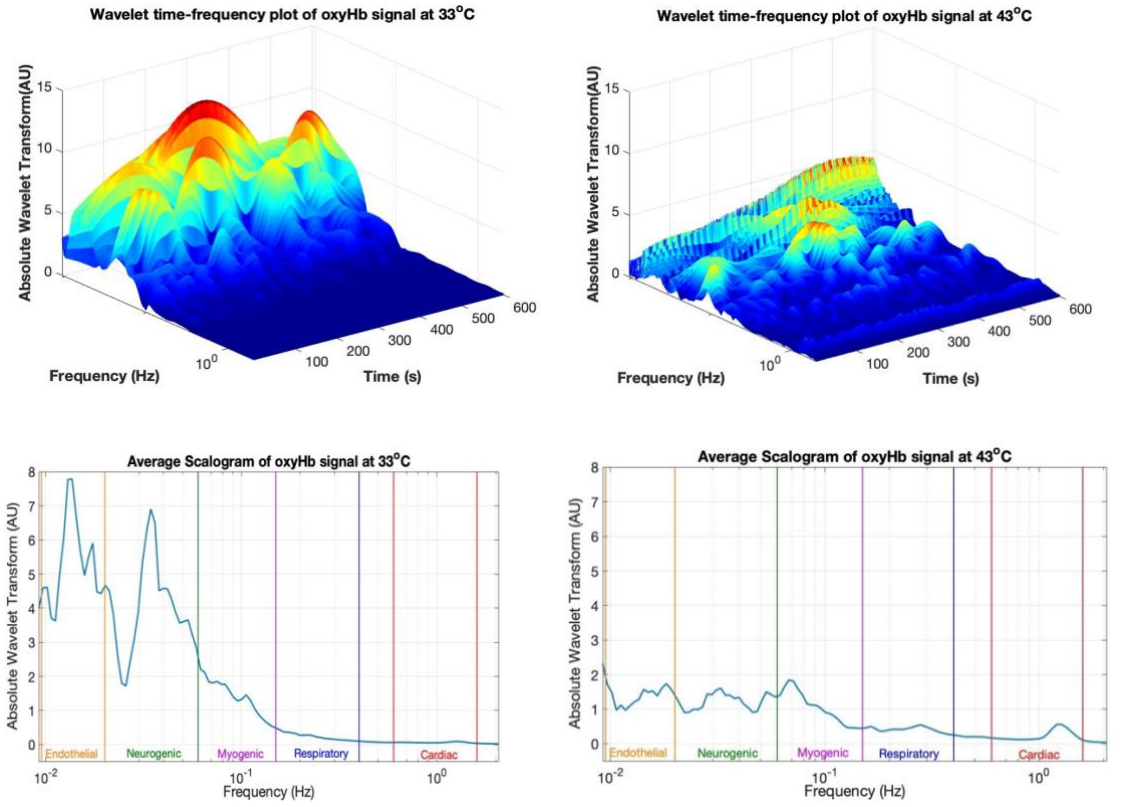

Figure 3.5 The periodic activity of oxyHb signals using Wavelet Transform, obtained from one healthy individual showing the differences at 33 ℃ and 43 ℃ (top plots) and the averaged scalograms showing the difference for each frequency band (bottom plots).

3.4 Discussion

The results of this work provide insight about the content of the frequency and time-localized frequency content of the blood flux and oxygenated haemoglobin signals in two haemodynamic steady states at 33℃ and 43℃. In the frequency domain, using Welch's PSD, there is a significant difference in the PSD bands for the BF signals at different temperatures. More specifically, the PSD of blood flux signals for all five frequency bands showed a significant change, in response to vasodilation caused by local heating. The HF cardiac band showed a remarkable increase at 43℃, in the PSD contribution, which is due to the temperature-induced vasodilated microvascular system [40]. Moreover, in the time domain, across the frequency bands in Figure 3.4 are suggestive of change in the contribution of endothelial, neurogenic, myogenic and cardiac oscillations during LTH for the BF signals. More specifically the contribution of these oscillations during heating increased by three times compared to the oscillations at 33℃ especially in the cardiac band. The findings of this study have shown the association of the local warming to the increase of the vasodilation and the impact in the spectral power for all frequency bands. As reported in other available literature [4, 8, 104], this may be due to the high metabolic demand of the tissue during LTH which causes the vasodilation by increasing BF and hence the oxygen delivery which exceeds the amount of oxygen required by the tissue.

In terms of the oxygenated haemoglobin signals the PSD analysis showed a similar trend of the signals during LTH in the cardiac band. Although, the total power failed to show any significant difference between the haemodynamic steady states. The increase of the spectra in the heart rate is consistent with strong modulation as a result of the direction of the generation of the heart function during local warming. This may also be because of the arteriovenous shunting of the blood in the external dermal layers [53]. The time domain analysis across the frequency bands in Figure 3.5, suggests enhanced cardiac frequency during vasodilation due to increase LTH. Despite the heartbeat being weak in the oxyHb signals at 33℃, it became visible during warming. In particular, the cardiac peak was absent in the oxyHb signal at 33℃, but during vasodilation it was clearly evident. This may indicate that the thermally induced vasodilation improves the delivery of the heartbeat wave to the circulatory system, so that it is also evident in the vasculature [54]. The measurements of oxyHb reflect the amount of light absorbed by the molecules of oxygenated haemoglobin, hence, the increase in oxyHb signals results from a higher number of these molecules present in the sampled volume. From a physiological perspective, the overall amount of haemoglobin is higher during thermally induced vasodilation thus, the vessels dilate and allow more blood to pass through the microvasculature. According to Kuliga [54], this pronounced increase of the heartbeat during LTH may be an early indicator of vascular stiffness however, more studies

need to be conducted to examine the vessel stiffness and its relationship with the microvascular response in local heating, in order to support this hypothesis.

In a similar study, Kuliga et al [104] using FFT demonstrated that tissue oxygenation signals oscillated over similar frequency ranges to those seen in BF signals (~0.0095-1.6 Hz), with relative contributions from both low and high frequency PSD bands. These data suggest that the low frequency oscillatory activities associated with the regulation of microvascular perfusion and tissue oxygenation may be modulated in a manner of lower variability of the oxyHb signals during LTH. The reduction of the relative spectra contribution and the wavelets in the lower frequency bands in oxyHb signals is also, consistent with recent studies using wavelets [114] and FFT [115] during warming of the skin. The decrease of the neurogenic activity during LTH is consistent with a reduction in sympathetic activity to reduce the vascular tone. Another finding is that the amplitude for the wavelets in the endothelial band was found to be substantially lower during local warming. The endothelium plays an important role in the control of the relaxation of smooth-muscles by releasing vasodilators such as endothelium-dependent nitric oxide (NO) [116]. However, the changes of the flow motion in lower frequencies during LTH have yet to be fully clarified.

In this study, the value to indicate statistical significance between the two haemodynamic steady states was 0.05, as the sampling size isn't large enough to detect any existing differences and thus, in order to minimise the probability of false negative, known in statistics as the type II error, the significance level, α, is increased [117]. According to Streiner [118], one of the disadvantages when correcting for multiple comparisons testing, is that the probability of type II error is increased and thus the chance of having no statistical significant difference is also increased. They also report that the decision whether to correct for multiplicity or not can be arguable and all types of error need to be taken into consideration before applying it.

3.5 Conclusion

The study presented in this chapter investigates the blood flux and oxygenated haemoglobin signal in the frequency and time-localized frequency domain during LTH. The methods evaluated in this chapter were able to detect the differences of the frequency content of both BF and oxyHb signal at 33℃ and 43℃. The PSD contribution of the cardiac rhythm of both BF and oxyHb signals showed a significant increase during local warming, whereas, the low frequency bands of BF signals showed a significant decline during LTH. However, the spectra for the oxyHb signals did not show a significant change in the low frequency endothelial and myogenic bands during local warming which suggests that the flow motion during LTH in the lower frequencies need to be further investigated. The low frequencies in the wavelets of the oxyHb signals at 33℃ appeared to be

higher and the cardiac rhythm was absent, however the heart beat activity became visible during warming-induced vasodilation. Overall, the frequency domain along with the time-localized and frequency domain analysis has been shown to offer significant information about the frequency characteristics of the microvascular system when the skin vasculature reaches maximal dilation perfusion. The next step will be to investigate the information content of the microvascular perfusion to identify more characteristic features describing the complexity of the flow motion. In the following chapter nonlinear complexity techniques will be applied in BF and oxyHb signals.

Chapter 4: Complexity and Multiscale Analysis of Microvascular Blood Flow and Oxygenation Signals Between Two Haemodynamic Steady States

In the previous Chapter the time-frequency analysis of LDF and Oxy signals was considered. Here, the feasibility of the using nonlinear complexity methods as a tool to identify altered microvascular function often associated with pathological conditions is investigated. The efficacy of multiscale nonlinear complexity methods was evaluated, to account for the multiple time-scales of processes modulating microvascular network perfusion. Conventional and multiscale variants of sample entropy (SampEn) were used to quantify signal regularity and Lempel and Ziv complexity (LZC) and effort to compress (ETC) complexity to determine the randomness. Finally, a thorough discussion of the outcomes of these analyses and the limitations of the data uses are presented.

4.1 Introduction

The maintenance of an adequate blood flow through a microvascular network, sufficient to meet the metabolic demands of the tissue, is dependent on local endothelial, metabolic, myogenic and neural vaso-mechanisms that determine vascular tone and flow patterns within the network [119]. Recently, Frisbee et al. [120] have shown attenuation of these flow patterns using chaotic network attractor analysis in an animal model of cardio-metabolic disease. They have argued that the consequent loss of physiological information content may contribute to disease risk [76, 121].

Time and frequency domain analysis and the contribution of spectral properties in frequency domains are the techniques most frequently applied to biosignals [26-28], including those derived from blood flow through the superficial dermal microvasculature [4, 36, 40]. The frequency and power of local oscillations that contribute to the total blood flow motion have been studied by many research groups [36, 105, 106]. It has been widely argued that time frequency analysis of the low frequency periodic oscillations in microvascular blood flux (BF) signals obtained using for example laser Doppler fluximetry (LDF) can provide non-invasive, mechanistic information on microvascular control [36, 122].

The regularity and the randomness of physiological signals has been explored using nonlinear methods such as entropy and complexity techniques, respectively, well suited for the analysis of short length signals such as ECG and respiratory flow signals [4, 75, 123-125]. Lempel-Ziv (LZ) complexity analysis has been applied to skin microvascular BF signals in humans [40] and in animal

models, [4, 126] in differing haemodynamic states. These studies have demonstrated clear differences in LZC between haemodynamic states. However, the relationship between the nonlinear dynamics of the BF signal and their impact on microvascular function remain to be clarified and the potential for complexity analysis as a diagnostic tool remain to be determined.

Conventional entropy and complexity methods have the drawback that they can only study the behaviour at one scale. To overcome this potential disadvantage, Costa, et al. [46] introduced an improved multiscale entropy algorithm to estimate entropy over multiple scales. Such multiscale analyses have been shown to be effective in understanding physiological signals in general [46, 123, 127]. Costa, et al. [76], applied the multiscale entropy in the cardiac interbeat interval to measure the regularity of the cardiac properties of young, elderly and subjects with heart failure in both waking and sleeping periods. They found good discrimination between these periods for all groups and reported that the multiscale entropy analysis is a valid method for quantifying the complexity of the biological signals across multiple spatial and temporal scales. Using multiscale LZ complexity, Kalev, et al. [128] were able to demonstrate a 86% classification accuracy by accounting for the different frequencies of information content in the EEG. Papaioannou, et al. [129], showed that the assessment of wavelet transform and multiscale complexity techniques on the temperature signals in patients with systematic inflammatory response syndrome, sepsis and septic shock, can be used to classify the early presence of a pathology.

In this chapter, conventional LZC is used to estimate and quantify symbolic binary sequences converted from BF signals at rest with the local skin temperature clamp at 33°C and during vasodilation induced through local thermal hyperaemia (LTH) at 43℃. LZ complexity is a method of quantifying the information present in a signal by estimating the number of production processes contained in the data. Here the encoding process, the epoch size and the type of the LZ complexity are introduced and applied in the BF signals on both haemodynamic steady states to investigate the changes on the signals and better understand this method using different parameters.

Although, the main aim of this chapter is to investigate the information content of BF and OXY signals derived from the microvasculature in two stable haemodynamic steady states at 33℃ and at 43℃ using the combined LDF and WLS probe as described in Chapter 3. First, the changes in entropy and complexity of the microcirculatory dynamics are explored using conventional sample entropy (SampEn), LZC and effort to compress (ETC) complexity methods. To understand the effect of scale on these nonlinear metrics and their efficacy in classifying these haemodynamic steady states the multiscale sample entropy (MSE), multiscale Lempel and Ziv (MLZC) complexity and multiscale effort to compress (METC) methods are then evaluated. To the best of our knowledge,

this study is the first to conduct the multiscale analysis of the simultaneously recorded blood flux and oxygenated haemoglobin signals of healthy subjects during skin local heating.

The hypothesis tested in this chapter was whether the complexity-based and multiscale-based analysis of blood flux and tissue oxygenation signals derived from the skin of healthy individuals under two imposed haemodynamic steady states will enable the characterisation of the flexibility/responsiveness of a microvascular network and thus has potential for clinical application in the prognosis and the diagnosis of pathophysiological conditions.

4.2 Analysis procedure

The data in this chapter were obtained from a group of 15 healthy young male volunteers, age was 29.2 ± 8.1 (mean ± SD), obtained from a previous study [54], and are described in more detail in chapter 3.

4.2.1 Epoch Size

Before calculating the LZ complexity, long binary sequences are usually divided into epochs.

- One way to do that is by dividing the sequence into epochs with the same epoch size and then calculating the complexity for each epoch [4-6, 130]. Here, the 24000 samples (600 seconds) signal, x, of each volunteer is divided into 15 epochs of 1600 samples (40 seconds) length for each epoch, which is a sufficient epoch for calculating the complexity as described in chapter 2.
- Another way to divide the binary sequence is by using a time delay with a sliding window with a delay for each window [91, 95, 96, 102]. Here, the 24000 samples (600 seconds) signal, x, is divided into 15 epochs so the sliding window is w = 1600 samples (40 seconds) and the delay is l = 40 samples (1 second). First, the complexity is calculated for the epoch with initial conditions: $[x(1),\ x(w)]$ and then, will be calculated for the row vectors: $\left[x\left((i \cdot l)+1\right),\ x((i \cdot l)+1+w)\right]$, where $i = 1,2,\dots n$, n = 600 - 40. Now, each sliding window will have size w and delay l.

In this work, both methods are used on the LZC yielding different information about the complexity of the signal, however only the first approach has been implemented in SampEn and ETC complexity methods as the second approach does not provide a sufficient number of samples for analysis using entropy method as mentioned in chapter 2 (section 2.5).

4.2.2 Multiscale Analysis Procedure

The multiscale analysis was applied in the BF and oxyHb time series, in order to get information in multiple scales, in other words at different sampling time constants. At the coarsest-grain of 24 scales, the shortest times series has 1000 samples, which is sufficient for analysis and is consistent with other literature [46, 78, 123]. Then, the SampEn, the LZC and the ETC complexity were calculated for each coarse-grained sequence as a function of the scale factor, τ. These procedures were then called multiscale entropy (MSE), multiscale Lempel and Ziv complexity (MLZC) and multiscale effort to compress complexity (METC).

4.3 Statistical and Classification Analysis

Statistical analysis was performed in IBM SPSS statistics 22 (IBM United Kingdom) and Microsoft Excel 2010 (Microsoft Corporation, US). Data were tested for the normal distribution using D'Agostino & Pearson omnibus normality test [113]. Data are presented as either mean ± standard mean error (SEM) for normally distributed data or median with interquartile range (IQR) for non-normally distributed data. Normally distributed data were compared using a Student t-test and non-normally distributed data using a Mann-Whitney U-test. In all cases a value of $p < 0.05$ was taken to indicate statistical significance.

Linear discriminant analysis (LDA) with leave-one-out cross-validation [131, 132] was applied to the complexity measures of both BF and oxyHb signals, to determine the classification accuracy between the two haemodynamic steady states. The LDA method was applied to transform the features from a higher dimensional space into a space with lower dimensions, which in this way the ratio of the distance between the means of the classes in the projected space and the scatter within each class is maximized and thereby the classes are maximally separated [132].The accuracy is assessed using the LOO cross-validation in which here 30 runs took place, and in each run the classifier trained the set apart from one sample which was presented as the test set.

4.4 Results

4.4.1 Results for LZC of blood flux signals at 33℃ and 43℃

Here, the LZ complexity was estimated in two haemodynamic steady states at 33℃ and at 43℃, for both exhaustive and the primitive complexity, using epochs of length 40 seconds and 1 second delay for each window as described above. The results, obtained from a representative volunteer

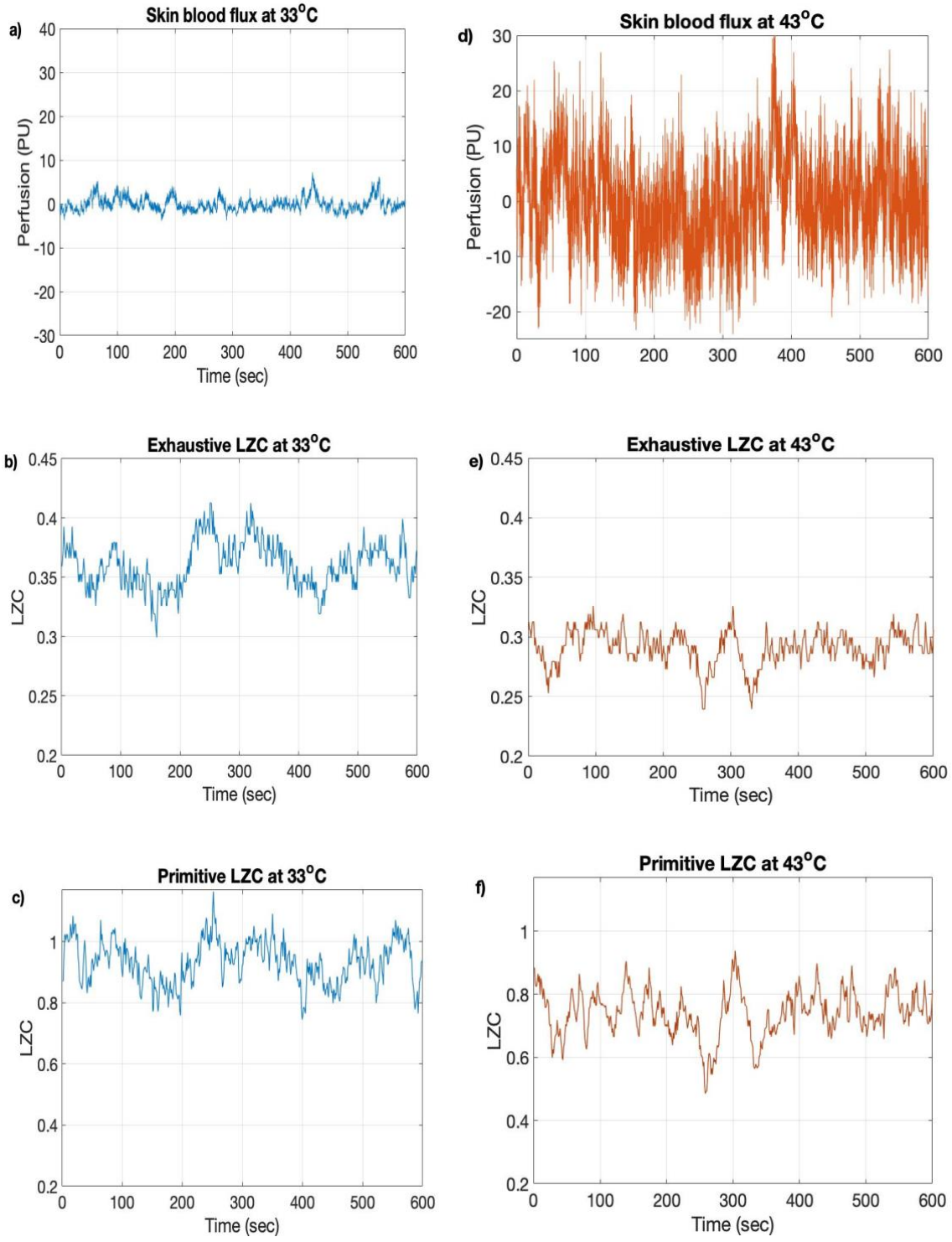

Figure 4.1 Example of detrended blood flux signals at (a) 33℃ and (d) 43℃. The corresponding Lempel and Ziv complexity with the exhaustive (b) and (e) and primitive (c) and (f)) type, using a 40 second moving window with a 1 second delay, at 33℃ (a-c) and at 43℃ (d-f). Plots are obtained from one volunteer (h0_02).

(h0_02), are presented in Figure 4.1a and 4.1d, showing a significant increase in blood flux signals during LTH.

The purpose of this investigation is to examine both the effect of the complexity type, exhaustive or primitive, along with LTH on the flow motion. The values of the complexity are higher at 33℃ (Figure 4.1b and 4.1c) compared to the ones at 43℃ (Figure 4.1e and 4.1f). The primitive type (Figure 4.1c and 4.1f) shows higher values of complexity than the exhaustive ones (Figure 4.1b and 4.1e), as it is expected from the literature in (see chapter 2, section 2.5). Thus, this makes the primitive values of LZC more random than when using the exhaustive type. The range for the primitive LZC is wider than the exhaustive and hence, they are seen to be more overlaps of the LZC values between the haemodynamic steady states than when using the exhaustive type. Therefore, in this study, the exhaustive type provides a more effective characterization of the blood flux data.

Additionally, the LZC using the sliding window was applied on the skin microvascular blood flow signals in two haemodynamic steady states as a possible usefulness of the sliding window technique to identify change of signals and as an attempt to capture the features in the LDF recordings. This study, did not show any significant change in the LZC that correspond to the features of the skin blood flux in each haemodynamic steady state.

To investigate the use of the exhaustive and primitive complexity measures on a bigger data set, LZC of the BF signals recorded for all 15 volunteers at 33℃ and 43℃, was calculated by dividing the signal into 15 epochs of 40-second length for each epoch. Figure 4.2a shows the exhaustive and Figure 4.2b the primitive complexity for all individuals at both temperatures and the mean LZC with error bands calculated with the SEM. A reduction in mean complexity is clearly visible using both complexity types, as skin temperature clamps from 33℃ to 43℃. Table 4.1 gives summary statistics for the LZ complexity at both temperatures for all epochs. Overall complexity falls from 0.32 ± 0.04, at 33℃ to 0.27 ± 0.03, at 43℃ (mean ± SD) for the exhaustive type and from 0.81 ± 0.12, at 33℃ to 0.68 ± 0.11, at 43℃ (mean ± SD) with the primitive type ($p < 0.05$).

To further investigate complexity changes in LDF with LTH a 20-minute segment covering the skin heating from 33℃ to 43℃, as illustrated in Figure 4.3a, from a representative volunteer (h0_02) is considered. Here, 40-second lengths of the LDF are transformed using the delta encoding and then LZC is evaluated. Epochs are separated by 1-second delay showing the time-varying complexity of the signal for exhaustive, in Figure 4.3b, and primitive in Figure 4.3c. Note that the range for the primitive LZC is wider than the exhaustive and hence, there are shown more overlaps of the LZC values between the haemodynamic steady states than when using the exhaustive type. The region

contained between the purple dashed lines shows where the skin temperature is increased from 33℃ to 43℃. The decrease in complexity identified in Figure 4.3 can be clearly seen as the local skin temperature increases to 43℃. Thus, the sliding window technique shows the changes in the LZC with time during increased local warming and therefore, might be suitable for determining where imposed stressors affect the flow of blood in the microvasculature, which is one of the aims of this research.

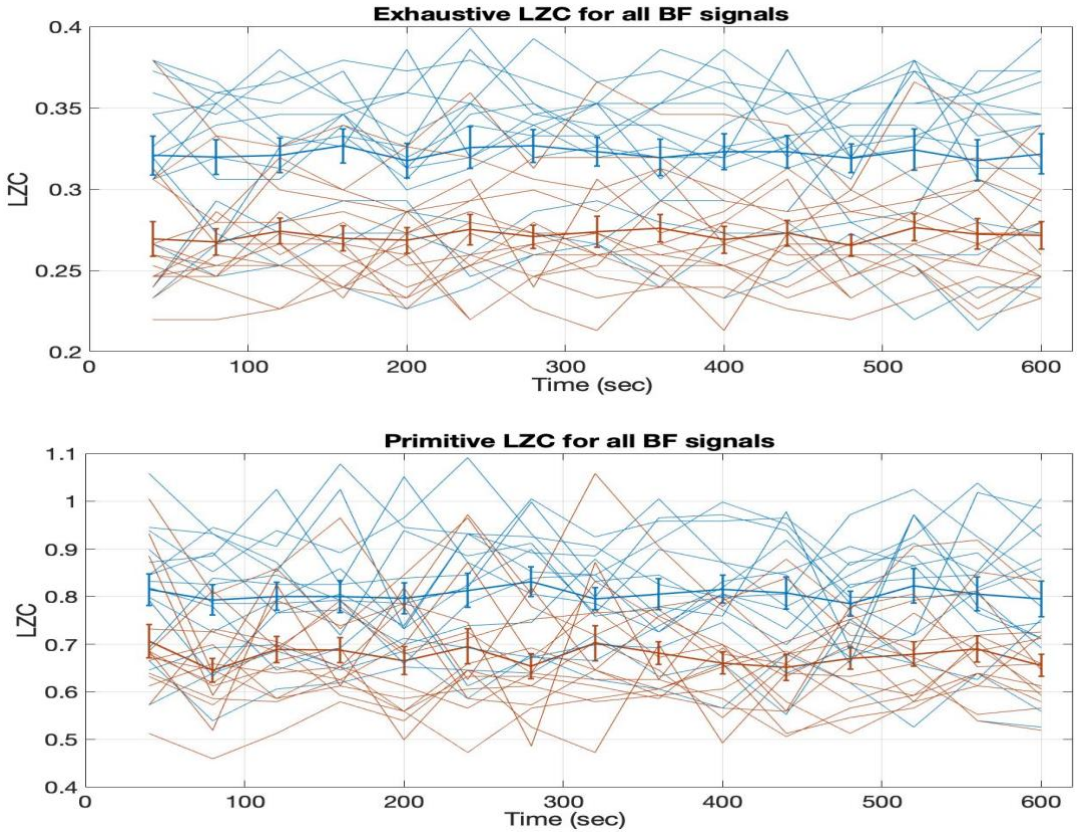

Figure 4.2 LZC for all 15 volunteers, using a 15-epoch division of 40 seconds for each epoch, at 33℃ (blue plots) and 43℃ (red plots) respectively for both exhaustive (a) and primitive (b) type. Averaged LZC with error bars, for exhaustive and primitive type, at 33℃ (blue bold plot) and 43℃ (red bold plot).

Table 4.1 Mean, SD, SEM of the LZC at 33℃ and at 43℃ respectively and the p-value for comparing the complexity at 33℃ and at 43℃, for both exhaustive and primitive type (n=15).

Temperature	**33**℃			**43**℃			**p-values**
	Mean	**SD**	**SEM**	**Mean**	**SD**	**SEM**	
Exhaustive type	0.32	0.04	0.01	0.27	0.03	0.01	<0.05
Primitive type	0.81	0.12	0.03	0.68	0.11	0.03	<0.05

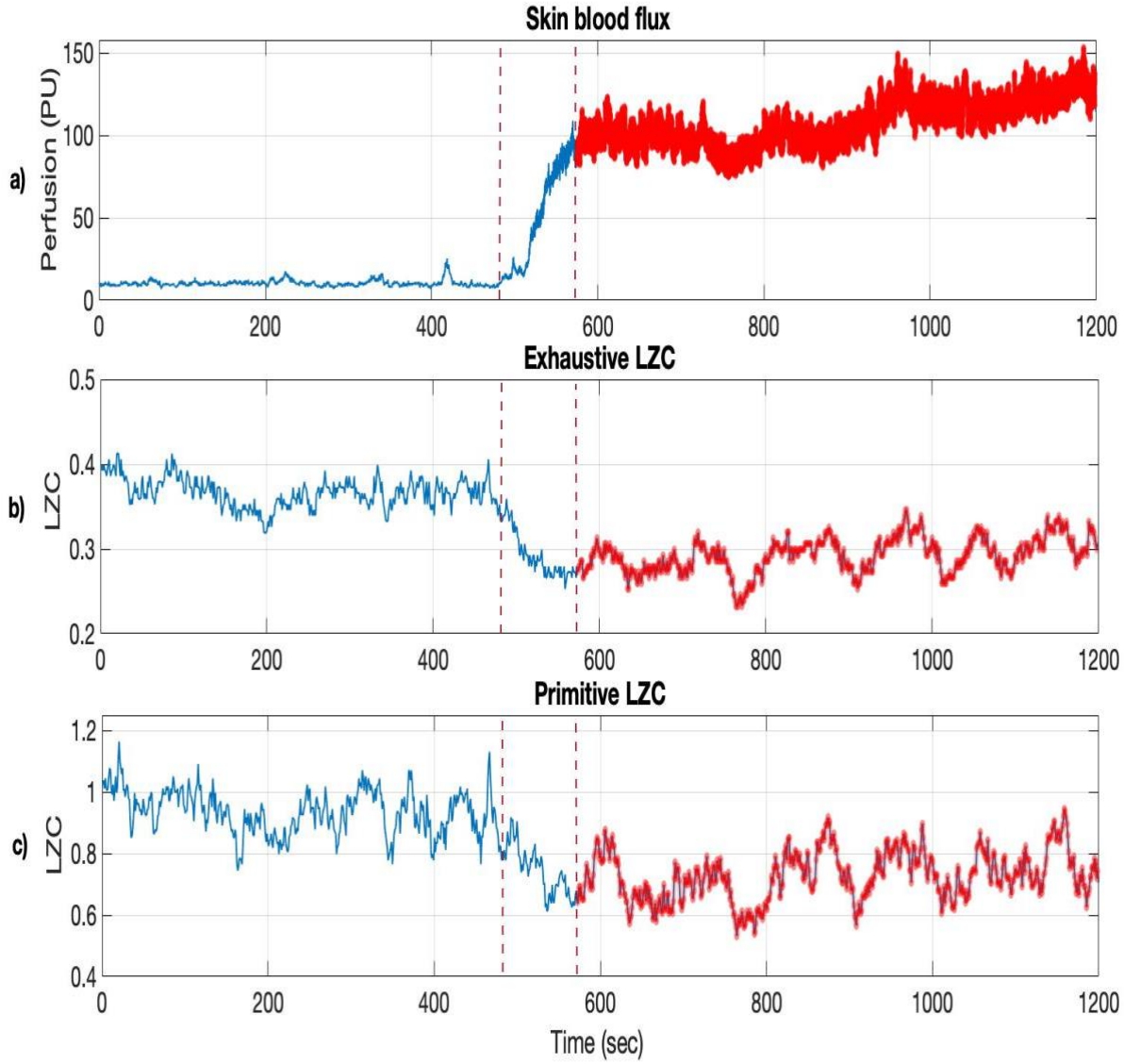

Figure 4.3 Illustration of a blood flux signal (a) and the corresponding LZC with the exhaustive (b) and primitive type (c), using a 40 second moving window with a 1 second delay, of a 20 minutes segment from 33℃ (blue signal) to 43℃ (red signal). The region between the purple dashed lines indicates the end of the 33℃ and the beginning of the heating at 43℃. Plots are obtained from one volunteer (h0_02).

4.4.2 Results for Complexity-based and Multiscale-based Analysis at 33℃ and 43℃

Here, the nonlinearity of the BF and oxyHb signals at the two haemodynamic steady states of 33℃ and 43℃ was computed for all methods (sample entropy, LZC and ETC complexity) by dividing the signals into 15 epochs for the 15 individuals as shown in Figure 4.4 and 4.5, respectively. Both signals presented lower values of entropy and complexity during LTH as compared with those at 33℃. Table 4.2 gives summary statistics for all complexity methods applied in BF and oxyHb signals

at both temperatures over the 15 epochs. Overall the SampEn index (mean value across the 15 epochs for each participant) showed a decrease in both BF and oxyHb signals with LTH.

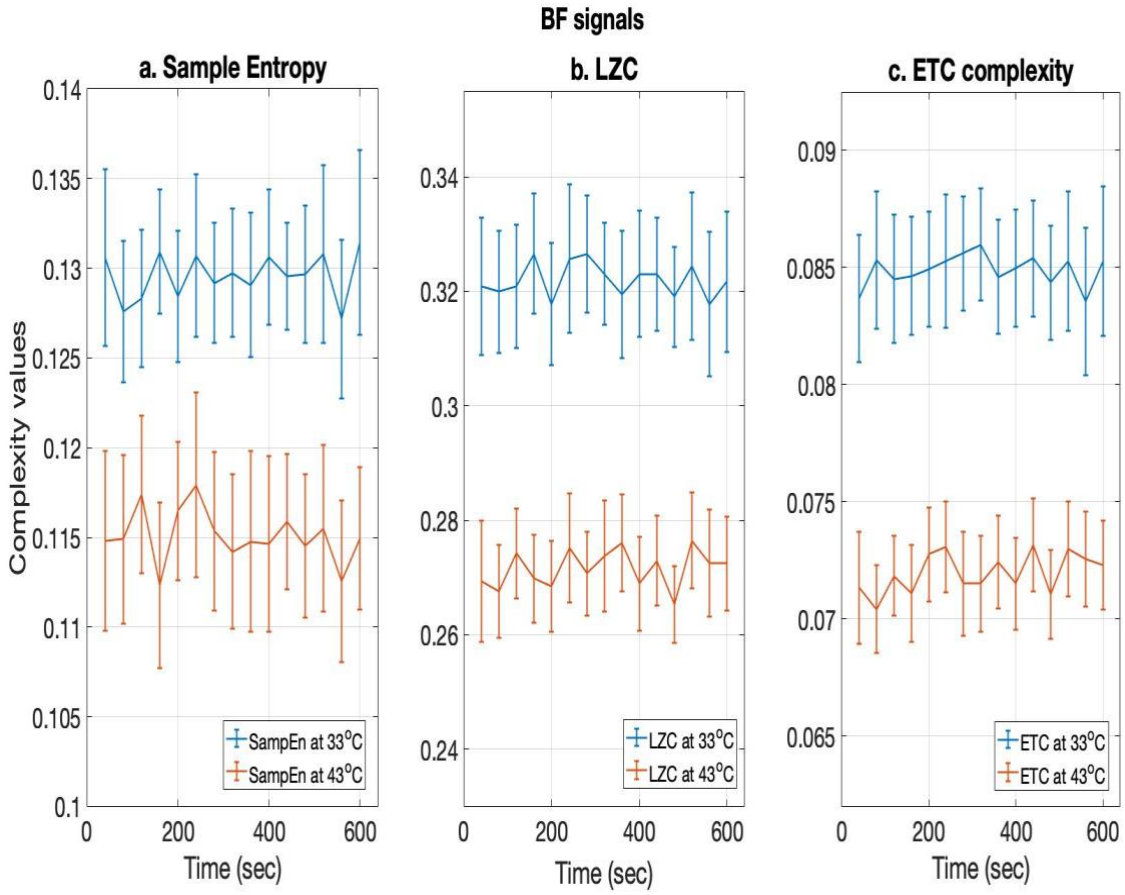

Figure 4.4 Changes in regularity and complexity of the blood flux signals for all 15 volunteers, in two haemodynamic steady states at 33℃ (blue) and at 43℃ (red). a) Sample Entropy, b) Lempel and Ziv complexity, c) Effort to compress complexity. Values are presented as means ± SEM.

Likewise, the LZC index showed a reduction in the complexity during local heating, in the BF signals, between the two haemodynamic steady states. The oxyHb signals showed a similar although more significant drop in LZ complexity ($p < 0.05$). Similar responses to the local heating were seen in the ETC complexity for BF and oxyHb signals showing a more substantial decline in the complexity at 43℃ ($p < 0.05$, for BF signals and $p < 0.05$, for oxyHb signals).

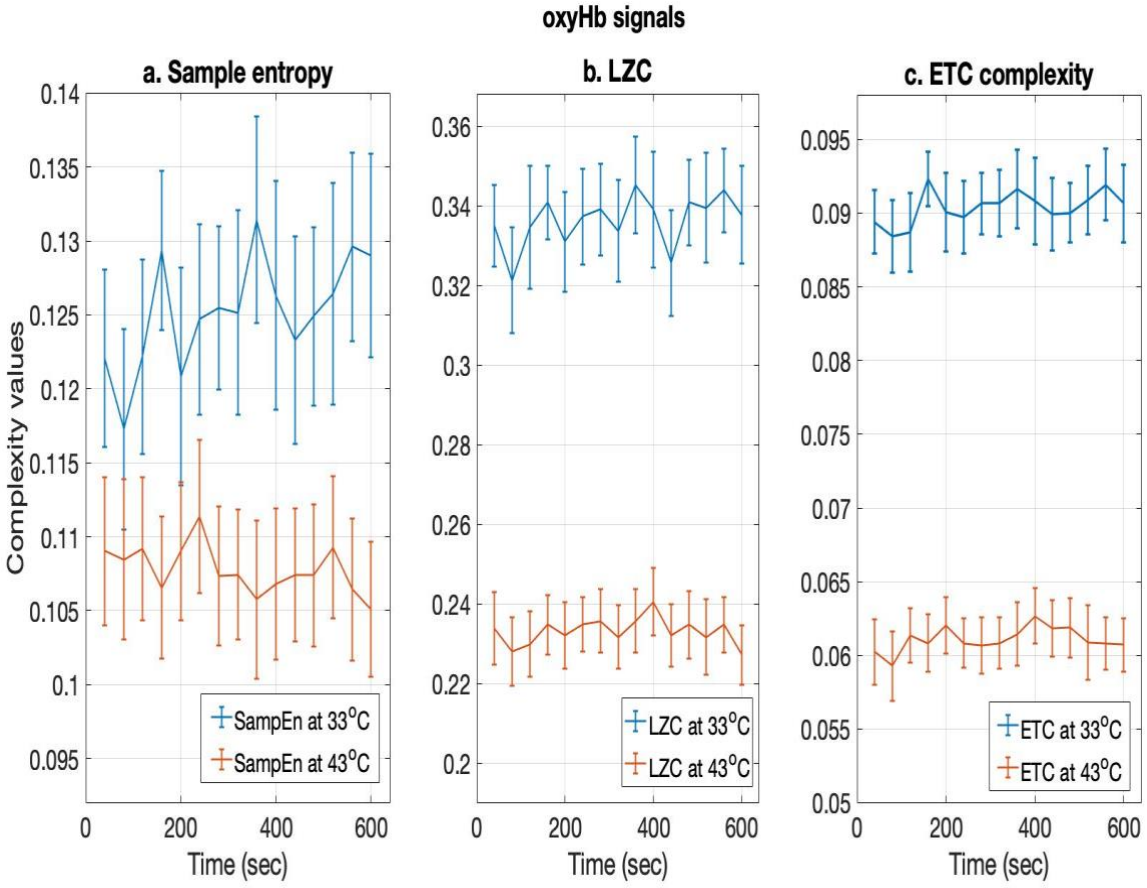

Figure 4.5 Values of the regularity and the complexity of the oxygenated haemoglobin signals for all 15 volunteers, in two haemodynamic steady states at 33℃ (blue) and at 43℃ (red). a) Sample Entropy, b) Lempel and Ziv complexity, c) Effort to compress complexity. Values are presented as means ± SEM.

Table 4.2 SampEn, LZC and ETC complexity methods at 33℃ and at 43℃ respectively for both BF and oxyHb signals (n=15). Data are presented as mean ± SEM.

	BF signals		**OxyHb signals**	
	33℃	**43**℃	**33**℃	**43**℃
SampEn	0.130 ± 0.004	0.115 ± 0.016*	0.125 ± 0.006	0.108 ± 0.005*
LZC	0.322 ± 0.010	0.272 ± 0.007*	0.336 ± 0.010	0.233 ± 0.007*
ETC	0.085 ± 0.002	0.072 ± 0.002*	0.090 ± 0.002	0.061 ± 0.002*

*Significant difference from 33℃, $p < 0.05$.

Multiscale analysis of both BF and oxyHb signals in the two haemodynamic steady states across all 15 participants are shown in Figure 4.6 and 4.7 respectively. The multiscale analysis of these signals showed a relatively compatible variability over the 24 scales at both temperatures. The BF

and oxyHb parameters measured under the two haemodynamic steady conditions are summarized in Table 4.4. The results showed lower variability of the MSE of the BF and oxyHb signals during local heating compared with the signals at 33℃ ($p<0.05$, for BF signals and $p < 0.05$, for oxyHb signals)**.**

Similarly, the MLZC and METC complexity values appeared less variable and had lower complexity of both BF and oxyHb signals at 43℃, showing a considerable drop for both signals during LTH. Figure 4.8 shows the boxplot of the entropy and complexity and the multiscale analysis for both BF and oxyHb signals showing the separation of the signals during LTH. It is shown that greater discrimination occurs in the oxyHb signals using the multiscale analysis ($p < 0.05$).

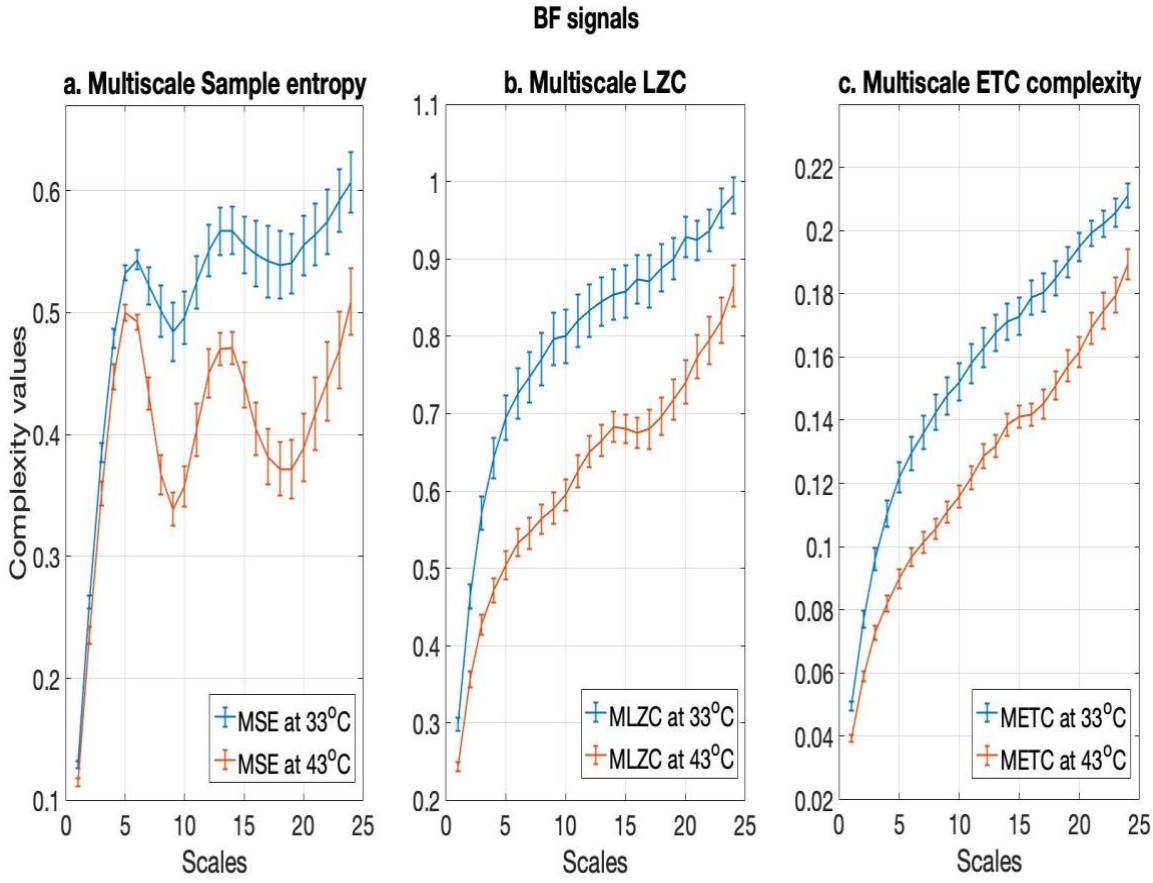

Figure 4.6 Average multiscale analysis for 15 blood flux signals in two haemodynamic steady states at 33℃ (blue) and at 43℃ (red). a) Multiscale Sample Entropy, b) Multiscale Lempel and Ziv complexity, c) Multiscale Effort to compress complexity. Values are presented as means ± SEM for n=15 healthy volunteers.

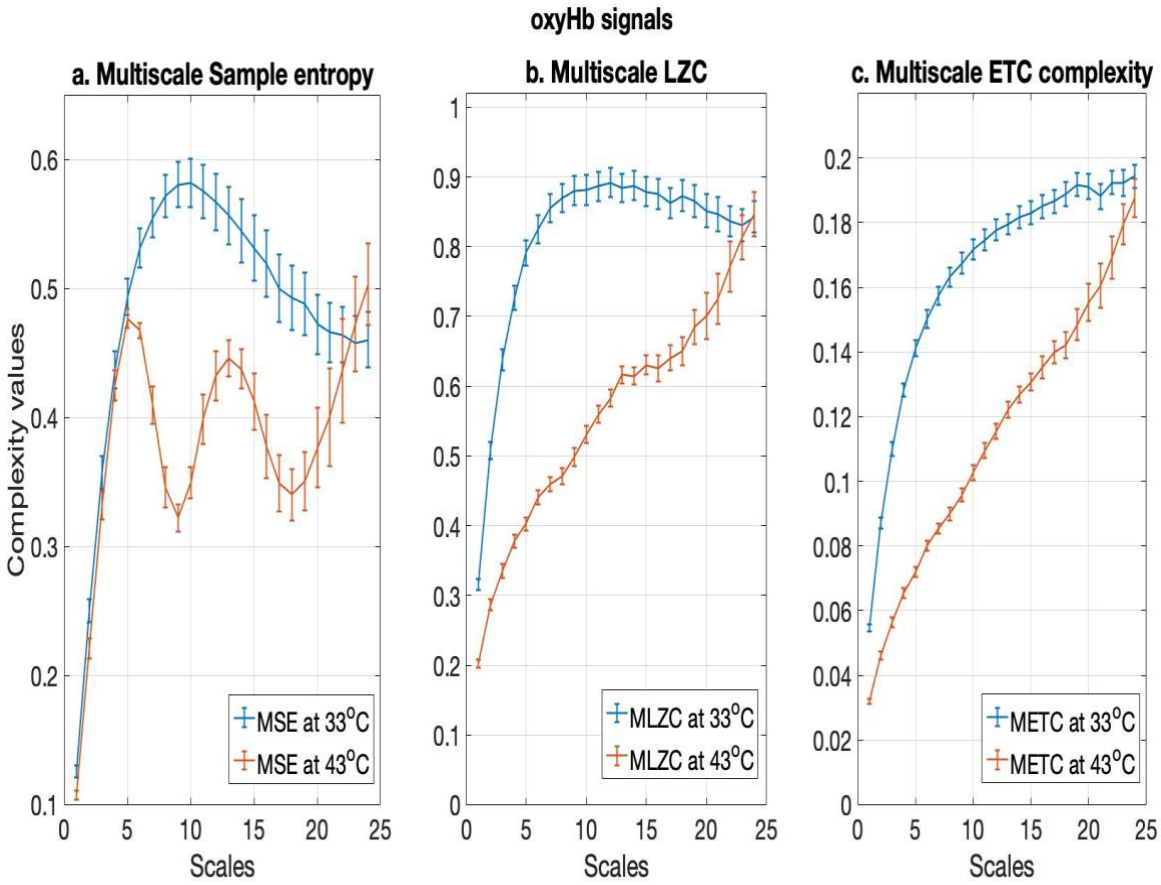

Figure 4.7 Average multiscale analysis for 15 oxygenated haemoglobin signals in two haemodynamic steady states at 33℃ (blue) and at 43℃ (red). a) Multiscale Sample Entropy, b) Lempel and Ziv complexity, c) Multiscale Effort to compress complexity. Values are presented as means ± SEM for n=15 healthy volunteers.

The largest difference of the multiscale analysis methods computed for all participants across 24 scales for the BF signals between the two haemodynamic steady states, was shown around scale factor 19 in the MSE indexes and around scale factor 9 in the MLZC and METC indexes. The weakest separation appears in scale 1 which is the traditional single-scale based entropy and complexity methods. For the oxyHb signals the strongest separation appears at around scale 9 for all methods. However, the smallest difference occurs at scale 4 in the MSE indexes and at scale 24 in both MLZC and METC indexes.

Table 4.3 MSE, MLZC and METC complexity methods at 33℃ and at 43℃ respectively for both BF and oxyHb signals (n=15). Data are presented as mean ± SEM.

	BF signals		**OxyHb signals**	
	33℃	**43**℃	**33**℃	**43**℃
MSE	0.507 ± 0.020	0.401 ± 0.012*	0.483 ± 0.023	0.383 ± 0.011*
MLZC	0.797 ± 0.043	0.578 ± 0.025*	0.809 ± 0.024	0.561 ± 0.019*
METC	0.156 ± 0.006	0.125 ± 0.004*	0.164 ± 0.004	0.115 ± 0.004*

*Significant difference from 33℃, $p < 0.05$.

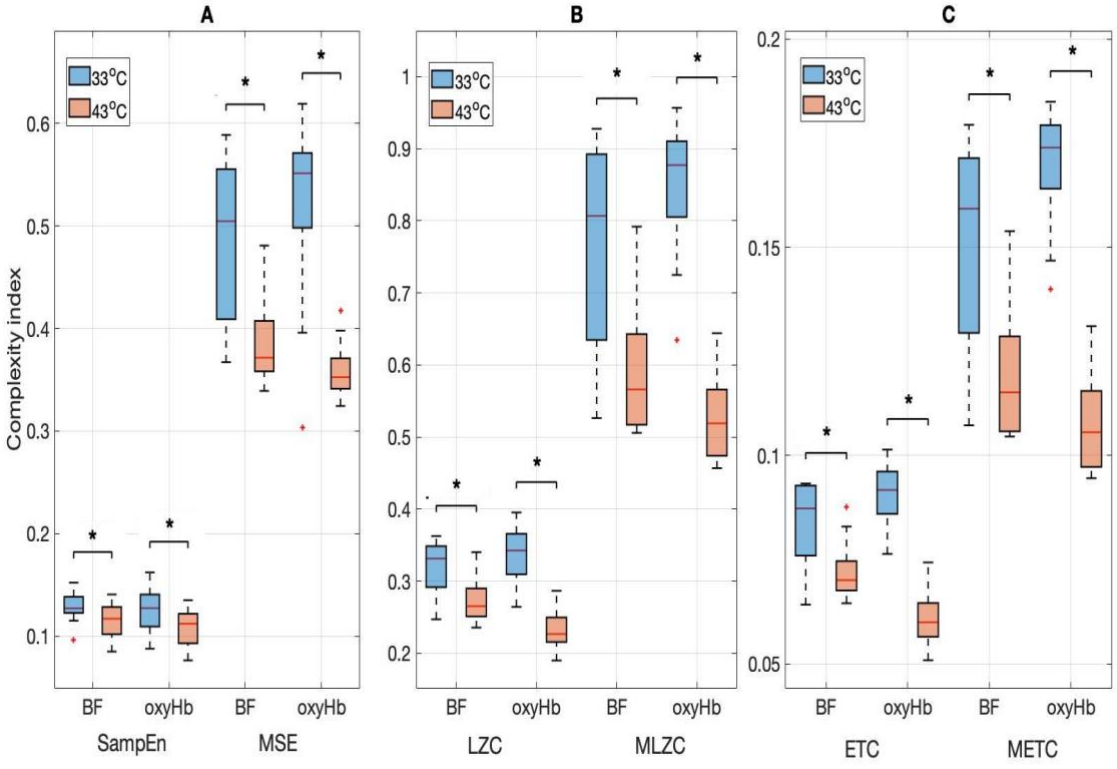

Figure 4.8 BF and oxyHb signals for all complexity and multiscale analysis expressed as mean value across 15 volunteers at 33℃ (blue) and at 43℃ (red). A. Sample entropy and Multiscale Sample Entropy, B. LZC and Multiscale LZC, C. ETC complexity and Multiscale ETC complexity ("*" indicate $p < 0.05$).

From Table 4.4 it is interesting to note that all three multiscale measures relating to the oxyHb signal indicate a good classification accuracy of the two haemodynamic steady states. The highest classification accuracy rates of 90% and 93.3% were reached with the MLZC and METC complexity, respectively. By this test it was shown that the characteristics of the multiscale analysis can be used

in classification algorithms to separate two different data sets. High accuracy was achieved using the multiscale complexity analysis (MLZC, METC), which indicates a classification effectiveness of the two haemodynamic steady states using the multiscale complexity measures and therefore, this may be valuable in clinical applications. The statistical analysis and classification accuracy for the SampEn, LZC and ETC complexity measures are shown in Table B.1 in Appendix B.

Table 4.4 Statistical analysis and classification accuracy for all multiscale methods of both BF and oxyHb signals between the two haemodynamic steady states.

Methods	**BF signals**		**oxyHb signals**	
	p-value	**Classification accuracy (%)**	**p-value**	**Classification accuracy (%)**
MSE	0.001	70.00	0.002	86.67
MLZC	0.001	73.33	<0.001	90.00
METC	0.001	73.33	<0.001	93.33

4.5 Discussion

The aim of this chapter was to estimate the randomness of the LDF time series in order to investigate the changes from the two haemodynamic states that have been previously reported to be associated with the mechanisms that influence the blood flow [4]. The LZC, in response to the local heating showed a significant reduction, which shows the variability of this technique in studying microvascular response to external stressors.

First, the time series had to be transformed into a binary sequence. Here, the encoding used is the delta encoding as it preserved more information about the characteristics of the dynamics of the signal. The choice of the epoch size is also important when calculating the LZC. Here, the division in 15 epochs with 40 seconds for each epoch was used for computing complexity consistent with previous work [4]. Analysis with a moving window of 10 seconds with 1 second delay for every window was also considered. The results of this analysis showed that the complexity could be time localised such that changes in complexity could be better visualised.

The type of complexity was also considered. The exhaustive method has shown to be the better choice for this work compared to the primitive one. It has been shown that the LZC for both exhaustive and primitive type is representative of regions of interest in the corresponding blood flux signal at 33℃ and at 43℃. By considering the location of peaks in the LDF signals, the LZC with the moving window can detect changes in the signal, similar to that presented by Aboy, et al. [91]

and Abasolo, et al. [102] from studies on the detection of intracranial pressure and epileptic seizure respectively, has been shown to be feasible.

The results also showed that LZC at 33°C and at 43°C is more discriminative with the exhaustive type of complexity, rather than the primitive type. The range of the values is wider for primitive than the exhaustive for the same raw data, which makes the complexity signals with the primitive type more variable. This justifies the selection of the exhaustive type of complexity used in this work.

The findings of the complexity analysis showed a decrease in complexity during dilated perfusion state at 43°C in the human skin, which is consistent with the study of LZC in the skin of monkeys, as addressed by Tigno, et al. [4]. Liao, et al. [126] in an additional study, reported a decrease in the complexity of myogenic activity by calculating the multifractal detrended fluctuation analysis, α, in healthy rats. These studies demonstrate a diagnostic potential of the complexity analysis in the microvascular blood flux signals.

Further investigation of the complexity of the blood flux signal with the transition from 33℃ to 43℃ was also examined. The LZC analysis with the moving window was able to detect differences in the transition period. It is notable that the exhaustive type was more sensitive in detecting these changes. As already described, the complexity decreases during the local heating, although the transition between the temperatures may also contain useful information about the randomness of the blood flux signal. By developing the LZC with the 30 epochs for the same blood flux signal, the decline in complexity at 43℃ is still obvious and possible to identify the changes during the transition.

The question of whether the information content in the BF and oxyHb signals derived from the skin microcirculation could be used to discriminate between two different haemodynamic states by examining the simultaneously recorded signals from a cohort of healthy male participants was also considered. First, the changes in entropy and complexity of the microcirculatory dynamics were studied, using conventional sample entropy (SampEn), LZC and effort to compress (ETC) complexity methods. The results show a significant decrease in the entropy together with a reduction in the complexity during the vasodilated perfusion state at 43℃, with a more substantial decline in the complexity measures. They further show that the multiscale analysis has the potential for distinguishing the two different haemodynamic states in both BF and oxyHb signals, with a better discrimination in the oxyHb signals.

Recent studies [109, 133], suggested that a greater variability of the blood flux may indicate a more effective microvascular system, whereas a lower variability in microvascular activity corresponds to a loss of the system's ability to adapt to pathophysiological conditions. As far as is known, there are no known previous studies to investigate the SampEn and ETC complexity of healthy human skin blood flux and oxygenation signals, recorded simultaneously at the same site, during local heating. These findings provide strong evidence that the complexity methods, in human skin microvascular blood flux and oxygenated haemoglobin signals, showed sensitivity to the effect of the heating. Here, lower entropy and complexity indexes with relatively consistent variation across the 15 epochs were found when microvascular flow approaches maximal dilation and network perfusion during heating. However, Liao, et al. [124] in a similar study investigating the sample entropy indexes in response to local heating of the sacral skin blood flow in people at risk for pressure ulcers, did not find any significant correlation with the skin vasodilatory function. They also reported that the nonlinear analysis is not always a consistent method for assessment of vasodilatory function.

The traditional methods measure for estimating entropy and complexity of a signal in one scale only. For this reason, the BF and oxyHb signals were further examined using multiscale analysis, in order to evaluate these methods in multiple scales. At low scales, all the multiscale nonlinear methods (MSE, MLZC and METC) yield small values of entropy and complexity. As the sampling rate decreases, the complexity increases until it reaches and passes the Nyquist frequency of the original time series. More specifically, by increasing the scale factor from $\tau = 1$ to $\tau = 12$, the sampling frequency which is $f_{s_{12}} = f_{s_{original}} / \ \tau = 3.33\ Hz$ reaches the Nyquist frequency which for the signals investigated here is $f_{N/2} = 2 \cdot f_{max} = 2 \cdot 1.6\ Hz = 3.2\ Hz$. It was observed that for the complexity measures there is a rapid increase until the scale factor around 12. At the higher scale factors, the complexity either decreases or becomes constant until scale factor around 20. The complexity after the scale factor 20 steadily increases. However, the entropy measures did not show the same changes through scales as the complexity methods. Humeau, et al. [127], in a recent study of the MSE analysis of LDF signals in healthy subjects, showed a similar behaviour of the MSE of the BF signal when filtered for the frequencies associated with heart rate (~0.6 - 2Hz). They reported that the increase and then decrease of the MSE over the scales may be because these signals are non-periodic and therefore the progression of complexity in multiple scales cannot be stable. They also suggested that this may be a representative indicator for the BF signals. It is also worth noting that during local heating around scale 24, the oxyHb signals become more complex (less regular) than those at 33°C using the MSE method and approaches that of those at 33°C using both MLZC and METC complexity measures. This increase in complexity at higher scales may be a

useful new index of increased adaptive capacity of the oxyHb signals in larger time scales possibly due to compensatory endothelial action.

The information of the signals during LTH using the multiscale analysis showed a similar decline to that when using the traditional methods. Here, it is shown that the multiscale analysis may be more valid than the traditional methods as it measures the complex characteristics of the biological signals in multiple spatial and temporal scales and is consistent with that reported by Kalev, et al. [128], examining EEG signals for objective measures of depression. These authors found that traditional LZC was unable to account for the high frequency components in the signals resulting in a 50% classification accuracy of people with depression and controls in their study. Using multiscale LZC, they were able to demonstrate an 86% classification accuracy by accounting for the different frequencies of information content in the EEG. Here, 73.3% and 90% classification accuracy of haemodynamic state using MLZC for BF and oxyHb, respectively, was presented [134]

All the nonlinear methods used, were able to distinguish between the two haemodynamic steady states. However, it was noticed that the complexity measures (LZC, ETC, MLZC and METC) showed a more significant separation than the entropy measures (SampEn and MSE), in both conventional and multiscale analysis. Recently, Balasubramanian and Nagaraj [75], estimated the SampEn, LZC and ETC complexity in R-R tachograms of healthy young and healthy old people in order to find the most efficient measure for a better separation between the two groups, found that LZC and ETC complexity were able to discriminate better between the two groups for very short lengths.

From this current study was found that, for the BF signals when using the multiscale analysis, there was a large difference between the two haemodynamic steady states, around scale factor 19 in the entropy indexes and around scale factor 9 in the complexity indexes. The weakest separation appears in scale 1 which is the scale studied by traditional entropy and complexity methods. For the oxyHb signals the strongest separation appears at around scale 9 for all methods. However, the smallest difference occurs at scale 4 in the entropy indexes and at scale 24 in the complexity indexes. It is also worth noting that the microvascular oxyHb signals showed better separation than the BF signals between the two haemodynamic steady states. This suggests that these measures may be valuable in clinical assessment in low perfusion states and in detecting early signs of sepsis. Other studies have also shown that pattern recognition methods are suitable for the discrimination between groups [131]. Pattern classification methods may be applied in future studies in order to classify the tissue perfusion features in different pathophysiological groups.

Recent studies [120], using chaotic network attractor analysis have shown that a declining

adaptability in flow patterns in a microvascular network may be a major indicator of CV and Met disease risk. They also suggest that the spatial distribution and temporal behaviour of microvascular network perfusion may be more suitable measures with which to understand microvascular disease.

4.6 Limitations

This study reveals the analysis of the information content of blood flow and oxygenation time series derived from the microvasculature in two haemodynamic steady states at 33℃ and 43℃ using both conventional and multiscale complexity methods. A major strength of this study is that by using LTH to assess microvascular reactivity and obtain two haemodynamic steady states, the nonlinear complexity methods were able to discriminate between the groups showing a better separation when using multiscale analysis. This study seeks to explore the feasibility of using nonlinear complexity methods as a tool for differentiating between two imposed microvascular haemodynamic steady states as a proof of concept for clinical application in the prognosis and the diagnosis of pathophysiological conditions. However, this study was conducted only in healthy male cohorts as when including women in a study group it is essential to match them for menstrual cycle. Therefore, this study was limited to young healthy males in order to reduce inter-individual variation as far as possible.

4.7 Conclusions

Nonlinear measures have been increasingly used to investigate the dynamics within the microcirculation and define different pathophysiological conditions. Here, the study on the Lempel and Ziv complexity (LZC) provides information about the choice of the different parameters such as epoch size and type of complexity from which the exhaustive type of complexity appears more sensitive in analysing the changes of the blood flow signals. Furthermore, the nonlinear properties of the BF and oxyHb signals using one entropy measures (sample entropy) and two complexity measures (Lempel and Ziv and effort to compress complexity) were studied, in order to identify the change of the vasodilation caused by local heating. From this study it is suggested that the complexity measures have more sensitivity for identifying changes in the microvascular function under an imposed stimulus than the entropy measures. Multiscale analysis, for the first time, has been used in BF and oxyHb signals recorded simultaneously at the same site to discriminate between two haemodynamic states, showing a more significant discrimination in the oxyHb signals. These findings also suggest that the significant attenuation of the network's flexibility and adaptability in face of an imposed stressor assessed using multiscale analysis of entropy and

complexity measures, makes this method a promising approach for further analysis of the microvascular function. For a better understanding of the nonlinear indexes of the microvascular function these methods now need to be extended to cohorts under pathological conditions. In the next chapter, these methods are applied to LDF data from a cohort of people with non-alcoholic fatty liver disease to examine if features of the disease influence the information in the signals from the microvasculature.

Chapter 5: Multi-Study Analysis of Microvascular Blood flow Variability in NAFLD Groups

In this chapter, the feasibility of the nonlinear complexity methods as a tool for differentiating between groups of individuals at an increased risk of developing cardiovascular disease (CVD) is investigated. The microvascular blood flow signals were recorded from the forearm skin of a group of sixty volunteers with the non-alcoholic fatty liver disease (NAFLD) grouped for absence or presence of type 2 diabetes (T2DM) and use of calcium channel blocker medication using the laser Doppler flowmetry (LDF). Both linear and nonlinear analysis have been applied to evaluated the signals within the frequency range (0.0095-1.6Hz) using the power spectral density and to quantify signal information content using both conventional and multiscale variants of LZC. The relationship between the relative power and complexity of the blood flux was also evaluated to investigate the changes of the frequency bands with time-scales. Finally, a thorough discussion of the outcomes of these analyses and the limitation of the data uses is presented.

5.1 Introduction

Microvascular perfusion has received much interest and been investigated in a range of physiological and pathophysiological states over the previous decade [1] . Approximately 20% of the general population suffer from CVD that is associated with the non-alcoholic fatty liver disease (NAFLD) and type 2 diabetes (T2DM) [135-138]. Non-alcoholic fatty liver disease is the concentration of fat in the liver without a significant consumption of alcohol or other liver diseases [139]. The progression of NAFLD occurs slowly ranging from steatosis to non-alcoholic steatohepatitis (NASH) and cirrhosis in the last stage of the disease and in many cases may lead into a hepatocellular carcinoma [137, 139]. There has been an emerging interest in investigating the microvascular function in NAFLD subjects showing higher complications in the microvasculature of people with such diseases [12, 140].

Recent studies [2, 3], have shown that in many disease states, such as metabolic disease and ageing, there appears to be a reduction in adaptive capabilities of the individual and a consequent loss of physiological information content. Time and frequency domain analysis have been applied on the blood flow signals to characterise the dynamics of the flow patterns. Power spectral analysis of local oscillations (0.0095～1.6Hz) that contribute to the total blood flow motion have been studied by many research groups [36, 105, 106]. Although, these linear methods alone have been insufficient for discriminating between different pathophysiological groups. Therefore, nonlinear

methods have been used widely to quantify the randomness of skin microvascular blood flow signals and evaluate microvascular impairment and CVD risk factors on vascular health and are well suited for the analysis of short length signals [5-8].

Recent studies have applied frequency and complexity approaches to BF signals derived from the skin in humans [104, 141] and in animal models [4, 126], demonstrating clear differences in complexity between different groups. Recently [120], from a study of the microvascular perfusion in lean and obese Zucker rats with features of metabolic syndrome, it was reported that the arterial blood flow bifurcations become lower as the risk for vascular dysfunction increases which means that the system is more adaptive in lean rather than the obese rats and that influences the ability to provide a more complex flow motion in obese rats. They also reported that, an increase spatial heterogeneous perfusion may contribute to the loss of the microvascular network flexibility and adaptability with increased cardiovascular risk. These studies demonstrate a diagnostic potential in investigating microvascular functionality using nonlinear analysis.

The aim of this multi-study is to examine the frequency and complexity of microvascular blood flow signals of people with non-alcoholic fatty liver disease (NAFLD) with increased risk of CVD. The microvascular function was investigated from volunteers with and without T2DM and from a smaller group using calcium channel blocker medication. First, the changes in time, frequency and complexity of the microcirculatory dynamics, are explored using power spectral density and LZC in single and multiple scales in order to understand the effect of scale on these nonlinear metrics and their efficacy in classifying between these groups. The spectral content of the LDF signal examined in the frequency domain to identify the spectral behaviour of the oscillatory processes influencing microvascular blood flow. The multiscale complexity was also assessed to examine if it was influenced by the time-scale of the different oscillatory rhythms. A further aim of this chapter is to test the hypothesis that the nonlinear methods can be feasible methods for differentiating between these groups and thus, can have a strong potential of identifying microvascular dysfunction.

5.2 Materials

5.2.1 Study Design

The data that were used for this study regarding NAFLD patients was a combined from two randomized, double blind, placebo-controlled trials, the WELCOME (Wessex Evaluation of Fatty Liver and Cardiovascular Markers in NAFLD with OMacor Therapy) and INSYTE (INvestigation of SYnbiotic TreatmEnt in NAFLD). Ethics approvals, informed and written consent were obtained before participants were enrolled into the clinical trials. Data collected from the WELCOME study

included NAFLD severity biomarkers, measures of insulin sensitivity, cardiovascular risk factors, measures of microvascular function and liver fat. The inclusion criteria for both studies included being older than 18 years and having radiological or biopsy-proven NAFLD. Some of the exclusion criteria involved having decompensated acute or chronic liver disease and viral hepatitis. Detailed information on different aspects of the studies are available from www.clinicaltrials.gov (WELCOME identifier: NCT00760513, INSYTE identifier NCT01680640) [144].

5.2.2 Measurements of the Microvascular Function

The signals were recorded using the laser Doppler flowmetry probe with fibre separation of 1.0 mm separation (moorCP1T-1000, Moor Instruments Ltd, UK), using a single point 785 nm, 1 mW power laser light source, for measuring the blood flux, at a sampling rate of 40 Hz. The calibration of the probes was performed using aqueous suspension of polystyrene latex particles whose Brownian motion provides a standard reference value. The probe was mounted using double sided sticky O-rings on the ventral surface of the non-dominant forearm, approximately 10cm from the wrist avoiding visible veins. In the WELCOME study, the baseline BF were recorded 15 minutes before post-occlusive reactive hyperaemia (PORH) using a pressure cuff placed around the upper arm inflated to 180 mm Hg for 3 minutes. In the INSYTE study, the participants had inspiratory breath holds allowing approximately 3 minutes extra recordings before the baseline BF.

All participants refrained from caffeine containing drinks and food for at least 2 hours and strenuous exercise for 24 hours before testing. Studies were performed in a temperature-controlled room maintained between 22 and 23.5°C. All participants were acclimatized for 30 minutes prior to testing. The mean resting forearm skin temperature measured during baseline recording was 29.4 $\pm$ 2.1°C. Laser Doppler measurements were made with the participants sitting comfortably with their arm supported at heart level.

5.2.3 Clinical Measurements

CVD risk score

The CVD risk percentage was assessed using the QRISK2 score which incorporates aspects of the traditional cardiovascular risk factors such as age, smoking, diabetes, obesity and hypertension. Past medical history such as having angina or myocardial infarction in 1st degree relative <60, stage 4 or 5 chronic kidney disease, atrial fibrillation, rheumatoid arthritis or blood pressure treatment were also incorporated into the final score. Furthermore, ethnicity and postcode were part of the algorithm. QRISK2 score can be generated despite one or more missing risk factors and has been able to predict the CVD risk reliably [145].

Risk factors for metabolic syndrome

In this study, metabolic syndrome was defined clinically, based on the presence of 3 or more of the following: (1) central obesity (waist circumference: men, $>$ 102 cm, women, $>$ 88 cm, in U.K.); (2) a high triglyceride level (1.7 mmol/L); (3) a low HDL-cholesterol level (men, $<$ 1.03 mmol/L; women, $<$1.29 mmol/L); (4) high blood pressure (systolic blood pressure $\geq$ 130 mm Hg or diastolic blood pressure $\geq$ 85 mm Hg) or antihypertensive drug treatment; (5) a high fasting plasma glucose concentration ($>$ 6.1 mmol/L) or drug treatment for T2DM.

Definition of Hypertension and Diabetes Mellitus (DM)

Hypertension was defined by systolic blood pressure $\geq$ 130 mm Hg or diastolic blood pressure $\geq$ 85 mm Hg or on antihypertensive drug treatment such as calcium channel blockers. Diabetes mellitus (DM) was defined by fasting glucose levels > 6.1 mmol/L or drug treatment for type 2 diabetes. Homeostasis model assessment-estimated insulin resistance (HOMA-IR), is used to estimate the insulin resistance by multiplying fasting plasma insulin by fasting plasma glucose and dividing the constant by 22.5. Values higher than 2 indicate early insulin resistance [146].

5.2.4 Subject Selection

The study was conducted on 60 volunteers with NAFLD chosen based on the quality of the raw signals, from the total of 200 participants from the combined WELCOME and INSYTE trials [144]. They were grouped for the absence (DM0) or presence (DM1) of T2DM, and use of calcium channel blocker medication (CB) with and without T2DM (5 participants with T2DM). The demographics for each group are summarised in Table 5.1.

Table 5.1 Demographics for DM0 (n=25), DM1 (n=23) and CB (n=12) groups.

	DM0	**DM1**	**CB**
Age	51.4 ± 12.5	49.5 ± 10.9	59.6 ± 5.6
Sex	14M/11F	11M/12F	6M/6F
BMI	33.3 ± 5.5	34.4 ± 5.8	34.6 ± 4.4
CVD risk (%)	9.7 ± 9.1	16.3 ± 9*	23.9 ± 8.9$^{*,+}$
Systolic BP (mm Hg)	138 ± 17	133 ± 16	141 ± 11
Diastolic BP (mm Hg)	82 ± 11	77.8 ± 13	83 ± 9
Hypertension (subjects)	19 (76%)	18 (78%)	12 (100%)

Diabetes duration (years)	-	7.4 ± 10.2	4.8 ± 3.4 (n=5)
METS (features)	3.1 ± 0.9	3.7 ± 1.1*	3.8 ± 0.8*
HOMA-IR	2.9 ± 1.1	6.3 ± 5.2*	3.5 ± 2.2+

*Significant difference from DM0, $p < 0.05$. +Significant difference from DM1, $p < 0.05$.

5.3 Methodology

5.3.1 Pre-processing

The blood flux recordings, performed from the Moor Software were exported to Matlab (R2019a, Mathworks, UK). The recordings were cut into 10-minute artefact-free segments at rest. Before estimating signal complexity, it is necessary to perform some pre-processing of the raw data. The analysis procedure used in this chapter is consistent with the previous chapters. The segments were filtered using a low pass finite impulse response (FIR) filter with 2Hz cut-off frequency, to attenuate high frequencies beyond the known range of microvascular oscillation and allow the frequencies of interest with a range from 0.0095 to 1.6Hz [36, 39]. FIR filter was chosen for designing and implementation convenience as well as for producing inherently stable oscillatory outputs. The data were then detrended by removing the mean and a stationarity test was performed on the processed data to examine whether the data have a consistent variance over time. This pre-processing ensures that the analysis of the signals is not biased by noise measurement or components outside the range of interest.

5.3.2 Linear Analysis

Time domain: Blood flux measurements were recorded in arbitrary perfusion units (PU). The blood flux was recorded at rest (RF) for over the final 5 minutes before perturbation, following with 3 minutes arterial occlusion and peak reactive hyperaemia. The dilator capacity was measured as the fold change MF/RF, determined as the ratio of mean peak of the PORH divided by the RF. The blood flux recordings, performed from the Moor Software were exported to Matlab (R2019a, Mathworks, UK). Figure 5.1 illustrates the BF outputs and the selection of the 10 minutes artefact free segments marked as grey of three individuals with absence, presence of T2DM and with calcium channel blockers medication, respectively.

Spectral analysis: Power spectral density (PSD) was estimated by Welch's method of fast Fourier transform (FFT) with a Hanning window size of 200 s and 50% overlap between windows over continuous 10 min recording periods. The power contribution was evaluated within the frequency range (0.0095-1.6 Hz) [36]. Total spectral power was estimated as the sum of absolute power across

the five frequency intervals (0.0095-1.6 Hz) plotted in a log axis as $10 \cdot \log_{10}$ PSD over frequency and expressed in dB/Hz. PSD contribution was calculated relative to total spectral power and is expressed as a fraction between 0 and 1.

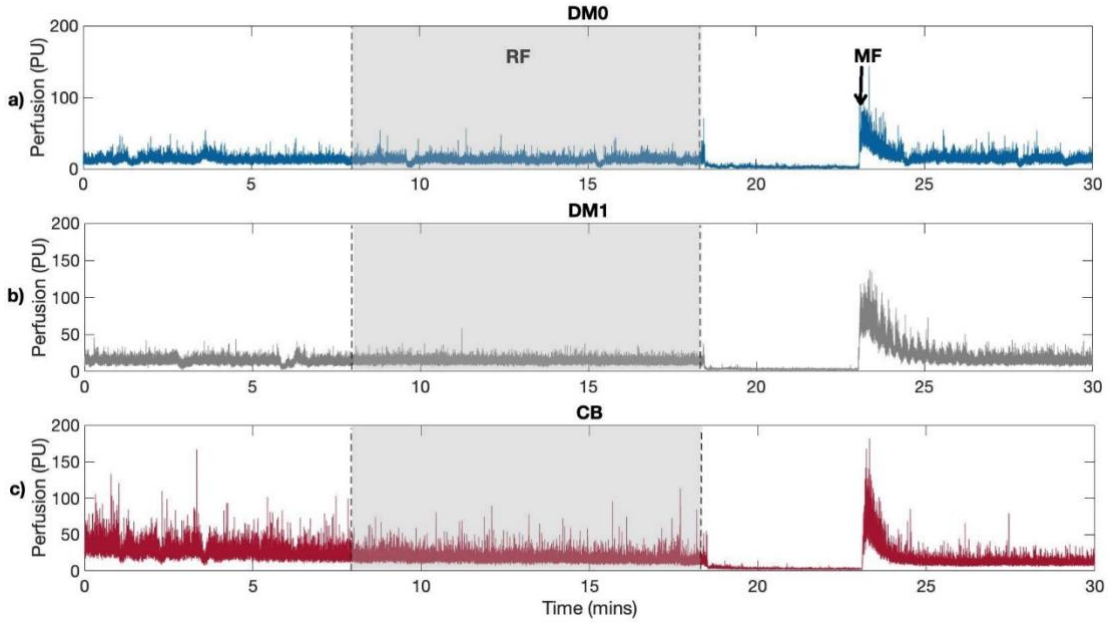

Figure 5.1 Example of raw microvascular blood flow signals and the selection of 10 minutes segment (grey area) from skin resting flux (RF) at the forearm at ambient room temperature and during PORH indicating maximal flux (MF) in a) individual without T2DM (DM0), b) individual with T2DM (DM1) and c) an individual with calcium channel blocker medication (CB).

Table 5.2 BF measurements at the forearm skin for DM0 (n=25), DM1 (n=23) and CB (n=12) groups. Data are presented as mean ± SD

	DM0	DM1	CB
BF at rest RF (PU)	11.5 ± 4.3	14.1 ± 5.2	19.6 ± 10.8*
Maximal BF MF (PU)	55.0 ± 25.4	62.1 ± 21.0	67.2 ± 33.1
Dilator capacity MF/RF (fold change)	4.8 ± 1.5	4.6 ± 1.3	3.7 ± 0.9*,+

*Significant difference from DM0, $P < 0.05$. +Significant difference from DM1, $p < 0.05$.

5.3.3 Nonlinear Analysis

Here, Lempel and Ziv complexity was chosen as a nonlinear complexity method for evaluating the changes of the NAFLD data. The selection of the LZC technique was chosen after testing the performance of the LZC on the blood flux signals and comparing them with the other entropy and

complexity measures which showed a greater sensitivity of the LZC for detecting changes in the microvascular function (supplemental material in Appendix C). The LZC was also calculated for each coarse-grained sequence, as a function of the scale factor, τ, and was evaluated in multiple scales. From previous work [104, 141], it was shown that the LZC measures can be used to discriminate between two haemodynamic steady states (resting and that induced by local thermal hyperaemia) and are thus a good candidate for the study presented here.

5.3.4 Statistical and Classification Analysis

Statistical analysis was performed using IBM SPSS Statistics 25 (IBM United Kingdom Limited, UK). Data were tested for normal distribution using D'Agostino & Pearson omnibus normality test and presented as either mean ± SD for normally distributed data or median with interquartile range (IQR) for non-normally distributed data. Normally distributed data were compared using a Student t-test and non-normally distributed data using a Mann-Whitney test. Spearman's rho correlations are presented for monotonic nonlinear correlation analysis of baseline data.

Mutual information (MI) was also computed in R statistical programming environment using the the Bioconductor package "minet" (Mutual Information NETwork inference, [147]) to measure the non-monotonic and nonlinear dependence among data [148]. The p-values for the MI were computed following a Monte-Carlo procedure based on 5000 permutations for each pair of variables [149]. A high MI between two variables indicates that the one variable is regularly associated with the other whereas, a MI of zero, means that the joint distribution between the variables holds no more information and the variables are considered independent. Similar to chapter 3, due to the small sampling size of the data, the probability of false negatives between the groups was minimised by setting the value of significance level, α, to 0.05 and therefore no multiple correction testing is applied [118]. Discriminant analysis with leave-one-out cross-validation (LOO) [150] was applied on both LZC and MLZC of the BF signals, to determine the classification accuracy between groups.

5.4 Results

There was a significant difference ($P < 0.05$) between CVD risk of the CB group and the other two groups and between DM0 and DM1, showing an increase in subjects with diabetes and hypertension than in DM0 subjects. Hypertension measures as well as the blood pressure measured using a standard sphygmomanometer before the test and after acclimatization, shows hypertension in all groups but no significant difference between them. Homeostatic model assessment of insulin resistance (HOMA-IR) data suggests that most subjects were insulin resistant

and subjects in the DM1 group were more insulin resistant than the subjects in DM0 and CB group. The features of metabolic syndrome (METS), indicate that most subjects have more than 3 features, however, DM1 and CB group had significantly more features of METS than the subjects without diabetes.

5.4.1 Time Domain Analysis

LDF provides arbitrary perfusion units of microvascular perfusion in the time domain and is frequently used with a vasoreactivity test, such as the PORH shown in Figure 5.1, to investigate dilator capacity and processes controlling local vascular tone. It is known that the LDF measures the concentration and velocity of the moving red blood cells and the penetration depth of the tissue depends on the laser power and wavelength which can exhibit significant spatial variation. Here, the signal in Figure 5.1a and 5.1b appears to have a lower mean value than that in Figure 5.1c derived from the CB group, which shows larger frequency variations. The resting blood flux (RF), determined as the mean BF measured before perturbation, and the fold change MF/RF, are shown in Table 5.2. The DM0 group was shown to have significantly lower RF than the CB group ($p < 0.05$), although there was no significant difference in resting flux between DM1 and CB. Dilator capacity is shown to be significantly reduced in CB group when compared with both DM0 ($p = 0.013$) and DM1 ($p = 0.044$).

5.4.2 Frequency Domain Analysis

All BF signals recorded from the 60 individuals exhibited multiple oscillatory components. In Figure 5.2 the PSD of resting BF signals across five bands for each group showed multiple oscillatory components. The individual PSD do not show any obvious tendencies in the frequency bands for each group. Although, as illustrated in Table 5.3, the average absolute PSD show some differences in the power for each band and the distributions. Here, the total absolute power shows a significant increase in the group with T2DM compared to the group without T2DM ($p = 0.040$) and a significant greater power in the CB group when compared to the DM0 group ($p = 0.010$). PSD values in the neurogenic ($p = 0.034$) and respiratory ($p = 0.049$) bands are significantly attenuated in CB groups compared to the DM1. DM0 was significantly attenuated in the LF bands (endothelial ($p = 0.049$), neurogenic ($p = 0.002$) and myogenic ($p = 0.034$)), when compared with the DM1 group. Greater power is present in the cardiac band for the CB group compared to both DM0 and DM1 ($p < 0.05$). There was no significant difference between the CB and both DM0 and DM1 group in the myogenic band. There were found no significant differences between groups with and without T2DM in the HF respiratory and cardiac bands.

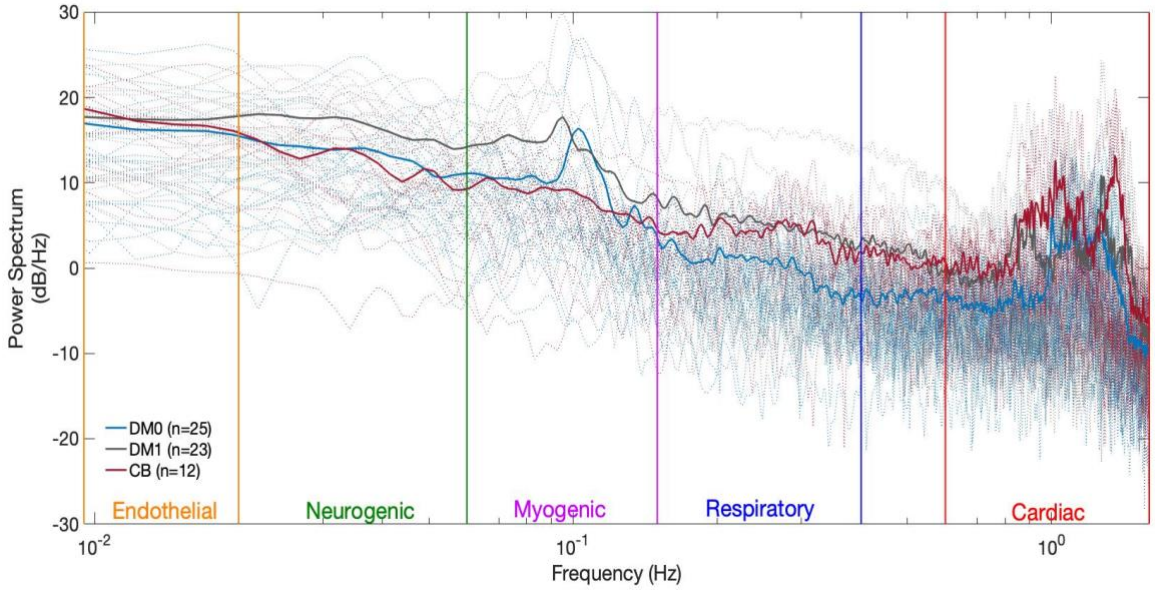

Figure 5.2 Power spectral density for each individual (dotted lines) and for the mean (solid lines) of each group DM0 (n=25) in blue, DM1 (n=23) in grey and CB (n=12) in maroon. PSD is plotted in a log axis as $10 \cdot \log_{10} \mathrm{PSD}$ over frequency.

Table 5.3 Absolute PSD contributions of resting BF signal across five frequency bands and total absolute power recorded at the skin forearm for DM0 (n=25), DM1 (n=23) and CB (n=12) groups. Data are presented as mean ± SD

	DM0	**DM1**	**CB**
Endothelial	0.73 ± 1.30	1.01 ± 0.96*	0.96 ± 0.90
Neurogenic	0.92 ± 1.42	1.91 ± 1.53*	0.79 ± 0.80+
Myogenic	1.15 ± 2.56	2.13 ± 3.87*	0.62 ± 0.51
Respiratory	0.26 ± 0.22	0.84 ± 2.17	0.64± 0.42*,+
Cardiac	1.04 ± 0.78	2.05 ± 3.23	3.87 ± 2.61*,+
Total PSD	4.11 ± 5.70	7.94 ± 10.08*	6.87 ± 3.94*

*Significant difference from DM0, $P < 0.05$. +Significant difference from DM1, $p < 0.05$.

The normalized PSD contribution calculating relative to total spectral power (0 – 1), of the CB group in the HF cardiac band, shown in Figure 5.3 and Table 5.4, increased significantly, showing values of 0.58 ±0.18 over DM0 with values of 0.25 ± 0.13 and DM1 with values of 0.34 ± 0.14 ($p < 0.05$ for both groups). Similarly, in the myogenic band the power of CB group showed a significant decrease compared to DM0 ($p < 0.05$) and DM1 ($p < 0.05$). Neurogenic power also decreased

substantially in the CB group compared with DM0 ($p < 0.05$) and DM1 ($p < 0.05$). There was found a significant increase in the neurogenic band in the group with T2DM when compared with the group without T2DM. The HF cardiac activity was also shown to be significant lower in the DM1 group when compared with DM0 group. No other differences were found between DM0 and DM1 group. While, frequency domain analysis may provide more detailed information of the rhythmic oscillatory variations within the different groups, although it still does not present a definite and reliable tool to discriminate between the groups.

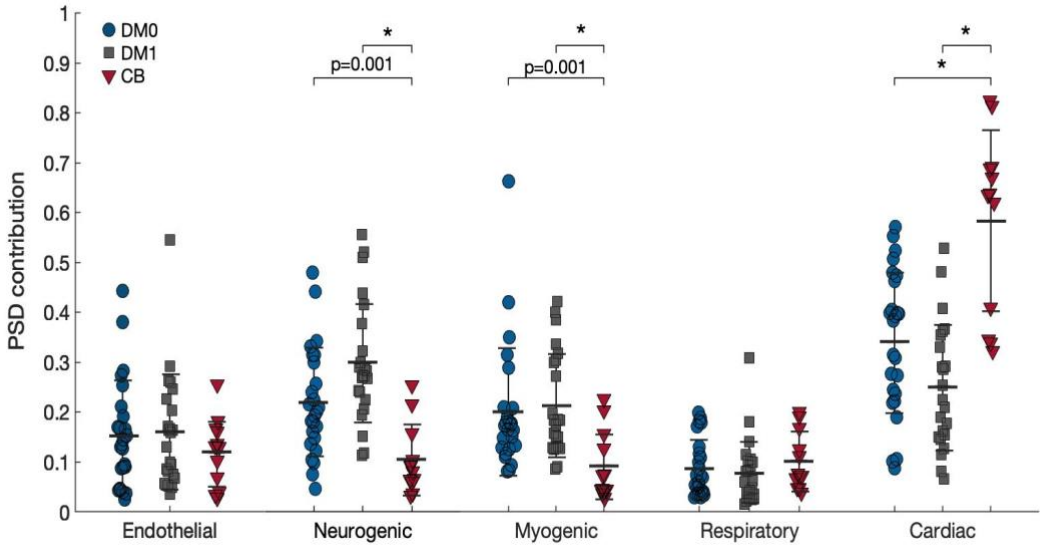

Figure 5.3 PSD contributions of resting BF signal across five frequency bands recorded at the skin forearm for DM0 n=25, DM1 n=23 and CB n=12. Data are presentes as median and IQR, $^{*}p < 0.05$.

Table 5.4 Normalized PSD contributions of resting BF signal across five frequency bands recorded at the skin forearm for DM0 (n=25), DM1 (n=23) and CB (n=12) groups. Data are presented as mean ± SD

	DM0	**DM1**	**CB**
Endothelial	0.15 ± 0.11	0.16 ± 0.11	0.12 ± 0.07
Neurogenic	0.22 ± 0.11	0.30 ± 0.12*	0.11 ± 0.07$^{*,+}$
Myogenic	0.20 ± 0.13	0.21 ± 0.10	0.09 ± 0.07$^{*,+}$
Respiratory	0.09 ± 0.06	0.07 ± 0.07	0.10 ± 0.06
Cardiac	0.34 ± 0.14	0.25 ± 0.13*	0.58 ± 0.18$^{*,+}$

*Significant difference from DM0, $P < 0.05$. $^{+}$Significant difference from DM1, $p < 0.05$.

5.4.3 Complexity Analysis

LZC was estimated for resting BF in all participants and showed relative consistency over the 15 epochs in all groups. Figure 5.4 shows that the BF signal appeared significantly less complex in the CB group than both DM0 and DM1 group. However, there was no difference found in the complexity in the absence or presence of T2DM alone. As shown in Table 5.5, the BF LZ-complexity index, fell from 0.315 $\pm$ 0.006 in the absence of T2DM to 0.305 $\pm$ 0.009 with T2DM and 0.270 ± 0.012 with calcium channel blocker use.

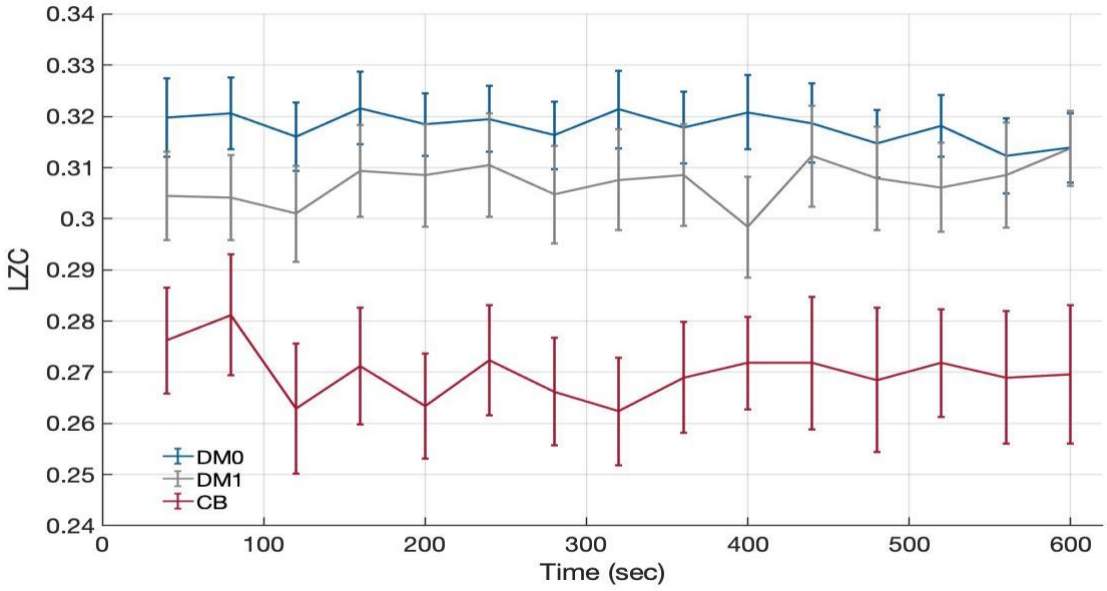

Figure 5.4 LZ complexity along the 15 epochs of resting BF signals of DM0 (n=25), DM1 (n=23) and CB (n=12) groups. Data are mean± SEM.

Table 5.5 LZ complexity for DM0 (n=25), DM1(n=23) and CB (n=12) groups. Data are mean± SEM.

	DM0	**DM1**	**CB**
LZ complexity	0.315 ± 0.006	0.305 ± 0.009	0.270 ± 0.012$^{*,+}$

*Significant difference from DM0, $P < 0.05$. $^{+}$Significant difference from DM1, $p < 0.05$.

Figure 5.5 shows the MLZC computed for all participants across 24 scales at different dominant frequencies of each scale corresponding to BF signal sampling rates of 40 Hz at scale τ = 1 to 1.67 Hz at scale τ = 24 where the vertical dotted line indicates the scale 12 (3.33 Hz) which is considered to be close to the Nyquist frequency of the blood flow signals ($f_{N/2} = 3.2$ Hz). Therefore, in order to keep the useful information of the signals and provide more meaningful analysis, LZC will be estimated up to scale 12.

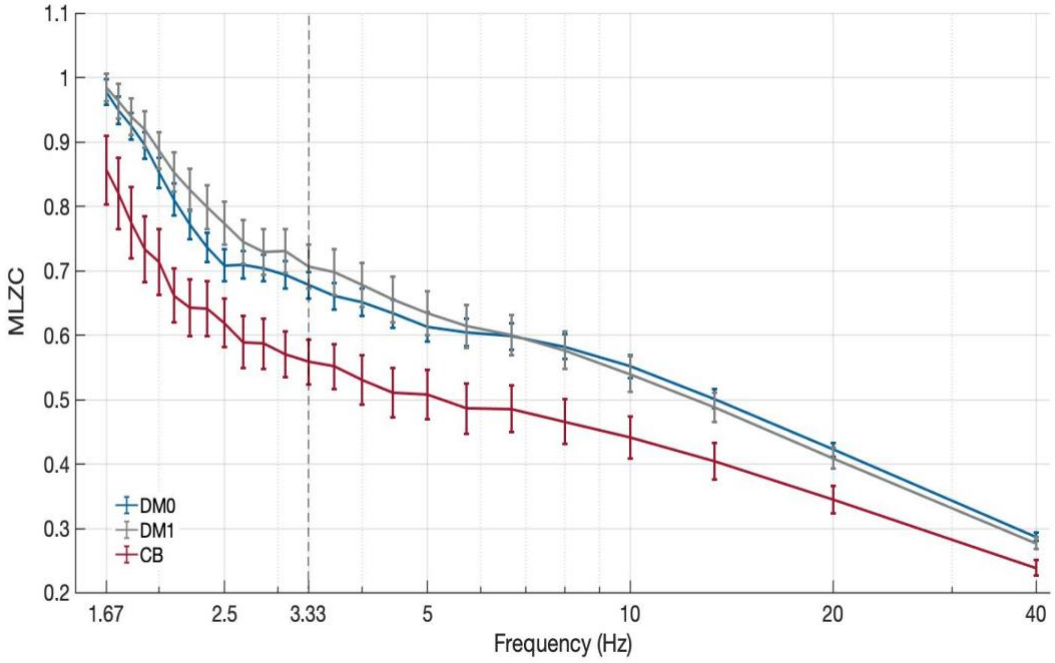

Figure 5.5 Average MLZC at different sampling frequencies corresponding to 24 scales of the resting BF signals measures in forearm skin. The vertical dotted line indicates the scale 12 corresponding to 3.33 Hz. Data are resented as mean ± SEM for DM0 (n=25), DM1 (n=23) and CB (n=12).

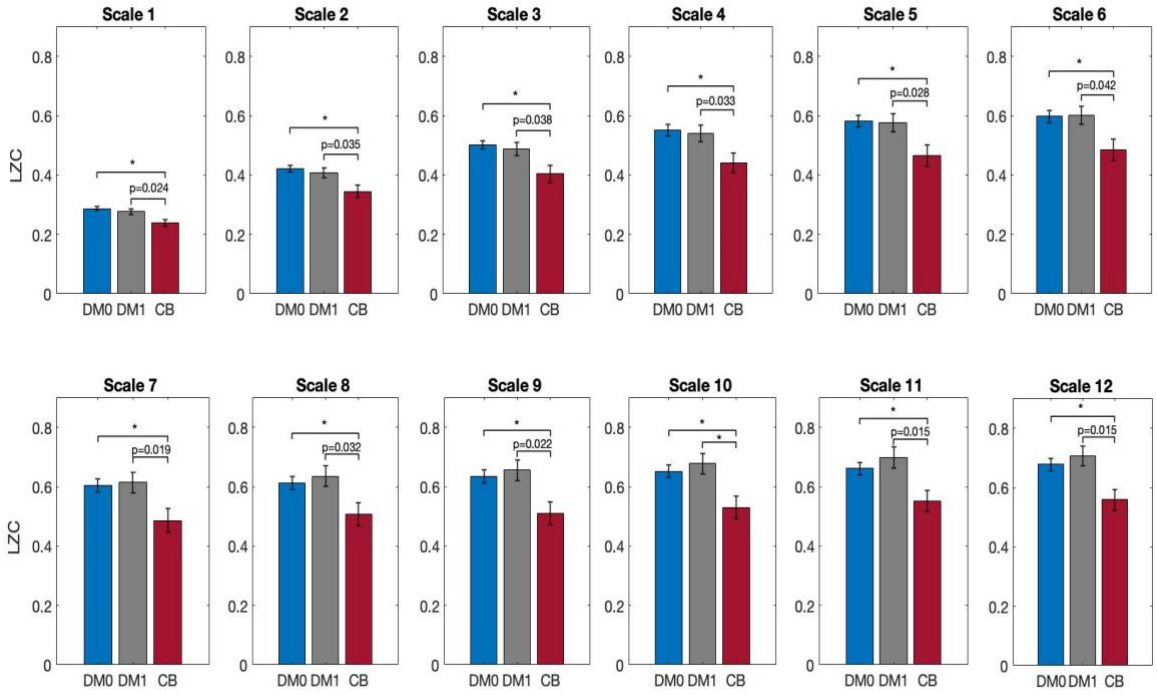

Figure 5.6 LZ complexity across 12 scales of the resting BF signals measures in forearm skin. Data are resented as mean ± SEM for DM0 (n=25), DM1 (n=23) and CB (n=12). $^{*}p < 0.05$.

Table 5.6 MLZC for the 12 scales for DM0 (n=25), DM1 (n=23) and CB (n=12) groups. Data are mean± SEM. Highest separability between DM0 - CB and DM1 - CB, is indicated in bold.

MLZC	DM0	DM1	CB
Scale 1	0.287 ± 0.006	0.277 ± 0.009	0.238 ± 0.011*,+
Scale 2	0.423 ± 0.010	0.409 ± 0.017	0.345 ± 0.021*,+
Scale 3	0.501 ± 0.015	0.488 ± 0.022	0.405 ± 0.029*,+
Scale 4	0.552 ± 0.018	0.540 ± 0.027	0.441 ± 0.033*,+
Scale 5	0.582 ± 0.020	0.576 ± 0.029	0.466 ± 0.035*,+
Scale 6	0.598 ± 0.021	0.601 ± 0.031	0.486 ± 0.036*,+
Scale 7	0.604 ± 0.021	0.614 ± 0.034	0.487 ± 0.039*,+
Scale 8	0.613 ± 0.023	0.635 ± 0.034	0.508 ± 0.038*,+
Scale 9	**0.634 ± 0.022**	0.655 ± 0.036	**0.511 ± 0.039*,+**
Scale 10	0.652 ± 0.021	0.678 ± 0.034	0.530 ± 0.038*,+
Scale 11	0.661 ± 0.021	0.698 ± 0.035	0.552 ± 0.035*,+
Scale 12	0.678 ± 0.021	**0.707 ± 0.034**	**0.559 ± 0.035*,+**

*Significant difference from DM0, $P < 0.05$. +Significant difference from DM1, $p < 0.05$.

In figure 5.6 is shown LZC from scale 1 (40 Hz) to scale 12 (3.33 Hz), where the CB group was significantly lower than both DM0 and DM1 at all scales. As shown in Table 5.6, the largest difference in the average complexity values of the 12-scale analysis, between the DM0 and CB groups was found in scale 9 (4.44 Hz) with values of 0.634 ± 0.022 in DM0 and 0.511 ± 0.039 ($p < 0.05$) in CB group. While the greatest separation between the DM1 and CB groups occurs in scale 12 (3.33 Hz) with values of 0.707 ± 0.034 in DM1 and 0.559 ± 0.035 ($p = 0.015$) in CB group. The lower difference between CB and both DM0 ($p < 0.05$) and DM1 ($p = 0.030$) was found at scale one which is the traditional single-scale based LZ complexity. There was found no significant difference in the complexity between subjects with and without diabetes across the 12 scales.

5.4.4 Classification Analysis

The 15 epochs of the LZC and the 12 scales of the MLZC were used as features against which to discriminate the different groups. Table 5.7 shows linear discriminant analysis with leave-one-out cross-validation applied for the LZC (left table) across 15 features (epochs) and MLZC (right table)

across 12 features (scales). The LDA classifier was able to correctly classify 30 out of 37 DM0 and CB subjects with the LZC features, giving 81.1% separability, while with MLZC features, the classification accuracy between these groups was 89.2% achieving the highest classification accuracy between the groups. The 12 features of the MLZC between DM1 and CB group, achieved 74.3% classification accuracy, whereas the LZC features were able to classify only 25 out of 35 subjects achieving the lowest separability between groups (71.4%).

Table 5.7 Confusion matrices and classification accuracy of the LDA classifier for LZC across 15 epochs and MLZC method across 12 scales for the three test groups.

LZC				**MLZC**			
	DM0	**CB**	**Classification accuracy (%)**		**DM0**	**CB**	**Classification accuracy (%)**
DM0	22	4	81.1 %	**DM0**	25	4	89.2 %
CB	3	8		**CB**	0	8	
	DM1	**CB**			**DM1**	**CB**	
DM1	18	5	71.4 %	**DM1**	18	4	74.3 %
CB	5	7		**CB**	5	8	

5.4.5 Association between Frequency Bands and MLZC

To understand how the spectral components of the BF signal influence its complexity, the correlations between the relative PSD contribution across the frequency bands of the BF signal and MLZC was examined, using the Spearman's rho correlation coefficient and mutual information. Figure 5.7a shows that the Spearman's rho correlation for the DM0 group, in the myogenic activity was negatively correlated with MLZC showing a stronger correlation up to scale 10 (4Hz sampling rate) and scales 15 (2.67Hz) and 16 (2.5Hz). In the respiratory band there was a positive strong correlation at scales 1 (40Hz), 2 (20Hz), 5 (8Hz) and 7 (5.7Hz) and for scale higher than 12 there was a positive strong correlation at scales 17 (2.35Hz), 19 (2.1Hz), 20 (2Hz) and 22 (1.82Hz). Power in the respiratory band for the DM1 group was strong positively correlated with MLZC up to scale 17 (2.35Hz), whereas the cardiac activity was strong negatively correlated from scale 10 (4Hz) up to scale 22 (1.82Hz). No significant correlation was found for the CB group with power in the frequency bands and MLZC.

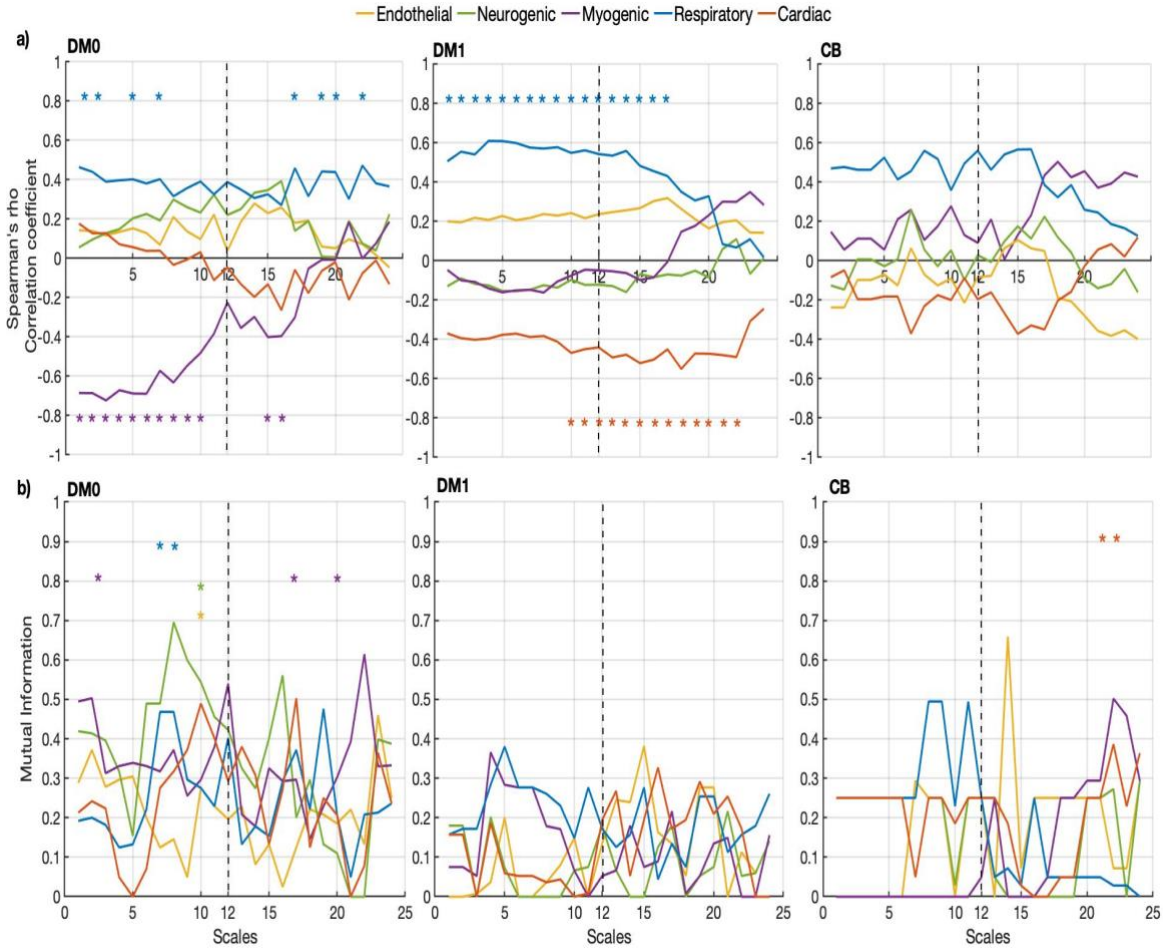

Figure 5.7 a) Spearman's rho correlation and b) mutual information between all frequency bands and the LZ complexity across 12 scales for DM0 (n=25), DM1 (n=23) and CB (n=12) groups. The vertical dotted line indicates the scale 12 corresponding to 3.33 Hz. $^{*}p < 0.05$.

Although, Spearman's rho correlation distinguishes between positive and negative correlations, the mutual information does not, though it measures the significant dependence between variables, by knowing how much information is shared about one variable knowing the state of the other variable, and vice versa In Figure 5.7b, MI showed a significantly high association in the respiratory band with LZC of the DM0 group at scales 7 (5.71 Hz) and 8 (5 Hz). The myogenic activity was associated at scale 3 (13.3 Hz), 16 (2.5 Hz) and 20 (2 Hz) whereas, the endothelial only at scale 10 (4 Hz). There was also a significant association with neurogenic activity and MLZC at scale 10 (4 Hz). There was no mutual information found for DM1 between the frequency bands and MLZC. In the CB group, MI showed a high association between the cardiac activity and LZC only at scales 21 (1.91 Hz) and 22 (1.82 Hz).

5.5 Discussion

5.5.1 Microvascular Function Measures

The parameters of the microvascular function measured with the vasoreactivity test were investigated between the groups studied here, in order to show their efficacy in discriminating between the three groups. The results shown here, were able to show significant increase in blood flow at rest in the group with the use calcium channel blockers when compared to the DM0 group although, they failed in discriminating between people with T2DM and calcium channel blockers. The dilator capacity was able to show significant changes between groups, showing a substantial decrease in the CB group due to vasodilation with the use of the antihypertensive treatment. This is also consistent with studies investigating the risk factors for cardiovascular disease and the impact in the microvascular function, suggesting that risk factors yield diminished dilator capacity of the blood vessels with presence of CVD [151, 152].

Even though, the results have shown differences between groups, these parameters alone show insufficient information which can be used to discriminate between groups and their significance still remains to be explained. Recent studies [9], have shown that common reactive test have shown to be reliable test, although they lack of reproducibility and their measures in time domain are still not fully elucidated. They also suggest that blood flow signals after being challenged, are complex and therefore more complex processing tools can be sufficient in predicting microvascular impairment [153]. Frisbee, et al. [120], in a recent study have also reported that markers of the microvascular perfusion may not always show useful information in understanding peripheral vascular disease risk and thus, more methods that determine the changes in the vasoreactivity remain to be established.

5.5.2 Powers Spectral Density Measures

As the total blood flow is modulated by local rhythmic oscillatory fluctuations that reflect the activity of the local vaso-control mechanisms within the frequency range (0.0095-1.6Hz) [39], frequency domain analysis was assessed in order to provide more detailed information about the changes in frequency and power of the oscillatory bands within the different groups. The frequency domain analysis has also been extensively applied in BF signals using FFT and wavelet analysis [36]. Even though wavelet analysis estimates the frequency content of the BF signals and the occurrence of changes in time, the outcome of this analysis however is often difficult to interpret and associate with microvascular activity [154]. In this study, the frequency domain analysis assessed using the Welch's PSD method to estimate the power in blood flow signals from groups at increase CVD risk.

The absolute power in the LDF signal over the frequency range of interest has been calculated to find the relative contribution of a frequency band and its impact on the overall flow motion.

This current study has shown that from the absolute PSD for each frequency band, it can be observed that the most significant differences between the group with the use of calcium blockers and people with and without diabetes occur in the HF respiratory and cardiac bands, showing a substantial increase in the power of the cardiac band in the CB group. Whereas a significant difference between DM1 and DM0 occur at LF bands. Examining the absolute total power in the group with T2DM and use of calcium channel blocker showed a significant increase when compared with the DM0 group. However, there was no difference in the total absolute power between the people with T2DM and calcium channel blockers. This increase in power of the BF signals in individual with increase CVD risk denotes increase in the signal fluctuation which can be interpreted as enhanced physiological activity in these groups. The values of the normalised PSD contributions of the five frequency bands, showed an increase in the power of BF signals of the neurogenic band and a decrease in the power of the cardiac bands on the T2DM group compared to the DM0 groups. It was also shown that with T2DM, the endothelial band contribution increased, although not significantly. With calcium channel blocker use, the distribution of the normalised power over the five frequency bands changed significantly. There was a significant decrease in the LF neurogenic and myogenic bands and a significant increase in the normalised power of the cardiac band when compared to both DM0 and DM1 groups.

A recent study by Hsiu, et al. [17], investigating the LDF signals in the foot and hand between diabetic, prediabetic and healthy humans, showed an increased normalised power of the cardiac band in the diabetic subjects and a diminished normalised power in the LF bands of the BF signals from the foot when compared to healthy subjects. Although, they found no difference in the frequency bands of the BF signals from the upper extremity, suggesting that the microvascular blood flow at the measurements in the hand may be a less impaired. However, this study is contradictory with the study by Tigno, et al. [4] investigating the power spectra energy and complexity of BF signals from the forearm of nondiabetic, prediabetic and diabetic monkeys during increased local heating. They found a significant increase in the myogenic band and a decline in the cardiac band in the T2DM compared to the nondiabetic subjects. Even though this study was obtained in monkeys and the corresponding human myogenic band is still uncertain, they suggest that the microvascular BF of the diabetic groups is modulated by lower frequency mechanisms.

Here, most of the power in the LDF signals from the calcium channel blocker treatment group lay in the heart beat rather than the LF bands indicating higher pulse wave reflection [155]. Whereas, the relative power in the LF bands alone revealed an overall decrease which was

prominent in the myogenic band. As it was reported in a recent study on a different set of NAFLD volunteers [156], the reduction of the myogenic band in this group is expected due to the use of calcium channel blockers. However, Ticcinelli, et al. [157], recently investigated HRV, respiratory and LDF signals simultaneously from young, aged and aged treated hypertensive volunteers using wavelet power on the BF signals and found an increase in the myogenic activity in the aged treated hypertensive group, suggesting the ability of the system to adjust in the face of a pathological challenge. They also reported a decrease in the coupling within the myogenic band in the aged treated hypertensive group suggesting that antihypertensive treatment do not improve the microvascular blood flow. Therefore, more measures need to be recorded simultaneously for extracting paraments in time domain that can be used to understand the oscillatory fluctuations of the blood flux and their clinical applicability. In this current study, the investigation of the power spectral density of the microvascular blood flow reveal more functional information about the microvascular blood flow dynamics however, this is still not a definite method to describe the oscillatory activity of these signals and is insufficient to reliably distinguish between the groups and provide consistent interpretation of microvascular function [40].

5.5.3 Complexity Measures

To investigate the nonlinear complex dynamics of the skin blood flow signals from the NAFLD individuals, LZ complexity analysis has been found to be a useful tool in estimating the signal variability between different groups [141, 156]. Even though, the power spectral density contribution of the BF signals can provide useful information about the frequency components modulating the total BF, however, they cannot estimate the variability of the fluctuation in the BF signals over multiple time scales. Here, the information content was investigated, to assess the variability in flow motion activity in vascular beds at risk of CVD in multiple time scales and improve discrimination between groups.

There is no known evidence about the complexity of the blood flow in people with fatty liver disease. However, as reported from Farrell, et al. [12], there is a statistically significant reduction of the microvascular blood flow in fatty livers when compared with healthy livers. West [29], in a study about the fractal physiology that takes into consideration the complexity of the human body, suggested that the loss of the complexity can be a characteristic of disease. Another study [4], performing LZ complexity on LDF signals from monkeys (non-diabetic, pre-diabetic and diabetic) demonstrated a lower complexity on the diabetic monkeys than on the non and pre-diabetic ones. Additionally, Frisbee, et al. [120] in a study applied in lean and obese Zucker rats using network attractors to indicate the CVD risk, reported a reduction of the arterial bifurcation as the risk for vascular dysfunction increases which means that the system is more adaptive in lean rather than

the obese rats and that influences the ability to provide a more complex signal in obese rats. In this study, was shown that LZC was lower in the group with T2DM than in the group without, although this was not significant. However, the group with calcium channel blocker showed a statistically significant reduction in complexity when compared with both DM0 and DM1 groups. This reduction in the complexity in groups at CVD risk, suggests the loss of the system flexibility and adaptability in the face of a pathophysiological condition [156].

Previously [128, 141, 156], was found that traditional LZ complexity was unable to account the complexity for the high frequency components of the signals showing a low separation between groups and therefore the multiscale analysis was applied to overcome this problem. In a previous application of MLZC to BF and oxygenation signals recorded in forearm skin clamped at 33°C and during local thermal hyperaemia at 43°C [141], was found that classification accuracy between these two haemodynamic states of up to 90% could be achieved. It was also observed that as the scales increase and the sampling rate decreases, LZC of the BF signals increases up to a sampling rate close to Nyquist frequency (3.2 Hz) and then either increases or becomes constant, suggesting that this progression of the complexity in multiple time scale is indicative of the signal stationarity. Here, a more progressive increase in the complexity of the DM1 group than the DM0 and CB group was observed, until scale 12 at sampling rate 3.3 Hz (Figure 5.5). After this sampling frequency, BF signals for all groups are poorly sampled and therefore the periodicity is lost and thus, complexity is further increased.

Many studies have used multiscale analysis to investigate the relation of the temporal structures of the signals and for extending the accuracy of the complexity measures [76, 131], whereas others have used scaling to explore the dependencies with different oscillatory activities of the signals [123, 128, 158]. Here, increasing the scales above 24 which is close to the that corresponding to the heart rate of the BF time series, is possible that the signal will contains more information. Although, in order to reach higher scales, longer recordings are required however, as shown from previous studies [123, 141], there is a limit on the number of samples required for sufficient accuracy in the estimation of complexity.

In this study, there were observed different scales at which the maximum separation between groups occurred with DM0-CB at scale $\tau = 9$ and DM1-CB at $\tau = 12$ whereas, the weakest separation appeared at scale 1 which is the scale studied by the traditional LZC. This is in accordance with a recent study by Ibanez-Molina, et al. [158], using multiscale LZC on EEG from healthy people at eyes closed and open, showing that traditional LZC was not able to differentiate between these two groups. They reported that LZC was able to appear differences in their variations of the frequency oscillations between these conditions only in multiple time scales of the signals.

Linear discriminant analysis classifiers are good for dimensionality reduction, they are easy in terms of implementation and can be very quickly trained. The LDA technique has been broadly used from face and optical character recognition [159-162] to clinical applications [128, 131, 134] and therefore has been a very promising tool for discriminating different pathophysiological groups. Here, the LDA classifier was examined in order to separate the groups DM0- CB and DM1-CB based on the complexity analysis in 15 epochs and the multiscale complexity in 12 scales. Overall, the LDA using the 12 features of the multiscale complexity exhibits better performance however, that was significantly better for the groups DM0 and CB with a classification accuracy 89.2%. In this current study, by increasing the number of the DM1 and CB groups, a better separability between these groups was achieved using the 12 features of MLZC (74.3%), than using the 24 features as reported in a previous similar study (68%) [156]. From this test was shown that the characteristics of the multiscale analysis can be used in classification algorithms to separate between different data sets.

5.5.4 Association between Multi-Study Analysis

Microvascular blood flow signals are modulated by five frequency bands which appear to vary with increase CVD risk. From the literature, it is known that heart rate variability contribute to complexity of the BF signal [163] and cardiac rhythm is modulated by respiratory oscillation [164]. The coupling of the two HF components offers a possible partial explanation as how the MLZC for each group is associated with the HF bands and why LZC progressively increases with scale. Previous studies [76], reported that the irregularity is lower as the respiratory modulation of the heart rate is higher in amplitude indicating the high association of complexity with the frequency bands. Therefore, at larger time scales where the sampling frequency decreases and lower frequencies are associated with the variability of the microvascular perfusion, the times series are likely to be more complex than the time series at shorter time scales. Here, respiratory and cardiac activity of DM1 group showed strong but opposite correlation at higher time scales. The contribution of the cardiac modulated by respiratory activity seems to determine the cause of why LZC increases with time scales. The strong negative correlation of cardiac activity with LZC at higher scales result to higher complexity in DM1 group compared to CB group which is highly significant in larger time scales.

Here, the respiratory activity for the DM0 group shown a high positive correlation in many scales and myogenic activity showed to be negatively correlated with LZC over multiple time scale for the DM0 group, which is consistent with its low periodicity in multiple time scales. Furthermore, there was no significant association with frequency bands and MLZC in CB group. This absence of significant associations in CB group may be a useful indicator of a diminished flow motion variability at increased CVD risk, although, the reasons behind it remain to be fully elucidated. In a previous similar study [156], the association between the frequency bands and the complexity was evaluated

in the entire dataset of participants with NAFLD, showing higher but opposite association between the HF bands and complexity at shorter time scales although, no significant correlation was found with LF components and complexity until the longest scales.

Even though, both Spearman's rho and MI measure the nonlinear association between groups, the results of these metrics did not always show similar association between the spectral power across the frequency bands and MLZC. After testing the data for normality, it was shown that the datasets are not normally distributed and therefore both Spearman's and MI were used as a metric of the nonlinear correlation between the variables, however MI revealed a relationship between variables to a degree of independence. Here, MI showed that the respiratory was highly associated with the complexity of the DM0. The myogenic band was closely related to the complexity for the DM0 group particularly at higher scales. Furthermore, CB group showed a strong association between the HF cardiac band and LZC in higher scales, which may be related with its periodic nature. Although, there was no other significant association between frequency bands an MLZC was diminished for both DM1 and CB groups. As mentioned before this may an indicator of microvascular dysfunction in these groups.

Many researches have used the mutual information to estimate the association between or pair of variables in terms of the information of the joint distribution of expression values that variables hold [148, 149, 165-167]. Recently Zhuang, et al. [168], used the mutual information to compare the information content between the variables of the kinematics from two monkeys and their frequency bands, showing a high performance of connectivity in the higher frequency bands using this metric. Other studies [169], also suggest that the mutual information can be an effective tool for selecting the most characterizing feature of continuous and discrete datasets in order to reduce the classification error between clusters of classifiers such as linear discriminant analysis and support vector machine. In this study, the MI was applied in the NAFLD datasets to show the nonlinear dependencies between MLZC and frequency bands, although further work will need to be done in future studies in order to use this technique as a potential tool for feature selection in machine learning that can classify between different groups.

5.6 Limitations

The current work reveals novel understanding of the relationship between time, frequency, and complexity analysis of time series derived from the microvasculature in the presence of increasing CVD risk although, there are also a number of limitations associated with this study. The calcium channel blocker group contained people with and without T2DM and was of small size, n = 12. The group with T2DM were being treated which will have impacted upon the recorded BF

measurements. Though, it was shown that differences could be detected between these groups through a systematic analysis of the recorded time series. It has been previously reported that WT analysis may provide more useful information of the LF components and their variation over time [36]. The FFT, unlike the WT, cannot easily be time-localized so it was unable to explore this here. It is reasonable to assume from the data presented here that the range and limits of the frequency bands will differ between individuals and pathophysiological conditions.

5.7 Conclusions

In this multi-study analysis of time, frequency, complexity-based and multiscale-based methods, it was investigated whether these methods could be used to analyze skin BF measurements to discriminate between different groups of individuals at increased risk of CVD. The combination of time, frequency and complexity analysis yields deeper understanding of the loss of system flexibility which may prevent the microvascular networks from adapting to an imposed stressor and some of the parameters that influence this. Examining the information content of the BF signal revealed a clear and significant difference in LZ complexity between the groups with and without calcium channel blockers and that this becomes more pronounced at certain time scales. Use of calcium channel blockers for the treatment of hypertension, showed a substantial decrease in the dilator capacity of the blood vessels and a diminished LF activity estimated using the power spectral density, whereas, the HF cardiac activity showed a significant increase. Moreover, by examining the association of the individual spectral bands with the different time scales in MSLZ, the findings provide strong evidence that particularly in the nondiabetic group, the influence of these modulators on information content in the BF signal is strongly associated with the time scale, although this connectivity was not always visible with increased CVD risk. The results further show that multiscale analysis has strong potential for discriminating between these different groups. These findings suggest that the significant attenuation of the network's flexibility and adaptability with increasing CVD risk make these methods a promising approach for further analysis of microvascular function. Nonlinear measures offer promise in discriminating more effectively between these different mechanistic influences on network functionality and flexibility and now need to be extended to cohorts under further pathological conditions.

Chapter 6: Attractor Reconstruction Analysis for Blood Flow Signals

In this chapter, a mathematical approach is employed to reconstruct the microvascular blood flow (BF) signals as a form of an attractor. Attractor reconstruction analysis has been previously used to determine changes in the shape and variability of quasi periodic signals, such as arterial blood pressure and electroencephalogram signals, achieving a two-dimensional attractor and providing features such as density and symmetry. LD BF signals are quasi periodic and quasi-stationary so, the attractor reconstruction method was investigated to test whether this method could be applied in signals derived from the microvascular perfusion. The basis and the implementation of attractor reconstruction analysis of the microvascular blood flux signals is first described. The efficacy of the attractor reconstruction method as a potential method of identifying changes in the microvascular function is then evaluated in the groups of people considered previously in this thesis, in order to characterise the changes of a range of blood flow dynamics. Finally, a discussion of the strengths and limitations of this method is presented.

6.1 Introduction to the attractor reconstruction

Microvascular blood flux signals have been quantified using both linear and nonlinear approaches. Previously, the time-dependent behaviour of microvascular blood flux [156] and tissue oxygenation [40, 141], was investigated using time series, power spectral density and complexity showing differences in both frequency composition and information content of the signals between various groups (as mentioned above). As mentioned in the previous chapters, time and frequency analysis have provided only limited interpretation of the microvascular function. It is known that the existence of nonlinearity in microvascular systems contain complex irregularities in the signals that can be more rigorously quantified using complexity analysis [45]. Previous studies [170, 171] have shown that “complex systems are neither completely regular nor completely random” and only few complexity measures can obtain valid values for both random and regular systems. A formal way of characterising the nature of a biological time series is by reconstructing the signals forming an attractor and studying the dynamics of the corresponding phase space trajectories so that the changes of the signals can be a related to the changes in the reconstructed attractor [31, 33, 172].

Attractor reconstruction was first introduced by Takens [173] establishing the delay embedding theorem also known as Taken’s theorem, and later developed by Sauer, et al. [34] putting this

method on a mathematical basis. They showed that providing any time delay τ and a dimension $d \geq 2$, then almost all delayed reconstruction states will be preserved from the original time series. Casdagli, et al. [174], also reported that the past and future characteristics of the time series hold information about the values that can be used to determine the time series in present time. Attractor reconstruction has been previously applied to various physiological data including blood pressure [172, 175, 176], plethysmographic [177], electroencephalographic (EEG) [178] and blood flow signals [44, 179-181]. The main reason of this progress is that the "strange" attractors reconstructed from the times series, using a suitable time delay and embedding dimension, contain properties that can be used to define the dynamics of the system and provide a visual representation of the system's stability [33].

The properties of the reconstructed attractor have been broadly quantified using nonlinear approaches, such as the Lyapunov exponent and correlation dimension [38, 44, 124, 163, 178, 179, 182-186]. These approaches examine how phase space trajectories changes into chaotic or stable systems over time and measure the shape of the attractor in phase space, respectively. However, these methods do not provide a visual representation of the time series shape and variability, are noise sensitive and usually are very much dependent on the parameters chosen for accurate estimation [31, 33, 187]. Recently, a new approach was introduced by Aston, et al. [172], attractor reconstruction (AR) method, which quantifies the changes in the morphology and variability of a quasi-periodic signal without affecting the signal information providing a two-dimensional colour scaled representation of the signal producing features like density and symmetry. These authors have applied AR analysis to arterial blood pressure (ABP) [172, 175, 188, 189], photoplethysmogram (PPG) [189] and electrocardiogram (ECG) signals [190], captured from animals and humans in a range of conditions and have shown to identify changes in the shape and variability of the cardiovascular waveform.

The main aim of this chapter is to test the hypothesis that the attractor reconstruction method can be used in the characterisation of the flexibility of the microvascular network. The changes of the microcirculatory dynamics using AR method are explored, to understand the applicability of this mathematical approach and its efficacy in discriminating between different groups.

6.2 Methodology

6.2.1 Conventional Methods for Attractor Reconstruction and Quantification

6.2.1.1 Phase space reconstruction

The space phase construction of a nonlinear signal has been previously applied to describe the multidimensional dynamics contained within that system [31, 33, 187]. The mathematical technique for the construction of an attractor relies on delayed space embedding and the basis is the delayed embedding theorem by Takens [173]. The phase space of a time series with N data, $x_n, n = 1, 2, \dots N$, is constructed in m-dimensions with τ time delay, as follows [31, 33]:

$$y_i = x_i, x_{i+\tau}, \dots, x_{i+(m-2)\tau}, x_{i+(m-1)\tau}, \text{ where } i = 1, 2, \dots, M \text{ and } M = N - (m-1)\tau \quad (6.1)$$

with M being less than N but covers the same properties of the original time series.

The appropriate choice of the parameters for the attractor reconstruction have concerned many studies over the last few decades. According to Takens [173], in theory the time delay, τ, is irrational, however, in reality it can be ideally estimated. Sauer, et al. [34] in a paper entitled "Embedology", suggested that time delay should be lower than the period of the signal, so that values of τ that are contained within one period will be correlated. A good choice for the estimation of the time delay is either the autocorrelation function (ACF) or the average mutual information function (AMIF). Both these approaches estimate the relationship of a time series with its delayed version. The important difference between these approaches is that ACF measure the linear correlation however, AMIF estimate the information loss of the delayed time series knowing the original one which indicates that AMIF is a nonlinear function. Both these functions have their maximum values when time delay is zero however, for ACF the delay, τ, is estimated when the correlation with its neighbouring values falls to zero and for AMIF the ideal τ is evaluated when the information between present and future values reaches its first relative minimum. An alternative technique for estimating time delay, τ as well as embedding dimension, m, introduced by Rosenstein, et al. [191], is by calculating the average displacement between data points of the attractor of the system using the following formula: $S_m(\tau) = \frac{1}{M}\sum_{i=1}^{M}\sqrt{\sum_{j=0}^{m-1}(x_{i+j\cdot\tau} - x_i)^2}$, where x_i is the data set and $M = N - (m-1)\tau$. The average displacement, $S_m(\tau)$, of the points of the attractor is plotted against the time delay and τ is observed when at the first decrease of less than 40% of its initial point occurs before it reaches a plateau. Although, as stated by the authors, the selection of the time delay can be often arbitrary as there may be unknown error such that the effect of noise in the system influences estimation of the correct optimal time delay.

The embedded parameters for a time series reconstruction have been also widely investigated [173, 192, 193]. Takens [173], from the embedding theorem, suggested that assuming an attractor with fractal dimensions D, then the embedding dimension for attractor reconstruction should be $m \geq 2D + 1$. Although, this theorem suggests that τ is arbitrarily chosen and in order to define m, one has to already know the attractor dimension D, which is not always the case. A well-known

approach investigating the proper time delay and embedding dimension for attractor reconstruction presented by Liebert, et al. [193], suggests that the points of a time series between present and delayed neighbours, when the embedding dimension is increased may become more distant points. This is method has been extensively used previously [193-197], and is known as the false nearest neighbour (FNN) and that is because the neighbours that remain near within sufficient embedding dimensions, m, are true and therefore m is chosen when the average number of FNN is minimized. Another technique for estimating the embedding dimension, proposed by Jackson [198], is singular-value decomposition (SVD) which is an optimal algebraic transformation that decomposes the matrix into its constituent matrices. SVD has been previously [199, 200] used to isolate the signals contained in the delayed signal and estimate the dimensional values.

The attractor reconstruction has been previously applied to chaotic systems, such as Lorenz attractors and logistic maps [192, 201-203], and has been shown to identify the structure of the trajectory when plotted in the phase space. When a reconstructed attractor is created using the optimal embedding parameters the characteristics in phase space are quantified using mathematical approaches, such as largest Lyapunov exponent, correlation dimension or entropy [177-179, 184] considered next.

6.2.1.2 Largest Lyapunov Exponent

The changes of the phase space trajectories can be used to interpret the changes of the time series [33]. A widely used approach to quantify these changes is the Lyapunov exponent ($\boldsymbol{\lambda}$) which is used to determine the average divergence of the nearest neighbours in phase space trajectories starting from their initial positions [187, 204, 205]. Mathematically, after reconstructing the phase space, y_i of $i = 1,2, \dots, M$ points where, $M = N - (m-1)\tau$, from the time series $x_n, n = 1,2, \dots N$ in an m-dimensions with τ time delay, define the initial distance from y_i and its j^{th} nearest neighbour y_j, $dist_j(0) = \underset{y_j}{min}\|y_i - y_j\|$, where, ||…|| denotes the Euclidean distance and $|i - j| >$ mean period of the time series. Then the distance between y_i and y_j with k-steps is $dist_j(i) = \|y_{i+k} - y_{j+k}\|$. The Lyapunov exponent can be then determined as [33, 204, 205]:

$$\lambda(i) = \frac{1}{k \cdot \Delta t} \frac{1}{(M-k)} \sum_{j=1}^{M-k} ln \frac{dist_j(i)}{dist_j(0)}, \tag{6.2}$$

and $dist_j(i)$ is then approximately related with λ as, $dist_j(i) = C_j e^{\lambda(k \cdot \Delta t)}$, where C_j is the initial separation and Δt is the sampling period of the signal. The largest Lyapunov exponent is then calculated using the least-square fit of the mean $\ln \mathrm{dist_j(i)}$ over all j as $\lambda(i) = \frac{1}{\Delta t} \langle ln\, dist_j(i) \rangle$, by estimating the slope of the linear parts.

The nature of the system can then be interpreted from the linear plot of the natural logarithm of the divergence over the data points of the system. A positive value of λ indicates that the trajectories in phase space diverge and therefore the system is more likely to be chaotic. On the contrary, an exponential convergence in the system and therefore a negative λ indicates that the system is more stable. If the plot does not show any linear parts, then the system may be dominated by noise and its determination inaccurate.

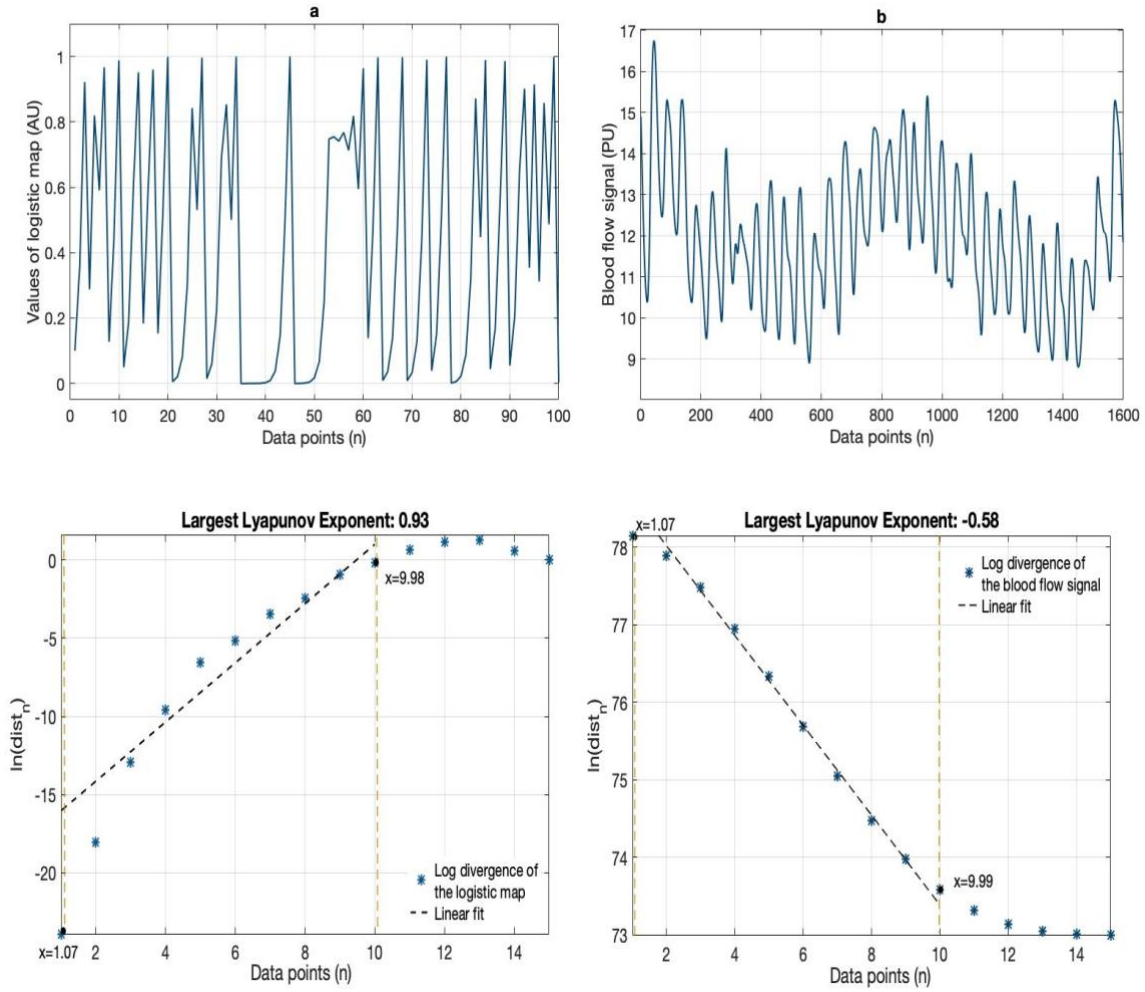

Figure 6.1 An estimation of the Lyapunov exponent based on the linear fit for a) a logistic map and b) a baseline blood flow signal at room temperature. The slope for the logistic map shows a divergence whereas the slope for the blood flow signal shows a convergence.

An interpretive example of the estimation of the Lyapunov exponent based on the slope of the natural logarithm of the divergence for a $\mathrm{n} = 100$ data point logistic map $\mathrm{x_n} = \mathrm{rx_n}(1 - \mathrm{x_n})$ with growth parameter $\mathrm{r} = 4$ is shown in Figure 6.1a and the convergence for a 40-second blood flow signal at room temperature ($\mathrm{n} = 1600$ data point) is shown in Figure 6.1b. As expected, the logistic map appeared to show an exponential divergence indicating the system to be more chaotic, whereas for the blood flow signal there was an exponential convergence indicating more regularity in the system. However, the range of the linear fit is arbitrarily chosen and from Figure 1a one can

see that the range of the linear fit is not very close to the data points and therefore a shorter range should be chosen to accurately determine the nature of the system.

Although, according to the literature [31, 33], a large range makes it difficult to determine accurately the Lyapunov exponent and small range shows a great similarity with their neighbour points before diverging, indicating a major limitation of this technique.

6.2.1.3 Correlation Dimension

Previously, the Lyapunov exponent has been described as an approach to quantify the similar changes in the trajectories of nonlinear systems. Here, a different approach, introduced by Grassberger and Procaccia [201], which characterises the shape of the phase space attractors, is discussed. Before measuring the correlation dimension, it is first necessary to calculate the correlation integral [31, 33, 201].The correlation integral measures the number of points that are correlated within a radius r around the points of the reconstructed attractor y_i of $i = 1,2, \dots, M$ points, from the time series $x_n, n = 1,2, \dots N$ in an m-dimension with time delay τ, and is defined as follows [201]:

$$C(r,m) = \frac{1}{M(M-1)} \sum_{i=1}^{M} \sum_{j=i+1}^{M} \Theta\left(r - \left\|x_i - x_j\right\|\right), \qquad M = N - (m-1)\tau \tag{6.3}$$

where, Θ is a unit step discontinuous function whose values are zero for negative arguments and 1 for positive, $x > 0$. The distance $\left\|x_i - x_j\right\|$ denotes the Euclidean distance between the neighbour points.

Grassberger and Procaccia [201] showed that the correlation dimension can be defined from the slope of the natural logarithm of the correlation integral, $C(r,m)$, against the natural logarithm of the radius, r, as:

$$D_c = \lim_{r \to \infty} \lim_{M \to \infty} \frac{d \ln C(r,m)}{d \ln r} . \tag{6.4}$$

The correlation dimension estimates the dimensionality of the reconstructed attractor investigating the self-similar properties of the system indicating that an attractor is chaotic when its fractal structure remains unchanged in multiple length scales.

6.2.2 Surrogate Data Analysis Test for Nonlinearity

In chapters 4 and 5, it has been mentioned that complex signals are not always the product of nonlinear systems, although if a signal appeared to be complicated then there is a good chance that it comes from a nonlinear system. Therefore, before applying any analysis on the data, it is

necessary to test them for nonlinearity. A simple though robust method introduced by Theiler, et al. [206], to check the nonlinearity of a time series is the surrogate data analysis. In this method the surrogate data are produced by randomising the phase of the original data, creating new data with the same means, variance, ACF and spectral power as the original, although the phase relations are different. The surrogate data are then compared with the original. If the original signal shows different results from the surrogate one, it contains nonlinearity, otherwise the original signal is linear [206, 207].

The procedure to produce the surrogate representation of a signal is described below as follows:

- The time series $x(t)$ is first, transformed into the frequency domain using the Fourier transform, achieving a value of $F(f) = \mathcal{F}\{x(t)\} = \int_{-\infty}^{\infty} x(t) \cdot e^{-j2\pi ft} dt$.
- At this point the magnitude $A(f) = \|F(x)\|$ and the phase θ of the signal still remains the same. Then, all the information of the phase for frequencies higher than the half of sampling frequency, is removed and the values of the low-frequency phase are used in random order to generate a new phase $\theta'(f)$.
- Next, a new Fourier transform $F'(f)$ is constructed by multiplying the magnitude with the Euler's complex for the new phase, $F'(f) = A(f) \cdot e^{-i|\theta(f)+\theta'(f)|}$.
- The surrogate signal $y(t)$ is achieved by taking the inverse Fourier transform ($\mathcal{F}^{-1}$) of $F'(f)$ such as, $y(t) = \mathcal{F}^{-1}\{F'(f) \cdot e^{i\theta'(f)}\}$.

The surrogate data analysis investigates whether the physiological data contain nonlinear features by comparing the nonlinear properties between the original blood flow signals and their surrogates. If a significant difference is observed in the index of the complexity measures, that will indicate that the blood flow signals are significantly different from being completely random data [208].

6.2.3 Symmetric Projection Attractor Reconstruction (SPAR) Analysis

The embedding theorem for the attractor reconstruction of continuous time series, has been widely applied to many types of physiological data such as heart rate [38], plethysmography [177], EEG [178] and blood flow signals [44, 179]. Even though this theory provides a visual representation of the multidimensional dynamics of a time series, a two-dimensional attractor has been used extensively to characterize the dynamic changes of biomedical signals [172, 175, 188, 189]. Attractor reconstruction (AR) analysis was first introduced by Aston, et al. [188], to determine the changes in the variability of heart rate in arterial blood pressure and ECG signals. The main aim of

this analysis is to perform and assess the variability of a quasi-periodic signal as a form of an attractor. The steps of the AR analysis are summarized below.

6.2.3.1 Attractor Reconstruction and Baseline Variation Removal

First, the signals are reconstructed using the embedding theorem [173] in three-dimensional space. With the time delay, τ, and embedding dimension $m = 3$, if the time series is $x(t)$ of a 40-second blood flow signal, as shown in Figure 6.2a, the two additional variables will be:

$$y(t) = x(t - \tau) \text{ and } z(t) = x(t - 2\tau). \tag{6.5}$$

As illustrated in Figure 6.2b and 6.2c, the reconstructed phase space of the signal can be now plotted in the (x, y, z) axis. Note that the past, present and future points in phase space correspond to the delayed time series.

Laser Doppler flowmetry data measures define the variation in blood flow in the body which occurs per unit time. As mentioned in Chapter 2, LDF signals consist of rhythmic oscillations which contribute to the total blood flow motion. In long recordings these oscillations are indistinguishable and the only information that is clearly seen is an often aperiodic signal which is drifting after few cycles due to variation in temperature. This indicates that blood flow signals fluctuate overtime and therefore are non-stationary. The removal of the baseline drift or variation has been prominent in many studies especially on ECG and PPG measurements [209-211].

A different technique for the removal of the baseline variation of the time series has been previously suggested [172], which projects the attractor in two-dimensional phase space, referred as phase plane perpendicular to the vector $(1, 1, 1)$, indicating that $\big(x(t), y(t), z(t)\big) \rightarrow (x(t) + c, y(t) + c, z(t) + c) = \big(x(t), y(t), z(t)\big) + c(1,1,1)$ for some $c \in \mathcal{R}$. In this way the reconstructed attractor is shifted by eliminating the vertical wander as well as the maxima and minima of the magnitude of the time series. The line with the direction of the vector $(1, 1, 1)$, which passes through the original attractor is referred as the central axis. From the central axis a unit vector is defined as, $v_1 = (1, 1, 1)^T/\sqrt{3}$ and the remaining two vectors are formed orthogonally from v_1 and defined as, $v_2 = (1, 1, -2)^T/\sqrt{6}$ and $v_3 = (1, -1, 0)^T/\sqrt{2}$, where T is denoted as the transpose of the matrix. Then, defining the matrix X as $\mathrm{X} = (\mathrm{x}, \mathrm{y}, \mathrm{z})^{\mathrm{T}}$ and a matrix $M = (v_1, v_2, v_3)$, then a new matrix is formed as $\mathrm{U} = \mathrm{M}^{\mathrm{T}}\,\mathrm{X}$, where $U = (u, v, w)^T$ and therefore the three new variables u, v and w will be:

$$u = v_1^T\, X = \frac{1}{\sqrt{3}}(x + y + z)\,,\ v = v_2^T\, X = \frac{1}{\sqrt{6}}(x + y - 2z) \text{ and } w = v_3^T\, X = \frac{1}{\sqrt{2}}\,(x - y). \tag{6.6}$$

The u, v and w trajectories derived from a 40-second blood flow signal can be seen in Figure 6.2d. It can be observed that the u variable illustrates the low-frequency variation of the signal, whereas the v and w variables are more stable than the original blood flow signal.

The name of this analysis has changed from the authors to Symmetric Projection Attractor Reconstruction (SPAR) analysis (M. Nandi, personal communication). Here, this term will be used as it reflects to the perpendicular projection of the reconstruction attractor described above.

6.2.3.2 Time Delay Selection

A simple way for estimating the periodicity of a time series is by using the Fourier transform and finding the more dominant frequencies. Although, the peaks in the frequencies from physiological signals often can be very wide and that makes it difficult to identify the exact largest frequency (~0.6-1.6Hz) [212].

As mentioned above, a well-known approach for the estimation of the time delay is either the ACF or the AMIF, that were defined before. Here ACF for a time series $x_n, n = 1,2, \dots N$, with $\bar{x}$ being the mean of the time series, then the time delay, τ, will be defined as: $ACF(\tau) = \frac{1}{N}\sum_{n=1}^{N-\tau}(x_n - \bar{x})\,(x_{n+\tau} - \bar{x})$. And the AMIF with probabilities $p(x_n)$ can be expressed as: $AMIF(\tau) = \sum_{x_n \epsilon X}\sum_{x_{n+\tau}\epsilon X} p(x_n, x_{n+\tau})\, log_2(\frac{p(x_n, x_{n+\tau})}{p(x_n)\cdot p(x_{n+\tau})})$. ACF describes the correlation of signal with its delayed self, whereas AMIF describes the information of the neighbouring values within the signal. In this study, AMIF is used where the first local minimum of the function is considered to be the average time delay, τ, and the highest local maximum is the average period, T, of the signal.

From previous studies [172], it has been shown that for any periodic signal, in order to achieve an attractor as stable as possible, the ideal time delay will be either $\tau = T/3$ or $\tau = 2\,T/3$. Blood flow signals consist of multiple frequency components (0.0095~1.6Hz) [36, 39], therefore, if the blood flow signal is dominated by the high frequency heart rate component (~0.6-1.6Hz), then assumingly that one cycle length oscillates around 1 second, the time delay will be $\tau = 1/3 \sim 0.33$ seconds. The two-dimensional plane (v, w) in Figure 6.2f will be defined as periodic, with period T when a symmetric equilateral triangular shape is observed.

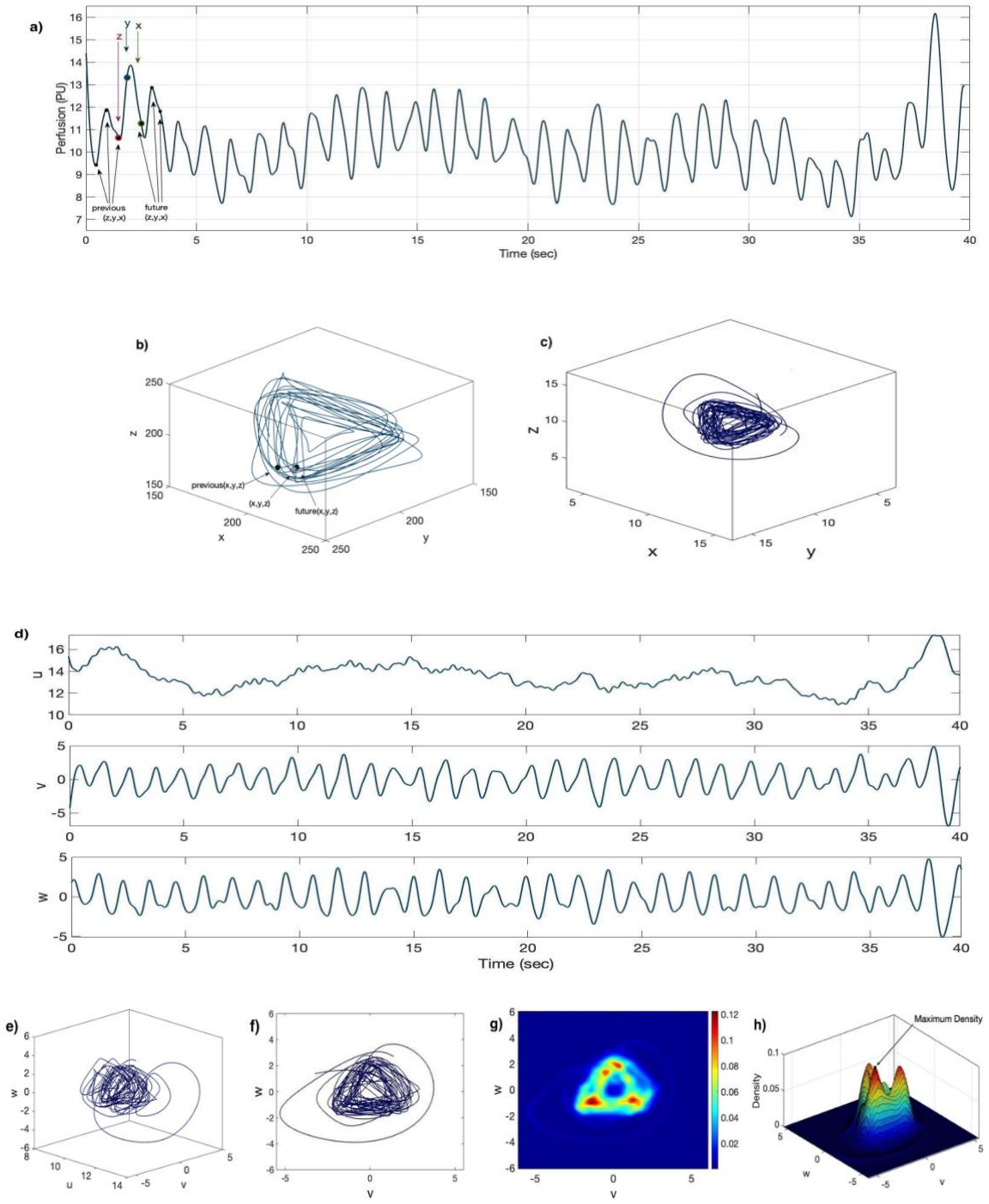

Figure 6.2. a) A 40-second skin blood flow signal from a healthy volunteer at baseline. b) The three-dimensional reconstructed attractor for the first 20-second of the BF signal to show the past, present and future points of the signal. c) The three-dimensional reconstructed attractor for 40-seconds of the BF signal. d) The u, v and w variables derived from the three-dimensional attractor shown in Figure 2c projected perpendicular to the vector $(1,1,1)$. e) The projection of the reconstructed attractor plotted on (u,v,w) variables. f) The attractor shown in Figure 6.2e projected onto the (v,w) plane. g) The density produced from the attractor in Figure 2f. h) 3-D representation of density and the (v,w) plane and the selection of maximal density.

6.2.3.3 Density generation and attractor measures

To better understand the morphology of the attractor referring to the shape and variability of the time series, the density, $D(\tau)$ is generated providing information based on the thickness or thinness of the attractor indicating the most frequent or infrequent overlap of the region. The density, $D(\tau)$, is obtained from the square grid of boxes in the plane (v, w) as shown in Figure 2g, with time delay, τ. Then the data are rotated in $2\pi/3$ and $4\pi/3$ to achieve $D_2(\tau)$ and $\mathrm{D}_3(\tau)$, respectively. The average density function will then be: $D_s(\tau) = (D(\tau) + D_2(\tau) + D_3(\tau))/3$. Here, it is also noted that $D_s(\tau)$ consists of the average of the three sides of the density $D(\tau)$ and therefore, if the attractor is symmetric then, $D_s(\tau) = D(\tau)$.

The density was calculated using a probability density estimate dependent on a normal kernel smoothing function [213]. The function of the kernel density estimation is expressed as: $\hat{f}(x) = \frac{1}{nh}\sum_{i=1}^{n} K\left(\frac{x-X_i}{h}\right)$, where n is the number of data points of time series x, X_i is a matrix of equal spaced points, K is the kernel smoothing function and h is the bandwidth of the kernel smoothing window optimised using the least-square cross validation approach with Gaussian kernels explained in [213]. Then, the density was generated on square grid of boxes and the volume of the density is normalised to one. An illustrative example of the density generated from the attractor in the (v, w) plane from a sine wave signal, $x(t) = 1 + (1/2) * (1 + sin(2\pi t))$, with $\tau = 0.3s$, is shown in Figure 6.3. Note that the sine wave shape of the signal, here, corresponds to the counterintuitive circular shape of the attractor. Here, the maximum density, $\mathrm{D}(\tau)$, will be considered as an attractor measure (Figure 6.2h).

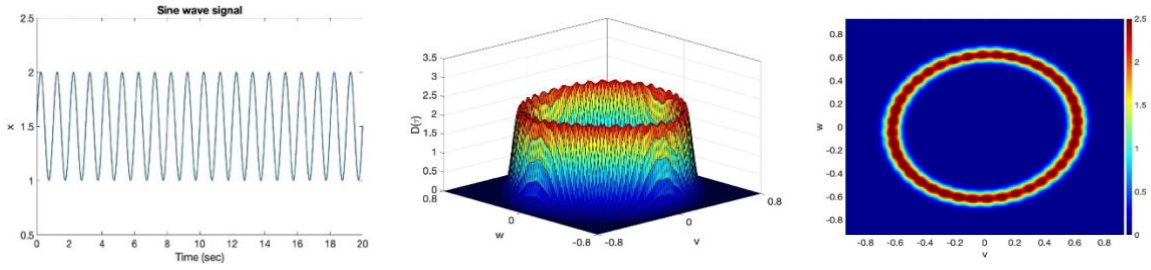

Figure 6.3 a) Sine wave signal and the corresponding density of the attractor in the (v, w) plane.

The morphology of the signal may change over time corresponding to variations of the shape and symmetry of the attractor and thus, it is essential to obtain a measure of quality and reliability of the attractor [172]. First, the radius of the circular orbit centred at $(0, 0)$ is calculated using the formula $r = \frac{\sqrt{3}h}{2\sqrt{2}}$, where here h denotes the amplitude of the signal (Figure 4). The polar angles, θ of the attractor over a radius are also calculated so the $sec\ \theta$ will be the division of the bottom side of the equilateral triangle from the centre over the adjoining side and will be defined as the mean of these angles. Then, the mean difference between these angles is defined as angular spread, $\theta_s =$

$\overline{[\theta_2 - \theta_1,\ \theta_3 - \theta_2]}$ where a value close to 0 indicate that the attractor is close to being symmetric. As shown previously in [189], in a study in ABP and PPG signals, the values of θ_s greater than $0.425\text{rad} \approx 24.4°$, indicate an unreliable attractor. In blood flow signals, the angular spread did not reach the limit of that suggested in the literature, as the BF signals differ from ABP or PPG signals thus, the values for the estimation of the angular spread, to define a reliable attractor were chosen when θ_s values were close to 0.

Additionally, the angle of rotation, θ_r, is defined to capture the fluctuating motion of the signal which corresponds to a clockwise rotation of the equilateral triangle in the (v, w) plane as indicated in Figure 6.4. As suggested in [172], applying the equation (6.6) in a signal $x(t)$, then, the edge of the triangle in the (v, w) plane, for $\tau = 1/3$, is $w = -\frac{h}{2\sqrt{2}},\ v\,\epsilon \left[-\frac{\sqrt{3}h}{2\sqrt{2}}, \frac{\sqrt{3}h}{2\sqrt{2}}\right]$ and therefore, the optimal angle of rotation is defined by the maximum value of the signal amplitude h and is given from the base of the triangle as $w = -\frac{h}{2\sqrt{2}} \cdot sec\,\theta_r, \theta_r\,\epsilon\,(0, \pi/2]$. The fact that the triangular shape of the signal results in the triangular shape of the attractor is not deliberate. As it is explained in [172], considering that the time delay is $\tau = T/3, T$ being the cycle of a periodic signal, then the resulting attractor will be an almost three-fold symmetric attractor in the (v, w) plane.

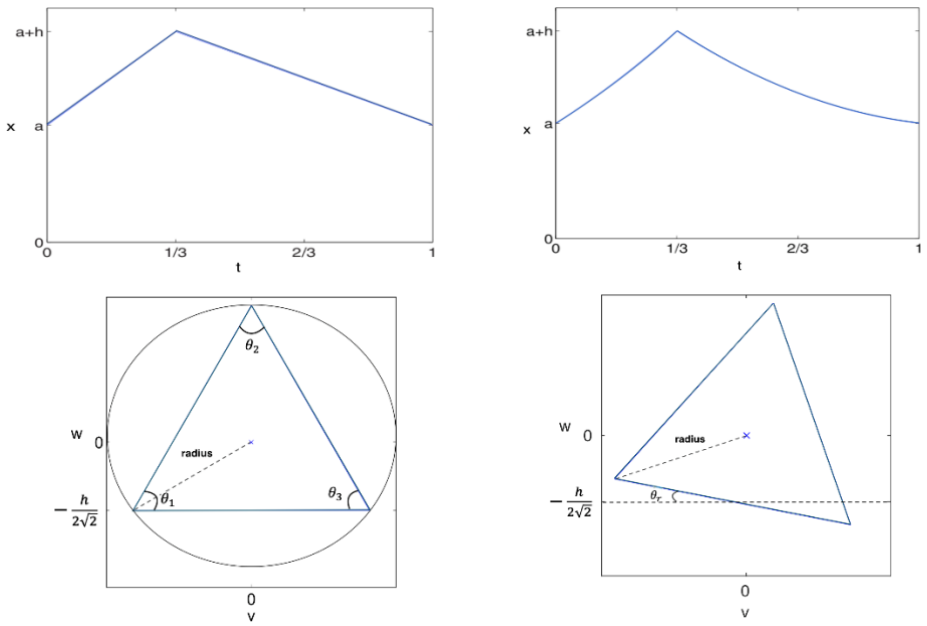

Figure 6.4 An illustration of an equilateral triangle in the (v, w) plane derived from linear periodic signal (left plots) indicating the radius and the polar angles and a clockwise rotated triangle derived from quadratic periodic signal with angle of rotation, θ_r (right). Figures reproduced from [172] (Open access journal).

6.3 Pre-processing and Analysis Procedure

BF signals are quasi periodic and quasi-stationary signals to which the attractor reconstruction analysis method can be applied. However, before performing this analysis, the data were filtered with a low pass finite impulse response (FIR) filter with 2 Hz cut-off frequency, to attenuate high frequencies beyond the known range of microvascular oscillation, 0.0095 - 1.6Hz [36].

In this study, the blood flow signals were divided into windows of 40 seconds each to provide sufficient cycles per window and sufficient data points. First, the SPAR method was tested on a 65-minutes blood flow signal of one healthy individual at resting skin temperature (20 minutes), then the heating block clamped at 33℃ (20 minutes), during transition from 33℃ to 43℃ (∼50 seconds) and at 43℃ (∼25 minutes). Then, to better interpret the two haemodynamic steady states, the BF signals recorded from entire dataset (n=15) where cut into 10-minute artefact-free segments at both 33℃ and 43℃ and SPAR was applied in each 40-second window. Similarly, the SPAR method was applied on each 40-second window of 10-minute blood flow recordings at rest from all 60 participants with NAFLD grouped with (DM1) and without T2DM (DM0), and use of calcium channel blocker medication (CB) with and without T2DM (nine with T2DM).

6.4 Statistical Analysis

Statistical analysis was performed using IBM SPSS Statistics 25 (IBM United Kingdom Limited, UK). Data were tested for normal distribution using D'Agostino & Pearson omnibus normality test and presented as either mean ± standard mean error (SEM) for normally distributed data or median with interquartile range (IQR) for non-normally distributed data. Normally distributed data were compared using a Student t-test and non-normally distributed data using a Mann-Whitney test. In all cases a value of $p < 0.05$ was taken to indicate statistical significance. Spearman's rho correlations are presented for monotonic nonlinear correlation analysis of baseline data. The kurtosis was also computed for each segment of the signals using Matlab's Statistic and Machine Learning Toolbox (R2019a, Mathworks, UK), to characterize the shape and symmetry of the segment's distribution. High values of kurtosis indicate that the data values are more peaked whereas, lower values indicate that there are less outliers in the data [214].

6.5 Classification Analysis

A binary support vector machine (SVM) classifier with leave-one-out (LOO) cross-validation was applied on the 15 non-overlapping epochs of 40-second recordings from the participants in each study to determine the classification accuracy between the groups. Previously, the linear

discriminant analysis has been used, for the data classification, however this method performs linear classification and its performance may reduce when applied in big data set. The SVM method, applied here, defines boundaries that maximise the distance between the closest to the boundary points of the two classes, also known as support vectors which are more indicative of potential errors [150]. The accuracy is assessed using the LOO cross-validation in which here 30 runs are used, and in each run the classifier trained the set apart from one sample which was presented as the test set. The resulting classification accuracy is the average of the runs.

From the confusion matrix of the SVM classifier for two classes under consideration, the sensitivity and specificity were also calculated. They are referred as the true positive of the SPAR features derived from the signals identified as features of one class and as a true negative rate of the SPAR features derived from the signals that are being identifies as features from the other class, respectively. The features of the SPAR analysis for BF signals at all studies were selected from the density, the shape and morphology of the attractors, however the feature selection might differ in each study due to the risk of selecting "bad" features, as explained in [215]. These features were then combined with the complexity measures, defined in the previous chapters and tested whether this combination will provide a better classification accuracy between the groups.

6.6 Results

The results from the surrogate analysis on the healthy group in two haemodynamic states showed a significant difference in the nonlinear index of largest Lyapunov exponent (LLE) and correlation dimension (CD) indicating that the blood flow signals contain nonlinear properties. It can be also noted that the estimates of LLE showed a significant decrease in the nonlinear properties of BF signals during LTH, being from positive at 43℃, to negative values at 43℃, whereas CD showed an increase during local warming.

The maximum density derived from the SPAR analysis showed a significant reduction in the blood flow signals ($p < 0.05$) during vasodilation due to LTH. Additionally, the study of individuals with NAFLD showed a significant decrease in the density measures of SPAR of the blood flux signals as the CVD risk increases becoming highly significant in the calcium channel blocker group.

6.6.1 SPAR Analysis of BF Signals between two Haemodynamic Steady States

The largest Lyapunov exponent and correlation dimension have been extensively used to characterise the nonlinear properties of the microvascular function [124, 179]. These techniques have been successfully used to validate data as nonlinear signals through surrogate analysis showing significant differences between the original and surrogate signals at 43℃ for LLE and CD,

as shown in Table 6.1. The estimates of LLE for the original blood flow signals show a substantial decrease during local warming with values from positive, 0.338 ± 0.196 at 33℃ to negative values, -0.807± 0.106 at 43℃, mean ± SEM, indicating a more periodic attractor during LTH. Although, the nonlinear index of CD is not consistent with that from nonlinear methods used previously, as it shows a significant increase from 2.804 ± 0.019 (at 33℃) to 2.957 ± 0.046 (at 43℃), mean ± SEM.

Table 6.1 Estimates of largest Lyapunov exponent (LLE) and correlation dimension (CD) of 10-minute blood flow signals at 33℃ and at 43℃ (n=15), and their significant difference between the original and 20 surrogate signals. Values are presented as mean ± SEM.

	33℃		**p-value**	**43**℃		**p-value**
	Original	**Surrogate**		**Original**	**Surrogate**	
LLE	0.338 ± 0.196	5.073 ± 0.024	<0.05	-0.807± 0.106*	2.535 ± 0.116*	<0.05
CD	2.804 ± 0.019	2.883 ± 0.001	0.028	2.957 ± 0.046*	2.972 ± 0.006*	0.075

*Significant difference from 33℃, $p < 0.05$.

Even though LLE and CD can be used to provide information about the nonlinear dynamics of a time series, the main aim of this study is to use the measures from the reconstructed attractor and provide information regarding the changes of the microvascular dynamics. Figure 6.5 shows the BF signal variability recorded from one individual, randomly selecting a window during a steady state at 33℃, during transition and during a steady state at 43℃, that illustrate the changes in different haemodynamic states. The windows of the blood flow signals in Figure 6.5a shows the segments from the signal in Figure 6.5b corresponding to the attractors in Figure 6.5c. The window of the BF signal at 33℃ is shown to be dense with many overlaps. The window at the transition time illustrates the BF signal during the last 40 seconds of the transition, showing the increase of the signal amplitude and therefore the attractor becomes wider and less dense. Similarly, the window at 43℃ shows the BF signal at 43℃ corresponding to larger attractor as the amplitude of the signals is increased. Here, the attractor was blurred, indicating a lower density. Note that the numbers in the colour bar for each attractor change indicating the change in density.

Table 6.2 illustrates the statistical analysis for all features of SPAR analysis and the classification accuracy of the SVM classifier to classify the blood flow signals from the overall dataset (n=15) between the two haemodynamic states using all the features of SPAR analysis. The time delay appeared to be approximately a third of a heart rate cycle in both haemodynamic states. The maximum density measure showed a significant decrease for signals at 43℃, from 0.116 (0.111) at 33℃ to $4.5 \cdot 10^{-4}$ ($5 \cdot 10^{-4}$) at 43℃, median (IQR).The angular spread values for both signal where close to 0 indicating a symmetric attractor at both temperatures. The angle of rotation also

exhibited significant differences between the states ($p < 0.05$), indicating that there was more fluctuation in the signals at 33℃. The radius of the attractor is proportional to the amplitude of the blood flow signal and therefore, it showed a significant increase during local warming ($p < 0.05$). Additionally, kurtosis of the distribution for the signals at 33℃ was substantially higher compared to the ones at 43℃ with values of 3.180 (0.730) at 33℃ and 2.498 (0.233) at 43℃, (median(IQR)) ($p < 0.05$), indicating that the signals during increased local warming become more stable.

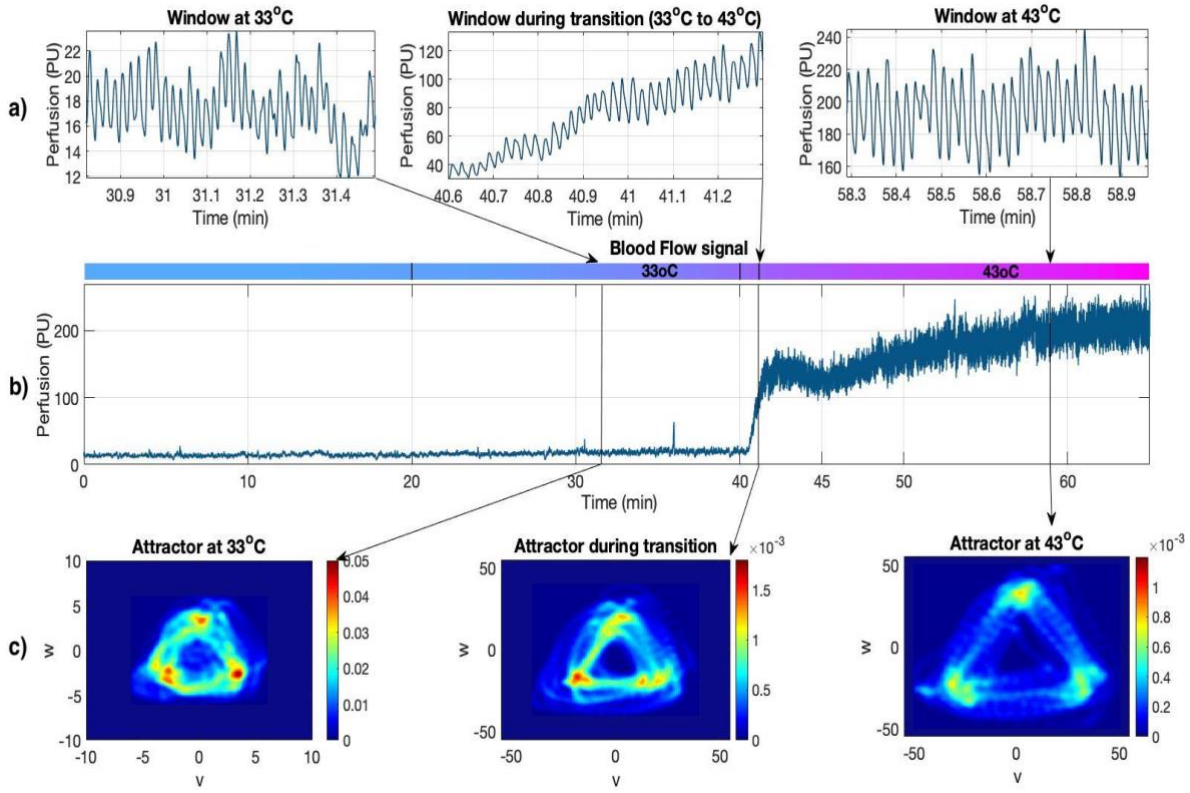

Figure 6.5 a) Windows of 40 seconds derived from the blood flow signal at 33 ℃, during transition time and at 43 ℃. b) A blood flow signal of one healthy volunteer at 33℃ and during local warming at 43℃. Lines indicate the end of each window. c) The reconstructed attractors for each of these windows. Angle of rotation for window at 33℃: 42.58°, during transition time: 16.76° and at 43℃: 8.23°.

The maximum density, the angle of rotation and the radius were chosen as SPAR features against which to discriminate the two haemodynamic states (Table 6.2). The binary support vector machine classifier with leave one out cross-validation applied on the 15 recordings × 15 subjects in the two groups (n=450), for the SPAR features was able to achieve a 96.7% classification accuracy between the states with a high specificity (100%) and a high sensitivity (99.1%). Although, the application of the combined SPAR analysis with complexity measures achieved a slightly higher separability between the states (99.6%).

Table 6.2 Statistical analysis of the SPAR analysis measures and classification accuracy for the SPAR and combined with complexity measures for blood flow signals between the two haemodynamic states.

SPAR measures	**Median (IQR)**		**SVM Classification measures**	
	33℃	**43**℃	**SPAR measures (n=450)**	**Combined measures (n=450)**
$\tau(\mathrm{sec})$	0.310 (0.025)	0.314 (0.008)		
$\max.\mathrm{D}(\tau)$	0.116 (0.111)	$4.5 \cdot 10^{-4}$ ($5 \cdot 10^{-4}$)*	Accuracy: 96.9%	Accuracy: 99.6%
θ_s (rad)	0.087 (0.006)	0.083 (0.007)	Sensitivity: 100%	Sensitivity: 99.1%
θ_r (rad)	1.042 (0.500)	0.613 (0.082)*	Specificity: 93.3%	Specificity: 100%
$r\ (a.u.)$	3.548 (1.460)	35.626 (21.675)*		

*Significant difference from 33℃, $p < 0.05$.

6.6.2 SPAR Analysis of BF Signals in NAFLD Group

The 10-minute resting skin blood flow signal segments recorded from the forearm in all 60 participants with NAFLD with T2DM (DM1), without T2DM (DM0), and with and without T2DM and using calcium channel blocker medication (CB), exhibited differences in the SPAR features in all groups. The time and frequency domain characteristics (shown in Chapter 5) as well as complexity values and SPAR measures shown here, for all 60 NAFLD participants showed a great association with each other. There was a high negative correlation between the resting BF and the maximum density of the SPAR measures in all three groups with r=-0.815, p < 0.05 in DM0, r=-0.848, p < 0.05 in DM1 and r=-0.806, p < 0.05 in the CB group.

There was, also a high positive correlation between the radius of the attractors and the resting BF more significantly at DM1, r=0.607, p=0.002. LZ complexity was positive correlated with the maximum density in DM0 (r=0.418, p=0.038) and DM1 (r=0.791, p < 0.05). Maximum density was highly negative correlated with the total power of the blood flow signals in all groups, however, there was no significant association with the power spectral in five bands. The angle of rotation was highly negative associated with the cardiac activity at DM0 (r=-0.402, p=0.047) and DM1 (r=-0.783, p < 0.05) although this association is lost in the CB group. The kurtosis of the distribution of the segments for the DM0 group was significantly higher compared to the other two the DM0 group was significantly higher compared to the other two groups showing a value of 3.049 (1.77) for the

DM0 group, 3.146 (0.86) for the DM1 group and 2.764 (0.68) for the CB group (median(IQR)) ($p < 0.05$), indicating that the signals derived from CB group are more stationary.

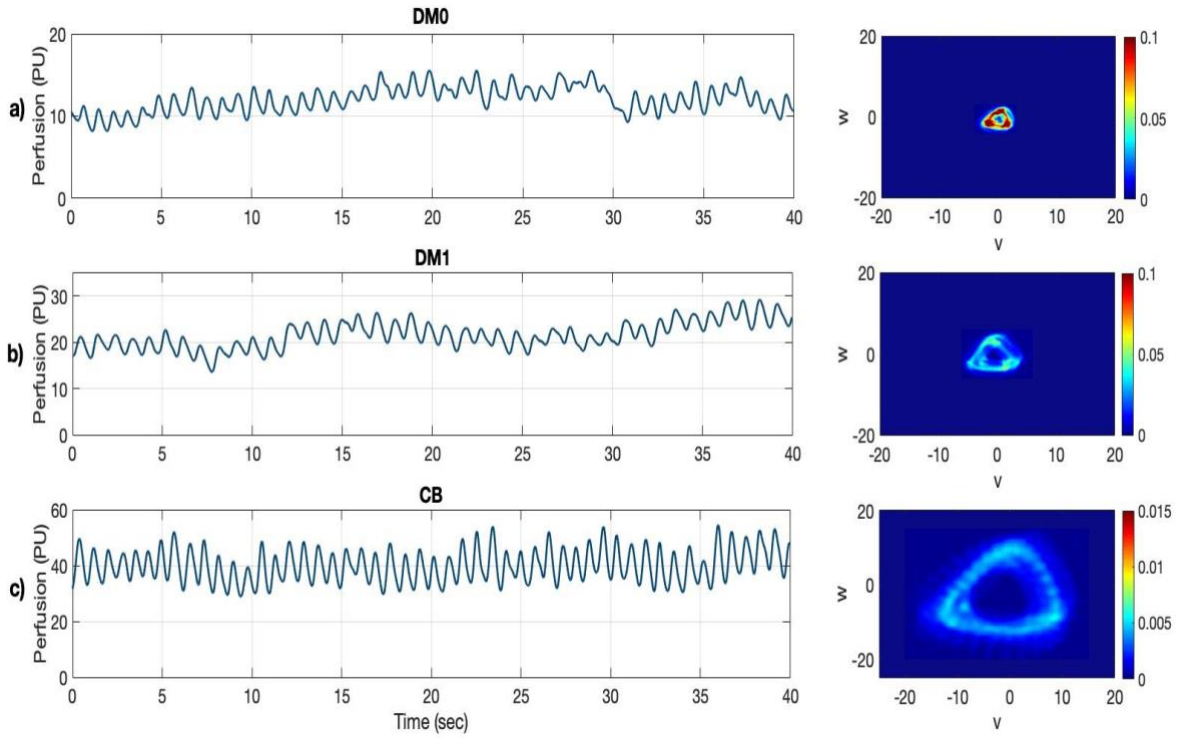

Figure 6.6 Examples of 40 seconds blood flow signals recorded from the skin at the forearm at ambient temperature and the shape and density of the reconstructed attractors in a) an individual from the DM0 group b) an individual from the DM1 group and a) an individual from the CB group. Angle of rotation for groups DM0: 35.22°, for DM1: 24.98° and for CB: 7.89°.

In Figure 6.6 it is shown how the signal variability changes in an individual from the DM0 group, an individual from the DM1 group, and an individual from the CB group without T2DM. Figure 6.6a and 6.6b shows the low amplitude of the signal for the DM0 group which is directly proportional to the small size of the attractor. In Figure 6.6c it is illustrated the high amplitude of the signal combined which corresponds to a larger attractor with significantly lower density. Again, note that the numbers in the colorbar for each attractor change indicating the change in density.

Table 6.3 illustrates the statistical analysis for all measures of SPAR analysis of the blood flow signals between the groups of people with (DM1) and without T2DM (DM0), and use of calcium channel blocker medication (CB) with and without T2DM (nine with T2DM). The maximum density measure showed a significant decrease for signals in the CB group 0.022 (0.037) whereas the highest density was shown in the DM0 group 0.097 (0.095), (median (IQR)). The angular spread values showed symmetric and reliable attractors at all groups, although it was slightly higher in DM1 and CB groups. The angle of rotation also exhibited significantly lower values for the CB group

when compared with both DM0 and DM1 groups ($p < 0.05$).The radius of the attractor was increased with the calcium channel blocker more significantly with the DM0 group ($p=0.038$).

Table 6.3 Statistical analysis of the SPAR measures for skin blood flow signals for the groups DM0 (n=25), DM1 (n=23), CB (n=12).

SPAR measures	**Median (IQR)**		
	DM0	**DM1**	**CB**
$\tau(\mathrm{sec})$	0.289 (0.042)	0.259 (0.056)*	0.315 (0.075)+
$\max.\mathrm{D}(\tau)$	0.097 (0.095)	0.073 (0.103)	0.022 (0.037)*,+
$\theta_s\ (\mathrm{rad})$	0.085 (0.021)	0.095 (0.033)	0.093 (0.045)
$\theta_r\ (\mathrm{rad})$	0.699 (0.276)	0.793 (0.624)	0.625 (0.065)*,+
$r(a.u.)$	4.122 (2.449)	4.748 (3.661)	6.594 (2.809)*

*Significant difference from DM0, $P < 0.05$. +Significant difference from DM1, $p < 0.05$.

The SPAR features were tested using a support vector machine classifier to discriminate the against the DM0 – CB for 15 recordings $\times$ 37 subjects in the two groups (n=555) and DM1 – CB groups for 15 recordings $\times$ 35 subjects in the two groups (n=525). The features selected against DM0 – CB as well as for DM1 – CB were the maximum density, the angle of rotation and the radius, as they show statistical significance between these groups. Table 6.4 shows that the SVM classifier comparing the DM0 and CB groups achieved a classification accuracy of 85.8% giving a high specificity although poor sensitivity indicating that there was a fairly small percentage (38.3%) of the SPAR features derived from the BF signal of the DM0 being identified as not having the features of the DM0 group. A higher separability was achieve using the combined SPAR analysis and LZ complexity measures between the DM0 and CB returning 91.2% classification accuracy. The SVM classifier achieved 83.2% classification accuracy between the DM1 and CB groups using the SPAR measures and 88.6% using the combined measures.

Table 6.4 SVM classification accuracy for the SPAR and combined with complexity measures between the groups DM0 – CB and DM1 – CB.

	SPAR measures		**Combined measures**	
	DM0 – CB (n=555)	**DM1 – CB (n=525)**	**DM0 – CB (n=555)**	**DM1 – CB (n=525)**
Accuracy	**85.8%**	**83.2%**	**91.2%**	**88.6%**
Sensitivity/Specificity	61.7% / 97.3%	71.7% / 89.3%	80.5% / 96%	71.7% / 89.9%

6.7 Discussion

This chapter investigates the application of the attractor reconstruction analysis of blood flow signals derived from the skin microcirculation. The main purpose of this chapter is to demonstrate the feasibility of the SPAR analysis in identifying changes in the morphology and variability of physiological data under differing conditions. The blood flow signals were first tested for nonlinearity using the surrogate data analysis showing a significant difference in the nonlinear index of LLE and CD, indicating that the blood flow signals contain nonlinear properties.

Furthermore, the results show that the amplitude of the signal is highly associated with the size and density of the attractor and therefore, a larger attractor is observed during the dynamic increase in amplitude of the signal. The findings examining the association in time and frequency domain dynamics of the blood flow signal, the SPAR and complexity measures provide strong evidence that the linear characteristics of the skin blood flow signals are strongly related with the nonlinear dynamics of the system. In this study, kurtosis was also used to characterise the shape and stationarity of the signals [216, 217]. This method showed that the signals becomes more stationary during vasodilation due to increased local warming or CB treatment.

6.7.1 Analysis of the Blood Flow Morphology of the Entire Signal

The aim of the attractor reconstruction analysis was to quantify the changes of the blood flow signal morphology and variability and its response during a dynamic changing state using data from various pathophysiological conditions. The attractor reconstruction has been extensively applied to microvascular perfusion signals [44, 179]. Parthimos, et al. [179], in a similar study investigating the nonlinear analysis of the blood flow signals from the forearm and foot of normal and diabetic with and without neuropathy volunteers used two-dimensional attractor reconstruction and measures of LLE and CD. They showed that these measures and the attractors provide useful evidence of nonlinearity in healthy individuals and in individuals with diabetes but without neuropathy groups.

In this study, LLE and CD provided information about the nonlinear dynamics of the BF signals, however the main aim is to use the measures from the reconstructed attractor and provide information regarding the changes of the microvascular dynamics. The SPAR analysis was then used to determine the changes in the variability of blood flow signals providing a visual representation of the multidimensional dynamics of the data in the form of an attractor.

From the study of the healthy group under two haemodynamic conditions, the attractors were generated from the entire signal obtained from one individual, under thermoneutral conditions, during the transition and at higher skin temperature. It was observed that the attractors generated

from the blood flow signal at 33℃ and during transition time appeared more defined with more overlaps. The attractor during the dynamic changing state showed a larger attractor than the attractor of the BF signal at 33℃ as it represents the amplitude of the signal. This finding is consistent with the recent studies [172, 175], using attractor reconstruction analysis in arterial blood pressure signals, suggesting that the size of the attractor is related with the signal amplitude.

The study of the NAFLD group illustrated the changes of the signal variability in an individual from the DM0 group, an individual from the DM1 group, and an individual from the CB group without T2DM. The low amplitude of the signal in the DM0 group was directly proportional to the small size of the attractor. It was also shown that the signal of the channel calcium blocker medication individual was less variable with a higher amplitude, corresponded to a significantly larger attractor with a lower density. Although, Nandi, et al. [175] in a recent study, suggested that the high variability of the arterial blood pressure signals from a mouse pre-antihypertensive treatment, corresponded to a less dense attractor, whereas post-treatment the signal became less variable and more periodic representing a higher density of the attractor.

As it has been also explained by Aston, et al. [172], when the arterial blood pressure signal becomes more periodic, the amplitude of the signal becomes slightly smaller and its trajectories in phase space become thinner providing a higher density. However, in blood flow signals, it is shown that during vasodilation due to increased local heating or due to a vasodilator drug, the amplitude increases showing a highly periodic signal and considering that the volume of the density is normalised to one, the attractor becomes wider and larger and therefore the maximum density is more probable to decrease.

In the study from the arterial blood pressure signals [172, 175], it was suggested that the thick bands of the attractor corresponded to the downstroke variability which represents the closure of the aortic valve and the increase in pressure at diastole [30] whereas, the thin bands represent an approximately periodic blood pressure signal. These authors, also stated that the dicrotic notch also known as downstroke concavity in the arterial blood pressure signals, corresponded to the clockwise attractor rotation. As mentioned in the literature review (see Chapter 2), the microvascular blood flow signals represent the concentration of the moving red blood cells and their interaction with the vessel walls, generated from the heartbeat and is influenced by periodic physiological oscillations [55]. These oscillation properties contribute to the total blood flow signals and reflect to the vasomotion and flow motion which can affect the signal variation [39]. Therefore, the attractor features representing the signal shape and variability can be interpreted differently depending on the physiological signals under investigation. Hence, the association of the blood flow

signal changes and the resultant changes in the attractor's shape and rotation can only be defined through systematic analysis.

6.7.2 Interpretation of SPAR Measures and Classification

In this study, the application of the symmetric projection attractor reconstruction analysis was demonstrated in blood flow signals providing measures and applying classification techniques to identify changes in groups with various pathological and physiological states. First, the time delay of the signals computed from the AMIF as one third of the period, was approximately one third of an average heart rate cycle for all groups and therefore the attractors were able to quantify the high-frequency component of the blood flow signals. González, et al. [180], in a recent study investigating the attractors of cerebral blood flow signals in human volunteers using nonlinear features to detect changes in cerebral blood flow during apnea, reported that the values of time delay using the AMIF technique, were able to provide high statistical significance level ($p<0.005$) between baseline and during apnea.

The study on a healthy cohort at the two haemodynamic steady states at 33℃ and at 43℃, showed significant changes in the SPAR measures. The findings demonstrate that the maximum density derived from the signals at 43℃ decreases during LTH, showing that as the amplitude of the signals increases during vasodilation due to increased local heating, the maximum density decreases. The angular spread for both groups appeared close to 0, indicating that in both haemodynamic states the attractors were symmetric. Recent studies [189], investigating ABP and PPG signals from human volunteers, suggest that the angular spread appeared to identify the performance and reliability of the attractor reconstruction method.

In the NAFLD cohort, the use of the vasodilator medication for the treatment of hypertension, showed a significant increase in the resting BF in the CB group against DM0 resulting to a substantial decrease in both the maximum density and the LZ complexity, indicating a lower variability of the BF signals with calcium channel blocker treatment. Similarly Frisbee, et al. [120], in a recent study using chaotic network attractor analysis, have shown a decline in the temporal adaptability and a more stable distribution of the flow patterns in a microvascular network of animal models with increased cardiovascular disease risk. The angle of rotation exhibited significantly high values for the DM1 group (~45°) when compared with CB group ($p<0.05$). Nandi, et al. [175], suggested that the rotation of the attractor in arterial pulse signals may be an indicator of an early stage of a disease or even a response to a drug treatment.

The SVM classifier using the leave one out cross-validation allows each of the individual recordings to be tested leaving one for training and thus avoiding slow processing time [218]. The

attractor features tested on each of the 15 healthy individuals using the SVM classifier, provided a strong classification between the states, however the combined features were able to show 99.6% classification accuracy which was significantly higher that the nonlinear methods (73.3%) used previously in the same dataset [141]. The SVM classifier comparing the DM0 and CB groups achieved a classification accuracy of 85.8% although, the highest separability was achieve using the combined SPAR and LZ complexity measures between the DM0 and CB returning 91.2% classification accuracy. The SVM classifier achieved 83.2% classification accuracy between the DM1 and CB groups using the SPAR measures and 88.6% using the combined measures. Here, the criteria used to select the optimal feature set was based on hypothesis testing determining the features with statistical significance between the groups.

According to the literature [150], a major issue related to the pattern recognition and high dimensional feature space is the so-called “curse of dimensionality” in which the number of data exhibit an exponential dependence with the feature dimensions, meaning that the more feature dimensions are added to the data the more complex are the computations for predicting certain quantities. It is therefore, important to minimise the number of features by selecting the most informative and retain a high classification accuracy. The most common technique for finding the optimal features is hypothesis testing however, more feature selection methods may be applied in future studies in order to find the “best” feature set for classifying pathophysiological groups.

6.8 Strengths and Limitations

The present study reveals the analysis of the attractor reconstruction of blood flow signals derived from the microvasculature in different pathological and physiological conditions. A major strengthen of this study is the use of different pathophysiological groups to quantify the microvascular network morphology was able to identify the changes of the features in shape and variability of the blood flow signals under different conditions. This study sought to use the measures from the reconstructed attractor by its symmetric projection to characterize the dynamic changes of microvascular perfusion signals. Additionally, this study examines the changes of the microcirculatory dynamics using attractor reconstruction analysis to understand the applicability of this mathematical approach in quasi periodic signals and its efficacy to discriminate between different groups. This study also, provides an explanation of the SPAR method that may complement clinical assessment of microvascular function.

There are also a number of limitations associated with this study. First, LDF signals consist of multiple frequency components (0.0095～1.6Hz) [36, 39], which are taken to reflect the activity of the local and systemic vaso-control mechanisms [109]. Therefore, the attractor features such as

attractor rotation representing the blood flow signal curvature shape cannot be easily described. Hence, more analysis should be done to define the association of the blood flow signal changes and the resultant changes in the attractor's shape and rotation.

Furthermore, in [172, 175], it is suggested that the only pre-processing analysis that is needed to ensure the quality of the attractors is the removal of artefacts. An additional study [189], also reported that non-periodic signals can provide inaccurate estimation of the parameters reconstructing unreliable attractors which will reduce the performance of SPAR analysis. This study also suggested that an attractor quality index based on the values of angular spread, determine the reliability of the attractor. In this current study, a pre-processing analysis was used to ensure that the high frequency noise is attenuated from the signals then, SPAR was applied in each segments of the signals without removing any outliers such as movement artifacts. Moreover, this study does not assure that all BF signals were approximately periodic which correspond to reliable attractors as recommended in the literature. Finally, the angular spread in this study did not reach the values suggested in the literature, as the BF signals differ from blood pressure signals and thus the threshold of the angular spread values, to separate between reliable and unreliable attractors, may differ in blood flow signals.

6.9 Conclusions

In this chapter the symmetric projection attractor reconstruction analysis was applied and the measures derived from the attractors were estimated, to better evaluate the changes of the microvascular network under a dynamic change in the skin microcirculation. The attractors and the SPAR measures combined with the nonlinear indexes were used in cohorts from different pathophysiological groups to quantify the microvascular network morphology and were able to identify the changes of the features in shape and variability of the blood flow signals under different conditions. These findings make the method a promising tool for further analysis of the microvascular function and it suggests that the SPAR measures could be used to identify changes in the microvascular system. More experiments need to be conducted to investigate changes in SPAR measures and evaluating microvascular dysfunction.

Chapter 7: Conclusions and Future Work

7.1 Conclusion

The work reported here, demonstrates the analysis of the complex flow motion characteristics from the human microcirculation in a range of pathophysiological states. Time and frequency domain analysis have been used to determine the signal values from the microvascular perfusion and their power contribution using the spectral analysis, within the frequency range (0.0095-1.6 Hz), respectively. These methods may not be sufficient for the investigation of complex dynamics of flow motion, and hence complexity analysis methods were used to describe the nonlinear characteristics of the LDF time series.

Here, nonlinear complexity methods were used to quantify the degree of signal regularity by evaluating the presence of repeated patterns providing complexity variants such as sample entropy (SampEn), Lempel and Ziv complexity (LZC) and effort to compress complexity (ETC). Since biological systems operate across multiple spatial and temporal scales, multiscale analysis was applied on these complexity measures to better quantify the information expressed by the microvascular dynamics over multiple time scales. Finally, the symmetric projection attractor reconstruction (SPAR) analysis was used, providing a quantitative characterisation of the microvascular system in phase space and a visual representation in the shape and variability of the signal producing a two-dimensional attractor with features like density and symmetry.

The major findings of this research can be summarised as:

- Power spectral density contribution of the BF and OXY signals exhibit different values across frequency bands at 33°C and during thermally induced vasodilation achieved by local skin warming to 43°C
- The findings showed a decline in all complexity values (SampEn, LZC and ETC complexity) during local warming for both blood flux and oxygenated haemoglobin signals.
- Multiscale complexity methods were able to better discriminate between haemodynamic states than conventional ones over multiple time-scales showing a good discrimination in complexity of both BF and oxyHb signals between the two haemodynamic steady states.
- LZC reduces for the groups at an increased cardiovascular disease risk and becomes more pronounced at certain time scales, showing that multiscale analysis has strong potential for discriminating between these different groups.

- The regulatory modulators and the information content in the BF signal from the groups at increase CVD risk were shown to change with the time scale.

- The symmetric projection attractor reconstruction analysis measures were able to identify changes in the morphology and variability of physiological data under different conditions.

- The highest separability was achieve using the combined SPAR and LZC measures between these groups.

In conclusion, the findings from this thesis reveal novel understanding of the potential for the time series analysis of the information content of the microcirculation. This study has shown that differences could be detected between different groups through a systematic analysis of the time series. Time and frequency domain analysis alone were inadequate to estimate the complex dynamics of the microvascular network during the application of a provocation, such as increased local heating and a vasodilator drug. Nonlinear analysis provides a better characterisation of the flexibility of the system in a range of pathophysiological conditions. Together these mathematical approaches were able to identify changes in the microvascular function.

7.2 Future work

Both linear and nonlinear analysis were thoroughly investigated in groups with pathophysiological conditions, providing important information about the modulators and the irregularities of the microvascular system. However, one of the issues that need to be considered in this study, is that there was a relatively small sample size of groups enforcing more extensive analysis in larger groups. It is also probable that changes of both linear and nonlinear measures will differ between individuals and thus, more studies need to be conducted to evaluate these changes.

Also, the nonlinear features were used for the data classification indicating the impact that the selection of the features holds in providing the optimal classification accuracy between the groups. Future studies should therefore, focus on classification techniques and predictive models to determine the most likely class associated with a given pattern from the microvascular perfusion signals. So far, most decision for helping in the diagnosis of the microvascular dysfunction, are made from medical staff or researchers although, often automated decision-making approaches can be time-saving and cost-effective. In medical applications, classes are associated to medical conditions and patterns can be any given feature representing in the datasets of the microvascular perfusion. The most common classification techniques, presented in this thesis, are linear classifiers such as linear discriminant analysis (LDA) for quicker and easier classification and support vector machines

(SVMs) for embedding the data in a higher dimensional feature space and producing nonlinear lines for the classification.

Although, a major issue related to the pattern recognition and high dimensional feature space is that the more feature dimensions are added to the data the more complex are the computations for predicting certain quantities. It is therefore, of a paramount importance to minimise the number of features by selecting and/or generating the most informative and retain a high-class discrimination accuracy. This is usually achieved with a combination of optimization feature selection techniques involving separability criteria, such as sequential feature selection algorithms for finding the “best” feature set. More machine learning methods that can produce more complex boundaries between classes, need to be evaluated such as, adaptive neural networks (ANNs) algorithms that learn from the input data and identify the two or more classes often simplifying the subjectivity of feature extraction.

Non-invasive techniques provide useful information to the medical team for enhancing diagnosis and intervention. However, the microcirculation is a highly complex system and It is essential to develop methods for feature selection and/or generation in order to provide an integrated understanding of the impact that the features hold on the ability to predict or define a human health and disease. Larger data sets and systematic analysis will help to identify more characteristic features describing to the physiology of microcirculation.

Appendix A Supplementary Figures

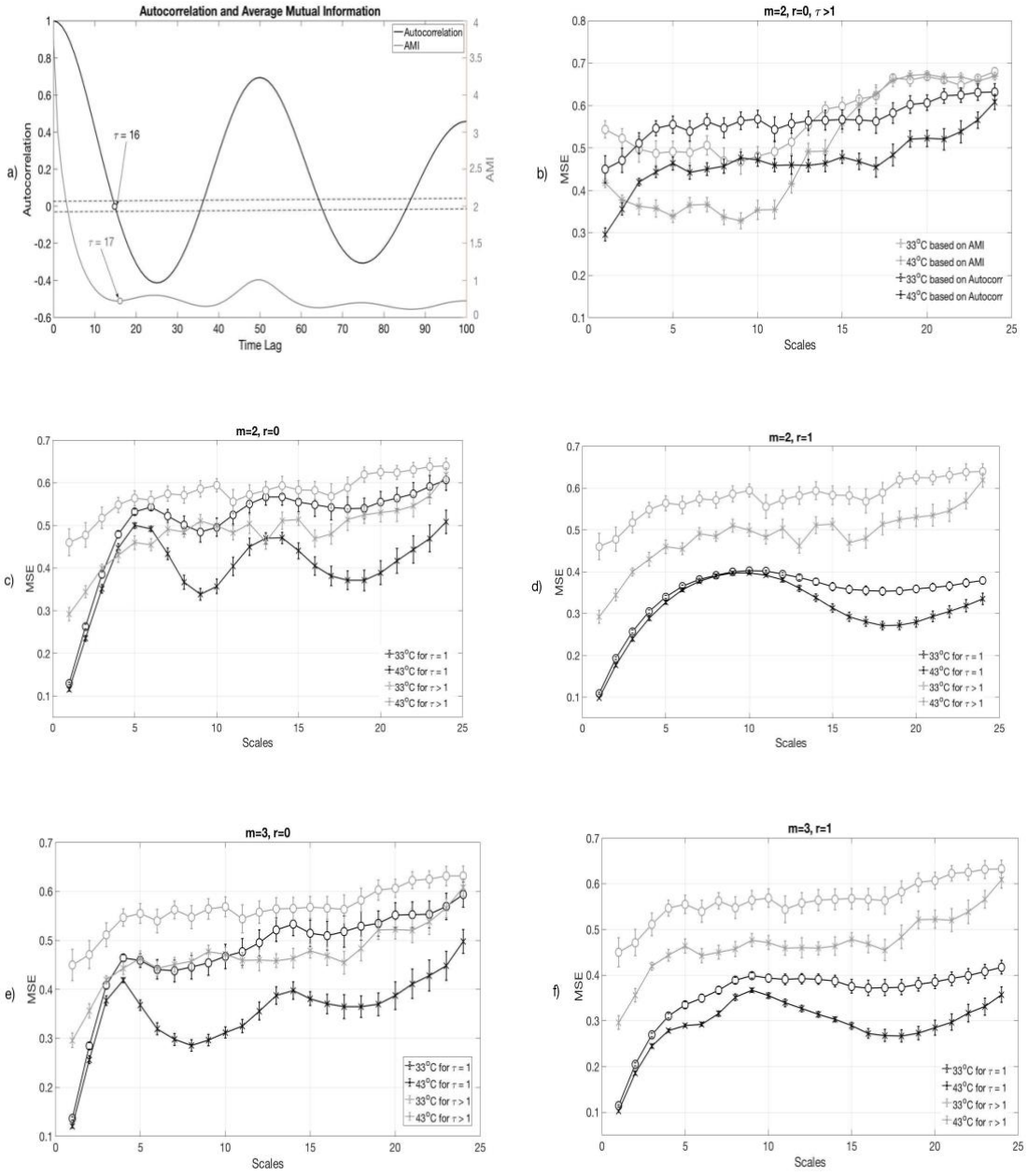

Figure A.1 An illustrative example of the binary SampEn in multiple scale (MSE) of the LDF signal from a healthy volunteer in two haemodynamic steady states (at 33 and 43 °C). a) Selection of time delay τ using the autocorrelation function (autocorr) and the averaged mutual information (AMI). b) MSE for $m = 2$ and $r = 0$ and for τ using the autocorr and the AMI. c) MSE for $m = 2$ and $r = 0$ and for $\tau = 1$ and $\tau > 1$, using the autocorr in every scale. d) MSE for $m = 2$ and $r = 1$ and for $\tau = 1$ and $\tau > 1$. e) MSE for $m = 3$ and $r = 0$ and for $\tau = 1$ and $\tau > 1$. f) MSE for $m = 3$ and $r = 1$ and for $\tau = 1$ and $\tau > 1$. The time delay for $\tau > 1$ was estimated for every scale using the autocorrelation function.

Appendix A: Supplementary Figures

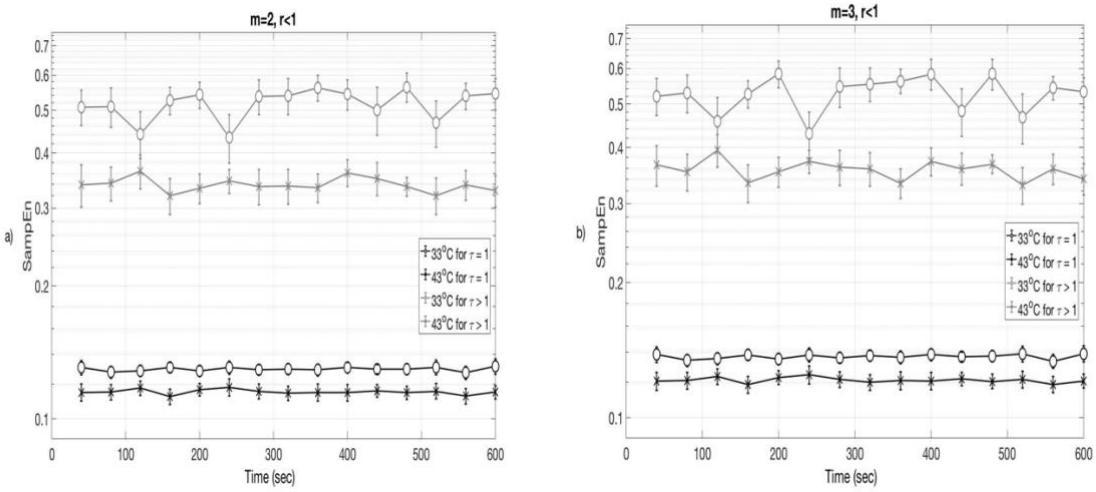

Figure A.2 a) SampEn for $m = 2$ and $r < 1$ and for $\tau = 1$ and $\tau > 1$, using the autocorrelation function for the selection of time delay τ in every scale. b) SampEn for $m = 3$ and $r < 1$ and for $\tau = 1$ and $\tau > 1$, using the autocorrelation function. It is shown that there is a good discrimination between the two temperatures for both time delays ($\tau = 1$ and $\tau > 1$) and for different parameters m ($m = 2$ and $m = 3$), when using the conventional binary SampEn measure.

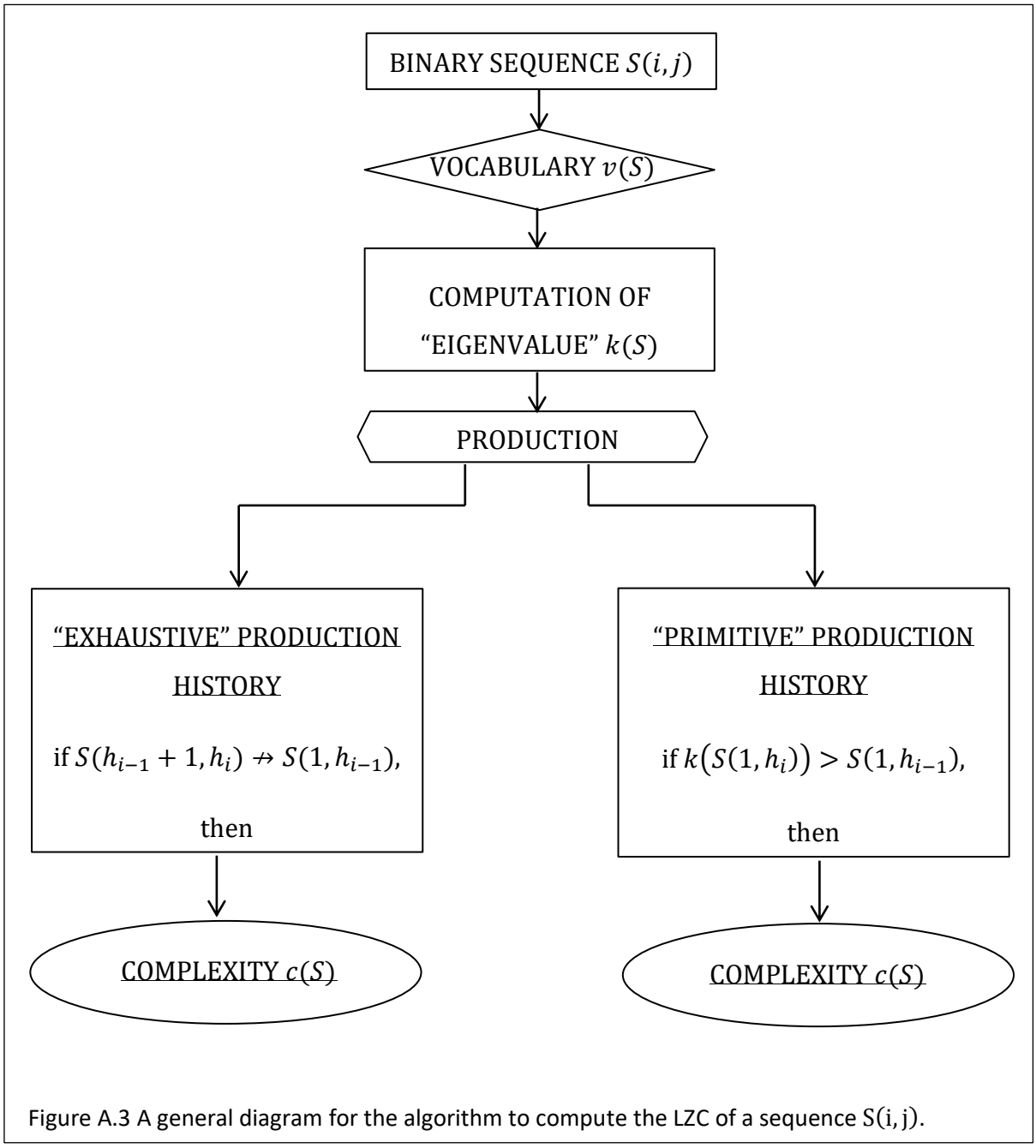

Figure A.3 A general diagram for the algorithm to compute the LZC of a sequence S(i, j).

Appendix B Supplementary Data

Table B.5 Statistical analysis and classification accuracy for all traditional complexity methods of both BF and oxyHb signals between the two haemodynamic steady states.

Methods	BF signals		oxyHb signals	
	p-value	Classification accuracy (%)	p-value	Classification accuracy (%)
SampEn	0.007	73.33	0.029	80.00
LZC	0.003	76.67	<0.001	90.00
ETC	0.002	76.67	<0.001	93.33

Appendix C Supplementary Figures

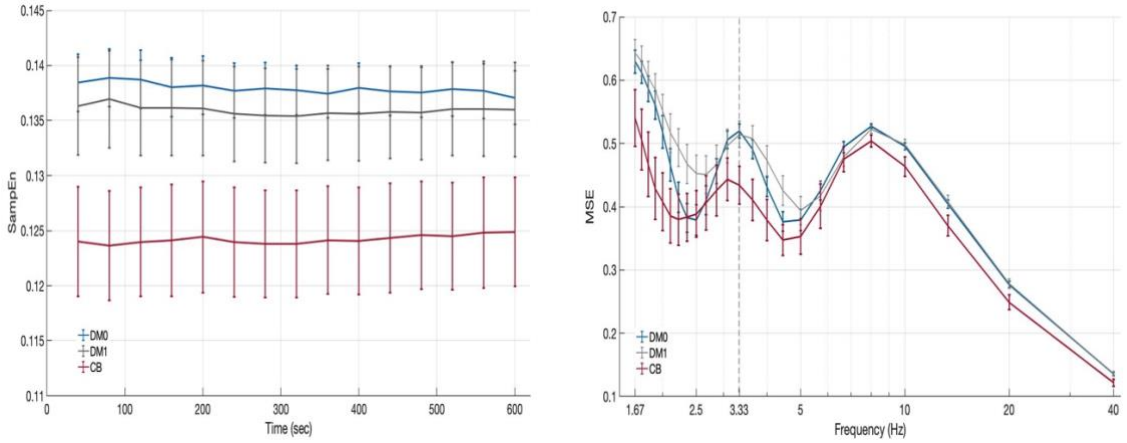

Figure C.4 Sample Entropy across 15 epochs and MSE at different frequencies

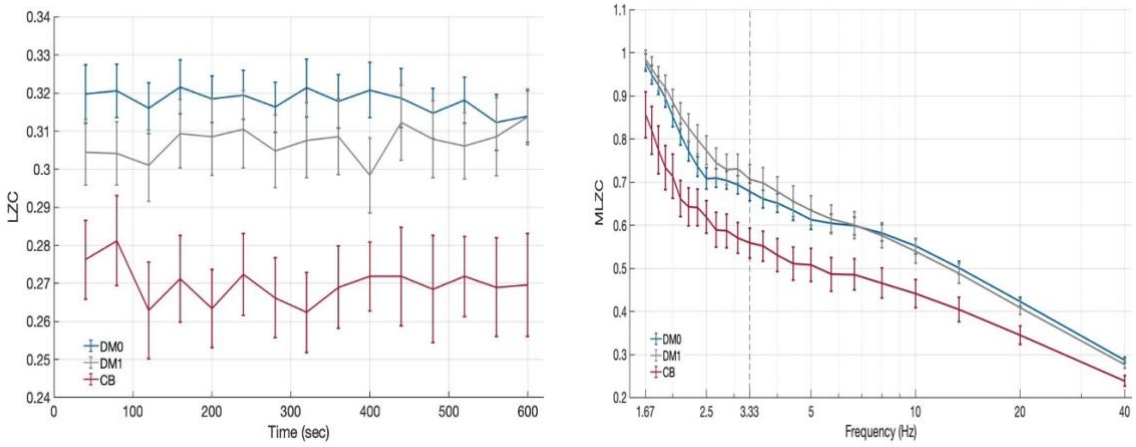

Figure C.5 LZC across 15 epochs and MLZC at different frequencies

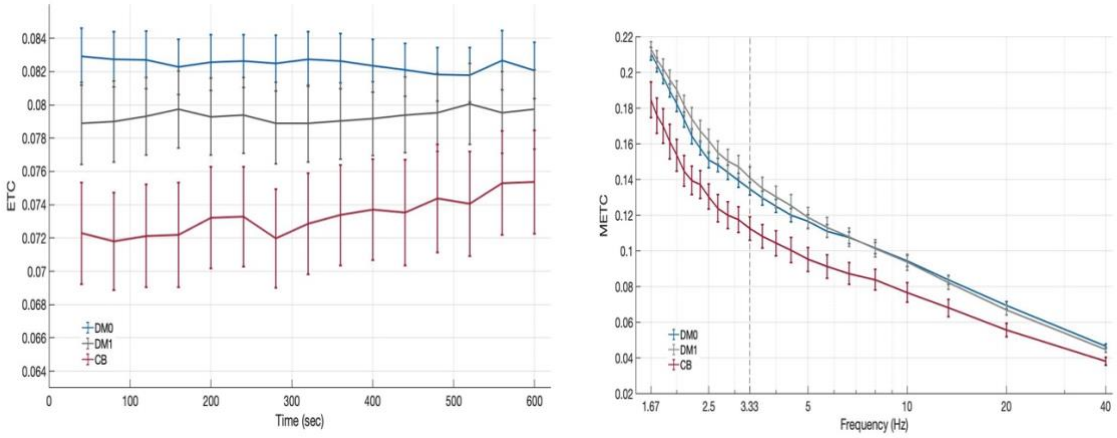

Figure C.6 ETC across 15 epochs and METC at different frequencies

Appendix D Supplementary Data

Table D.6 Estimates of largest Lyapunov exponent (LLE) and correlation dimension (CD) of 10-minute blood flow signals from DM0 (n=25), DM1 (n=23) and CB (n=12) groups, and their significant difference between the original and 20 surrogate signals. Values are presented as mean ± SEM.

	LLE		CD	
	Original	**Surrogate**	**Original**	**Surrogate**
DM0	-0.993 ± 0.081	3.975 ± 0.160	2.854 ± 0.042	2.905 ± 0.011
DM1	-0.757± 0.069	4.103 ± 0.140	2.801 ± 0.056	2.878 ± 0.011
CB	-0.637 ± 0.129$^{*,+}$	3.425 ± 0.222	3.091 ± 0.039$^{*,+}$	2.931 ± 0.010^{+}
DM0 – CB p-value	0.010	0.061	<0.05	0.142
DM1 – CB p-value	0.049	0.797	<0.05	0.006

*Significant difference from 33℃, $p < 0.05$. $^{+}$Significant difference from DM1, $p < 0.05$.

References

[1] P. Scarborough, P. Bhatnagar, K. K. Wickramasinghe, S. Allender, C. Foster, and M. Rayner, "The economic burden of ill health due to diet, physical inactivity, smoking, alcohol and obesity in the UK: an update to 2006-07 NHS costs," *Journal of Public Health,* vol. 33, no. 4, pp. 527-535, Dec 2011, doi: 10.1093/pubmed/fdr033.

[2] www.diabetes.org.uk. *Diabetes UK*. [Online]. Available: www.diabetes.org.uk.

[3] S. E. Holden, C. D. Poole, C. L. Morgan, and C. J. Currie, "Evaluation of the incremental cost to the National Health Service of prescribing analogue insulin," *Bmj Open,* vol. 1, no. 2, 2011 2011, Art no. e000258, doi: 10.1136/bmjopen-2011-000258.

[4] X. T. Tigno, B. C. Hansen, S. Nawang, R. Shamekh, and A. M. Albano, "Vasomotion becomes less random as diabetes progresses in monkeys," *Microcirculation,* vol. 18, no. 6, pp. 429-39, Aug 2011, doi: 10.1111/j.1549-8719.2011.00103.x.

[5] A. M. Albano, P. D. Brodfuehrer, C. J. Cellucci, X. T. Tigno, and P. E. Rapp, "Time series analysis, or the quest for quantitative measures of time dependent behavior," 2008.

[6] X. S. Zhang, R. J. Roy, and E. W. Jensen, "EEG complexity as a measure of depth of anesthesia for patients," *Ieee Transactions on Biomedical Engineering,* vol. 48, no. 12, pp. 1424-1433, Dec 2001, doi: 10.1109/10.966601.

[7] X. Zhang and P. Zhou, "Sample entropy analysis of surface EMG for improved muscle activity onset detection against spurious background spikes," *Journal of Electromyography and Kinesiology,* vol. 22, no. 6, pp. 901-907, Dec 2012, doi: 10.1016/j.jelekin.2012.06.005.

[8] A. T. Del Pozzi, J. T. Miller, and G. J. Hodges, "The effect of heating rate on the cutaneous vasomotion responses of forearm and leg skin in humans," *Microvasc Res,* vol. 105, pp. 77-84, May 2016, doi: 10.1016/j.mvr.2016.01.004.

[9] M. Roustit and J. L. Cracowski, "Non ‐ invasive Assessment of Skin Microvascular Function in Humans: An Insight Into Methods," *Microcirculation,* vol. 19, no. 1, pp. 47-64, 2012, doi: 10.1111/j.1549-8719.2011.00129.x.

[10] M. P. de Boer *et al.*, "Insulin-induced changes in microvascular vasomotion and capillary recruitment are associated in humans," *Microcirculation,* vol. 21, no. 5, pp. 380-7, Jul 2014, doi: 10.1111/micc.12114.

[11] G. F. Clough *et al.*, "Functional dilator capacity is independently associated with insulin sensitivity and age in central obesity and is not improved by high dose statin treatment," *Microcirculation,* vol. 18, no. 1, pp. 74-84, Jan 2011, doi: 10.1111/j.1549-8719.2010.00070.x.

[12] G. C. Farrell, N. C. Teoh, and R. S. McCuskey, "Hepatic microcirculation in fatty liver disease," *Anatomical Record-Advances in Integrative Anatomy and Evolutionary Biology,* vol. 291, no. 6, pp. 684-692, Jun 2008, doi: 10.1002/ar.20715.

[13] B. Treml *et al.*, "Cutaneous Microvascular Blood Flow and Reactivity in Hypoxia," (in English), *Frontiers in Physiology,* Original Research vol. 9, no. 160, 2018-March-06 2018, doi: 10.3389/fphys.2018.00160.

[14] B. Fromy *et al.*, "Aging-Associated Sensory Neuropathy Alters Pressure-Induced Vasodilation in Humans," *Journal of Investigative Dermatology,* vol. 130, no. 3, pp. 849-855, 2010/03/01/ 2010, doi: https://doi.org/10.1038/jid.2009.279.

[15] M. Roustit and J. L. Cracowski, "Assessment of endothelial and neurovascular function in human skin microcirculation," *Trends Pharmacol Sci,* vol. 34, no. 7, pp. 373-84, Jul 2013, doi: 10.1016/j.tips.2013.05.007.

[16] V. E. Brunt, J. A. Miner, J. R. Meendering, P. F. Kaplan, and C. T. Minson, "17β-Estradiol and Progesterone Independently Augment Cutaneous Thermal Hyperemia But Not Reactive Hyperemia," *Microcirculation,* vol. 18, no. 5, pp. 347-355, 2011/07/01 2011, doi: 10.1111/j.1549-8719.2011.00095.x.

[17] H. Hsiu, H.-F. Hu, and H.-C. Tsai, "Differences in laser-Doppler indices between skin-surface measurement sites in subjects with diabetes," *Microvascular Research,* vol. 115, pp. 1-7, 2018/01/01/ 2018, doi: https://doi.org/10.1016/j.mvr.2017.07.004.

[18] J. Sandby-Møller, T. Poulsen, and H. Wulf, "Epidermal Thickness at Different Body Sites: Relationship to Age, Gender, Pigmentation, Blood Content, Skin Type and Smoking Habits," *Acta dermato-venereologica,* vol. 83, pp. 410-3, 02/01 2003, doi: 10.1080/00015550310015419.

[19] P. Henriksson, U. L. F. Diczfalusy, and A. Freyschuss, "Microvascular Reactivity in Response to Smoking and Oral Antioxidants in Humans," *Microcirculation,* vol. 19, no. 1, pp. 86-93, 2012/01/01 2012, doi: 10.1111/j.1549-8719.2011.00125.x.

[20] R. Fries, K. Shariat, H. von Wilmowsky, and M. Böhm, "Sildenafil in the Treatment of Raynaud's Phenomenon Resistant to Vasodilatory Therapy," *Circulation,* vol. 112, no. 19, pp. 2980-2985, 2005/11/08 2005, doi: 10.1161/CIRCULATIONAHA.104.523324.

[21] D. H. J. Thijssen, D. J. Green, and M. T. E. Hopman, "Blood vessel remodeling and physical inactivity in humans," *Journal of Applied Physiology,* vol. 111, no. 6, pp. 1836–1845, 2011, doi: https://doi.org/10.1152/japplphysiol.00394.2011.

[22] M. D. Stern, "INVIVO EVALUATION OF MICROCIRCULATION BY COHERENT LIGHT-SCATTERING," *Nature,* vol. 254, no. 5495, pp. 56-58, 1975 1975, doi: 10.1038/254056a0.

[23] A. Humeau, W. Steenbergen, H. Nilsson, and T. Stromberg, "Laser Doppler perfusion monitoring and imaging: novel approaches," *Med Biol Eng Comput,* vol. 45, no. 5, pp. 421-35, May 2007, doi: 10.1007/s11517-007-0170-5.

[24] H. Y. Liu, M. Kohl-Bareis, and X. B. Huang, "Design of a tissue oxygenation monitor and verification on human skin," in *Clinical and Biomedical Spectroscopy and Imaging Ii*, vol. 8087, N. Ramanujam and J. Popp Eds., (Proceedings of SPIE. Bellingham: Spie-Int Soc Optical Engineering, 2011.

[25] M. J. Leahy, F. F. M. de Mul, G. E. Nilsson, and R. Maniewski, "Principles and practice of the laser-Doppler perfusion technique," *Technology and Health Care,* vol. 7, pp. 143-162, 1999, doi: 10.3233/THC-1999-72-306.

[26] J. L. Semmlow, *Biosignal and Medical Image Processing, Second Edition*. CRC Press, 2011.

[27] A. Aldroubi and M. Unser, *Wavelets in Medicine and Biology*. Taylor & Francis, 1996.

[28] P. Flandrin, *Time-Frequency/Time-Scale Analysis*. Elsevier Science, 1998.

[29] B. J. West, "Fractal physiology and the fractional calculus: a perspective," *Frontiers in Physiology,* vol. 1, 2010 2010, Art no. 12, doi: 10.3389/fphys.2010.00012.

[30] J. Alastruey, A. A. E. Hunt, and P. D. Weinberg, "Novel wave intensity analysis of arterial pulse wave propagation accounting for peripheral reflections," (in eng), *Int J Numer Method Biomed Eng,* vol. 30, no. 2, pp. 249-279, 2014, doi: 10.1002/cnm.2602.

[31] J. L. Semmlow and B. Griffel, *Biosignal and Medical Image Processing, Third Edition*. CRC Press, 2014.

[32] M. Escabí, "Chapter 11 - Biosignal Processing," in *Introduction to Biomedical Engineering (Third Edition)*, J. D. Enderle and J. D. Bronzino Eds. Boston: Academic Press, 2012, pp. 667-746.

[33] H. Kantz and T. Schreiber, *Nonlinear Time Series Analysis*, 2 ed. Cambridge: Cambridge University Press, 2003.

[34] T. Sauer, J. A. Yorke, and M. Casdagli, "Embedology," *Journal of Statistical Physics,* vol. 65, no. 3, pp. 579-616, 1991/11/01 1991, doi: 10.1007/BF01053745.

[35] D. Belo, J. Rodrigues, J. R. Vaz, P. Pezarat-Correia, and H. Gamboa, "Biosignals learning and synthesis using deep neural networks," *BioMedical Engineering OnLine,* vol. 16, no. 1, p. 115, 2017/09/25 2017, doi: 10.1186/s12938-017-0405-0.

[36] A. Stefanovska, M. Bracic, and H. D. Kvernmo, "Wavelet analysis of oscillations in the peripheral blood circulation measured by laser Doppler technique," *Ieee Transactions on Biomedical Engineering,* vol. 46, no. 10, pp. 1230-1239, Oct 1999, doi: 10.1109/10.790500.

[37] M. Rossi, A. Carpi, C. Di Maria, F. Galetta, and G. Santoro, "Spectral analysis of laser Doppler skin blood flow oscillations in human essential arterial hypertension," *Microvascular Research,* vol. 72, no. 1, pp. 34-41, 2006/07/01/ 2006, doi: https://doi.org/10.1016/j.mvr.2006.04.001.

[38] U. Rajendra Acharya, K. Paul Joseph, N. Kannathal, C. M. Lim, and J. S. Suri, "Heart rate variability: a review," *Medical and Biological Engineering and Computing,* vol. 44, no. 12, pp. 1031-1051, 2006/12/01 2006, doi: 10.1007/s11517-006-0119-0.

[39] P. Kvandal, S. A. Landsverk, A. Bernjak, A. Stefanovska, H. D. Kvernmo, and K. A. Kirkeboen, "Low-frequency oscillations of the laser Doppler perfusion signal in human skin," *Microvasc Res,* vol. 72, no. 3, pp. 120-7, Nov 2006, doi: 10.1016/j.mvr.2006.05.006.

[40] K. Z. Kuliga, R. Gush, G. F. Clough, and A. J. Chipperfield, "Time-dependent Behavior of Microvascular Blood Flow and Oxygenation: a Predictor of Functional Outcomes," *IEEE Transactions on Biomedical Engineering,* vol. PP, no. 99, pp. 1-1, 2017, doi: 10.1109/TBME.2017.2737328.

[41] M. Folgosi-Correa and G. E. C. Nogueira, *Quantifying low-frequency fluctuations in the laser Doppler flow signal from human skin*. 2011, p. 25.

[42] M. Bračič, P. McClintock, and A. Stefanovska, "Characteristic frequencies of the human blood distribution system," vol. 502, 2000, pp. 146-153.

[43] C. E. Shannon, "A Mathematical Theory of Communication," *Bell System Technical Journal,* vol. 27, no. 3, pp. 379-423, 1948/07/01 1948, doi: 10.1002/j.1538-7305.1948.tb01338.x.

[44] K. Bräuer and M. Hahn, "Nonlinear analysis of blood flux in human vessels," *Physics in Medicine and Biology,* vol. 44, no. 7, pp. 1719-1733, 1999/01/01 1999, doi: 10.1088/0031-9155/44/7/311.

[45] S. De Brouwer, D. H. Edwards, and T. M. Griffith, "Simplification of the quasiperiodic route to chaos in agonist-induced vasomotion by iterative circle maps," *American Journal of Physiology-Heart and Circulatory Physiology,* vol. 274, no. 4, pp. H1315-H1326, 1998/04/01 1998, doi: 10.1152/ajpheart.1998.274.4.H1315.

[46] M. Costa, A. L. Goldberger, and C. K. Peng, "Multiscale entropy analysis of complex physiologic time series," *Physical Review Letters,* vol. 89, no. 6, Aug 5 2002, Art no. 068102, doi: 10.1103/PhysRevLett.89.068102.

[47] R. J. Levick, Arnold, Ed. *An introduction to cardiovascular physiology*, 4 ed. Arnold Publication, 2003, p. 372.

[48] F. Feihl, L. Liaudet, and B. Waeber, "The macrocirculation and microcirculation of hypertension," *Current Hypertension Reports,* vol. 11, no. 3, pp. 182-189, Jun 2009, doi: 10.1007/s11906-009-0033-6.

[49] R. Wells, *The Microcirculation in Clinical Medicine*. Acad. Press, 1973.

[50] P. F. d. A. Tafner, F. K. Chen, R. F. Rabello, T. D. Corrêa, R. C. d. F. Chaves, and A. N. Serpa, "Recent advances in bedside microcirculation assessment in critically ill patients," (in por

eng), *Rev Bras Ter Intensiva,* vol. 29, no. 2, pp. 238-247, Apr-Jun 2017, doi: 10.5935/0103-507X.20170033.

[51] E. Calzia, Z. Iványi, and P. Radermacher, *Determinants of Blood Flow and Organ Perfusion* (Functional Hemodynamic Monitoring. Update in Intensive Care and Emergency Medicine). Berlin, Heidelberg: Springer, 2005, p. 14.

[52] Z. D. Draelos and P. T. Pugliese, *Physiology of the Skin*, 3 ed. Allured Business Media, 2000.

[53] I. M. Braverman, "The cutaneous microcirculation," *J Investig Dermatol Symp Proc,* vol. 5, no. 1, pp. 3-9, Dec 2000, doi: 10.1046/j.1087-0024.2000.00010.x.

[54] K. Z. Kuliga, "Simultaneous, Non-invasive Measurements of Skin Blood Flow and Oxygenation in Healthy Humans," Doctor of Philosophy, Faculty of Medicine, University of Southampton, 2016.

[55] H. Lenasi, *Assessment of Human Skin Microcirculation and Its Endothelial Function Using Laser Doppler Flowmetry*. INTECH Open Access Publisher, 2011.

[56] N. Stergiopulos, C. A. Porret, S. De Brouwer, and J. J. Meister, "Arterial vasomotion: effect of flow and evidence of nonlinear dynamics," *American Journal of Physiology-Heart and Circulatory Physiology,* vol. 274, no. 6, pp. H1858-H1864, Jun 1998. [Online]. Available: <Go to ISI>://WOS:000073980600002.

[57] A. Humeau-Heurtier, E. Guerreschi, P. Abraham, and G. Mahe, "Relevance of Laser Doppler and Laser Speckle Techniques for Assessing Vascular Function: State of the Art and Future Trends," *Ieee Transactions on Biomedical Engineering,* vol. 60, no. 3, pp. 659-666, Mar 2013, doi: 10.1109/tbme.2013.2243449.

[58] J. L. Cracowski, C. T. Minson, M. Salvat-Melis, and J. R. Halliwill, "Methodological issues in the assessment of skin microvascular endothelial function in humans," *Trends in Pharmacological Sciences,* vol. 27, no. 9, pp. 503-508, Sep 2006, doi: 10.1016/j.tips.2006.07.008.

[59] J. Bhattacharya, P. P. Kanjilal, and V. Muralidhar, "Analysis and characterization of photo-plethysmographic signal," *Ieee Transactions on Biomedical Engineering,* vol. 48, no. 1, pp. 5-11, Jan 2001, doi: 10.1109/10.900243.

[60] E. J. Abbink, H. Wollersheim, P. M. Netten, and P. Smits, "Reproducibility of skin microcirculatory measurements in humans, with special emphasis on capillaroscopy," *Vascular Medicine,* vol. 6, no. 4, pp. 203-210, 2001 2001, Art no. Unsp 1358-863x(01)vm396oa, doi: 10.1177/1358836x0100600401.

[61] W. Groner *et al.*, "Orthogonal polarization spectral imaging: A new method for study of the microcirculation," *Nature Medicine,* vol. 5, no. 10, pp. 1209-1213, Oct 1999. [Online]. Available: <Go to ISI>://WOS:000082933200051.

[62] C. E. Thorn and A. C. Shore, "The role of perfusion in the oxygen extraction capability of skin and skeletal muscle," *Am J Physiol Heart Circ Physiol,* vol. 310, no. 10, pp. H1277-84, May 15 2016, doi: 10.1152/ajpheart.00047.2016.

[63] J.-L. Cracowski and M. Roustit, "Current Methods to Assess Human Cutaneous Blood Flow: An Updated Focus on Laser-Based-Techniques," *Microcirculation,* vol. 23, no. 5, pp. 337-344, Jul 2016, doi: 10.1111/micc.12257.

[64] R. B. Northrop, *Non-invasive instrumentation and measurement in medical diagnosis* (Biomedical engineering). CRC Press, 2002, p. 480p. .

[65] I. Fredriksson, C. Fors, and J. Johansson, "Laser Doppler Flowmetry - a Theoretical Framework," 2007.

[66] M. J. Leahy, F. F. M. de Mul, G. E. Nilsson, R. Maniewski, and A. Liebert, "Developments in laser Doppler blood perfusion monitoring," in *Opto-Ireland 2002: Optics and Photonics Technologies and Applications, Pts 1 and 2*, vol. 4876, W. J. Blau *et al.* Eds., (Proceedings of the Society of Photo-Optical Instrumentation Engineers (Spie), 2003, pp. 128-139.

[67] www.moor.co.uk. *Moor Insrtuments Ltd*, 2001. [Online]. Available: http://www.moor.co.uk

[68] G. Clough, A. Chipperfield, C. Byrne, F. de Mul, and R. Gush, "Evaluation of a new high power, wide separation laser Doppler probe: potential measurement of deeper tissue blood flow," *Microvasc Res,* vol. 78, no. 2, pp. 155-61, Sep 2009, doi: 10.1016/j.mvr.2009.05.003.

[69] J. C. Zhong, A. M. Seifalian, G. E. Salerud, and G. E. Nilsson, "A mathematical analysis on the biological zero problem in laser Doppler flowmetry," *Ieee Transactions on Biomedical Engineering,* vol. 45, no. 3, pp. 354-364, Mar 1998, doi: 10.1109/10.661160.

[70] T. Jue and K. Masuda, *Application of Near Infrared Spectroscopy in Biomedicine*. Springer US, 2013.

[71] A. V. Oppenheim and R. W. Schafer, *Discrete-time signal processing*. Upper Saddle River: Pearson (in English), 2010.

[72] S. M. Kay, *Modern Spectral Estimation: Theory and Application/Book and Disk*. PTR Prentice Hall, 1988.

[73] X. Mi, H. Ren, Z. Ouyang, W. Wei, and K. Ma, "The use of the Mexican Hat and the Morlet wavelets for detection of ecological patterns," *Plant Ecology,* vol. 179, no. 1, pp. 1-19, 2005/07/01 2005, doi: 10.1007/s11258-004-5089-4.

[74] A. Bernjak, J. Cui, S. Iwase, T. Mano, A. Stefanovska, and D. L. Eckberg, "Human sympathetic outflows to skin and muscle target organs fluctuate concordantly over a wide range of time-

varying frequencies," *J Physiol,* vol. 590, no. 2, pp. 363-75, Jan 15 2012, doi: 10.1113/jphysiol.2011.214528.

[75] K. Balasubramanian and N. Nagaraj, "Aging and cardiovascular complexity: effect of the length of RR tachograms," *Peerj,* vol. 4, Dec 2016, Art no. e2755, doi: 10.7717/peerj.2755.

[76] M. Costa, A. L. Goldberger, and C. K. Peng, "Multiscale entropy analysis of biological signals," *Physical Review E,* vol. 71, no. 2, Feb 2005, Art no. 021906, doi: 10.1103/PhysRevE.71.021906.

[77] S. M. Pincus, "Approximate entropy as a measure of system complexity," *Proceedings of the National Academy of Sciences of the United States of America,* vol. 88, no. 6, pp. 2297-2301, 1991. [Online]. Available: http://www.ncbi.nlm.nih.gov/pmc/articles/PMC51218/.

[78] J. S. Richman and J. R. Moorman, "Physiological time-series analysis using approximate entropy and sample entropy," *American Journal of Physiology-Heart and Circulatory Physiology,* vol. 278, no. 6, pp. H2039-H2049, Jun 2000. [Online]. Available: <Go to ISI>://WOS:000087573500038.

[79] A. N. Kolmogorov, "Entropy per unit time as a metric invariant of automorphism," *Doklady of Russian Academy of Sciences,* vol. 124, pp. 754-755, 1959.

[80] P. Grassberger and I. Procaccia, "ESTIMATION OF THE KOLMOGOROV-ENTROPY FROM A CHAOTIC SIGNAL," *Physical Review A,* vol. 28, no. 4, pp. 2591-2593, 1983, doi: 10.1103/PhysRevA.28.2591.

[81] S. M. Pincus, "Assessing serial irregularity and its implications for health," in *Population Health and Aging: Strengthening the Dialogue between Epidemiology and Demography*, vol. 954, M. Weinstein, A. I. Hermalin, and M. A. Stoto Eds., (Annals of the New York Academy of Sciences, 2001, pp. 245-267.

[82] S. M. Pincus and A. L. Goldberger, "Physiological time-series analysis: what does regularity quantify?," *American Journal of Physiology - Heart and Circulatory Physiology,* vol. 266, no. 4, pp. H1643-H1656, 1994.

[83] K. Balasubramanian, S. S. Nair, and N. Nagaraj, "Classification of periodic, chaotic and random sequences using approximate entropy and Lempel–Ziv complexity measures," *Pramana,* vol. 84, no. 3, pp. 365-372, 2015, doi: 10.1007/s12043-015-0938-3.

[84] H. Hsiu, C. L. Hsu, H. F. Hu, F. C. Hsiao, and S. H. Yang, "Complexity analysis of beat-to-beat skin-surface laser-Doppler signals in diabetic subjects," *Microvasc Res,* vol. 93, pp. 9-13, May 2014, doi: 10.1016/j.mvr.2014.02.009.

[85] A. Humeau, F. Chapeau-Blondeau, D. Rousseau, P. Rousseau, W. Trzepizur, and P. Abraham, "Multifractality, sample entropy, and wavelet analyses for age-related changes in the peripheral cardiovascular system: Preliminary results," *Med. Phys.,* vol. 35, no. 2, pp. 717-723, Feb 2008, doi: 10.1118/1.2831909.

[86] N. Nagaraj and K. Balasubramanian, "Three perspectives on complexity: entropy, compression, subsymmetry," (in English), *Eur Phys J-Spec Top,* vol. 226, no. 15, pp. 3251-3272, Dec 2017, doi: 10.1140/epjst/e2016-60347-2.

[87] A. Lempel and J. Ziv, "On the complexity of finite sequences," *IEEE Trans. Inf. Theory,* vol. IT-22, no. 1, pp. 75–81, 1976.

[88] N. Nagaraj, K. Balasubramanian, and S. Dey, "A new complexity measure for time series analysis and classification," (in English), *Eur. Phys. J.-Spec. Top.,* Article vol. 222, no. 3-4, pp. 847-860, Jul 2013, doi: 10.1140/epjst/e2013-01888-9.

[89] L. F. Liu and S. X. Miao, "The complexity of binary sequences using logistic chaotic maps," *Complexity,* vol. 21, no. 6, pp. 121-129, Jul-Aug 2016, doi: 10.1002/cplx.21672.

[90] X. S. Zhang, Y. S. Zhu, N. V. Thakor, and Z. Z. Wang, "Detecting ventricular tachycardia and fibrillation by complexity measure," *Ieee Transactions on Biomedical Engineering,* vol. 46, no. 5, pp. 548-555, May 1999, doi: 10.1109/10.759055.

[91] M. Aboy, R. Hornero, D. Abasolo, and D. Alvarez, "Interpretation of the Lempel-Ziv complexity measure in the context of biomedical signal analysis," *IEEE Trans Biomed Eng,* vol. 53, no. 11, pp. 2282-8, Nov 2006, doi: 10.1109/TBME.2006.883696.

[92] Y. Zhang, S. Wei, H. Liu, L. Zhao, and C. Liu, "A novel encoding Lempel-Ziv complexity algorithm for quantifying the irregularity of physiological time series," *Comput Methods Programs Biomed,* vol. 133, pp. 7-15, Sep 2016, doi: 10.1016/j.cmpb.2016.05.010.

[93] A. C. Yang, S. S. Hseu, H. W. Yien, A. L. Goldberger, and C. K. Peng, "Linguistic analysis of the human heartbeat using frequency and rank order statistics," *Phys Rev Lett,* vol. 90, no. 10, p. 108103, Mar 14 2003, doi: 10.1103/PhysRevLett.90.108103.

[94] M. Ferrario *et al.*, "Multiparameter Analysis of Heart Rate Variability Signal for the Investigation of High Risk Fetuses," in *2009 Annual International Conference of the Ieee Engineering in Medicine and Biology Society, Vols 1-20*, (IEEE Engineering in Medicine and Biology Society Conference Proceedings, 2009, pp. 4662-+.

[95] R. Hornero, M. Aboy, and D. Abasolo, "Analysis of intracranial pressure during acute intracranial hypertension using Lempel-Ziv complexity: further evidence," *Med Biol Eng Comput,* vol. 45, no. 6, pp. 617-20, Jun 2007, doi: 10.1007/s11517-007-0194-x.

[96] J. Hu, J. Gao, and J. C. Principe, "Analysis of biomedical signals by the lempel-Ziv complexity: the effect of finite data size," *IEEE Trans Biomed Eng,* vol. 53, no. 12 Pt 2, pp. 2606-9, Dec 2006, doi: 10.1109/TBME.2006.883825.

[97] T. Skoric, O. Mohamoud, B. Milovanovic, N. Japundzic-Zigon, and D. Bajic, "Binarized cross-approximate entropy in crowdsensing environment," (in English), *Comput. Biol. Med.,* Article vol. 80, pp. 137-147, Jan 2017, doi: 10.1016/j.compbiomed.2016.11.019.

[98] A. M. Fraser and H. L. Swinney, "Independent coordinates for strange attractors from mutual information," *Physical Review A,* vol. 33, no. 2, pp. 1134-1140, 02/01/ 1986, doi: 10.1103/PhysRevA.33.1134.

[99] F. Kaffashi, R. Foglyano, C. G. Wilson, and K. A. Loparo, "The effect of time delay on Approximate & Sample Entropy calculations," *Physica D: Nonlinear Phenomena,* vol. 237, no. 23, pp. 3069-3074, 2008/12/01/ 2008, doi: https://doi.org/10.1016/j.physd.2008.06.005.

[100] A. N. Kolmogorov, "Three approaches to the quantitative definition of information," *Problems of Information Transmission,* vol. 1, no. 1, pp. 1-7, // 1965, doi: citeulike-article-id:225357.

[101] K. Limniotis, N. Kolokotronis, and N. Kalouptsidis, "On the Nonlinear complexity and Lempel-Ziv complexity of finite length sequences," *Ieee Transactions on Information Theory,* vol. 53, no. 11, pp. 4293-4302, Nov 2007, doi: 10.1109/tit.2007.907442.

[102] D. Abasolo, C. J. James, and R. Hornero, "Non-linear analysis of intracranial electroencephalogram recordings with approximate entropy and Lempel-Ziv complexity for epileptic seizure detection," *Conference proceedings : ... Annual International Conference of the IEEE Engineering in Medicine and Biology Society. IEEE Engineering in Medicine and Biology Society. Annual Conference,* vol. 2007, pp. 1953-6, 2007 2007. [Online]. Available: <Go to ISI>://MEDLINE:18002366.

[103] W. Ebeling and M. A. Jiménez-Montaño, "On grammars, complexity, and information measures of biological macromolecules," *Mathematical Biosciences,* vol. 52, no. 1, pp. 53-71, 1980/11/01/ 1980, doi: http://dx.doi.org/10.1016/0025-5564(80)90004-8.

[104] K. Z. Kuliga, E. F. McDonald, R. Gush, C. Michel, A. J. Chipperfield, and G. F. Clough, "Dynamics of microvascular blood flow and oxygenation measured simultaneously in human skin," *Microcirculation,* vol. 21, no. 6, pp. 562-73, Aug 2014, doi: 10.1111/micc.12136.

[105] P. Kvandal, A. Stefanovska, M. Veber, H. D. Kvenumo, and K. A. Kirkeboen, "Regulation of human cutaneous circulation evaluated by laser Doppler flowmetry, iontophoresis, and spectral analysis: importance of nitric oxide and prostaglandines," *Microvascular Research,* vol. 65, no. 3, pp. 160-171, May 2003, doi: 10.1016/s0026-2862(03)00006-2.

[106] M. Rossi, S. Bertuglia, M. Varanini, A. Giusti, G. Santoro, and A. Carpi, "Generalised wavelet analysis of cutaneous flow-motion during post-occlusive reactive hyperaemia in patients with peripheral arterial obstructive disease," *Biomedicine & Pharmacotherapy,* vol. 59, no. 5, pp. 233-239, Jun 2005, doi: 10.1016/j.biopha.2004.01.008.

[107] P.-C. Sun, C.-D. Kuo, L.-Y. Chi, H.-D. Lin, S.-H. Wei, and C.-S. Chen, "Microcirculatory vasomotor changes are associated with severity of peripheral neuropathy in patients with type 2 diabetes," *Diabetes & Vascular Disease Research,* vol. 10, no. 3, pp. 270-276, May 2013, doi: 10.1177/1479164112465443.

[108] M. Benedicic, A. Bernjak, A. Stefanovska, and R. Bosnjak, "Continuous wavelet transform of laser-Doppler signals from facial microcirculation reveals vasomotion asymmetry," *Microvasc Res,* vol. 74, no. 1, pp. 45-50, Jul 2007, doi: 10.1016/j.mvr.2007.02.007.

[109] G. F. Clough, K. Z. Kuliga, and A. J. Chipperfield, "Flow motion dynamics of microvascular blood flow and oxygenation: Evidence of adaptive changes in obesity and type 2 diabetes mellitus/insulin resistance," *Microcirculation,* vol. 24, no. 2, 2017, doi: 10.1111/micc.12331.

[110] J. M. B. Newman, R. M. Dwyer, P. St-Pierre, S. M. Richards, M. G. Clark, and S. Rattigan, "Decreased microvascular vasomotion and myogenic response in rat skeletal muscle in association with acute insulin resistance," *Journal of Physiology-London,* vol. 587, no. 11, pp. 2579-2588, Jun 1 2009, doi: 10.1113/jphysiol.2009.169011.

[111] P. Goupillaud, A. Grossmann, and J. Morlet, "CYCLE-OCTAVE AND RELATED TRANSFORMS IN SEISMIC SIGNAL ANALYSIS," *Geoexploration,* vol. 23, no. 1, pp. 85-102, 1984 1984, doi: 10.1016/0016-7142(84)90025-5.

[112] A. Bernjak, P. B. Clarkson, P. V. McClintock, and A. Stefanovska, "Low-frequency blood flow oscillations in congestive heart failure and after beta1-blockade treatment," *Microvasc Res,* vol. 76, no. 3, pp. 224-32, Nov 2008, doi: 10.1016/j.mvr.2008.07.006.

[113] R. B. D'Agostino, A. Belanger, and R. B. D'Agostino, "A Suggestion for Using Powerful and Informative Tests of Normality," *The American Statistician,* vol. 44, no. 4, pp. 316-321, 1990/11/01 1990, doi: 10.1080/00031305.1990.10475751.

[114] L. W. Sheppard, V. Vuksanovic, P. V. E. McClintock, and A. Stefanovska, "Oscillatory dynamics of vasoconstriction and vasodilation identified by time-localized phase coherence," *Physics in Medicine and Biology,* vol. 56, no. 12, pp. 3583-3601, Jun 2011, doi: 10.1088/0031-9155/56/12/009.

[115] B. Gryglewska, M. Necki, M. Cwynar, T. Baron, and T. Grodzicki, "Local heat stress and skin blood flowmotion in subjects with familial predisposition or newly diagnosed hypertension," *Blood Pressure,* vol. 19, no. 6, pp. 366-372, Dec 2010, doi: 10.3109/08037051.2010.488053.

[116] D. B. Cines *et al.*, "Endothelial cells in physiology and in the pathophysiology of vascular disorders," *Blood,* vol. 91, no. 10, pp. 3527-3561, May 1998. [Online]. Available: <Go to ISI>://WOS:000073515700001.

[117] A. Banerjee, U. B. Chitnis, S. L. Jadhav, J. S. Bhawalkar, and S. Chaudhury, "Hypothesis testing, type I and type II errors," (in eng), *Ind Psychiatry J,* vol. 18, no. 2, pp. 127-131, 2009, doi: 10.4103/0972-6748.62274.

[118] D. L. Streiner, "Best (but oft-forgotten) practices: the multiple problems of multiplicity—whether and how to correct for many statistical tests," *The American Journal of Clinical Nutrition,* vol. 102, no. 4, pp. 721-728, 2015, doi: 10.3945/ajcn.115.113548.

[119] M. Intaglietta, "Vasomotion and flowmotion: physiological mechanisms and clinical evidence," *Vascular Medicine Review,* vol. 1, pp. 101-112, 1990.

[120] J. C. Frisbee *et al.*, "Increased peripheral vascular disease risk progressively constrains perfusion adaptability in the skeletal muscle microcirculation," *Am J Physiol Heart Circ Physiol,* vol. 310, no. 4, pp. H488-504, Feb 15 2016, doi: 10.1152/ajpheart.00790.2015.

[121] J. C. Frisbee, A. G. Goodwill, S. J. Frisbee, J. T. Butcher, F. Wu, and P. D. Chantler, "Microvascular perfusion heterogeneity contributes to peripheral vascular disease in metabolic syndrome," *J Physiol,* vol. 594, no. 8, pp. 2233-43, Apr 15 2016, doi: 10.1113/jphysiol.2014.285247.

[122] E. G. Salerud, T. Tenland, G. E. Nilsson, and P. A. Oberg, "RHYTHMICAL VARIATIONS IN HUMAN-SKIN BLOOD-FLOW," (in English), *International Journal of Microcirculation-Clinical and Experimental,* Article vol. 2, no. 2, pp. 91-102, 1983. [Online]. Available: <Go to ISI>://WOS:A1983QW01400002.

[123] A. Humeau, B. Buard, G. Mahe, D. Rousseau, F. Chapeau-Blondeau, and P. Abraham, "Multiscale entropy of laser Doppler flowmetry signals in healthy human subjects," (in English), *Med. Phys.,* Article vol. 37, no. 12, pp. 6142-6146, Dec 2010, doi: 10.1118/1.3512796.

[124] F. Y. Liao, D. W. Garrison, and Y. K. Jan, "Relationship between nonlinear properties of sacral skin blood flow oscillations and vasodilatory function in people at risk for pressure ulcers," (in English), *Microvascular Research,* Article vol. 80, no. 1, pp. 44-53, Jul 2010, doi: 10.1016/j.mvr.2010.03.009.

[125] L. S. Correa, E. Laciar, V. Mut, B. F. Giraldo, A. Torres, and Ieee, "Multi-parameter Analysis of ECG and Respiratory Flow Signals to Identify Success of Patients on Weaning Trials," in *2010 Annual International Conference of the Ieee Engineering in Medicine and Biology Society*, (IEEE Engineering in Medicine and Biology Society Conference Proceedings, 2010, pp. 6070-6073.

[126] F. Liao, W. D. O'Brien, Jr., and Y. K. Jan, "Assessing complexity of skin blood flow oscillations in response to locally applied heating and pressure in rats: implications for pressure ulcer risk," *Physica A,* vol. 392, no. 20, Oct 15 2013, doi: 10.1016/j.physa.2013.06.007.

[127] A. Humeau, G. Mahe, F. Chapeau-Blondeau, D. Rousseau, and P. Abraham, "Multiscale Analysis of Microvascular Blood Flow: A Multiscale Entropy Study of Laser Doppler Flowmetry Time Series," (in English), *Ieee Transactions on Biomedical Engineering,* Article vol. 58, no. 10, pp. 2970-2973, Oct 2011, doi: 10.1109/tbme.2011.2160865.

[128] K. Kalev, M. Bachmann, L. Orgo, J. Lass, H. Hinrikus, and Ieee, "Lempel-Ziv and Multiscale Lempel-Ziv Complexity in Depression," in *2015 37th Annual International Conference of the Ieee Engineering in Medicine and Biology Society*, (IEEE Engineering in Medicine and Biology Society Conference Proceedings, 2015, pp. 4158-4161.

[129] V. E. Papaioannou, I. G. Chouvarda, N. K. Maglaveras, and I. A. Pneumatikos, "Temperature variability analysis using wavelets and multiscale entropy in patients with systemic inflammatory response syndrome, sepsis, and septic shock," (in English), *Crit. Care,* Article vol. 16, no. 2, p. 15, 2012, Art no. R51, doi: 10.1186/cc11255.

[130] Y. T. Zhang, S. S. Wei, C. Di Maria, and C. Y. Liu, "Using Lempel-Ziv Complexity to Assess ECG Signal Quality," *Journal of Medical and Biological Engineering,* vol. 36, no. 5, pp. 625-634, Oct 2016, doi: 10.1007/s40846-016-0165-5.

[131] M. Costa and J. A. Healey, "Multiscale entropy analysis of complex heart rate dynamics: Discrimination of age and heart failure effects," in *Computers in Cardiology 2003, Vol 30*, vol. 30, A. Murray Ed., (Computers in Cardiology. New York: Ieee, 2003, pp. 705-708.

[132] A. Tharwat, T. Gaber, A. Ibrahim, and A. E. Hassanien, *Linear discriminant analysis: A detailed tutorial*. 2017, pp. 169-190.

[133] B. Gryglewska *et al.*, "Fractal dimensions of skin microcirculation flow in subjects with familial predisposition or newly diagnosed hypertension," *Cardiology Journal,* vol. 18, no. 1, pp. 26-32, Jan 2011. [Online]. Available: <Go to ISI>://WOS:000289320800005.

[134] M. Thanaj, A. J. Chipperfield, and G. F. Clough, "Multiscale Analysis of Microvascular Blood Flow and Oxygenation," Singapore, 2019: Springer Singapore, in World Congress on Medical Physics and Biomedical Engineering 2018, pp. 195-200.

[135] I. Barchetta *et al.*, "No effects of oral vitamin D supplementation on non-alcoholic fatty liver disease in patients with type 2 diabetes: a randomized, double-blind, placebo-controlled trial," *Bmc Medicine,* vol. 14, Jun 29 2016, Art no. 92, doi: 10.1186/s12916-016-0638-y.

[136] N. Chalasani *et al.*, "The diagnosis and management of non‐alcoholic fatty liver disease: Practice Guideline by the American Association for the Study of Liver Diseases, American College of Gastroenterology, and the American Gastroenterological Association," *Hepatology,* vol. 55, no. 6, pp. 2005-2023, 2012, doi: 10.1002/hep.25762.

[137] K. G. Tolman, V. Fonseca, A. Dalpiaz, and M. H. Tan, "Spectrum of liver disease in type 2 diabetes and management of patients with diabetes and liver disease," *Diabetes Care,* vol. 30, no. 3, pp. 734-743, Mar 2007, doi: 10.2337/dc06-1539.

[138] G. Targher and C. D. Byrne, "Nonalcoholic Fatty Liver Disease: A Novel Cardiometabolic Risk Factor for Type 2 Diabetes and Its Complications," *The Journal of Clinical Endocrinology & Metabolism,* vol. 98, no. 2, pp. 483-495, 2013, doi: 10.1210/jc.2012-3093.

[139] L. S. Bhatia, N. P. Curzen, P. C. Calder, and C. D. Byrne, "Non-alcoholic fatty liver disease: a new and important cardiovascular risk factor?," *European Heart Journal,* vol. 33, no. 10, pp. 1190-1200, 2012, doi: 10.1093/eurheartj/ehr453.

[140] A. J. Krentz, G. Clough, and C. D. Byrne, "Vascular Disease in the Metabolic Syndrome: Do We Need to Target the Microcirculation to Treat Large Vessel Disease?," *Journal of Vascular Research,* vol. 46, no. 6, pp. 515-526, 2009. [Online]. Available: https://www.karger.com/DOI/10.1159/000226220.

[141] M. Thanaj, A. J. Chipperfield, and G. F. Clough, "Analysis of microvascular blood flow and oxygenation: Discrimination between two haemodynamic steady states using nonlinear measures and multiscale analysis," *Comput. Biol. Med.,* vol. 102, pp. 157-167, 2018/11/01/ 2018, doi: https://doi.org/10.1016/j.compbiomed.2018.09.026.

[142] Clinicaltrials.gov. "Investigation of Synbiotic Treatment in NAFLD (INSYTE)." https://clinicaltrials.gov/ct2/show/NCT01680640?term=INSYTE&cond=NAFLD&rank=1 (accessed.

[143] Clinicaltrials.gov. "Treatment of Non Alcoholic Fatty Liver Disease With n-3 Fatty Acids." https://clinicaltrials.gov/ct2/show/NCT00760513?id=NCT00760513&rank=1 (accessed.

[144] E. Scorletti *et al.*, "Design and rationale of the WELCOME trial: A randomised, placebo controlled study to test the efficacy of purified long chain omega-3 fatty treatment in non-alcoholic fatty liver disease," *Contemporary Clinical Trials,* vol. 37, no. 2, pp. 301-311, 2014/03/01/ 2014, doi: https://doi.org/10.1016/j.cct.2014.02.002.

[145] G. S. Collins and D. G. Altman, "Predicting the 10 year risk of cardiovascular disease in the United Kingdom: independent and external validation of an updated version of QRISK2," *BMJ : British Medical Journal,* vol. 344, 2012, doi: 10.1136/bmj.e4181.

[146] A. L. F. d. A. Salgado, L. d. Carvalho, A. C. Oliveira, V. N. d. Santos, J. G. Vieira, and E. R. Parise, "Insulin resistance index (HOMA-IR) in the differentiation of patients with non-alcoholic fatty liver disease and healthy individuals," *Arquivos de Gastroenterologia,* vol. 47, pp. 165-169, 2010. [Online]. Available: http://www.scielo.br/scielo.php?script=sci_arttext&pid=S0004-28032010000200009&nrm=iso.

[147] P. E. Meyer, F. Lafitte, and G. Bontempi, "minet: A R/Bioconductor Package for Inferring Large Transcriptional Networks Using Mutual Information," *BMC Bioinformatics,* journal article vol. 9, no. 1, p. 461, October 29 2008, doi: 10.1186/1471-2105-9-461.

[148] T. M. Cover and J. A. Thomas, *Elements of information theory*. New York: Wiley (in English), 1991.

[149] A. Mora, R. Sicari, L. Cortigiani, C. Carpeggiani, E. Picano, and E. Capobianco, "Prognostic models in coronary artery disease: Cox and network approaches," *Royal Society Open Science,* vol. 2, no. 2, p. 140270, 02/11

08/27/received

01/13/accepted 2015, doi: 10.1098/rsos.140270.

[150] S. Theodoridis and K. Koutroumbas, *Pattern Recognition, 4rth Edition* (Pattern Recognition, 4rth Edition). Amsterdam: Elsevier Science Bv (in English), 2009, pp. 1-961.

[151] D. N. Granger, S. F. Rodrigues, A. Yildirim, and E. Y. Senchenkova, "Microvascular Responses to Cardiovascular Risk Factors," *Microcirculation,* vol. 17, no. 3, pp. 192-205, 2010, doi: 10.1111/j.1549-8719.2009.00015.x.

[152] G. Clough, V. L'Esperance, M. Turzyniecka, A. Krentz, and C. D. Byrne, *Decreased microvascular funtional vasodilatory reserve and features of the metabolic syndrome*. 2008.

[153] E. Figueiras, M. Roustit, S. Semedo, L. F. R. Ferreira, J. L. Crascowski, and A. Humeau, "Sample entropy of laser Doppler flowmetry signals increases in patients with systemic sclerosis," *Microvascular Research,* vol. 82, no. 2, pp. 152-155, 2011/09/01/ 2011, doi: https://doi.org/10.1016/j.mvr.2011.05.007.

[154] J. J. Valletta, "Dynamic Modelling of the Effect of Habitual Physical Activity on Glycaemic Control and the Microvasculature in people with Type 1 Diabetes," Doctor of Philosophy, Faculty of Engineering and Environment and Faculty of Medicine, University of Southamton, 2011.

[155] C. R. Pozzobon, R. A. O. C. Gismondi, R. Bedirian, M. C. Ladeira, M. F. Neves, and W. Oigman, "Functional vascular study in hypertensive subjects with type 2 diabetes using losartan or amlodipine," (in eng), *Arq Bras Cardiol,* vol. 103, no. 1, pp. 51-59, 2014/07// 2014, doi: 10.5935/abc.20140089.

[156] A. J. Chipperfield, M. Thanaj, E. Scorletti, C. D. Byrne, and G. F. Clough, "Multi-domain analysis of microvascular flow motion dynamics in NAFLD," *Microcirculation,* vol. 0, no. 0, p. e12538, 2019/02/25 2019, doi: 10.1111/micc.12538.

[157] V. Ticcinelli *et al.*, "Coherence and Coupling Functions Reveal Microvascular Impairment in Treated Hypertension," (in English), *Frontiers in Physiology,* Original Research vol. 8, no. 749, 2017-October-13 2017, doi: 10.3389/fphys.2017.00749.

[158] A. J. Ibanez-Molina, S. Iglesias-Parro, M. F. Soriano, and J. I. Aznarte, "Multiscale Lempel-Ziv complexity for EEG measures," *Clinical Neurophysiology,* vol. 126, no. 3, pp. 541-548, Mar 2015, doi: 10.1016/j.clinph.2014.07.012.

[159] P. N. Belhumeur, J. P. Hespanha, and D. J. Kriegman, "Eigenfaces vs. Fisherfaces: recognition using class specific linear projection," *IEEE Transactions on Pattern Analysis and Machine Intelligence,* vol. 19, no. 7, pp. 711-720, 1997, doi: 10.1109/34.598228.

[160] Y. Jian, A. F. Frangi, Y. Jing-Yu, Z. David, and J. Zhong, "KPCA plus LDA: a complete kernel Fisher discriminant framework for feature extraction and recognition," *IEEE Transactions on Pattern Analysis and Machine Intelligence,* vol. 27, no. 2, pp. 230-244, 2005, doi: 10.1109/TPAMI.2005.33.

[161] S. Mika, G. Ratsch, J. Weston, B. Scholkopf, A. Smola, and K. Muller, "Constructing descriptive and discriminative nonlinear features: Rayleigh coefficients in kernel feature spaces," *IEEE Transactions on Pattern Analysis and Machine Intelligence,* vol. 25, no. 5, pp. 623-628, 2003, doi: 10.1109/TPAMI.2003.1195996.

[162] C. Xilin, Y. Jie, Z. Jing, and A. Waibel, "Automatic detection and recognition of signs from natural scenes," *IEEE Transactions on Image Processing,* vol. 13, no. 1, pp. 87-99, 2004, doi: 10.1109/TIP.2003.819223.

[163] R. Sassi *et al.*, *Advances in heart rate variability signal analysis: Joint position statement by the e-Cardiology ESC Working Group and the European Heart Rhythm Association co-endorsed by the Asia Pacific Heart Rhythm Society*. 2015.

[164] A. E. Simms, J. F. R. Paton, A. M. Allen, and A. E. Pickering, "Is augmented central respiratory-sympathetic coupling involved in the generation of hypertension?," *Respiratory Physiology & Neurobiology,* Article vol. 174, pp. 89-97, 1 2010, doi: 10.1016/j.resp.2010.07.010.

[165] D. Francois, V. Wertz, and M. Verleysen, *The permutation test for feature selection by mutual information* (14th European Symposium on Artificial Neural Networks, ESANN 2006). 2007, pp. 239-44.

[166] A. J. Butte and I. S. Kohane, *Mutual information relevance networks: Functional genomic clustering using pairwise entropy measurements*. 2000, pp. 418-29.

[167] L. Paninski, "Estimation of Entropy and Mutual Information," vol. 15, no. 6, pp. 1191-1253, 2003, doi: 10.1162/089976603321780272.

[168] J. Zhuang, W. Truccolo, C. Vargas-Irwin, and J. P. Donoghue, "Decoding 3-D Reach and Grasp Kinematics From High-Frequency Local Field Potentials in Primate Primary Motor Cortex," *IEEE Transactions on Biomedical Engineering,* vol. 57, no. 7, pp. 1774-1784, 2010, doi: 10.1109/TBME.2010.2047015.

[169] P. Hanchuan, L. Fuhui, and C. Ding, "Feature selection based on mutual information criteria of max-dependency, max-relevance, and min-redundancy," *IEEE Transactions on Pattern Analysis and Machine Intelligence,* vol. 27, no. 8, pp. 1226-1238, 2005, doi: 10.1109/TPAMI.2005.159.

[170] D. J. Watts and S. H. Strogatz, "Collective dynamics of 'small-world' networks," *Nature,* vol. 393, no. 6684, pp. 440-442, 1998/06/01 1998, doi: 10.1038/30918.

[171] G. Tononi, G. M. Edelman, and O. Sporns, "Complexity and coherency: integrating information in the brain," *Trends in Cognitive Sciences,* vol. 2, no. 12, pp. 474-484, 1998/12/01/ 1998, doi: https://doi.org/10.1016/S1364-6613(98)01259-5.

[172] P. J. Aston, M. I. Christie, Y. H. Huang, and M. Nandi, "Beyond HRV: attractor reconstruction using the entire cardiovascular waveform data for novel feature extraction," *Physiological measurement,* vol. 39, no. 2, pp. 024001-024001, 2018, doi: 10.1088/1361-6579/aaa93d.

[173] F. Takens, "Detecting Strange Attractors in Turbulence," in *Dynamical Systems and Turbulence, Warwick 1980, Lecture Notes in Mathematics* vol. 898, ed: Springer, Berlin, 1981, pp. 366-381.

[174] M. Casdagli, S. Eubank, J. D. Farmer, and J. Gibson, "State space reconstruction in the presence of noise," *Physica D: Nonlinear Phenomena,* vol. 51, no. 1, pp. 52-98, 1991/08/01/ 1991, doi: https://doi.org/10.1016/0167-2789(91)90222-U.

[175] M. Nandi, J. Venton, and P. Aston, "A novel method to quantify arterial pulse waveform morphology: attractor reconstruction for physiologists and clinicians," vol. 39, p. 104008, 2018, doi: 10.1088/1361-6579/aae46a.

[176] D. Dutt and S. M. Krishnan, *Application of phase space technique to the analysis of cardiovascular signals*. 1999.

[177] A. H. D. Vélez, H. G. González-Hernández, and B. R. Guerra, "Attractor reconstruction for plethysmographic biosignals," in *2014 International Conference on Electronics, Communications and Computers (CONIELECOMP)*, 26-28 Feb. 2014 2014, pp. 94-98, doi: 10.1109/CONIELECOMP.2014.6808574.

[178] X. Wang, J. Meng, G. Tan, and L. Zou, "Research on the relation of EEG signal chaos characteristics with high-level intelligence activity of human brain," *Nonlinear Biomedical Physics,* vol. 4, no. 1, p. 2, 2010/04/27 2010, doi: 10.1186/1753-4631-4-2.

[179] D. Parthimos, O. Schmiedel, J. N. Harvey, and T. M. Griffith, "Deterministic nonlinear features of cutaneous perfusion are lost in diabetic subjects with neuropathy," *Microvascular Research,* vol. 82, no. 1, pp. 42-51, Jul 2011, doi: 10.1016/j.mvr.2011.02.006.

[180] C. González, E. W. Jensen, P. L. Gambús, and M. Vallverdú, "Poincaré plot analysis of cerebral blood flow signals: Feature extraction and classification methods for apnea detection," *PLOS ONE,* vol. 13, no. 12, p. e0208642, 2018, doi: 10.1371/journal.pone.0208642.

[181] M. A. Basarab, N. S. Konnova, D. A. Basarab, and D. D. Matsievskiy, "Digital signal processing of the Doppler blood flow meter using the methods of nonlinear dynamics," in *2017 Progress In Electromagnetics Research Symposium - Spring (PIERS)*, 22-25 May 2017 2017, pp. 1715-1720, doi: 10.1109/PIERS.2017.8262026.

[182] L. Mangin, G. Lesèche, A. Duprey, and C. Clerici, "Ventilatory Chaos Is Impaired in Carotid Atherosclerosis," *PLoS ONE,* vol. 6, no. 1, p. e16297, 01/28

09/19/received

12/20/accepted 2011, doi: 10.1371/journal.pone.0016297.

[183] H. N. Shan, Z. Q. Wang, J. Wang, P. L. Wang, and Ieee, "Comparison and analysis of the Lyapunov exponents of blood flow signal of healthy and stenotic artery," in *2004 8th International Conference on Control, Automation, Robotics and Vision, Vols 1-3*, (International Conference on Control Automation Robotics and Vision, 2004, pp. 211-216.

[184] R. Carvajal, N. Wessel, M. Vallverdú, P. Caminal, and A. Voss, "Correlation dimension analysis of heart rate variability in patients with dilated cardiomyopathy," *Computer Methods and Programs in Biomedicine,* vol. 78, no. 2, pp. 133-140, 2005/05/01/ 2005, doi: https://doi.org/10.1016/j.cmpb.2005.01.004.

[185] R. Carvajal *et al.*, "Dimensional analysis of HRV in hypertrophic cardiomyopathy patients," *IEEE Engineering in Medicine and Biology Magazine,* vol. 21, no. 4, pp. 71-78, 2002, doi: 10.1109/MEMB.2002.1032644.

[186] W. S. Tirsch, M. Keidel, S. Perz, H. Scherb, and G. Sommer, "Inverse covariation of spectral density and correlation dimension in cyclic EEG dynamics of the human brain," *Biological Cybernetics,* vol. 82, no. 1, pp. 1-14, Jan 2000, doi: 10.1007/pl00007957.

[187] P. Grassberger, T. Schreiber, and C. Schaffrath, "NONLINEAR TIME SEQUENCE ANALYSIS," *International Journal of Bifurcation and Chaos,* vol. 01, no. 03, pp. 521-547, 1991/09/01 1991, doi: 10.1142/S0218127491000403.

[188] P. J. Aston, M. Nandi, M. I. Christie, and Y. H. Huang, "Comparison of attractor reconstruction and HRV methods for analysing blood pressure data," in *Computing in Cardiology 2014*, 7-10 Sept. 2014 2014, pp. 437-440.

[189] P. H. Charlton *et al.*, "Measurement of cardiovascular state using attractor reconstruction analysis," in *2015 23rd European Signal Processing Conference (EUSIPCO)*, 31 Aug.-4 Sept. 2015 2015, pp. 444-448, doi: 10.1109/EUSIPCO.2015.7362422.

[190] J. V Lyle *et al.*, "Beyond HRV: Analysis of ECG signals using attractor reconstruction," 2018.

[191] M. T. Rosenstein, J. J. Collins, and C. J. De Luca, "Reconstruction expansion as a geometry-based framework for choosing proper delay times," *Physica D: Nonlinear Phenomena,* vol. 73, no. 1, pp. 82-98, 1994/05/15/ 1994, doi: https://doi.org/10.1016/0167-2789(94)90226-7.

[192] J. P. Eckmann and D. Ruelle, "Ergodic theory of chaos and strange attractors," *Reviews of Modern Physics,* vol. 57, no. 3, pp. 617-656, 07/01/ 1985, doi: 10.1103/RevModPhys.57.617.

[193] W. Liebert, K. Pawelzik, and H. G. Schuster, "Optimal Embeddings of Chaotic Attractors from Topological Considerations," *Europhysics Letters (EPL),* vol. 14, no. 6, pp. 521-526, 1991/03/15 1991, doi: 10.1209/0295-5075/14/6/004.

[194] H. S. Kim, R. Eykholt, and J. D. Salas, "Nonlinear dynamics, delay times, and embedding windows," *Physica D,* vol. 127, no. 1-2, pp. 48-60, Mar 1 1999, doi: 10.1016/s0167-2789(98)00240-1.

[195] M. B. Kennel, R. Brown, and H. D. I. Abarbanel, "Determining embedding dimension for phase-space reconstruction using a geometrical construction," *Physical Review A,* vol. 45, no. 6, pp. 3403-3411, 03/01/ 1992, doi: 10.1103/PhysRevA.45.3403.

[196] M. Kennel and H. D I Abarbanel, *False neighbors and false strands: A reliable minimum embedding dimension algorithm*. 2002, p. 026209.

[197] L. Y. Cao, "Practical method for determining the minimum embedding dimension of a scalar time series," *Physica D,* vol. 110, no. 1-2, pp. 43-50, Dec 1 1997, doi: 10.1016/s0167-2789(97)00118-8.

[198] J. E. Jackson, *A User's Guide to Principal Components* (John Wiley & Sons). New York, NY, 1991.

[199] M. Lei, Z. Wang, and Z. Feng, "A method of embedding dimension estimation based on symplectic geometry," *Physics Letters A,* vol. 303, no. 2, pp. 179-189, 2002/10/14/ 2002, doi: https://doi.org/10.1016/S0375-9601(02)01164-7.

[200] A. I. Mees, P. Rapp, and L. S. Jennings, *Singular Value Decomposition and Embedding Dimension*. 1987, pp. 340-346.

[201] P. Grassberger and I. Procaccia, "Characterization of Strange Attractors," *Physical Review Letters,* vol. 50, no. 5, pp. 346-349, 01/31/ 1983, doi: 10.1103/PhysRevLett.50.346.

[202] H. D. I. Abarbanel, R. Brown, J. J. Sidorowich, and L. S. Tsimring, "The analysis of observed chaotic data in physical systems," *Reviews of Modern Physics,* vol. 65, no. 4, pp. 1331-1392, 10/01/ 1993, doi: 10.1103/RevModPhys.65.1331.

[203] L. M. Pecora, L. Moniz, J. Nichols, and T. L. Carroll, "A unified approach to attractor reconstruction," *Chaos: An Interdisciplinary Journal of Nonlinear Science,* vol. 17, no. 1, p. 013110, 2007/03/01 2007, doi: 10.1063/1.2430294.

[204] S. Sato, M. Sano, and Y. Sawada, "Practical Methods of Measuring the Generalized Dimension and the Largest Lyapunov Exponent in High Dimensional Chaotic Systems," *Progress of Theoretical Physics,* vol. 77, no. 1, pp. 1-5, 1987, doi: 10.1143/PTP.77.1.

[205] M. T. Rosenstein, J. J. Collins, and C. J. De Luca, "A practical method for calculating largest Lyapunov exponents from small data sets," *Physica D: Nonlinear Phenomena,* vol. 65, no. 1, pp. 117-134, 1993/05/15/ 1993, doi: https://doi.org/10.1016/0167-2789(93)90009-P.

[206] J. Theiler, S. Eubank, A. Longtin, B. Galdrikian, and J. Doyne Farmer, "Testing for nonlinearity in time series: the method of surrogate data," *Physica D: Nonlinear Phenomena,* vol. 58, no. 1, pp. 77-94, 1992/09/15/ 1992, doi: https://doi.org/10.1016/0167-2789(92)90102-S.

[207] T. Schreiber and A. Schmitz, "Improved Surrogate Data for Nonlinearity Tests," *Physical Review Letters,* vol. 77, no. 4, pp. 635-638, 07/22/ 1996, doi: 10.1103/PhysRevLett.77.635.

[208] P. E. Rapp, "A guide to dynamical analysis," *Integrative Physiological and Behavioral Science,* vol. 29, no. 3, pp. 311-327, 1994/07/01 1994, doi: 10.1007/BF02691335.

[209] M. Kaur, B. Singh, and Seema, *Comparison of different approaches for removal of Baseline wander from ECG signal*. IJCA Proc. Int. Conf. Emerging Trends in Technology, 2011, pp. 30-4.

[210] A. Fasano, V. Villani, and L. Vollero, "Baseline wander estimation and removal by quadratic variation reduction," in *2011 Annual International Conference of the IEEE Engineering in Medicine and Biology Society*, 30 Aug.-3 Sept. 2011 2011, pp. 977-980, doi: 10.1109/IEMBS.2011.6090221.

[211] A. K. Bhoi, S. Sarkar, P. Mishra, and G. Savita, *Pre-processing of PPG Signal with Performance based Methods*. 2019.

[212] M. Christie *et al.*, *Mathematical Modelling of Heart Rate Changes in the Mouse*. 2013.

[213] B. Silverman, *Density Estimation For Statistics And Data Analysis*. 1986.

[214] A. Papoulis and U. Pillai, *Probability, random variables and stochastic processes*, Fourth ed. New York: McGraw-Hill, 2001.

[215] S. Theodoridis, *Machine Learning: A Bayesian and Optimization Perspective*. Elsevier, 2015.

[216] A. Gatouillat *et al.*, "Cognitive tasks during walking affect cerebral blood flow signal features in middle cerebral arteries and their correlation to gait characteristics," (in eng), *Behav Brain Funct,* vol. 11, no. 1, pp. 29-29, 2015, doi: 10.1186/s12993-015-0073-9.

[217] J. Antoni, "The spectral kurtosis: a useful tool for characterising non-stationary signals," *Mechanical Systems and Signal Processing,* vol. 20, no. 2, pp. 282-307, 2006/02/01/ 2006, doi: https://doi.org/10.1016/j.ymssp.2004.09.001.

[218] H. Li *et al.*, "Heartbeat classification using different classifiers with non-linear feature extraction," vol. 38, no. 9, pp. 1033-1040, 2016, doi: 10.1177/0142331215620697.